Karlsruher Institut für Technologie

A holistic framework for electromagnetic scattering simulations based on the T-matrix method

Zur Erlangung des akademischen Grades eines

DOKTORS DER NATURWISSENSCHAFTEN (Dr. rer. nat.)

von der KIT-Fakultät für Physik des
Karlsruher Instituts für Technologie (KIT)
angenommene

DISSERTATION

von

M. Sc. Dominik Timo Beutel

am Institut für Theoretische Festkörperphysik

Tag der mündlichen Prüfung:	8. Dezember 2023
Referent:	Prof. Dr. Carsten Rockstuhl
Korreferent:	Prof. Dr. Vassilios Yannopapas

This work (with the exception of reprinted or adapted tables and figures for which the copyright is held by the respective journal) is licensed under a Creative Commons "Attribution-ShareAlike 4.0 International" license. To view a copy of the license, visit `https://creativecommons.org/licenses/by-sa/4.0/deed.en`.

Abstract

We investigate electromagnetic scattering phenomena by further developing and using the T-matrix method. Capitalizing on the analytical properties of spherical or cylindrical wave solutions to expand electromagnetic fields in a basis adapted to the localized nature of a scatterer, we can efficiently study the interaction between scatterers in finite, disordered or infinite, periodic arrangements. Thereby, we can describe a wide variety of artificial photonic materials used for applications such as sensing, imaging, or photonic computing. The chosen T-matrix method approach simplifies the analysis by separating the shape and material properties of the scatterers from their arrangement and lattice structure. Besides providing a solid theoretical framework to obtain analytical insights into these photonic materials, our approach is also an extraordinary computational tool that allows performing parameter studies or bridging of different length scales efficiently.

However, especially for periodic structures that we emphasize in this thesis to some extent, the success of the T-matrix method sensitively hinges on efficient expressions to calculate the arising lattice sums. Using Ewald's method, we derive expressions that can consider complex unit cells, i.e., unit cells containing multiple scatterers, in one-, two-, and three-dimensional lattices. These expressions converge orders of magnitude faster and are numerically more robust than direct summation approaches.

The lattice sums and functions related to the T-matrix method are implemented in a novel open-source program *treams*, which provides a holistic framework for various computations using T-matrices in the spherical and cylindrical basis and, additionally, an S-matrix description in the plane wave basis. Combining these different basis sets unlocks the opportunity to explore a wide range of applications. Furthermore, *treams* fully supports chiral material parameters.

Besides the implementation, we additionally present the application of this newly developed computational tool to selected problems. We outline its use in large parameter studies to design helicity-preserving cavities that enhance chiral signals, for the multi-scale modeling of molecular materials, and for the homogenization of artificial photonic materials made from periodically arranged constituents. Moreover, in connection with additional methods to compute the focusing with high-aperture lenses, we show how this framework can be used for highly specialized applications in multi-photon direct laser writing. Other applications of the presented methods include the simulation of moiré lattices, the investigation of anti-reflective coatings for solar cells, the analytical investigation of metasurface properties, the inverse design of bound states in the continuum, or the simulation of self-assembled plasmonic nanostructures.

Many major accomplishments were already achieved while developing this framework and applying it to selected contemporary challenges in computational nanophotonics. However, many more aspects remain to be explored, among which the description of non-linear photonic materials would be one example. Also, translating the current framework to other physical systems covered by similar equations would be a fascinating research endeavor.

Zusammenfassung

Wir untersuchen elektromagnetische Streuphänomene, indem wir die T-Matrix-Methode weiterentwickeln und anwenden. Wir profitieren dabei von den analytischen Eigenschaften der zugrundeliegenden sphärischen oder zylindrischen Wellen, um die Wechselwirkung zwischen Streuern in endlichen, ungeordneten und unendlichen, periodischen Anordnungen zu berechnen. Dadurch können wir künstliche photonische Materialien, die für Anwendung wie Sensoren, Bildgebung, oder dem optische Rechnen verwendet werden, abbilden. Die gewählte T-Matrix-Methode vereinfacht die Analyse, indem die Form und Materialeigenschaften der Streuer von ihrer Anordnung und der Gitterstruktur getrennt werden. Neben der Bereitstellung eines fundierten theoretischen Rahmens, um analytische Erkenntnisse zu gewinnen, sind die hier entwickelten Methoden ein außergewöhnliches Rechenwerkzeug, um Parameterstudien oder die Multi-Skalen-Modellierung effizient durchzuführen.

Der Erfolg der T-Matrix-Methode, gerade für periodische Strukturen, die wir in dieser These besonders unterstreichen, hängt jedoch von effizienten Ausdrücken für die auftretenden Gittersummen ab. Unter Verwendung der Ewaldschen Methode leiten wir Ausdrücke für komplexe Einheitszellen, d.h. Einheitszellen die mehrere Streuer enthalten, in ein-, zwei- und dreidimensionalen Gittern her. Diese Ausdrücke konvergieren um Größenordnungen schneller und sind numerisch stabiler als direkte Summen.

Alle entwickelten Funktionen sind in einem neuen quelloffenen Programm, *treams*, implementiert, das ein umfassendes Programmiergerüst für Berechnungen mit T-Matrizen in der sphärischen und zylindrischen Basis und zusätzlich in der S-Matrix-Beschreibung in der Ebene-Wellen-Basis bereitstellt. Die Kombination dieser verschiedenen Basen eröffnet die Möglichkeit, eine große Auswahl an Anwendung zu untersuchen. Des Weiteren werden chirale Materialparameter von *treams* vollständig unterstützt.

Neben der Implementierung stellen wir auch die Anwendung dieses neuen Programms auf ausgewählte Probleme vor. Wir skizzieren die Verwendung von *treams* in großen Parameterstudien für den Entwurf von helizitätserhaltenden Resonatoren zur Verstärkung chiraler Signale, für die Multi-Skalen-Modellierung molekularer Materialien und für die Homogenisierung von künstlichen photonischen Materialien aus periodisch angeordneten Elementarzellen. Außerdem zeigen wir, wie diese Methode für spezifische Anwendungen im Multiphotonen-Direct-Laser-Writing in Verbindung mit Verfahren zur Berechnung der Fokussierung mit Linsen großer numerische Apertur verwendet werden kann. Andere Anwendungen der vorgestellten Methoden beinhalten die Simulation von Moirégittern, die Untersuchung antireflektierender Beschichtungen für Solarzellen, die analytische Untersuchung der Eigenschaften von Metaoberflächen, das inverse Design von gebunden Zuständen im Kontinuum oder die Simulation von selbst-assemblierten Nanostrukturen.

Viele wesentliche Ergebnisse wurden bereits in der Entwicklung dieses Rahmens und seiner Anwendung auf ausgewählte Probleme in der Nanophotonik erreicht. Jedoch verbleiben viele Aspekte zur weiteren Untersuchung, z. B. die Beschreibung nichtlinearer photonischer Materialien. Zudem wäre seine Übertragung auf andere physikalische Systeme, die von ähnlichen Gleichungen beschrieben werden, ein faszinierendes Forschungsvorhaben.

Publications

As part of the work on this thesis, I was involved in the research published in the peer-reviewed articles and conference publications listed below. The publications set in bold contribute to the content of the thesis.

Peer-reviewed articles

[P1] M. A. A. Abouelatta, A. Safari, M. Z. Alam, X. Garcia-Santiago, D. Beutel, L. Cheng, R. W. Boyd, C. Rockstuhl, and R. Alaee, “Optically tunable bianisotropy in a sphere made from an epsilon-near-zero material,” Optics Letters **48**, 783–786 (2023).

[P2] **D. Beutel, P. Scott, M. Wegener, C. Rockstuhl, and I. Fernandez-Corbaton, “Enhancing the optical rotation of chiral molecules using helicity preserving all-dielectric metasurfaces,” Applied Physics Letters 118, 221108 (2021).**

[P3] D. Beutel, A. Groner, C. Rockstuhl, C. Rockstuhl, and I. Fernandez-Corbaton, “Efficient simulation of biperiodic, layered structures based on the T-matrix method,” Journal of the Optical Society of America B **38**, 1782–1791 (2021).

[P4] **D. Beutel, I. Fernandez-Corbaton, and C. Rockstuhl, “Unified lattice sums accommodating multiple sublattices for solutions of the Helmholtz equation in two and three dimensions,” Physical Review A 107, 013508 (2023).**

[P5] D. Dams, D. Beutel, X. Garcia-Santiago, C. Rockstuhl, and R. Alaee, “Moiré flat bands in strongly coupled atomic arrays,” Optical Materials Express **13**, 2003–2019 (2023).

[P6] J. Feis, D. Beutel, J. Köpfler, X. Garcia-Santiago, C. Rockstuhl, M. Wegener, and I. Fernandez-Corbaton, “Helicity-Preserving Optical Cavity Modes for Enhanced Sensing of Chiral Molecules,” Physical Review Letters **124**, 033201 (2020).

[P7] I. Fernandez-Corbaton, D. Beutel, C. Rockstuhl, A. Pausch, and W. Klopper, “Computation of electromagnetic properties of molecular ensembles,” ChemPhysChem **21**, 878–887 (2020).

[P8] P. Garg, A. G. Lamprianidis, D. Beutel, T. Karamanos, B. Verfürth, and C. Rockstuhl, “Modeling four-dimensional metamaterials: a T-matrix approach to describe time-varying metasurfaces,” Optics Express **30**, 45832–45847 (2022).

[P9] S. Gladyshev, T. D. Karamanos, L. Kuhn, D. Beutel, T. Weiss, C. Rockstuhl, and A. Bogdanov, “Inverse design of all-dielectric metasurfaces with accidental bound states in the continuum,” Nanophotonics **12**, 3767–3779 (2023).

[P10] R. Grillo, D. Beutel, U. Cataldi, C. Rockstuhl, and T. Bürgi, “Self-Assembled Arrays of Gold Nanorod-Decorated Dielectric Microspheres with a Magnetic Dipole Response in the Visible Range for Perfect Lensing and Cloaking Applications,” ACS Applied Nano Materials **3**, 6108–6117 (2020).

[P11] D. Grzelak, M. Tupikowska, D. Vila-Liarte, D. Beutel, M. Bagiński, S. Parzyszek, M. Góra, C. Rockstuhl, L. M. Liz-Marzán, and W. Lewandowski, “Liquid Crystal Templated Chiral Plasmonic Films with Dynamic Tunability and Moldability,” Advanced Functional Materials **32**, 2111280 (2022).

[P12] **A. Münchinger, V. Hahn, D. Beutel, S. Woska, J. Monti, C. Rockstuhl, E. Blasco, and M. Wegener, “Multi-Photon 4D Printing of Complex Liquid Crystalline Microstructures by In Situ Alignment Using Electric Fields,” Advanced Materials Technologies 7, 2100944 (2022).**

[P13] M. Pawlak, M. Bagiński, P. Llombart, D. Beutel, G. González-Rubio, E. Górecka, C. Rockstuhl, J. Mieczkowski, D. Pociecha, and W. Lewandowski, “Tuneable helices of plasmonic nanoparticles using liquid crystal templates: molecular dynamics investigation of an unusual odd–even effect in liquid crystalline dimers,” Chemical Communications **58**, 7364–7367 (2022).

[P14] A. Rahimzadegan, T. D. Karamanos, R. Alaee, A. G. Lamprianidis, D. Beutel, R. W. Boyd, and C. Rockstuhl, “A Comprehensive Multipolar Theory for Periodic Metasurfaces,” Advanced Optical Materials, 2102059 (2022).

[P15] P. Scott, X. Garcia-Santiago, D. Beutel, C. Rockstuhl, M. Wegener, and I. Fernandez-Corbaton, “On enhanced sensing of chiral molecules in optical cavities,” Applied Physics Reviews **7**, 041413 (2020).

[P16] D. Theobald, D. Beutel, L. Borgmann, H. Mescher, G. Gomard, C. Rockstuhl, and U. Lemmer, “Simulation of light scattering in large, disordered nanostructures using a periodic T-matrix method,” Journal of Quantitative Spectroscopy and Radiative Transfer **272**, 107802 (2021).

[P17] S. Woska, A. Münchinger, D. Beutel, E. Blasco, E. Blasco, J. Hessenauer, O. Karayel, P. Rietz, S. Pfleging, R. Oberle, C. Rockstuhl, M. Wegener, and H. Kalt, “Tunable photonic devices by 3D laser printing of liquid crystal elastomers,” Optical Materials Express **10**, 2928–2943 (2020).

[P18] **B. Zerulla, M. Krstić, D. Beutel, C. Holzer, C. Wöll, C. Rockstuhl, and I. Fernandez-Corbaton, “A Multi-Scale Approach for Modeling the Optical Response of Molecular Materials Inside Cavities,” Advanced Materials 34, 2200350 (2022).**

[P19] B. Zerulla, C. Li, D. Beutel, S. Oßwald, C. Holzer, J. Bürck, S. Bräse, C. Wöll, I. Fernandez-Corbaton, L. Heinke, C. Rockstuhl, and M. Krstić, “Exploring Functional Photonic Devices made from a Chiral Metal–Organic Framework Material by a Multiscale Computational Method,” Advanced Functional Materials **2023**, 2301093 (2023).

[P20] **B. Zerulla, R. Venkitakrishnan, D. Beutel, M. Krstić, C. Holzer, C. Rockstuhl, and I. Fernandez-Corbaton, “A T-Matrix Based Approach to Homogenize Artificial Materials,” Advanced Optical Materials 11, 2201564 (2023).**

[P21] **R. Zvagelsky, F. Mayer, D. Beutel, C. Rockstuhl, G. Gomard, and M. Wegener, “Towards *in-situ* diagnostics of multi-photon 3D laser printing using optical coherence tomography,” Light: Advanced Manufacturing 3, 1 (2022).**

Articles submitted for review

[S1] **D. Beutel, I. Fernandez-Corbaton, and C. Rockstuhl, “Treams – A T-matrix scattering code for nanophotonic computations,” `10.48550/arXiv.2309.03182` (2023), preprint.**

[S2] B. Zerulla, D. Beutel, C. Holzer, I. Fernandez-Corbaton, C. Rockstuhl, and M. Krstić, “A Multi-Scale Approach to Simulate the Nonlinear Optical Response of Molecular Nanomaterials,” `10.48550/arXiv.2308.16625` (2023), preprint.

Conference publications

[C1] D. Beutel, A. Groner, T. Höß, C. Rockstuhl, and I. Fernandez-Corbaton, “Efficient Simulation of Bi-periodic, Layered Structures with the T-Matrix Method,” in 2020 Fourteenth International Congress on Artificial Materials for Novel Wave Phenomena (Metamaterials) (Sept. 2020), pp. 110–112.

[C2] D. Beutel, C. Rockstuhl, and I. Fernandez-Corbaton, “T-Matrix based Scattering Analysis of Photonic Materials with Periodicity in Different Dimensions,” EPJ Web of Conferences **266**, 05003 (2022).

[C3] J. Feis, D. Beutel, J. Köpfler, X. Garcia-Santiago, C. Rockstuhl, M. Wegener, and I. Fernandez-Corbaton, “An Achiral Optical Cavity with Helicity-Preserving Modes for Enhanced Sensing of Chiral Molecules,” in Light-Matter Interactions Towards the Nanoscale, edited by M. Cesaria, A. Calà Lesina, and J. Collins, NATO Science for Peace and Security Series B: Physics and Biophysics (2022), pp. 317–319.

[C4] I. Fernandez-Corbaton, F. Graf, J. Feis, J. Koepfler, D. Beutel, X. Garcia-Santiago, C. Rockstuhl, and M. Wegener, “Helicity preserving dielectric metasurfaces for enhanced detection of chiral molecules (Conference Presentation),” in Metamaterials, Metadevices, and Metasystems 2019, Vol. 11080 (Sept. 9, 2019), 110800S.

[C5] I. Fernandez-Corbaton, J. Feis, J. Koepfler, D. Beutel, X. Garcia-Santiago, C. Rockstuhl, and M. Wegener, “Helicity-preserving optical cavity modes for enhanced sensing of chiral molecules (Conference Presentation),” in Metamaterials XII, Vol. 11344 (Apr. 2, 2020), p. 113440C.

[C6] T. D. Karamanos, D. Beutel, and C. Rockstuhl, “Multipolar analysis of quasi bound states in the continuum in a dielectric metasurface,” in 2021 Fifteenth International Congress on Artificial Materials for Novel Wave Phenomena (Metamaterials) (Sept. 2021), pp. 191–193.

[C7] M. Krstić, C. Holzer, B. Zerulla, D. Beutel, C. Li, L. Heinke, C. Wöll, I. Fernandez-Corbaton, and C. Rockstuhl, “How can (TD-)DFT improve multi-scale optical simulations of novel nano-materials and devices?” In CLEO 2023 (2023), paper FM1E.3 (May 7, 2023), FM1E.3.

[C8] A. Münchinger, E. Blasco, V. Hahn, D. Beutel, S. Woska, J. Monti, C. Rockstuhl, and M. Wegener, “3D two-photon printing of hetero-microstructures by in-situ alignment of liquid-crystal elastomers,” in Laser 3D Manufacturing VIII, Vol. 11677 (Mar. 5, 2021), p. 116770I.

[C9] C. Rockstuhl, A. Rahimzadegan, T. D. Karamanos, R. Alaee, A. G. Lamprianidis, D. Beutel, R. W. Boyd, C. Holzer, M. Krstić, B. Zerulla, and I. Fernandez-Corbaton, “A comprehensive multipolar theory for metasurfaces and metamaterials,” in Metamaterials XIII, Vol. PC12130 (May 24, 2022), PC1213001.

[C10] P. Scott, X. Garcia-Santiago, D. Beutel, C. Rockstuhl, M. Wegener, and I. Fernandez-Corbaton, “On enhanced sensing of chiral molecules in optical cavities,” in Photonic and Phononic Properties of Engineered Nanostructures XI, Vol. 11694 (Mar. 5, 2021), p. 116941D.

[C11] B. Zerulla, M. Krstic, D. Beutel, C. Holzer, C. Rockstuhl, and I. Fernandez-Corbaton, “Molecules in (fancy) cavities,” in Nanophotonics IX, Vol. PC12131 (May 24, 2022), PC1213111.

Contents

List of Figures

List of Tables

List of Listings

1 | Introduction

Artificial photonic materials offer unprecedented possibilities to shape the interaction of light and matter. Thereby, unique novel optical properties can be achieved. These properties emerge from the precisely tailored designs of individual constituents of these artificial materials in combination with the interaction of the constituents in bulks – often in periodic arrangements – on the macroscopic scale. The properties of artificial photonic materials can be used in many applications, such as fishnet structures with a negative refractive index for optical cloaking and lensing [1], Huygens' metasurfaces fulfilling the Kerker condition for near-zero reflectivity [2], or topological photonic insulators for back-scattering free mode guiding [3]. Novel research directions study further inclusion of non-local effects [4] or of time-varying materials [5]. These developments can be used, for example, to achieve high-throughput optical computing [6] or to implement the concept of a photonic lab on a chip [7].

These advancements are based on the complementary developments in different scientific fields. Here, physics is traditionally described by its two branches experimental and theoretical physics. Novel experimental approaches, for example, to fabricate photonic structures with higher precision, smaller features, or from previously unused materials, can realize innovative designs to implement concepts previously explored only theoretically. Conversely, unique and unusual properties of materials require the development of new theoretical models to describe them. However, the development of more complex theoretical models and the ever-increasing possibilities of structures that can be realized experimentally require ultimately computational tools for their exploration. Facilitated by more powerful computers, the new branch of computational physics becomes more important. Sophisticated computational methods based on theoretical models allow the prediction of the physical properties of novel photonic materials.

The development of fabrication methods for artificial materials is under active research. Depending on the type of materials, additive methods can be used, such as direct laser writing [8], or self-assembly methods, for example, to fabricate metal-organic frameworks [9] or DNA-origami structures [10]. However, the prediction and theoretical analysis of the properties of artificial materials fabricated with such methods can pose a computational challenge. These challenges include the presence of different physically relevant length scales, that have to be bridged, or many different design parameters, that have to be explored. Currently widely used methods to solve electromagnetic scattering, such as finite difference schemes, finite-element methods, or Fourier modal methods, can reach their limitations [11]. For example, largely different length scales in the structure require different scales of discretization to be simulated accurately and, simultaneously, must stay practically feasible. Also, changing parameters, such as the lattice constant, can require completely new calculations. Moreover, high demands on the computing infrastructure can also create challenges due to their resource requirements which increases energy consumption and cost. Therefore, novel approaches to simulate electromagnetic scattering become necessary. Specialized simulation approaches can be used to respond to these challenges. One such approach is the transition matrix (T-matrix) method [12].

In essence, the T-matrix is an efficient way to encode the scattering response from an object under arbitrary direction or polarization of the illumination by using basis sets tailored to the scattering problem. The interaction between multiple particles can be solved analytically. The T-matrix method has several benefits. Its central object of interest, the matrix itself, is a very compact description of the scattering properties of a single object. Thereby, it is efficient for solving systems involving many scatterers. Moreover, by computing the interaction analytically, the required computational effort is reduced offering also an opportunity for gradient-based optimizations. The separation of the single scatterer properties from the interaction calculations is beneficial to accommodate different length scales. It also allows the separation of lattice and scatterer effects in photonic materials.

In this thesis, we explore the application of the T-matrix method for various problems in the field of artificial photonic materials. We not only apply the T-matrix for finite structures, but particularly for infinite, periodic arrays. As it turns out, the efficient application of the T-matrix calculation in the presence of periodic boundary conditions needs highly specialized expressions to calculate lattice sums. We package T-matrix method functions and efficient lattice sums in a holistic software framework. From the outset, we also include the possibility to describe scattering in the presence of electromagnetically chiral materials to further increase the range of applications. We use the derived methods to simulate artificial materials and structures and analyze their properties. Furthermore, we explore these methods in combination with other matrix-based approaches to study the printing process of artificial materials.

The structure of this thesis can be approximately described as the transition from theoretical and mathematical methods to numerical and computational topics, which, finally, are used in several applications. The foundation of thesis is the scattering theory and its application which is described in Chapter 2. We begin with Maxwell's equations and the associated constitutive relations. With several applications involving electromagnetic chirality in mind, we emphasize on formulating the solutions to Maxwell's equations correspondingly, which means that we benefit from using modes of well-defined helicity. We continue by describing the T-matrix method. We formulate the calculation of the interaction for aperiodic clusters of scatterers and in the presence of periodic boundary conditions. Thereby, we cover a wide range of potential applications in the field of artificial photonic materials. Furthermore, we describe related matrix-based methods for stratified media that can be combined with the T-matrix approach, such as S-matrices and transfer matrices. Furthermore, we explain simulation methods for high numerical aperture lenses.

Although the T-matrix method equations for the interaction between scatterers in periodically repeated unit cells can be written down quite concisely, the calculation of the interaction is a computational challenge caused by a particular type of lattice sums, which appears. These sums for lattices are the focus of Chapter 3. We develop a unified method to derive exponentially convergent series for two types of solutions: spherical waves and cylindrical waves. These waves constitute the basis sets for which we formulated the T-matrices in the preceding chapter. An emphasis in the derivation, which is a significant complication, is put on complex unit cells, i.e., unit cells containing more than one object. The derived lattice sums are then comprehensively validated.

Chapter 4 gives an overview of the structure and the capabilities of the developed software package *treams*. This software, which is now published as an open-source package, provides a comprehensive framework for T-matrix and S-matrix computations. It combines the T-matrix method, using spherical and cylindrical wave solutions, with the exponentially convergent lattice sums. Thereby, it can – in addition to applying the T-matrix method to finite clusters – solve multi-scattering equations in the presence of periodic boundary conditions. Moreover, all functionality is designed to include modes of well-defined helicity and, therefore, chiral media can be included in the computations without restrictions. The introduction of *treams* is concluded with several examples to validate the accuracy and a discussion of actions to ensure the quality of the code.

Based on this computational framework, we study several applications in Chapter 5. We investigate helicity-preserving cavities for the enhancement of optical rotation signals. Such sensing schemes can distinguish molecules with different handedness, which is crucial, for example, in biomedical applications. Furthermore, we study different setups for direct laser writing in special conditions: The printing process in birefringent media and the presence and influence of inhomogeneities on the printing process are investigated. Furthermore, we study molecular arrays. By combining the derived methods with quantum-chemical simulations of individual molecules, the properties of such novel artificial materials can be calculated *ab-initio*. We also investigate a connection of the T-matrix method to the homogenization, i.e., the description of photonic materials by effective material parameters. The range of applications highlights the versatility of the approach to solve electromagnetic scattering as described in this thesis and implemented in *treams*.

The concluding Chapter 6 summarizes the results of the thesis. Furthermore, we give a brief overview on other applications of *treams* that are not covered in detail in this thesis. Finally, we provide an outlook on future research directions based on the results of this thesis.

2 | Electromagnetic scattering

The mathematical description of electromagnetic phenomena in classical physics is based on Maxwell's equations. Those equations precisely describe the properties and behavior of electromagnetic fields and their interaction with matter from the ultraviolet and the visible down to static frequencies. Excluding quantum effects at extremely small distances and highest energies, Maxwell's equations have great predictive power. They are, therefore, not only used to explain natural phenomena but also to engineer novel designs for a myriad of applications.

In our thesis, we focus on scattering processes based on general and widely applicable methods. These methods are used to explore in Chapter 5 a small subset of applications. The core concept in the theoretical description of scattering processes are wave solutions to Maxwell's equations, which we introduce in Section 2.1. As a starting point, Maxwell's equations in media are postulated and the involved fields are defined. On their own, however, Maxwell's equations do not completely constrain the solutions. So, they must be combined with suitable constitutive relations. For the particular choice of constitutive relations used in this thesis in combination with Maxwell's equations, we obtain the Helmholtz wave equation in a homogeneous medium. We make extensive use of the solution theory for the vector Helmholtz equation to arrive at several solution sets for Maxwell's equations used in the remainder of the thesis. These solution sets are important, as arbitrary solutions to Maxwell's equations can always be written as a superposition of the elements of these solution sets.

The solutions we introduce are particularly useful in combination with the concept of T-matrices [12] described in Section 2.2, which are a cornerstone to calculate the scattering response from structures of interest in the following chapters. In essence, the T-matrix describes how an incident field, expanded in a suitable solution set, on an object is scattered. The scattered field is equally expanded in a suitable basis set. The amplitudes of the expansion are expressed in vectors, and the T-matrix connects them in a matrix-vector product. Such basic description offers efficient methods to calculate the interaction in multi-scattering scenarios for both, aperiodic and periodic cases. To explain this in a sufficient detail, we introduce different methods to compute T-matrices for a wide range of scattering objects and, furthermore, describe several transformations that can be applied to T-matrices, such as rotations, translations, or the change between different basis sets.

We give an outline of the method to compute the lattice sums that arise when performing multi-scattering calculations with periodic boundary conditions in Section 2.3. The general idea underlying the so-called Ewald method [13] is explained and an overview of known results for various cases is given. However, a more detailed discussion of our novel and unified approach is the content of Chapter 3.

In the final section of this chapter, Section 2.4, we also introduce the methods used to study the optical response from stratified media in combination with plane wave expansions, which are based on scattering matrices (S-matrices). Additionally, for focus calculations with Richards and Wolf integrals [14] in anisotropic media, we use methods based on transfer matrices.

2.1 Electromagnetic wave solutions

Maxwell's equations as stated in Subsection 2.1.1 describe electromagnetic fields in different settings. We set the focus on time-harmonic waves propagating in the absence of free charges and currents. These waves are a result of imposing certain restrictions onto the materials involved – mainly the condition to respond linearly to electromagnetic fields – by the choice of constitutive relations made in Subsection 2.1.2. The combination of Maxwell's equations and the constitutive relations leads to the Helmholtz wave equation, which we solve in spherical, cylindrical, and Cartesian coordinates in Subsection 2.1.3 resulting in vector spherical, cylindrical, and plane waves, respectively [15].

2.1.1 Maxwell's equations

Due to their relevance throughout numerous fields and branches of physics, mathematics, and engineering, Maxwell's equations have been stated in various ways. Here, we use one of the most common starting points: the electromagnetic equations in real space and time-domain [16, 17]

$$\nabla \cdot \boldsymbol{D}(\boldsymbol{r}, t) = \rho_{\text{ext}}(\boldsymbol{r}, t) \tag{2.1a}$$

$$\nabla \cdot \boldsymbol{B}(\boldsymbol{r}, t) = 0 \tag{2.1b}$$

$$\nabla \times \boldsymbol{E}(\boldsymbol{r}, t) = -\frac{\partial}{\partial t}\boldsymbol{B}(\boldsymbol{r}, t) \tag{2.1c}$$

$$\nabla \times \boldsymbol{H}(\boldsymbol{r}, t) = \boldsymbol{j}_{\text{ext}}(\boldsymbol{r}, t) + \frac{\partial}{\partial t}\boldsymbol{D}(\boldsymbol{r}, t)\,, \tag{2.1d}$$

with the electric displacement $\boldsymbol{D}(\boldsymbol{r}, t)$, the magnetic flux density $\boldsymbol{B}(\boldsymbol{r}, t)$, the electric field $\boldsymbol{E}(\boldsymbol{r}, t)$, and the magnetic field $\boldsymbol{H}(\boldsymbol{r}, t)$. In this, so-called macroscopic, formulation the microscopic charges and currents of matter are included into the definition of the fields and only the external charges are explicitly included. While the microscopic charges give rise to the material properties that are finally expressed as constitutive relations, external charges $\rho_{\text{ext}}(\boldsymbol{r}, t)$ and currents $\boldsymbol{j}_{\text{ext}}(\boldsymbol{r}, t)$ are assumed to be absent in all scenarios considered in the remainder of this thesis.

Next, we want to express these time-domain equations in frequency-domain. In essence, we can write, while assuming a linear response, an arbitrary field in time domain as a superposition of time harmonic solutions that each differ in frequency, and the following Maxwell's equations capture the spatial behavior of the amplitudes of these time-harmonic solutions. Each time-dependent vector field is expressed by its Fourier transform as defined in Appendix A. Then, we arrive at Maxwell's equations in Fourier domain

$$\nabla \cdot \tilde{\boldsymbol{D}}(\boldsymbol{r}, k_0) = 0 \tag{2.2a}$$

$$\nabla \cdot \tilde{\boldsymbol{B}}(\boldsymbol{r}, k_0) = 0 \tag{2.2b}$$

$$\nabla \times \tilde{\boldsymbol{E}}(\boldsymbol{r}, k_0) = \mathrm{i}ck_0\tilde{\boldsymbol{B}}(\boldsymbol{r}, k_0) \tag{2.2c}$$

$$\nabla \times \tilde{\boldsymbol{H}}(\boldsymbol{r}, k_0) = -\mathrm{i}ck_0\tilde{\boldsymbol{D}}(\boldsymbol{r}, k_0)\,. \tag{2.2d}$$

We use the vacuum wave number $k_0 = \frac{\omega}{c}$, where c is the speed of light in vacuum, instead of the angular frequency ω as variable. This simplifies the implementation later because an explicit assumption of the units of length and time can be omitted. As a last modification, we normalize all fields such that they have the same units as the electric field, namely $\boldsymbol{\mathcal{H}}(\boldsymbol{r}, k_0) = Z_0 \tilde{\boldsymbol{H}}(\boldsymbol{r}, k_0)$, $\boldsymbol{\mathcal{D}}(\boldsymbol{r}, k_0) = \frac{1}{\epsilon_0} \tilde{\boldsymbol{D}}(\boldsymbol{r}, k_0)$, and $\boldsymbol{\mathcal{B}}(\boldsymbol{r}, k_0) = c \tilde{\boldsymbol{B}}(\boldsymbol{r}, k_0)$ for which we use, in addition to c, the free space impedance Z_0, and the vacuum permittivity ϵ_0. For a uniform notation, we also introduce $\boldsymbol{\mathcal{E}}(\boldsymbol{r}, k_0) = \tilde{\boldsymbol{E}}(\boldsymbol{r}, k_0)$ although the electric field definition remains unmodified. Now, in a stretch of notation where the divergence and curl operators act on each half of the six-component vectors, the Maxwell equations can be written concisely as

$$\nabla \cdot \begin{pmatrix} \boldsymbol{\mathcal{D}}(\boldsymbol{r}, k_0) \\ \boldsymbol{\mathcal{B}}(\boldsymbol{r}, k_0) \end{pmatrix} = 0 \tag{2.3a}$$

$$\nabla \times \begin{pmatrix} \boldsymbol{\mathcal{E}}(\boldsymbol{r}, k_0) \\ \boldsymbol{\mathcal{H}}(\boldsymbol{r}, k_0) \end{pmatrix} = k_0 \begin{pmatrix} 0 & \mathrm{i} \\ -\mathrm{i} & 0 \end{pmatrix} \begin{pmatrix} \boldsymbol{\mathcal{D}}(\boldsymbol{r}, k_0) \\ \boldsymbol{\mathcal{B}}(\boldsymbol{r}, k_0) \end{pmatrix} . \tag{2.3b}$$

The first equation mostly enforces transversality of the displacement field in the absence of sources and of the magnetic flux density. The second equation expresses a connection between the different electromagnetic fields and is the source of dynamically evolving fields. At this point, however, it gets necessary to introduce an additional relation between these fields to complete this otherwise under-determined set of equations.

2.1.2 Constitutive relations for bi-anisotropic and chiral media

The constitutive relations provide exactly that relation, which, in general, can be any functional $\{\boldsymbol{\mathcal{D}}, \boldsymbol{\mathcal{B}}\} = F[\{\boldsymbol{\mathcal{E}}, \boldsymbol{\mathcal{H}}\}]$. However, for many realistic materials additional restrictions can be imposed that greatly simplify this functional [17]. We return to the time-domain formulation for a brief period to make these restrictions apparent.

We begin with requiring a linear relation between those fields. As it turns out, this is a reasonable assumption for many optical systems when the amplitudes of the fields are not excessively large. For sufficiently low field strengths, a linear approximation is usually possible. Typically, non-linear effects such as higher harmonic generation or the Kerr effect appear under strong fields [18]. We also require locality and time-invariant materials to arrive at [17]

$$\frac{1}{\epsilon_0} \boldsymbol{D}(\boldsymbol{r}, t) = \boldsymbol{E}(\boldsymbol{r}, t) + \int_{-\infty}^{\infty} \mathrm{d}t' \, \left[\mathbf{R}_{\mathrm{ee}}(\boldsymbol{r}, t - t') \boldsymbol{E}(\boldsymbol{r}, t') + \mathbf{R}_{\mathrm{em}}(\boldsymbol{r}, t - t') Z_0 \boldsymbol{H}(\boldsymbol{r}, t')\right] \tag{2.4}$$

$$c_0 \boldsymbol{B}(\boldsymbol{r}, t) = Z_0 \boldsymbol{H}(\boldsymbol{r}, t) + \int_{-\infty}^{\infty} \mathrm{d}t' \, \left[\mathbf{R}_{\mathrm{me}}(\boldsymbol{r}, t - t') \boldsymbol{E}(\boldsymbol{r}, t') + \mathbf{R}_{\mathrm{mm}}(\boldsymbol{r}, t - t') Z_0 \boldsymbol{H}(\boldsymbol{r}, t')\right] , \tag{2.5}$$

where we introduced four response functions $\mathbf{R}_{\mathrm{ee}}(\boldsymbol{r}, t - t')$, $\mathbf{R}_{\mathrm{em}}(\boldsymbol{r}, t - t')$, $\mathbf{R}_{\mathrm{me}}(\boldsymbol{r}, t - t')$, and $\mathbf{R}_{\mathrm{mm}}(\boldsymbol{r}, t - t')$ that are, in general, matrix-valued. Additionally, temporal causality requires that the response functions are zero for $t' > t$. Applying the convolution theorem, these integrals become simple multiplications after a Fourier transformation to the frequency domain. Thus, these relations can be written compactly as

$$\begin{pmatrix} \boldsymbol{\mathcal{D}}(\boldsymbol{r}, k_0) \\ \boldsymbol{\mathcal{B}}(\boldsymbol{r}, k_0) \end{pmatrix} = \begin{pmatrix} \boldsymbol{\epsilon}(\boldsymbol{r}, k_0) & \boldsymbol{\chi}(\boldsymbol{r}, k_0) + \mathrm{i}\boldsymbol{\kappa}(\boldsymbol{r}, k_0) \\ \boldsymbol{\chi}^{\mathsf{T}}(\boldsymbol{r}, k_0) - \mathrm{i}\boldsymbol{\kappa}^{\mathsf{T}}(\boldsymbol{r}, k_0) & \boldsymbol{\mu}(\boldsymbol{r}, k_0) \end{pmatrix} \begin{pmatrix} \boldsymbol{\mathcal{E}}(\boldsymbol{r}, k_0) \\ \boldsymbol{\mathcal{H}}(\boldsymbol{r}, k_0) \end{pmatrix} , \tag{2.6}$$

where we use again the normalized fields introduced in the previous section. The electric-electric and the magnetic-magnetic couplings are expressed with the relative permittivity $\boldsymbol{\epsilon}(\boldsymbol{r}, k_0)$ and the relative permeability $\boldsymbol{\mu}(\boldsymbol{r}, k_0)$, respectively. The electric-magnetic and the magnetic-electric coupling are already decomposed into the non-reciprocity parameter $\boldsymbol{\chi}(\boldsymbol{r}, k_0)$ and the chirality parameter $\boldsymbol{\kappa}(\boldsymbol{r}, k_0)$. As the name suggests, reciprocal materials, which are inarguably an important class of matter, have a vanishing non-reciprocity parameter [17]. The entire six-by-six matrix, as defined here, is unitless. It is called bi-anisotropic tensor and, likewise, materials where no substantial further simplifications can be made are bi-anisotropic materials.

Further simplifications of Eq. (2.6) can be made depending on the symmetries and properties of the material. If the off-diagonal blocks vanish, a material is called anisotropic. Certain cases of scattering in the presence of anisotropic material parameters are discussed in Section 2.4 with an application in Section 5.2. Alternatively, if we impose spatial isotropy, all four material parameters become scalar functions. For non-vanishing off-diagonals, the material is called bi-isotropic. An important class of materials in this thesis are isotropic chiral materials, where the constitutive relations become

$$\begin{pmatrix} \boldsymbol{\mathcal{D}}(\boldsymbol{r}, k_0) \\ \boldsymbol{\mathcal{B}}(\boldsymbol{r}, k_0) \end{pmatrix} = \begin{pmatrix} \epsilon(\boldsymbol{r}, k_0) & \mathrm{i}\kappa(\boldsymbol{r}, k_0) \\ -\mathrm{i}\kappa(\boldsymbol{r}, k_0) & \mu(\boldsymbol{r}, k_0) \end{pmatrix} \begin{pmatrix} \boldsymbol{\mathcal{E}}(\boldsymbol{r}, k_0) \\ \boldsymbol{\mathcal{H}}(\boldsymbol{r}, k_0) \end{pmatrix} . \tag{2.7}$$

The combination of Maxwell's equations in frequency domain with these constitutive relations now forms a fully determined set of equations. In the following, we discuss the Helmholtz wave equation that, as we show subsequently, is closely related to the connection of Eqs. (2.3) and (2.7) in the case of homogeneous media, i.e., if the material parameters are independent of the spatial coordinate $\boldsymbol{r}$. Thus, we can use the solutions of the Helmholtz wave equation to construct solutions to Maxwell's equations.

2.1.3 Solutions to the Helmholtz wave equation and their application to Maxwell's equations

In this section, we introduce the scalar and vector Helmholtz equation. The solutions to this equation are later used to construct solutions for Maxwell's equations. The Helmholtz wave equation can be written as [15]

$$(\nabla^2 - k^2) f(\boldsymbol{r}, k) = \operatorname{div} \operatorname{grad} f(\boldsymbol{r}, k) - k^2 f(\boldsymbol{r}, k) = 0 \tag{2.8}$$

for a scalar field $f(\boldsymbol{r}, k)$ and wave number k. For a vector field $\boldsymbol{f}(\boldsymbol{r}, k)$, it is written as

$$(\nabla^2 - k^2) \boldsymbol{f}(\boldsymbol{r}, k) = \operatorname{grad} \operatorname{div} \boldsymbol{f}(\boldsymbol{r}, k) - \operatorname{curl} \operatorname{curl} \boldsymbol{f}(\boldsymbol{r}, k) - k^2 \boldsymbol{f}(\boldsymbol{r}, k) = 0 \, . \tag{2.9}$$

The operator ∇^2 is the scalar or vector Laplacian, respectively. A vast knowledge on the solutions of the scalar Helmholtz equation has been developed; separable solutions in eleven systems of coordinates are known [15]. From those cases, we use the solutions in Cartesian, cylindrical, and spherical coordinates. The definition and used convention of the coordinates are given in Appendix B. The first set of solutions are plane waves

$$f_{\hat{\boldsymbol{k}}}(\boldsymbol{r}, k) = \mathrm{e}^{\mathrm{i}\boldsymbol{k}\boldsymbol{r}} \, , \tag{2.10}$$

where the wave vector $\boldsymbol{k} = k\hat{\boldsymbol{k}}$ fulfills $\boldsymbol{k}^2 = k^2$ and $\boldsymbol{kr} = \boldsymbol{k} \cdot \boldsymbol{r}$ is the scalar product. Second, we have cylindrical waves

$$f^{(n)}_{k_z m}(\boldsymbol{r}, k) = Z^{(n)}_m(k_\rho \rho) \mathrm{e}^{\mathrm{i}m\varphi + \mathrm{i}k_z z}\,, \tag{2.11}$$

with $Z^{(n)}_m(\cdot)$ the Bessel functions of first ($n = 1$) and second ($n = 2$) kind or the Hankel functions of first ($n = 3$) and second ($n = 4$) kind [19]. The radial part of the wave vector is defined by $k_\rho = \sqrt{k^2 - k_z^2}$ and $m \in \mathbb{Z}$. Here and in the remainder of the thesis, we select the branch with the complex phase in $[0, \pi)$ for the square root. Third, there are spherical waves

$$f^{(n)}_{lm}(\boldsymbol{r}, k) = z^{(n)}_l(kr) Y_{lm}(\theta, \varphi) \tag{2.12}$$

with spherical Bessel or Hankel functions of first and second kind $z^{(n)}_l(\cdot)$ indexed analogously to their cylindrical counterparts and the spherical harmonics $Y_{lm}(\theta, \varphi)$. Multiple conventions for the definition of the spherical harmonics exist: See Appendix C for the convention used in this thesis. The modes are indexed by $l \in \mathbb{N}_0$ and $m \in \{-l, -l + 1, \dots, l\}$.

In six of the coordinate systems with separable solutions, particularly for the cylindrical, spherical, and Cartesian coordinates, it is possible to construct solutions to the vector equation from the scalar solutions by a general procedure [15]. From the scalar solution $f_\nu(\boldsymbol{r}, k)$, where we use ν as a general index into the set of solutions, we obtain three vector solutions by

$$\boldsymbol{L}_\nu(\boldsymbol{r}, k) = \nabla f_\nu(\boldsymbol{r}, k), \tag{2.13a}$$

$$\boldsymbol{M}_\nu(\boldsymbol{r}, k) = \nabla \times [\boldsymbol{v} f_\nu(\boldsymbol{r}, k)], \tag{2.13b}$$

$$\boldsymbol{N}_\nu(\boldsymbol{r}, k) = \frac{\nabla}{k} \times \boldsymbol{M}_\nu(\boldsymbol{r}, k)\,, \tag{2.13c}$$

where $\boldsymbol{v}$ is a pilot vector that depends on the choice of the coordinate system. In Cartesian and cylindrical coordinates, we use $\boldsymbol{v} = \hat{\boldsymbol{z}}$ and in spherical coordinates $\boldsymbol{v} = \boldsymbol{r}$. The three solutions can be associated with three different polarizations. The solutions $\boldsymbol{M}_\nu(\boldsymbol{r}, k)$ and $\boldsymbol{N}_\nu(\boldsymbol{r}, k)$ are divergence-free and, thus, are transverse fields, whereas $\boldsymbol{L}_\nu(\boldsymbol{r}, k)$ is longitudinal. Therefore, since we work with Maxwell's equations in the absence of sources, the focus is set on the solutions $\boldsymbol{M}_\nu(\boldsymbol{r}, k)$ and $\boldsymbol{N}_\nu(\boldsymbol{r}, k)$.

We note that the solutions $\boldsymbol{M}_\nu(\boldsymbol{r}, k)$ are orthogonal to the pilot vector $\boldsymbol{v}$. This means that in Cartesian and cylindrical coordinates the solutions are orthogonal to the z-direction. In spherical coordinates, the solutions are orthogonal to the radial direction. Later, when expanding the electric field in these waves, the solutions $\boldsymbol{M}_\nu(\boldsymbol{r}, k)$ are called transverse electric (TE) and the solutions $\boldsymbol{N}_\nu(\boldsymbol{r}, k)$ are called transverse magnetic (TM) [16]. However, the reference for that nomenclature differs between Cartesian and cylindrical waves on the one hand and spherical waves on the other hand.

Another property we can assess directly from the definition in Eqs. (2.13a) to (2.13c) together with the scalar solutions is their parity. The scalar plane waves in Eq. (2.10) change the direction of propagation under parity as does the k_z component of the cylindrical waves. Moreover, the scalar cylindrical waves in Eq. (2.11) obtain a factor $(-1)^m$ under parity due to the transformation $\varphi \to \varphi + \pi$, and the scalar spherical waves inherit the parity $(-1)^l$ from the transformation properties of the spherical waves. The vector solutions, therefore, also have simple transformations under parity: The waves $\boldsymbol{L}_\nu(\boldsymbol{r}, k)$ and $\boldsymbol{M}_\nu(\boldsymbol{r}, k)$ get an additional factor -1 under the parity transformation in comparison to the scalar solution transformation, while the solutions $\boldsymbol{N}_\nu(\boldsymbol{r}, k)$ do not. Due to these simple transformation properties under the parity operation, we refer to the basis consisting of $\boldsymbol{M}_\nu(\boldsymbol{r}, k)$ and $\boldsymbol{N}_\nu(\boldsymbol{r}, k)$ as parity basis.

The Helmholtz wave equation is a linear differential equation. Therefore, linear combinations of solutions are themselves solutions of the Helmholtz equation. This property can be used to obtain solutions of well-defined helicity. The helicity operator is the projection of the spin onto the linear momentum. For the functions defined in real space and frequency domain, the representation of the operator is $\frac{\nabla\times}{k}$ [20]. Using the definitions of the transverse solutions in Eqs. (2.13b) and (2.13c) in combination with Eq. (2.9), we find that by applying the helicity operator on one of the transverse solutions $\boldsymbol{M}_\nu(\boldsymbol{r}, k)$ or $\boldsymbol{N}_\nu(\boldsymbol{r}, k)$ generates the other. So, solutions that are eigenfunctions of the helicity operator with eigenvalues ±1 are readily defined by

$$\boldsymbol{A}_{\nu\pm}(\boldsymbol{r}, k) = \frac{\boldsymbol{N}_\nu(\boldsymbol{r}, k) \pm \boldsymbol{M}_\nu(\boldsymbol{r}, k)}{\sqrt{2}}\,. \tag{2.14}$$

As a result, we have two sets of solutions for the Helmholtz equation that will be used later on: the helicity basis and the parity basis. We finish these more abstract discussions of the solutions and will shortly derive the concrete definitions of the functions of the parity basis.

Vector plane waves

The vector plane waves with a wave vector expressed by its Cartesian components $\boldsymbol{k} = k_x\hat{\boldsymbol{x}} + k_y\hat{\boldsymbol{y}} + k_z\hat{\boldsymbol{z}} = k\hat{\boldsymbol{k}}$ are given by

$$\boldsymbol{M}_{\hat{\boldsymbol{k}}}(\boldsymbol{r}, k) = \mathrm{i}\frac{k_y\hat{\boldsymbol{x}} - k_x\hat{\boldsymbol{y}}}{k_\rho}\mathrm{e}^{\mathrm{i}\boldsymbol{k}\boldsymbol{r}} = -\mathrm{i}\hat{\boldsymbol{\varphi}}_{\boldsymbol{k}}\mathrm{e}^{\mathrm{i}\boldsymbol{k}\boldsymbol{r}} \tag{2.15a}$$

$$\boldsymbol{N}_{\hat{\boldsymbol{k}}}(\boldsymbol{r}, k) = \frac{-k_xk_z\hat{\boldsymbol{x}} - k_yk_z\hat{\boldsymbol{y}} + k_\rho^2\hat{\boldsymbol{z}}}{k_\rho k}\mathrm{e}^{\mathrm{i}\boldsymbol{k}\boldsymbol{r}} = -\hat{\boldsymbol{\theta}}_{\boldsymbol{k}}\mathrm{e}^{\mathrm{i}\boldsymbol{k}\boldsymbol{r}}\,. \tag{2.15b}$$

The expression is normalized by dividing through $k_\rho = \sqrt{k_x^2 + k_y^2}$. That normalization makes the functions unitless, and it also allows us to write those functions efficiently by using the unit vectors of the spherical coordinates. Note, however, that for complex-valued components, these modes are not normalized to unit strength. Furthermore, we define these functions for $k_x = 0 = k_y$, thus, $\hat{\boldsymbol{k}} = \pm\hat{\boldsymbol{z}}$ by

$$\boldsymbol{M}_{\pm\hat{\boldsymbol{z}}}(\boldsymbol{r}, k) = -\mathrm{i}\hat{\boldsymbol{y}}\mathrm{e}^{\mathrm{i}k_zz} \tag{2.16a}$$

$$\boldsymbol{N}_{\pm\hat{\boldsymbol{z}}}(\boldsymbol{r}, k) = \mp\hat{\boldsymbol{x}}\mathrm{e}^{\mathrm{i}k_zz}\,, \tag{2.16b}$$

which corresponds to applying first the limit $k_y \to 0^+$ and then $k_x \to 0^+$. These parity modes can be seen, as mentioned above, as TE and TM modes with respect to the x-y-plane or, equivalently, as the s- and p-polarized modes. The waves of well-defined helicity derived from these modes are circularly polarized for real-valued wave vectors.

An alternative indexing of these modes is useful in the presence of periodic boundaries in two directions. Instead of the three components of the normalized wave vector $\hat{\boldsymbol{k}}$, we

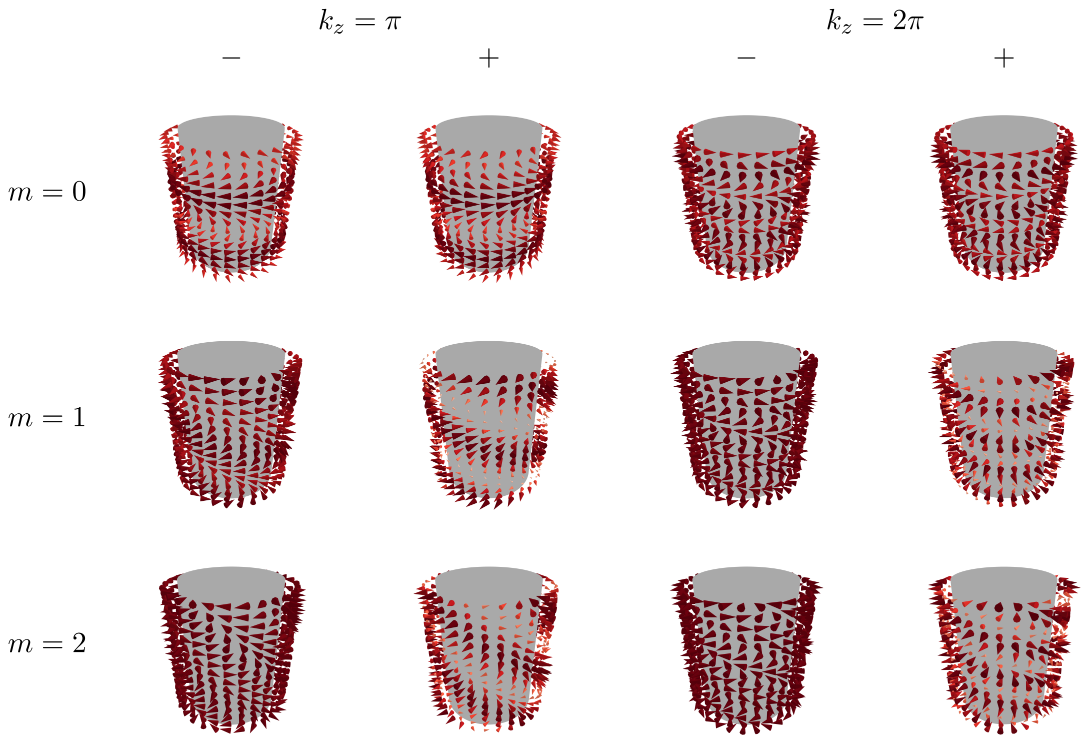

Figure 2.1: Visualization of vector cylindrical waves on a cylindrical surface. The fields $\mathrm{Re}(\boldsymbol{A}^{(3)}_{k_z m s}(\boldsymbol{r}, k))$ are shown for $k_z = \pi$ and $k_z = 2\pi$ and non-negative values of m. We set $k = 5$, thus, the two shown cases illustrate the fields for purely real and purely imaginary values of k_ρ and evaluate the fields at the cylinder radius $\rho = 0.2$. Each column corresponds to one helicity. The cones show the direction of the electric field. The color scale from white to dark red indicates the normalized strength of the electric field. The fields for negative values of m are related to the shown fields by symmetry.

define two components, e.g., for periodicity in the x-y-plane $\boldsymbol{k}_\parallel = k_x \hat{\boldsymbol{x}} + k_y \hat{\boldsymbol{y}}$. Then, the remaining third component is given by $k_z = d\sqrt{k^2 - k_x^2 - k_y^2}$ where $d = \pm 1$ specifies the principle direction of propagation. Hence, we can also use $\boldsymbol{M}_{\boldsymbol{k}_\parallel, d}(\boldsymbol{r}, k)$ and $\boldsymbol{N}_{\boldsymbol{k}_\parallel, d}(\boldsymbol{r}, k)$ to uniquely define a plane wave mode. To avoid confusion with the index for positive and negative helicity, we use the notation $d = \uparrow$ for $d = 1$ and $d = \downarrow$ for $d = -1$.

Vector cylindrical waves

The second set of solutions used in this thesis are vector cylindrical waves. They are given by

$$\boldsymbol{M}^{(n)}_{k_z m}(\boldsymbol{r}, k) = \left(\mathrm{i}m \frac{Z^{(n)}_m(k_\rho \rho)}{k_\rho \rho} \hat{\boldsymbol{\rho}} - Z^{(n)\prime}_m(k_\rho \rho) \hat{\boldsymbol{\varphi}} \right) \mathrm{e}^{\mathrm{i}m\varphi + \mathrm{i}k_z z} \tag{2.17a}$$

$$\boldsymbol{N}^{(n)}_{k_z m}(\boldsymbol{r}, k) = \left(\mathrm{i}\frac{k_z}{k} Z^{(n)\prime}_m(k_\rho \rho) \hat{\boldsymbol{\rho}} - m \frac{k_z}{k} \frac{Z^{(n)}_m(k_\rho \rho)}{k_\rho \rho} \hat{\boldsymbol{\varphi}} + \frac{k_\rho}{k} Z^{(n)}_m(k_\rho \rho) \hat{\boldsymbol{z}} \right) \mathrm{e}^{\mathrm{i}m\varphi + \mathrm{i}k_z z} \,, \tag{2.17b}$$

where we applied again a normalization by dividing through k_ρ. Like in the case of vector plane waves, this normalization makes the modes unitless. Furthermore, it results in the following expressions for $k_\rho = 0$

$$\boldsymbol{M}^{(n)}_{k_z m}(\boldsymbol{r}, k) = \begin{cases} \frac{\mathrm{i}\hat{\boldsymbol{\rho}} \mp \hat{\boldsymbol{\varphi}}}{2} \mathrm{e}^{\mathrm{i}k_z z \pm \mathrm{i}\varphi} = \frac{\mathrm{i}\hat{\boldsymbol{x}} \mp \hat{\boldsymbol{y}}}{2} \mathrm{e}^{\mathrm{i}k_z z} & m = \pm 1 \\ 0 & \text{otherwise} \end{cases} \tag{2.18a}$$

$$\boldsymbol{N}^{(n)}_{k_z m}(\boldsymbol{r}, k) = \begin{cases} \frac{\pm\mathrm{i}\hat{\boldsymbol{\rho}} - \hat{\boldsymbol{\varphi}}}{2} \mathrm{e}^{\mathrm{i}k_z z \pm \mathrm{i}\varphi} = \pm \frac{\mathrm{i}\hat{\boldsymbol{x}} \mp \hat{\boldsymbol{y}}}{2} \mathrm{e}^{\mathrm{i}k_z z} & m = \pm 1 \text{ and } k_z = k \\ -\frac{\pm\mathrm{i}\hat{\boldsymbol{\rho}} - \hat{\boldsymbol{\varphi}}}{2} \mathrm{e}^{\mathrm{i}k_z z \pm \mathrm{i}\varphi} = \mp \frac{\mathrm{i}\hat{\boldsymbol{x}} \mp \hat{\boldsymbol{y}}}{2} \mathrm{e}^{\mathrm{i}k_z z} & m = \pm 1 \text{ and } k_z = -k \\ 0 & \text{otherwise} \end{cases}, \tag{2.18b}$$

which are well-defined limits of the general expressions above. Note that in this limiting case, the modes $\boldsymbol{M}^{(n)}_{k_z m}(\boldsymbol{r}, k)$ and $\boldsymbol{N}^{(n)}_{k_z m}(\boldsymbol{r}, k)$ become degenerate. When we now change to the modes of well-defined helicity, we find the following pattern: For positive helicity only the modes with $m = \pm 1$ and $k_z = \pm k$, i.e., positive linear and angular momentum are non-zero and the modes $m = \mp 1$ and $k_z = \mp k$ vanish. For negative helicity the opposite pattern occurs. This property is expected but useful to verify.

Most often, we use the vector cylindrical waves with $n = 1$, which we call *regular* due to them being finite in the whole space of $\boldsymbol{r} \in \mathbb{R}^3$, and the waves with $n = 3$ that fulfill the radiation condition, which we call *singular*. As an example, we illustrate the vector cylindrical waves of well-defined helicity for a small set of values in Fig. 2.1, namely we show non-negative values of m for two cases: purely real values and purely imaginary values of k_ρ. The negative values of m can be obtained by symmetry. Essentially, taking the mirror image where the z-axis lies in the mirror plane, flips m and helicity.

Vector spherical waves

Finally, there are the vector spherical waves. Instead of directly applying the definitions of Eqs. (2.13a) to (2.13c) onto Eq. (2.12), we define the vector spherical harmonics first. They can be directly derived from the (scalar) spherical harmonics $Y_{lm}(\theta, \varphi)$ by [16]

$$\begin{aligned} \boldsymbol{X}_{lm}(\theta, \varphi) &= \frac{\nabla \times \boldsymbol{r}}{\sqrt{l(l+1)}} Y_{lm}(\theta, \varphi) \\ &= \underbrace{\sqrt{\frac{(2l+1)}{4\pi l(l+1)} \frac{(l-m)!}{(l+m)!}}}_{=N_{lm}} \left(\mathrm{i}\pi_{lm}(\cos\theta)\hat{\boldsymbol{\theta}} - \tau_{lm}(\cos\theta)\hat{\boldsymbol{\varphi}}\right) \mathrm{e}^{\mathrm{i}m\varphi} \end{aligned} \tag{2.19a}$$

$$\boldsymbol{Y}_{lm}(\theta, \varphi) = \hat{\boldsymbol{r}} \times \boldsymbol{X}_{lm}(\theta, \varphi) = N_{lm} \left(\tau_{lm}(\cos\theta)\hat{\boldsymbol{\theta}} + \mathrm{i}\pi_{lm}(\cos\theta)\hat{\boldsymbol{\varphi}}\right) \mathrm{e}^{\mathrm{i}m\varphi} \tag{2.19b}$$

$$\boldsymbol{Z}_{lm}(\theta, \varphi) = \mathrm{i}\hat{\boldsymbol{r}} Y_{lm}(\theta, \varphi)\,, \tag{2.19c}$$

with the angular functions $\pi_{lm}(\cos\theta) = m\frac{P_l^m(\cos\theta)}{\sin\theta}$ and $\tau_{lm}(\cos\theta) = \frac{\partial P_l^m(\cos\theta)}{\partial\theta}$. The functions $P_l^m(\cdot)$ are the associated Legendre polynomials defined in Appendix C. We also define the normalization factor N_{lm} for later use. The operator $\boldsymbol{r} \times \nabla$ is proportional to the angular momentum operator. The vector spherical harmonics constitute an orthonormal set by obeying [16]

$$\int_0^\pi \mathrm{d}\theta \sin\theta \int_0^{2\pi} \mathrm{d}\varphi \boldsymbol{X}_{l'm'}{}^*(\theta, \varphi) \boldsymbol{X}_{lm}(\theta, \varphi) = \delta_{ll'}\delta_{mm'} \tag{2.20}$$

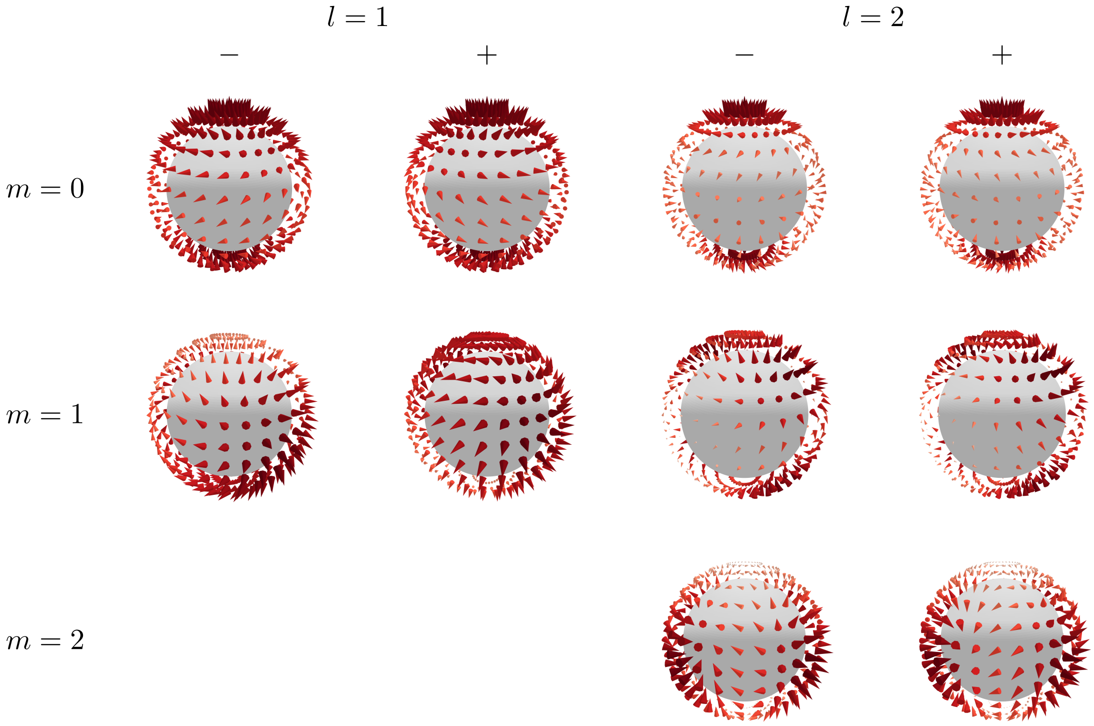

Figure 2.2: Visualization of vector spherical waves on a spherical surface. The dipolar ($l = 1$) and quadrupolar ($l = 2$) orders of $\mathrm{Re}(\boldsymbol{A}^{(3)}_{lms}(\boldsymbol{r}, k))$ are shown for non-negative values of m in each row. Each column corresponds to one helicity. The cones show the direction of the electric field. The color scale from white to dark red indicates the normalized strength of the electric field. The fields for negative values of m are related to the shown fields by symmetry.

and

$$\int_0^\pi \mathrm{d}\theta \sin\theta \int_0^{2\pi} \mathrm{d}\varphi \boldsymbol{Y}_{l'm'}{}^*(\theta,\varphi)\boldsymbol{X}_{lm}(\theta,\varphi) = 0 \tag{2.21}$$

$$\int_0^\pi \mathrm{d}\theta \sin\theta \int_0^{2\pi} \mathrm{d}\varphi \boldsymbol{Z}_{l'm'}{}^*(\theta,\varphi)\boldsymbol{X}_{lm}(\theta,\varphi) = 0 \tag{2.22}$$

as well as the analogous relations for $\boldsymbol{Y}_{lm}(\theta,\varphi)$ and $\boldsymbol{Z}_{lm}(\theta,\varphi)$. With these functions, the vector spherical waves can be written as

$$\boldsymbol{M}_{lm}^{(n)}(\boldsymbol{r},k) = \boldsymbol{X}_{lm}(\theta,\varphi) z_l^{(n)}(kr) \tag{2.23a}$$

$$\boldsymbol{N}_{lm}^{(n)}(\boldsymbol{r},k) = \boldsymbol{Y}_{lm}(\theta,\varphi)\left(\frac{z_l^{(n)}(kr)}{kr} + z_l^{(n)\prime}(kr)\right) + \sqrt{l(l+1)}\boldsymbol{Z}_{lm}(\theta,\varphi)\frac{z_l^{(n)}(kr)}{kr}\,. \tag{2.23b}$$

These functions $\boldsymbol{M}_{lm}^{(n)}(\boldsymbol{r},k)$ and $\boldsymbol{N}_{lm}^{(n)}(\boldsymbol{r},k)$ are zero for $l = 0$, which mathematically expresses the absence of electromagnetic monopole waves. The lowest non-zero multipole order is the dipolar order. Again, we use mostly the regular and singular modes with $n = 1$ and $n = 3$ later. The singular modes fulfill the radiation condition in three dimensions [16].

Similarly to the vector cylindrical waves, visualizations of the vector spherical waves of well-defined helicity are shown in Fig. 2.2. We show the dipolar and quadrupolar fields for non-negative values of m, as the negative values can be obtained by mirror symmetry again. With the vector plane, cylindrical, and spherical waves defined, we have completed the foundation works on defining the solutions with which we will work in the following. These are, however, solutions to the Helmholtz equation. We now make the connection to Maxwell's equations in the presence of isotropic chiral constitutive relations.

Wave solutions to Maxwell's equations

We first insert the constitutive relation Eq. (2.7) into the final form of Maxwell's equations we arrived at in Eq. (2.3) to eliminate the fields $\boldsymbol{\mathcal{D}}(\boldsymbol{r},k_0)$ and $\boldsymbol{\mathcal{B}}(\boldsymbol{r},k_0)$ from them. Equation (2.3b) then becomes

$$\nabla \times \begin{pmatrix} \boldsymbol{\mathcal{E}}(\boldsymbol{r},k_0) \\ \boldsymbol{\mathcal{H}}(\boldsymbol{r},k_0) \end{pmatrix} = k_0 \begin{pmatrix} \kappa(k_0) & \mathrm{i}\mu(k_0) \\ -\mathrm{i}\epsilon(k_0) & \kappa(k_0) \end{pmatrix} \begin{pmatrix} \boldsymbol{\mathcal{E}}(\boldsymbol{r},k_0) \\ \boldsymbol{\mathcal{H}}(\boldsymbol{r},k_0) \end{pmatrix} \tag{2.24}$$

and, as long as the determinant of the bi-isotropic tensor is non-zero, namely $\epsilon(k_0)\mu(k_0) \neq \kappa^2(k_0)$, Eq. (2.3a) can be converted to

$$\nabla \cdot \begin{pmatrix} \boldsymbol{\mathcal{E}}(\boldsymbol{r},k_0) \\ \boldsymbol{\mathcal{H}}(\boldsymbol{r},k_0) \end{pmatrix} = 0\,. \tag{2.25}$$

For practical applications, the vanishing determinant is not an issue since the chirality parameter is usually orders of magnitude smaller than the permittivity.

Equations (2.24) and (2.25) do not mix solutions with different k_0, which is a result of both, Maxwell's equations and the constitutive relations, being linear. Thus, we can solve these equations for each k_0 separately. Furthermore, in time-domain, the fields are observable quantities and, thus, have to be real valued, which relates the positive and negative frequency fields. It also connects real and imaginary parts of the material parameters, such as the permittivity, which are known as Kramers-Kronig relations [16]. Based on these observations, we can restrict all further discussions to monochromatic, positive frequency fields, which changes k_0 from being the conjugated variable of the time t in the Fourier transform to a parameter. We indicate this change by separating it with a semi-colon. The electric field is then given by

$$\boldsymbol{E}(\boldsymbol{r},t) = \operatorname{Re}\left(\boldsymbol{\mathcal{E}}(\boldsymbol{r};k_0)\mathrm{e}^{-\mathrm{i}ck_0t}\right) . \tag{2.26}$$

The replacement

$$\boldsymbol{\mathcal{E}}(\boldsymbol{r},k_0') = \frac{1}{2c}\left(\delta(k_0-k_0')\boldsymbol{\mathcal{E}}(\boldsymbol{r};k_0) + \delta(k_0+k_0')\boldsymbol{\mathcal{E}}^*(\boldsymbol{r};k_0)\right) \tag{2.27}$$

can always recover the original Fourier transform for the monochromatic field and can be tested by applying Eq. (A.1) to Eq. (2.27), which results in Eq. (2.26). However, using $\boldsymbol{\mathcal{E}}(\boldsymbol{r};k_0)$ is often more convenient than using $\boldsymbol{\mathcal{E}}(\boldsymbol{r},k_0)$ because the delta distributions do not need to be carried explicitly.

If we assume an achiral material for the moment, we set the chirality parameter to zero. Then, the typical approach to find a solution is: First, apply the curl twice in Eq. (2.24) to eliminate one of the fields $\boldsymbol{\mathcal{E}}(\boldsymbol{r};k_0)$ or $\boldsymbol{\mathcal{H}}(\boldsymbol{r};k_0)$, and, second, use Eq. (2.25) to arrive at Eq. (2.9) with the wave number in the medium $k(k_0) = \sqrt{\epsilon(k_0)\mu(k_0)}k_0$. Once we arrived at that point, we can immediately use all results of the Helmholtz equation to express the fields either in parity modes $\boldsymbol{M}_\nu(\boldsymbol{r},k)$ and $\boldsymbol{N}_\nu(\boldsymbol{r},k)$ or modes of well-defined helicity $\boldsymbol{A}_{\nu\pm}(\boldsymbol{r},k_\pm)$ in a Cartesian, spherical, or cylindrical basis, respectively.

The presence of chiral matter makes this approach less straightforward, because applying the curl twice no longer eliminates one of the two remaining fields. Therefore, we try to find fields different from $\boldsymbol{\mathcal{E}}(\boldsymbol{r};k_0)$ and $\boldsymbol{\mathcal{B}}(\boldsymbol{r};k_0)$ that diagonalize Eq. (2.24). From a straightforward calculation of the eigenvectors of the matrix in Eq. (2.24), we find

$$\boldsymbol{\mathcal{G}}_\pm(\boldsymbol{r};k_0) = \frac{\boldsymbol{\mathcal{E}}(\boldsymbol{r};k_0) \pm \mathrm{i}Z(k_0)\boldsymbol{\mathcal{H}}(\boldsymbol{r};k_0)}{\sqrt{2}} , \tag{2.28}$$

which are also known as Riemann-Silberstein vectors or Beltrami fields [21, 22], and $Z(k_0) = \sqrt{\frac{\mu(k_0)}{\epsilon(k_0)}}$ is the relative impedance. The corresponding eigenvalues are $\pm n_\pm(k_0) = \pm\sqrt{\epsilon(k_0)\mu(k_0)} + \kappa(k_0)$. As the variable name suggests, these eigenvalues correspond to two different refractive indices and, so, two different wave numbers $k_\pm(k_0) = k_0 n_\pm(k_0)$. Thereby, we have two separate equations

$$\nabla \times \boldsymbol{\mathcal{G}}_\pm(\boldsymbol{r};k_0) = \pm k_\pm(k_0)\boldsymbol{\mathcal{G}}_\pm(\boldsymbol{r};k_0) . \tag{2.29}$$

Now, it is possible to apply the curl twice as in the achiral case and, in combination with the vanishing divergence of $\boldsymbol{\mathcal{G}}_\pm(\boldsymbol{r};k_0)$, we arrive again at the Helmholtz equation. Thus, we know that these fields are solutions of the Helmholtz equation. Equation (2.29), however, is stricter than the Helmholtz equation. In fact, it requires fields of pure helicity as solutions and we can expand $\boldsymbol{\mathcal{G}}_\pm(\boldsymbol{r};k_0)$ as

$$\boldsymbol{\mathcal{G}}_\pm(\boldsymbol{r};k_0) = \sqrt{2}\sum_\nu a_{\nu\pm}\boldsymbol{A}_{\nu\pm}(\boldsymbol{r},k_\pm(k_0)) , \tag{2.30}$$

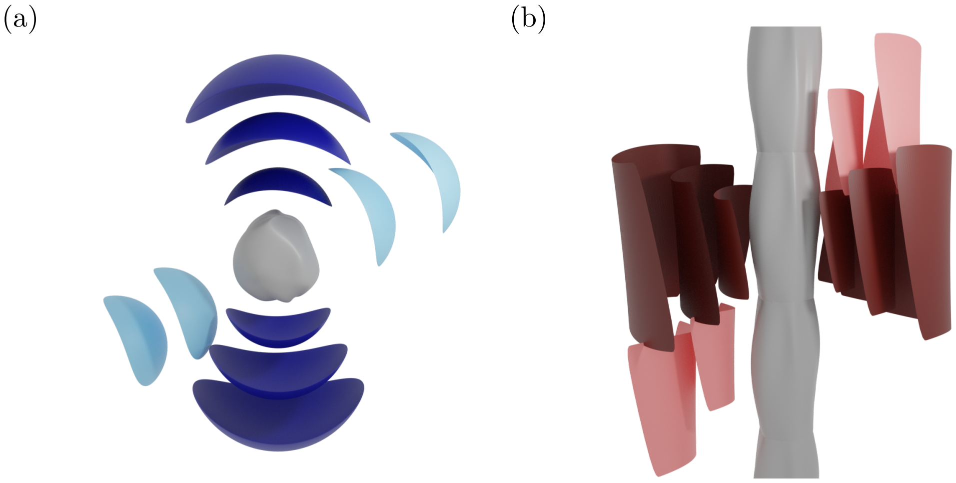

Figure 2.3: Artistic illustration of the scattering process described with spherical and cylindrical T-matrices. Panel (a) shows the vector spherical waves in blue scattered from a finite size gray object. The incident field in light color gets scattered to a dark spherical wave. In panel (b), the vector cylindrical waves are shown in red. The scatterer is an elongated object with a periodic shape along its axis. The actual shape of the fields are shown in Figs. 2.1 and 2.2.

with the expansion coefficients $a_{\nu\pm}$. Returning to a description of the electromagnetic waves as electric and magnetic fields, this leads to the expansions

$$\boldsymbol{\mathcal{E}}(\boldsymbol{r};k_0) = \sum_{s=\pm1}\sum_{\nu} a_{\nu s}\boldsymbol{A}_{\nu s}(\boldsymbol{r},k_s(k_0)) \tag{2.31}$$

and

$$\boldsymbol{\mathcal{H}}(\boldsymbol{r};k_0) = -\frac{\mathrm{i}}{Z(k_0)}\sum_{s=\pm1}\sum_{\nu} s a_{\nu s}\boldsymbol{A}_{\nu s}(\boldsymbol{r},k_s(k_0))\,. \tag{2.32}$$

These general solutions (the expansion in terms of the displacement field and the magnetic flux density are given in Appendix D) of Maxwell's equations together with the concrete solutions for the Helmholtz equation in Cartesian, cylindrical, and spherical coordinates provide now many possible starting points to solve various scattering problems. For this purpose, the next questions revolve around how to include scatterers with different material properties – up to now the solution is only applicable for homogeneous spaces – and how to treat multiple scattering and interaction between different particles.

2.2 The T-matrix method for vector spherical and cylindrical waves

A very successful approach to efficiently compute the scattering response of an individual scatterer and of clusters of particles is the T-matrix method [23]. Originally, it was developed using vector spherical waves [12]. However, the method can be applied equally well using vector cylindrical waves [24]. We start with outlining several methods, analytical and numerical, to obtain the T-matrix. Then, we proceed from single object T-matrices to multi-scattering scenarios in the presence and absence of periodic boundaries. Finally, we give an overview over regularly used transformations that can be applied to perform various actions on the T-matrix.

Generally, the T-matrix method relies on the separation of the total electric field $\boldsymbol{\mathcal{E}}(\boldsymbol{r}; k_0) = \boldsymbol{\mathcal{E}}_{\text{inc}}(\boldsymbol{r}; k_0) + \boldsymbol{\mathcal{E}}_{\text{sca}}(\boldsymbol{r}; k_0)$ outside the considered scatterer into an incident and a scattered part. By using suitable functions for the incident and scattered field, namely the regular and singular fields of the vector spherical and cylindrical waves, this separation can be written conveniently as

$$\boldsymbol{\mathcal{E}}_{\text{inc}}(\boldsymbol{r}; k_0) = \sum_{s=\pm 1} \sum_{\nu} a_{\nu s} \boldsymbol{A}^{(1)}_{\nu s}(\boldsymbol{r}, k_s(k_0)) \tag{2.33}$$

$$\boldsymbol{\mathcal{E}}_{\text{sca}}(\boldsymbol{r}; k_0) = \sum_{s=\pm 1} \sum_{\nu} p_{\nu s} \boldsymbol{A}^{(3)}_{\nu s}(\boldsymbol{r}, k_s(k_0)) \,, \tag{2.34}$$

where the expansion coefficients of the incident field are $a_{\nu s}$ and those of the scattered field are $p_{\nu s}$. Note that in comparison to the previous section the general index ν now only includes the combination l and m or k_z and m and not the parameter n any more. We can expand the incident field in regular modes only because they are the only fields finite at the origin for vector spherical and cylindrical waves. The scattered field has to fulfill the radiation condition [16], so only the singular modes can contribute. While we define the T-matrix here only in the helicity basis, it can be also defined using the parity modes. However, we restrict the discussion to helicity modes for brevity.

If we now consider an isolated scatterer placed at the origin of the coordinate system, the electric field around the scatterer can be expanded in those modes. As long as the scatterer responds linearly to the incident field, the relation between the incident and scattered field coefficients can be written as

$$p_{\nu s} = \sum_{s'=\pm 1} \sum_{\nu'} T_{\nu s \nu' s'} a_{\nu' s'} \,, \tag{2.35}$$

where the coefficients $T_{\nu s \nu' s'}$ encode the transition from incident mode ν' with helicity s' to the scattered mode ν with helicity s. In general, it gets necessary to truncate the inclusion of the modes ν and ν' for a numerical evaluation. It turns the infinitely large space of solutions into a finite set. Then, the expression above can be written as a matrix equation

$$\boldsymbol{p} = \mathbf{T}\boldsymbol{a} \,. \tag{2.36}$$

It needs to be clarified, when such a truncation is justified. In the case of vector spherical waves, the scatterer is required to have a finite size. Then, for a sufficiently large truncation order, the error introduced by omitting all higher multipole orders is negligible. Extremely tiny objects, like molecules or truly nanoparticles, can effectively be described by a dipolar approximation. The objects are simply too small to probe the spatial variation of the incident field. For many practical problems in the field of nanooptics, the expansion can be truncated at order four or five. In case of the vector cylindrical waves, the scatterer must be finite in the x-y-plane. In the z-direction, it is highly beneficial for the scattering structure to have a periodicity. Then, the at least discrete translation symmetry along the z-direction implies that only those values of k_z couple that differ in multiples of the reciprocal lattice. Otherwise, all modes from a continuous spectrum of values of k_z couple with each other. Thus, we assume that if we apply the T-matrix method using the vector cylindrical waves, the scatterer is periodic in the z-direction. As a result, we can truncate k_z to a finite number of diffraction orders that mainly contribute to the field. All higher diffraction orders are then highly evanescent and can be neglected for scattering calculations. An exemplary structure of a general object described by a T-matrix are shown in Fig. 2.3 in panels (a) and (b) for vector spherical and cylindrical waves, respectively.

2.2.1 Computing T-matrices for arbitrarily shaped scatterers

While the calculation of the scattering response by the T-matrix is a simple matrix multiplication, we still need to describe how the T-matrix coefficients can be obtained. We discuss two methods. First, we describe how to calculate analytically the scattering from spheres and cylinders consisting of chiral materials and having potentially several concentric shells. For simple spheres, these coefficients are known as Mie coefficients [25]. Second, we describe one possible method to calculate the T-matrix of arbitrarily shaped particles using finite-element calculations. Note that a range of other methods exists to calculate T-matrix coefficients, such as the extended boundary condition method [12, 26], also known as null-field method, or the method of distributed dipoles [27]. The T-matrix of molecules can be obtained from quantum-chemical simulations by relating the resulting polarizability matrices with the T-matrix entries [P7]. We also want to remark that one can parametrize the possible values of the T-matrix of a general isotropic object using Mie angles [28].

Analytical solutions for multi-layered spheres and cylinders

The most general cases solved here are multi-layered spheres in the vector spherical wave basis and multi-layered infinitely long cylinders in the vector cylindrical wave basis. First, we fix the wave number k_0, which we omit as argument to the material parameters for a conciser notation. In both cases, we have the inner core with radius r_1 and ρ_1 made of a material with parameters ϵ_1, μ_1, and κ_1. Here, the field has to be expanded in regular modes only, because the field has to be finite in the center. Then, an arbitrary finite number of $N-1$ concentric shells with radii r_i or ρ_i and ϵ_i, μ_i, and κ_i for $i \in \{2, \dots, N\}$ can follow. Finally, the embedding medium is characterized by the material parameters ϵ_{N+1}, μ_{N+1}, and κ_{N+1}.

Now, we impose the condition that at each of the N interfaces the tangential components of $\boldsymbol{\mathcal{E}}(\boldsymbol{r}; k_0)$ and $\boldsymbol{\mathcal{H}}(\boldsymbol{r}; k_0)$ are continuous. For spheres, this leads to [29–31]

$$\hat{\boldsymbol{r}} \times \boldsymbol{\mathcal{E}}(\boldsymbol{r}, k_0)\big|_{r=r_i-0} = \hat{\boldsymbol{r}} \times \boldsymbol{\mathcal{E}}(\boldsymbol{r}, k_0)\big|_{r=r_i+0} \tag{2.37a}$$

$$\hat{\boldsymbol{r}} \times \boldsymbol{\mathcal{H}}(\boldsymbol{r}, k_0)\big|_{r=r_i-0} = \hat{\boldsymbol{r}} \times \boldsymbol{\mathcal{H}}(\boldsymbol{r}, k_0)\big|_{r=r_i+0} \tag{2.37b}$$

and for cylinders to [31]

$$\hat{\boldsymbol{\rho}} \times \boldsymbol{\mathcal{E}}(\boldsymbol{r}, k_0)\big|_{\rho=\rho_i-0} = \hat{\boldsymbol{\rho}} \times \boldsymbol{\mathcal{E}}(\boldsymbol{r}, k_0)\big|_{\rho=\rho_i+0} \tag{2.38a}$$

$$\hat{\boldsymbol{\rho}} \times \boldsymbol{\mathcal{H}}(\boldsymbol{r}, k_0)\big|_{\rho=\rho_i-0} = \hat{\boldsymbol{\rho}} \times \boldsymbol{\mathcal{H}}(\boldsymbol{r}, k_0)\big|_{\rho=\rho_i+0} \,. \tag{2.38b}$$

We can now project onto individual coefficients of the expansions in Eqs. (2.33) and (2.34). For spheres this is done by multiplying with $\boldsymbol{X}^*_{lm}(\theta,\varphi)$ or $\boldsymbol{Y}^*_{lm}(\theta,\varphi)$ and integrating over the angles as shown in Eqs. (2.20) to (2.22). For the cylinder, we multiply with either $\hat{\boldsymbol{\varphi}}\mathrm{e}^{-\mathrm{i}(m\varphi+k_z z)}$ or $\hat{\boldsymbol{z}}\mathrm{e}^{-\mathrm{i}(m\varphi+k_z z)}$ and integrate over φ and z. This then leads to equations of the structure

$$\begin{pmatrix} \boldsymbol{\Psi}^{(1)}_{\nu,i+1,i} & \boldsymbol{\Psi}^{(3)}_{\nu,i+1,i} \\ \boldsymbol{\Xi}^{(1)}_{\nu,i+1,i} & \boldsymbol{\Xi}^{(3)}_{\nu,i+1,i} \end{pmatrix} \begin{pmatrix} a_{\nu,-,i+1} \\ a_{\nu,+,i+1} \\ p_{\nu,-,i+1} \\ p_{\nu,+,i+1} \end{pmatrix} = \begin{pmatrix} \boldsymbol{\Psi}^{(1)}_{\nu,i,i} & \boldsymbol{\Psi}^{(3)}_{\nu,i,i} \\ \boldsymbol{\Xi}^{(1)}_{\nu,i,i} & \boldsymbol{\Xi}^{(3)}_{\nu,i,i} \end{pmatrix} \begin{pmatrix} a_{\nu,-,i} \\ a_{\nu,+,i} \\ p_{\nu,-,i} \\ p_{\nu,+,i} \end{pmatrix}, \tag{2.39}$$

where the matrices $\boldsymbol{\Psi}^{(n)}_{\nu,j,i}$ are a result from applying Eqs. (2.37a) and (2.38a), and $\boldsymbol{\Xi}^{(n)}_{\nu,j,i}$ come from Eqs. (2.37b) and (2.38b), the index j refers to the material parameters and the index i to the radius. For the spherical waves and the sphere, the matrices are

$$\boldsymbol{\Psi}^{(n)}_{l,j,i} = \boldsymbol{\Psi}^{(n)}_{l}(x_-,x_+) = \begin{pmatrix} -z^{(n)}_l(x_-) & z^{(n)}_l(x_+) \\ \frac{(x_- z^{(n)}_l(x_-))'}{x_-} & \frac{(x_+ z^{(n)}_l(x_+))'}{x_+} \end{pmatrix} \tag{2.40}$$

and

$$\boldsymbol{\Xi}^{(n)}_{l,j,i} = \boldsymbol{\Xi}^{(n)}_{l}(x_-,x_+) = \frac{1}{Z_j} \begin{pmatrix} z^{(n)}_l(x_-) & z^{(n)}_l(x_+) \\ -\frac{(x_- z^{(n)}_l(x_-))'}{x_-} & \frac{(x_+ z^{(n)}_l(x_+))'}{x_+} \end{pmatrix}, \tag{2.41}$$

with l replacing ν. For the sphere, the coefficients are the same for all values of m. The argument $x_\pm$ is a shorthand for the size parameter $k_\pm r_i$, with $k_\pm$ depending on the material parameters ϵ_j, μ_j, and κ_j. For the cylindrical waves and the cylinder, we have

$$\boldsymbol{\Psi}^{(n)}_{k_z m,j,i} = \boldsymbol{\Psi}^{(n)}_{k_z m}(x_-,x_+) = \begin{pmatrix} -\frac{k_{\rho,-}}{k_-} Z^{(n)}_m(x_-) & -\frac{k_{\rho,+}}{k_+} Z^{(n)}_m(x_+) \\ -\frac{k_z}{k_-}\frac{m Z^{(n)}_m(x_-)}{x_-} + {Z^{(n)}_m}'(x_-) & -\frac{k_z}{k_+}\frac{m Z^{(n)}_m(x_+)}{x_+} - {Z^{(n)}_m}'(x_+) \end{pmatrix} \tag{2.42}$$

and

$$\boldsymbol{\Xi}^{(n)}_{k_z m,j,i} = \boldsymbol{\Xi}^{(n)}_{k_z m}(x_-,x_+) = \frac{1}{Z_j} \begin{pmatrix} \frac{k_{\rho,-}}{k_-} Z^{(n)}_m(x_-) & -\frac{k_{\rho,+}}{k_+} Z^{(n)}_m(x_+) \\ \frac{k_z}{k_-}\frac{m Z^{(n)}_m(x_-)}{x_-} - {Z^{(n)}_m}'(x_-) & -\frac{k_z}{k_+}\frac{m Z^{(n)}_m(x_+)}{x_+} - {Z^{(n)}_m}'(x_+) \end{pmatrix}, \tag{2.43}$$

where $x_\pm = k_{\rho\pm}\rho_i$. As a next step, we can invert the left-hand-side in Eq. (2.39) for all interfaces to obtain the matrix

$$\mathbf{M}_{\nu,N} = \begin{pmatrix} \boldsymbol{\Psi}^{(1)}_{\nu,N+1,N} & \boldsymbol{\Psi}^{(3)}_{\nu,N+1,N} \\ \boldsymbol{\Xi}^{(1)}_{\nu,N+1,N} & \boldsymbol{\Xi}^{(3)}_{\nu,N+1,N} \end{pmatrix}^{-1} \begin{pmatrix} \boldsymbol{\Psi}^{(1)}_{\nu,N,N} & \boldsymbol{\Psi}^{(3)}_{\nu,N,N} \\ \boldsymbol{\Xi}^{(1)}_{\nu,N,N} & \boldsymbol{\Xi}^{(3)}_{\nu,N,N} \end{pmatrix}. \tag{2.44}$$

This matrix has a quite compact form for spheres and in the case of $k_z = 0$ also for cylinders. These expressions are given in Appendix E. With these matrices and the requirement that in the innermost material, i.e., the core of the particle, the singular fields must vanish to have physically plausible finite field values, we get

$$\begin{pmatrix} a_{\nu,-,N+1} \\ a_{\nu,+,N+1} \\ p_{\nu,-,N+1} \\ p_{\nu,+,N+1} \end{pmatrix} = \mathbf{M}_{\nu,N} \dots \mathbf{M}_{\nu,2} \begin{pmatrix} \boldsymbol{\Psi}^{(1)}_{\nu,2,1} & \boldsymbol{\Psi}^{(3)}_{\nu,2,1} \\ \boldsymbol{\Xi}^{(1)}_{\nu,2,1} & \boldsymbol{\Xi}^{(3)}_{\nu,2,1} \end{pmatrix}^{-1} \begin{pmatrix} \boldsymbol{\Psi}^{(1)}_{\nu,1,1} \\ \boldsymbol{\Xi}^{(1)}_{\nu,1,1} \end{pmatrix} \begin{pmatrix} a_{\nu,-,1} \\ a_{\nu,+,1} \end{pmatrix} . \tag{2.45}$$

The four-by-two matrix on the right-hand side can be separated in two parts: the upper two-by-two matrix relates the incident fields to the internal fields and the lower part relates the scattered with the internal fields. After eliminating the internal fields from these equations, we obtain the T-matrix coefficients for each of the modes.

Numerical solutions

For other shapes than multi-layered spheres or cylinders, it is usually necessary to calculate the T-matrix numerically. A range of methods exists for this purpose: the discrete dipoles method [27], the extended boundary condition method [12, 26], or solving the scattering with a full wave solver and decomposing the incident and scattered fields into vector spherical or cylindrical waves [32, 33].

We use mostly the method of solving the scattering problem with general purpose Maxwell solvers, usually based on the finite-element method. However, it is also possible to use finite difference methods. In principle, the object is illuminated with multiple incident fields that can be decomposed into vector spherical or cylindrical wave coefficients $\boldsymbol{a}_i$ and then, after solving the scattering problem for that illumination, the scattered field is also decomposed resulting in the corresponding expansion coefficients $\boldsymbol{p}_i$. After N illuminations, we obtain the linear system of equations

$$\begin{pmatrix} \boldsymbol{p}_1 & \boldsymbol{p}_2 & \cdots & \boldsymbol{p}_N \end{pmatrix} = \mathbf{T} \begin{pmatrix} \boldsymbol{a}_1 & \boldsymbol{a}_2 & \cdots & \boldsymbol{a}_N \end{pmatrix} , \tag{2.46}$$

that can then be solved for the unknown matrix $\mathbf{T}$. For an equal number N of illuminations to the dimension of $\mathbf{T}$, this is just the inversion of the matrix consisting of the incident field illuminations. Therefore, the illuminations have to be chosen such that the coefficient vectors are linearly independent. However, it can be beneficial to use a larger number of illuminations [33]. Then, the overdetermined system can be solved, e.g., by the method of least squares. Most often, the illumination is chosen to be plane waves [33] or spherical waves [32]. The former are useful because they have rather simple and analytical expansion coefficients and their implementation is typically included natively in general purpose Maxwell solvers. The latter are less frequently available as direct implementations in general purpose Maxwell solvers, but offer the advantage that every incident spherical wave mode can be excited separately. Hence, the matrix containing the incident field coefficients becomes a unit matrix and the step of matrix inversion can be omitted.

The decomposition of the scattered fields is conceptually most simple using a spherical or cylindrical surface enclosing the scatterer completely for spherical and cylindrical waves, respectively. Then, the properties of the vector spherical harmonics in Eqs. (2.20) to (2.22) leads to

$$\frac{1}{\sqrt{2}} \boldsymbol{\Psi}^{(3)}_{l}(x_-, x_+) \begin{pmatrix} p_{lm,+} \\ p_{lm,-} \end{pmatrix} = \begin{pmatrix} \int \mathrm{d}\Omega \boldsymbol{X}^*_{lm}(\theta, \varphi) \boldsymbol{\mathcal{E}}_{\mathrm{sca}}(\boldsymbol{r}; k_0) \\ \int \mathrm{d}\Omega \boldsymbol{Y}^*_{lm}(\theta, \varphi) \boldsymbol{\mathcal{E}}_{\mathrm{sca}}(\boldsymbol{r}; k_0) \end{pmatrix} , \tag{2.47}$$

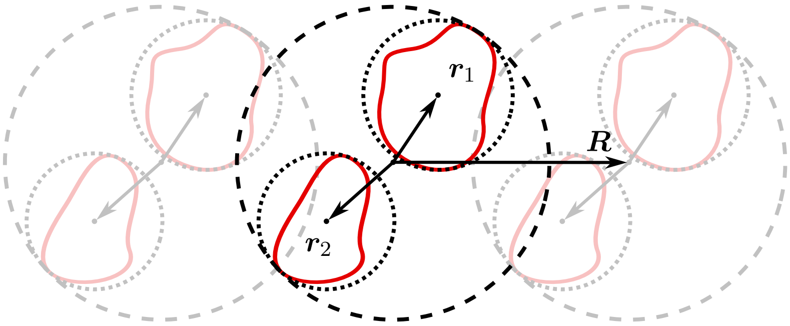

Figure 2.4: Geometry of two particles described by T-matrices in a periodic arrangement. For the two particles with red outlines, the individual circumscribing circles are shown as dotted lines. In a local description the expansion is valid in the domain outside of these circles. The dashed circle marks the domain of validity for a global T-matrix, describing both particles as a combined object. Note that in a periodic arrangement it is possible that for a small lattice pitch the description of scattering in a global description is not valid due to overlapping circumscribing spheres. However, the local description can still be used in the computation. For spherical and cylindrical waves, this two-dimensional figure generalizes two three dimensions by replacing the circumscribing circles with spheres or cylinders, respectively.

where the matrix on the left-hand side is defined in Eq. (2.40). The same procedure, but as in the analytical solution with suitable projectors for cylindrical waves, leads to

$$\frac{1}{\sqrt{2}}\boldsymbol{\Psi}^{(3)}_{k_z m}(x_-, x_+)\begin{pmatrix} p_{k_z m,+} \\ p_{k_z m,-} \end{pmatrix} = \frac{1}{2\pi a_z}\begin{pmatrix} \int \mathrm{d}\Omega \hat{\boldsymbol{z}} \mathrm{e}^{-\mathrm{i}(m\varphi + k_z z)} \boldsymbol{\mathcal{E}}_{\mathrm{sca}}(\boldsymbol{r}; k_0) \\ \int \mathrm{d}\Omega \hat{\boldsymbol{\varphi}} \mathrm{e}^{-\mathrm{i}(m\varphi + k_z z)} \boldsymbol{\mathcal{E}}_{\mathrm{sca}}(\boldsymbol{r}; k_0) \end{pmatrix} \tag{2.48}$$

using the matrix from Eq. (2.42). However, this simple approach is numerically less stable than more sophisticated methods and it requires large computational domains in cases where the circumscribing sphere or cylinder is much larger than the object itself. Then, it is useful to apply other methods [34]. However, this simple approach is useful for chiral embedding materials where two different wave numbers have to be considered.

2.2.2 Multi-scattering in clusters with and without periodic boundaries

Up to now, the T-matrix method is limited to single objects, but many phenomena in physics appear due to the interaction of multiple objects. Moreover, if periodic boundary conditions are considered, the interaction between objects in different unit cells of the lattice has to be included. When using the vector spherical or cylindrical waves, these interactions can be computed analytically, which comes with several benefits. First, the evaluation of the analytic formulas can be very efficient. In the case of periodicity, however, it will only be efficient after the substantial manipulations derived in Chapter 3. Second, it is possible to separate the object properties from the arrangement properties to a large extent and, thereby, analyze them separately. Third, it becomes quite simple to bridge different length scales. Finally, the analytic formulas can also be differentiated to perform gradient based optimizations [35].

Initially, we consider a system without periodic boundaries. We start by considering N particles described by T-matrices $\mathbf{T}_i$ at the positions $\boldsymbol{r}_i$ with $i \in \{i, \dots, N\}$. An example for two particles is shown in Fig. 2.4, the grayed-out part of the figure only applies to periodic boundaries. Each particle is illuminated by the field $\boldsymbol{a}_i$, and we want to solve for the scattered fields $\boldsymbol{p}_i$. Considering Eq. (2.36) as a starting point, the illumination on particle i does not only consists of the external illumination but additionally includes the scattered fields from all other particles [23]

$$\boldsymbol{p}_i = \mathbf{T}_i \left(\boldsymbol{a}_i + \sum_{j \neq i} \mathbf{C}^{(3)}(\boldsymbol{r}_i - \boldsymbol{r}_j) \boldsymbol{p}_j \right) . \tag{2.49}$$

The scattered field at $\boldsymbol{r}_j$ is expanded into a regular field incident on $\boldsymbol{r}_i$ by the matrix $\mathbf{C}^{(3)}(\boldsymbol{r}_i - \boldsymbol{r}_j) = \mathbf{C}^{(3)}_{ij}$. For vector spherical waves, this matrix contains the coefficients $A^{(3)}_{l'm',lm}(\boldsymbol{r} - \boldsymbol{r}', k_\pm)$ and $B^{(3)}_{l'm',lm}(\boldsymbol{r} - \boldsymbol{r}', k_\pm)$ that relate the fields (see Appendix F) [26, 36, 37]

$$\boldsymbol{A}^{(3)}_{lm\pm}(\boldsymbol{r}, k_\pm) = \sum_{l'=1}^{\infty} \sum_{m'=-l'}^{l'} \left(A^{(3)}_{l'm',lm}(\boldsymbol{r} - \boldsymbol{r}', k_\pm) \pm B^{(3)}_{l'm',lm}(\boldsymbol{r} - \boldsymbol{r}', k_\pm) \right) \boldsymbol{A}^{(1)}_{l'm'\pm}(\boldsymbol{r}', k_\pm) \tag{2.50}$$

at two positions for $|\boldsymbol{r} - \boldsymbol{r}'| > |\boldsymbol{r}'|$. Note that the fields of well-defined helicity are not mixed by this operation. However, parity modes generally get mixed. In the vector cylindrical wave basis the translation formula has with

$$\boldsymbol{A}^{(3)}_{k_z m\pm}(\boldsymbol{r}, k_\pm) = \sum_{m'=-\infty}^{\infty} H^{(3)}_{m-m'}(\sqrt{k_\pm^2 - k_z^2} \rho_{\boldsymbol{r}-\boldsymbol{r}'}) \mathrm{e}^{\mathrm{i}(m-m')\varphi_{\boldsymbol{r}-\boldsymbol{r}'} + \mathrm{i}k_z(z-z')} \boldsymbol{A}^{(1)}_{k_z m'\pm}(\boldsymbol{r}', k_\pm) \tag{2.51}$$

for $\rho_{\boldsymbol{r}-\boldsymbol{r}'} > \rho_{\boldsymbol{r}'}$ also a quite simple form. With the knowledge of Eqs. (2.50) and (2.51), the system of equations in Eq. (2.49) can be directly solved by

$$\boldsymbol{p}_\text{local} = \underbrace{\left[\mathbb{1} - \mathbf{T}_\text{diag} \mathbf{C}^{(3)} \right]^{-1} \mathbf{T}_\text{diag}}_{\mathbf{T}_\text{local}} \boldsymbol{a}_\text{local} \tag{2.52}$$

where $\boldsymbol{p}_\text{local}$ and $\boldsymbol{a}_\text{local}$ are vectors containing all coefficients from $\boldsymbol{p}_i$ and $\boldsymbol{a}_i$, respectively, ordered by particle index i, and $\mathbf{T}_\text{diag}$ is a block-diagonal matrix that holds the individual T-matrices ordered accordingly. The matrix $\mathbf{C}^{(3)}$ consists block-wise of the matrices $\mathbf{C}^{(3)}_{ij}$ on the off-diagonals and has zeros in the blocks of the diagonal. That simply expresses the fact that each particle does not generate a scattered field that acts as an illumination on itself. By defining the matrix $\mathbf{T}_\text{local}$, the structure of Eq. (2.52) becomes similar to Eq. (2.36). The difference is mainly that the combination of all objects described by the local T-matrix is given in a vector wave basis with not only one but multiple origins. We see in this expression that the interaction with the other particles modifies the T-matrix of each individual object, and we speak of a renormalization. The incident field has to be expanded separately at each origin into $\boldsymbol{a}_\text{local}$, and the total scattered field is obtained by a combination of the contributions from all particle positions defined by the coefficients $\boldsymbol{p}_{\text{local}}$. The local description is valid in the domain outside the dotted lines in Fig. 2.4.

It is possible to convert the local description of the cluster of particles into a global description, i.e., all fields are defined with respect to a single origin. This can be achieved by the translation coefficients [26, 36, 37]

$$\boldsymbol{A}^{(n)}_{lm\pm}(\boldsymbol{r},k_\pm) = \sum_{l'=1}^{\infty}\sum_{m'=-l'}^{l'} \left(A^{(1)}_{l'm',lm}(\boldsymbol{r}-\boldsymbol{r}',k_\pm) \pm B^{(1)}_{l'm',lm}(\boldsymbol{r}-\boldsymbol{r}',k_\pm)\right)\boldsymbol{A}^{(n)}_{l'm'\pm}(\boldsymbol{r}',k_\pm) \tag{2.53}$$

and [24]

$$\boldsymbol{A}^{(n)}_{k_z m\pm}(\boldsymbol{r},k_\pm) = \sum_{m'=-\infty}^{\infty} J_{m-m'}\left(\sqrt{k_\pm^2-k_z^2}\,\rho_{\boldsymbol{r}-\boldsymbol{r}'}\right)\mathrm{e}^{\mathrm{i}(m-m')\varphi_{\boldsymbol{r}-\boldsymbol{r}'}+\mathrm{i}k_z(z-z')}\boldsymbol{A}^{(n)}_{k_z m'\pm}(\boldsymbol{r}',k_\pm)\,, \tag{2.54}$$

with $n \in \{1,3\}$, which are the same as those in Eqs. (2.50) and (2.51) but with the (spherical) Hankel functions of the first kind replaced with (spherical) Bessel functions. For $n = 3$, these expressions are only valid for $|\boldsymbol{r}-\boldsymbol{r}'| < |\boldsymbol{r}'|$ or $\rho_{\boldsymbol{r}-\boldsymbol{r}'} < \rho_{\boldsymbol{r}'}$, respectively. Then, the global incident field $\boldsymbol{a}$ defined at $\boldsymbol{r}_0 = 0$ can be expanded as

$$\boldsymbol{a}_{\text{local}} = \begin{pmatrix} \mathbf{C}^{(1)}_{10} \\ \mathbf{C}^{(1)}_{20} \\ \vdots \\ \mathbf{C}^{(1)}_{N0} \end{pmatrix} \boldsymbol{a} \tag{2.55}$$

and the global scattered field is obtained by

$$\boldsymbol{p} = \begin{pmatrix} \mathbf{C}^{(1)}_{01} & \mathbf{C}^{(1)}_{02} & \dots & \mathbf{C}^{(1)}_{0N} \end{pmatrix} \boldsymbol{p}_{\text{local}}\,. \tag{2.56}$$

Finally, the global matrix of the cluster is

$$\mathbf{T} = \begin{pmatrix} \mathbf{C}^{(1)}_{01} & \mathbf{C}^{(1)}_{02} & \dots & \mathbf{C}^{(1)}_{0N} \end{pmatrix} \mathbf{T}_{\text{local}} \begin{pmatrix} \mathbf{C}^{(1)}_{10} \\ \mathbf{C}^{(1)}_{20} \\ \dots \\ \mathbf{C}^{(1)}_{N0} \end{pmatrix}\,. \tag{2.57}$$

Describing a cluster in the local and global basis has different benefits and downsides [38]. Typically, the trade-off is between a lower multipolar order required to describe the individual scatterers, but having to expand the field around multiple positions and a larger multipolar order for the, in total, larger spatial extent of the cluster, but having to expand the field only around the point $\boldsymbol{r}_0 = 0$. Furthermore, the domain where the local field expansion is valid is larger in comparison to the valid domain of global field expansion. The difference is illustrated by the larger radius of the dashed line in Fig. 2.4 in comparison to the dotted lines. Thus, the field between the particles is only correctly described in the local description.

Now, we want to consider periodic boundaries. We index the particles with two indices: the N positions for all particles in one unit cell with letters $i, j \in \{1, \dots, N\}$ and the different lattice sites with their lattice vectors $\boldsymbol{R}$. The lattice vectors are elements of the set $\Lambda = \{\sum_{i=1}^{d} n_i \boldsymbol{u}_i | n_i \in \mathbb{Z}\}$ that defines the lattice with basis vectors $\boldsymbol{u}_i$ spanning one unit cell. A lattice can extend in $d \in \{1, 2, 3\}$ spatial dimensions. In the case of vector cylindrical waves that are assumed to be inherently periodic along the z-axis the lattice dimension has to be $d \leq 2$.

We choose the unit cell at $\boldsymbol{R} = 0$ to be the reference unit cell. Then, we can change Eq. (2.49) to

$$\boldsymbol{p}_{i,0} = \mathbf{T}_i \left(\boldsymbol{a}_{i,0} + \sum_{j=1}^{N} \sum_{\boldsymbol{R} \in \Lambda}{}' \mathbf{C}^{(3)}(\boldsymbol{r}_i - \boldsymbol{r}_j - \boldsymbol{R}) \boldsymbol{p}_{j,\boldsymbol{R}} \right) \tag{2.58}$$

for the inclusion of periodicity in the T-matrix calculation [39]. It is now required to sum over all particles in all unit cells, with the exception of the selected particle i in the reference unit cell. This exclusion of the term where $\boldsymbol{r}_i - \boldsymbol{r}_j - \boldsymbol{R} = 0$ is indicated by the prime next to the lattice sum. To bring this expression into a manageable form, we now have to assume a common wave vector tangential to the lattice $\boldsymbol{k}_\parallel$. The tangential wave vector describes the phase difference between different unit cells, namely $\boldsymbol{a}_{i,\boldsymbol{R}} = \boldsymbol{a}_{i,0} \mathrm{e}^{\mathrm{i}\boldsymbol{k}_\parallel \boldsymbol{R}}$ and $\boldsymbol{p}_{i,\boldsymbol{R}} = \boldsymbol{p}_{i,0} \mathrm{e}^{\mathrm{i}\boldsymbol{k}_\parallel \boldsymbol{R}}$. This is nothing else than the Bloch theorem that we impose here. With this assumption, we can write the equation as

$$\boldsymbol{p}_{i,0} = \mathbf{T}_i \left(\boldsymbol{a}_{i,0} + \sum_{j=1}^{N} \underbrace{\sum_{\boldsymbol{R} \in \Lambda}{}' \mathbf{C}^{(3)}(\boldsymbol{r}_i - \boldsymbol{r}_j - \boldsymbol{R}) \mathrm{e}^{\mathrm{i}\boldsymbol{k}_\parallel \boldsymbol{R}} \boldsymbol{p}_{j,0}}_{=\tilde{\mathbf{C}}_{ij}^{(3)}} \right) \tag{2.59}$$

that expresses the scattered and incident fields only in quantities from the reference unit cell. The general layout of the scattering with periodic boundary conditions is shown in Fig. 2.4 where the grayed-out part shows the neighboring unit cells. It can be seen that with such periodic boundary conditions complex unit cells, i.e., unit cells with more than one particle, can sometimes only be described in a local basis, because the domains where the global T-matrix description is valid overlap between adjacent unit cells. The trade-off here is in the more complex lattice sums required for complex unit cells and which we derive in Chapter 3. We define the expansion coefficients of the scattered fields as incident fields in a lattice with an added tilde to the variable name. This lets us write the final multi-scattering in an analogous fashion to Eq. (2.52)

$$\tilde{\boldsymbol{p}}_{\mathrm{local}} = \underbrace{\left[\mathbb{1} - \mathbf{T}_{\mathrm{diag}} \tilde{\mathbf{C}}^{(3)} \right]^{-1} \mathbf{T}_{\mathrm{diag}}}_{\tilde{\mathbf{T}}_{\mathrm{local}}} \tilde{\boldsymbol{a}}_{\mathrm{local}} \,, \tag{2.60}$$

where we find the local T-matrix renormalized by the lattice interaction. The result are scattered field coefficients in the reference unit cell. As a reminder that the total scattered field is only obtained after summing up the scattered fields of all unit cells, we also add a tilde to the variable name. We do so similarly for the incident field, because it has to fulfill the same phase relation among the unit cells defined by $\boldsymbol{k}_\parallel$. But, unlike for the scattered field, when evaluating the incident field, it is not necessary to include the lattice explicitly. Furthermore, it is possible to expand the scattered fields in the lattice back into regular fields in the reference unit cell by $\tilde{\mathbf{C}}^{(3)}\tilde{\boldsymbol{p}}_{\text{local}}$. This expansion is useful when evaluating the scattered fields after solving the scattering problem for a particular illumination.

Up to now, we always implicitly assumed that the term in brackets can be inverted, which is, indeed, usually the case. However, finding eigenvectors of that term with vanishing or very small eigenvalues indicates long lived lattice modes. This is an aspect that can be exploited when discussing resonances sustained in certain photonic materials.

In summary, with Eqs. (2.52) and (2.60) we have expressions to solve the scattering problem without and with periodic boundary conditions. In the first case, the analytically known translation coefficients make calculations for a cluster of particles very efficient, and with Eq. (2.57) we can describe it as if it were a single object. In the latter case, the efficiency of the method mainly relies on the efficiency of the lattice sum that is necessary to calculate the translation coefficients. Finding and implementing such efficient expressions for all possible lattice dimensions is one of the major results of this thesis. We elaborate on them in more detail in the following chapter. The lattice sums constitute the basis to the physical insights gained in the various applications that are discussed in the final chapter of the thesis. .

While the T-matrix provides a very efficient description of the scattering process, we also want to mention the S-matrix. We use it with the vector plane wave expansion, but it can in principle also be used for vector spherical and cylindrical waves. The S-matrix relates incoming and outgoing fields expanded in a helicity basis by $\boldsymbol{A}^{(3)}_{\nu,\pm}(\boldsymbol{r}, k_\pm(k_0))$ and $\boldsymbol{A}^{(4)}_{\nu,\pm}(\boldsymbol{r}, k_\pm(k_0))$. It is defined as

$$\boldsymbol{\mathcal{E}}_{\text{in}}(\boldsymbol{r}; k_0) = \sum_{s=\pm1} \sum_{\nu} \frac{a_{\nu s}}{2} \boldsymbol{A}^{(4)}_{\nu s}(\boldsymbol{r}, k_s(k_0)) \tag{2.61}$$

$$\boldsymbol{\mathcal{E}}_{\text{out}}(\boldsymbol{r}; k_0) = \sum_{s=\pm1} \sum_{\nu} \frac{a_{\nu s} + 2p_{\nu s}}{2} \boldsymbol{A}^{(3)}_{\nu s}(\boldsymbol{r}, k_s(k_0)) \,. \tag{2.62}$$

Thus, the S-matrix is $\mathbf{S} = \mathbb{1} + 2\mathbf{T}$. Another option is to separate the regular part and irregular part as

$$\boldsymbol{\mathcal{E}}_{\text{reg}}(\boldsymbol{r}; k_0) = \sum_{s=\pm1} \sum_{\nu} (a_{\nu s} + p_{\nu s}) \boldsymbol{A}^{(1)}_{\nu s}(\boldsymbol{r}, k_s(k_0)) \tag{2.63}$$

$$\boldsymbol{\mathcal{E}}_{\text{irr}}(\boldsymbol{r}; k_0) = \sum_{s=\pm1} \sum_{\nu} \mathrm{i} p_{\nu s} \boldsymbol{A}^{(2)}_{\nu s}(\boldsymbol{r}, k_s(k_0)) \,, \tag{2.64}$$

where the transition is described by the reactance matrix $\mathbf{K}$. Its relation to the T- and S-matrix is given by [40]

$$\mathbf{K} = -\mathrm{i}\frac{\mathbf{T}}{\mathbb{1} + \mathbf{T}} = \mathrm{i}\frac{\mathbb{1} - \mathbf{S}}{\mathbb{1} + \mathbf{S}} \,. \tag{2.65}$$

In both cases, the matrix in the numerator and the inverse matrix of the denominator commute, so the order of their action does not need to be specified. Although in principle equal, each of these matrices are a useful representation of the scattering process depending on the exact task at hand [40].

2.2.3 Rotations, translations, and other transformations

In the previous sections, we discussed different basis sets, T-matrices and S-matrices that are based on the solutions to Maxwell's equations and how to calculate the interaction between multiple objects represented by those matrices. However, the analytical expressions for the different wave functions allow a range of further applications enlarging the range of scattering scenarios that can be solved.

Rotations

We discuss arbitrary rotations of vector spherical waves and rotations about the z-axis for vector cylindrical and plane waves. For vector spherical waves, applying a rotation about the Euler angles α, β, γ in the zyz-convention, is expressed by the Wigner-D-matrices [41] as

$$\mathbf{R}(\alpha,\beta,\gamma)\boldsymbol{A}^{(n)}_{lms}(\mathbf{R}^{-1}(\alpha,\beta,\gamma)\boldsymbol{r},k) = \sum_{m'=-l}^{l} D^{l}_{mm'}(\alpha,\beta,\gamma)\boldsymbol{A}^{(n)}_{lm's}(\boldsymbol{r},k)\,, \tag{2.66}$$

where

$$\mathbf{R}(\alpha,\beta,\gamma) = \mathbf{R}_z(\alpha)\mathbf{R}_y(\beta)\mathbf{R}_z(\gamma)\,, \tag{2.67}$$

with

$$\mathbf{R}_z(\alpha) = \begin{pmatrix} \cos\alpha & -\sin\alpha & 0 \\ \sin\alpha & \cos\alpha & 0 \\ 0 & 0 & 1 \end{pmatrix} \quad \text{and} \quad \mathbf{R}_y(\beta) = \begin{pmatrix} \cos\beta & 0 & \sin\beta \\ 0 & 1 & 0 \\ -\sin\beta & 0 & \cos\beta \end{pmatrix}. \tag{2.68}$$

These rotations are taken to be in an active sense, namely, we rotate the waves and not the coordinate frame. However, with the chosen Euler angle convention, we can switch to the passive transformation by reversing the order of the angles applied. For vector cylindrical waves, the rotation by β about the z-axis is done with

$$\mathbf{R}_z(\beta)\boldsymbol{A}^{(n)}_{k_z ms}(\mathbf{R}_z^{-1}(\beta)\boldsymbol{r},k) = \mathrm{e}^{-\mathrm{i}m\beta}\boldsymbol{A}^{(n)}_{k_z ms}(\boldsymbol{r},k)\,, \tag{2.69}$$

and for vector plane waves, we use

$$\mathbf{R}_z(\beta)\boldsymbol{A}_{\hat{\boldsymbol{k}}s}(\mathbf{R}_z^{-1}(\beta)\boldsymbol{r},k) = \boldsymbol{A}_{\mathbf{R}_z(\beta)\hat{\boldsymbol{k}}s}(\boldsymbol{r},k) \tag{2.70}$$

to change the direction of the wave vector and polarizations accordingly.

Translations

Translations for vector spherical and cylindrical fields are given by Eqs. (2.53) and (2.54), where one stays within the same type of mode, namely, regular fields are translated to regular fields and singular fields are translated to singular fields. The translation formula for plane waves is simply the multiplication

$$\boldsymbol{A}_{\hat{\boldsymbol{k}}s}(\boldsymbol{r}+\boldsymbol{R},k) = \mathrm{e}^{\mathrm{i}\boldsymbol{k}\boldsymbol{R}}\boldsymbol{A}_{\hat{\boldsymbol{k}}s}(\boldsymbol{r},k) \tag{2.71}$$

by the corresponding phase factor.

Regular field expansions

The transformations so far only concerned transformations within the same type of solution, for example, spherical waves are rotated to other spherical waves. However, an important part is also the connection of different basis sets, which we summarize here. First, we have the relation

$$\begin{pmatrix} \boldsymbol{M}_{\hat{\boldsymbol{k}}}(\boldsymbol{r},k) \\ \boldsymbol{N}_{\hat{\boldsymbol{k}}}(\boldsymbol{r},k) \end{pmatrix} = \sum_{l=1}^{\infty} \sum_{m=-l}^{l} 4\pi \mathrm{i}^{l-1} N_{lm} \mathrm{e}^{-\mathrm{i}m\varphi_{\boldsymbol{k}}} \begin{pmatrix} \tau_{lm}(\theta_{\boldsymbol{k}}) & \pi_{lm}(\theta_{\boldsymbol{k}}) \\ \pi_{lm}(\theta_{\boldsymbol{k}}) & \tau_{lm}(\theta_{\boldsymbol{k}}) \end{pmatrix} \begin{pmatrix} \boldsymbol{M}^{(1)}_{lm}(\boldsymbol{r},k) \\ \boldsymbol{N}^{(1)}_{lm}(\boldsymbol{r},k) \end{pmatrix} \tag{2.72}$$

of vector plane waves and vector spherical waves [P3, 23] that can be derived by combining the expansion of plane waves propagating in the z-direction [16] with the rotation operators [42] defined above. Next, we have the relation of vector cylindrical and plane waves,

$$\begin{pmatrix} \boldsymbol{M}_{\hat{\boldsymbol{k}}}(\boldsymbol{r},k) \\ \boldsymbol{N}_{\hat{\boldsymbol{k}}}(\boldsymbol{r},k) \end{pmatrix} = \sum_{m=-\infty}^{\infty} \mathrm{i}^{m} \mathrm{e}^{-\mathrm{i}m\varphi_{\boldsymbol{k}}} \begin{pmatrix} \boldsymbol{M}^{(1)}_{k_z m}(\boldsymbol{r},k) \\ \boldsymbol{N}^{(1)}_{k_z m}(\boldsymbol{r},k) \end{pmatrix}, \tag{2.73}$$

which is a direct result of applying Eqs. (2.13b) and (2.13c) to the plane wave expansion in cylindrical coordinates (see Appendix G). With these results, it becomes straightforward to obtain

$$\begin{pmatrix} \boldsymbol{M}^{(1)}_{k_z m}(\boldsymbol{r},k) \\ \boldsymbol{N}^{(1)}_{k_z m}(\boldsymbol{r},k) \end{pmatrix} = \sum_{l=m}^{\infty} 4\pi \mathrm{i}^{l-m-1} N_{lm} \begin{pmatrix} \tau_{lm}(\theta_{\boldsymbol{k}}) & \pi_{lm}(\theta_{\boldsymbol{k}}) \\ \pi_{lm}(\theta_{\boldsymbol{k}}) & \tau_{lm}(\theta_{\boldsymbol{k}}) \end{pmatrix} \begin{pmatrix} \boldsymbol{M}^{(1)}_{lm}(\boldsymbol{r},k) \\ \boldsymbol{N}^{(1)}_{lm}(\boldsymbol{r},k) \end{pmatrix} \tag{2.74}$$

by comparison of the coefficients for the expansion of vector plane waves in vector spherical and cylindrical waves [43].

Basis change of periodic scattered waves

In the following, we derive transformations to connect different basis sets in the presence of periodic boundary conditions. More precisely, we transform scattered wave solutions in different lattices into basis sets suited for the respective periodicity as discussed earlier. For example, a chain of spherical wave solutions can be transformed to scattered cylindrical waves. Such a change of basis comes with the benefit that evaluations of the field and other quantities become more efficient. However, the trade-off comes by a changed domain of validity as shown in Fig. 2.5. Note that this change can also be used to overcome limitations that are specific to only some basis sets.

We begin with integral representations of the scattered waves into plane waves. Such relations can be derived with the plane wave expansions of the scalar spherical and cylindrical waves (see Appendix G) and applying Eqs. (2.13b) and (2.13c). As a result, we get

$$\boldsymbol{M}^{(3)}_{lm}(\boldsymbol{r},k) = \frac{1}{2\pi \mathrm{i}^l} \iint_{\mathbb{R}^2} \frac{\mathrm{d}k_x \mathrm{d}k_y}{k^2 \gamma_{xy}} \boldsymbol{X}_{lm}(\theta_{\boldsymbol{k}},\varphi_{\boldsymbol{k}}) \mathrm{e}^{\mathrm{i}(k_x x + k_y y + k_z z)} \tag{2.75a}$$

$$= \frac{1}{2\pi \mathrm{i}^l} \iint_{\mathbb{R}^2} \frac{\mathrm{d}k_x \mathrm{d}k_z}{k^2 \gamma_{xz}} \boldsymbol{X}_{lm}(\theta_{\boldsymbol{k}},\varphi_{\boldsymbol{k}}) \mathrm{e}^{\mathrm{i}(k_x x + k_y y + k_z z)} \tag{2.75b}$$

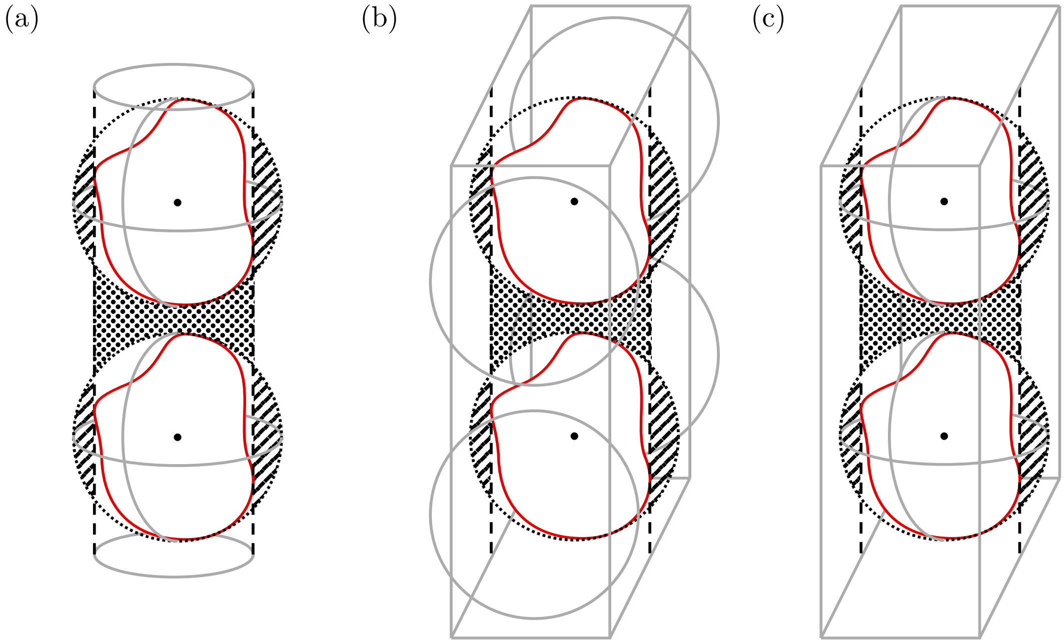

Figure 2.5: Domains of validity for different expansions. In all three panels, the outline of a particle is shown as solid red line with the center point marked and a circumscribing circle shown as dotted black line. A periodic arrangement is indicated in the vertical direction. This periodic arrangement is enclosed by two straight dashed lines. Two different domains are marked: The dotted area outside the circles but between the dashed lines and the hatched area inside the circles but outside of the dashed lines. Although the cross-section in all three panels looks identical, they correspond to the following three transitions as indicated by the gray lines:

(a) from spherical to cylindrical waves, where the paper plane corresponds to the x-z-plane with the x-direction along the horizontal,

(b) from cylindrical to plane waves, where the paper plane corresponds to the x-y-plane with the y-direction along the horizontal, and

(c) from spherical to plane waves, where the paper plane corresponds to the x-z-plane (or another plane spanned by the z-axis and a lattice vector) with the z-direction along the horizontal.

Hence, in the first and third case, the dotted circles are cross-sections of the circumscribing spheres and in the second case the cross-sections of the circumscribing cylinders. The vector spherical and cylindrical waves, respectively, are valid outside the dotted circles. After the transition to cylindrical waves in case one and plane waves in cases two and three the domain of validity is bounded by the dashed straight lines. Thus, due to the transition, the valid domain changes as follows: The dotted area is excluded after the transition but the hatched area gets added to the valid domain.

and

$$\boldsymbol{N}_{lm}^{(3)}(\boldsymbol{r}, k) = \frac{1}{2\pi \mathrm{i}^{l-1}} \iint_{\mathbb{R}^2} \frac{\mathrm{d}k_x \mathrm{d}k_y}{k^2 \gamma_{xy}} \hat{\boldsymbol{k}} \times \boldsymbol{X}_{lm}(\theta_{\boldsymbol{k}}, \varphi_{\boldsymbol{k}}) \mathrm{e}^{\mathrm{i}(k_x x + k_y y + k_z z)} \tag{2.76a}$$

$$= \frac{1}{2\pi \mathrm{i}^{l-1}} \iint_{\mathbb{R}^2} \frac{\mathrm{d}k_x \mathrm{d}k_z}{k^2 \gamma_{xz}} \hat{\boldsymbol{k}} \times \boldsymbol{X}_{lm}(\theta_{\boldsymbol{k}}, \varphi_{\boldsymbol{k}}) \mathrm{e}^{\mathrm{i}(k_x x + k_y y + k_z z)} \tag{2.76b}$$

for scattered spherical waves [44], where we use

$$\gamma_{ij} = \sqrt{1 - \frac{k_i^2 + k_j^2}{k^2}} \tag{2.77}$$

for $i, j \in \{x, y, z\}$. The value of the wave vector component absent in the integral is given by the constitutive relations. However, its sign needs to be determined, which depends on the component of $\boldsymbol{r}$ corresponding to the direction of the wave vector that is not included in the integral, namely z in the first version and y in the second one. For positive or negative values, the sign of the corresponding value k_z and k_y is taken to be positive or negative, respectively. Hence, the plane waves in the integral are always outgoing from the origin and evanescent modes decay away from the origin. A similar expansion given by [45]

$$\boldsymbol{M}_{k_z,m}^{(3)}(\boldsymbol{r}, k) = \frac{1}{\pi \mathrm{i}^{m+1}} \int_{-\infty}^{\infty} \frac{\mathrm{d}k_x}{k\gamma_{xz}} \hat{\boldsymbol{\varphi}}_{\boldsymbol{k}} \mathrm{e}^{\mathrm{i}(k_x x + k_y y + k_z z + m\varphi_{\boldsymbol{k}})} \tag{2.78a}$$

$$\boldsymbol{N}_{k_z,m}^{(3)}(\boldsymbol{r}, k) = -\frac{1}{\pi \mathrm{i}^{m}} \int_{-\infty}^{\infty} \frac{\mathrm{d}k_x}{k\gamma_{xz}} \hat{\boldsymbol{\theta}}_{\boldsymbol{k}} \mathrm{e}^{\mathrm{i}(k_x x + k_y y + k_z z + m\varphi_{\boldsymbol{k}})} \tag{2.78b}$$

represents cylindrical waves by an integral over plane waves where the discontinuity is along $y = 0$.

Periodic spherical waves to plane waves We solve each of the lattice sums in a case-by-case manner, starting with vector spherical waves in a two-dimensional lattice in the x-y-plane. Taking the integral expression of Eq. (2.75a) combined with Poisson's sum formula (see Eq. (A.5)), we get

$$\sum_{\boldsymbol{R} \in \Lambda_2} \boldsymbol{M}_{lm}^{(3)}(\boldsymbol{r} - \boldsymbol{R}, k) \mathrm{e}^{\mathrm{i}\boldsymbol{k}_\parallel \boldsymbol{R}} = \frac{2\pi N_{lm}}{A k^2 \mathrm{i}^l} \sum_{\boldsymbol{Q} \in \Lambda_2^*} \left(\mathrm{i}\pi_{lm}(\theta_{\boldsymbol{k}}) \hat{\boldsymbol{\theta}}_{\boldsymbol{k}} - \tau_{lm}(\theta_{\boldsymbol{k}}) \hat{\boldsymbol{\varphi}}_{\boldsymbol{k}}\right) \frac{\mathrm{e}^{\mathrm{i}\boldsymbol{k}\boldsymbol{r} + \mathrm{i}m\varphi_{\boldsymbol{k}}}}{\sqrt{1 - \frac{(\boldsymbol{k}_\parallel + \boldsymbol{Q})^2}{k^2}}} \tag{2.79}$$

for the TE spherical waves. We note that $\boldsymbol{k} = \boldsymbol{k}_\parallel + \boldsymbol{Q} \pm \hat{\boldsymbol{z}} \sqrt{k^2 - (\boldsymbol{k}_\parallel + \boldsymbol{Q})^2}$ for $z \gtrless 0$ and A is the area of one unit cell. Now, we can compare this expression with the explicit formulas for the plane waves in Eq. (2.15). Analogously, we obtain a relation between TM spherical waves and plane waves such that we can write

$$\begin{aligned} &\sum_{\boldsymbol{R} \in \Lambda_2} \begin{pmatrix} \boldsymbol{M}_{lm}^{(3)}(\boldsymbol{r} - \boldsymbol{R}, k) \\ \boldsymbol{N}_{lm}^{(3)}(\boldsymbol{r} - \boldsymbol{R}, k) \end{pmatrix} \mathrm{e}^{\mathrm{i}\boldsymbol{k}_\parallel \boldsymbol{R}} \\ &\quad = -\frac{2\pi \mathrm{i} N_{lm}}{A k^2 \mathrm{i}^l} \sum_{\boldsymbol{Q} \in \Lambda_2^*} \frac{\mathrm{e}^{\mathrm{i}m\varphi_{\boldsymbol{k}}}}{\sqrt{1 - \frac{(\boldsymbol{k}_\parallel + \boldsymbol{Q})^2}{k^2}}} \begin{pmatrix} \tau_{lm}(\theta_{\boldsymbol{k}}) & \pi_{lm}(\theta_{\boldsymbol{k}}) \\ \pi_{lm}(\theta_{\boldsymbol{k}}) & \tau_{lm}(\theta_{\boldsymbol{k}}) \end{pmatrix} \begin{pmatrix} \boldsymbol{M}_{\boldsymbol{k}_\parallel + \boldsymbol{Q}, \mathrm{sign}(z)}(\boldsymbol{r}, k) \\ \boldsymbol{N}_{\boldsymbol{k}_\parallel + \boldsymbol{Q}, \mathrm{sign}(z)}(\boldsymbol{r}, k) \end{pmatrix}, \end{aligned} \tag{2.80}$$

where we index the plane wave functions by two components and the direction of the remaining third component that is implicitly defined by the dispersion relation as described above.

Periodic spherical waves to cylindrical waves The second case are spherical waves in a one-dimensional lattice along the z-direction. Using the same procedure, but the representation in Eq. (2.75a) for the vector spherical waves, we obtain

$$\begin{aligned}\sum_{\boldsymbol{R}\in\Lambda_1} &\boldsymbol{M}_{lm}^{(3)}(\boldsymbol{r}-\boldsymbol{R},k)\mathrm{e}^{\mathrm{i}\boldsymbol{k}_\parallel\boldsymbol{R}} \\ &= \frac{N_{lm}}{ak\mathrm{i}^l}\sum_{\boldsymbol{Q}\in\Lambda_1^*}\int_{-\infty}^{\infty}\frac{\mathrm{d}k_x\mathrm{e}^{\mathrm{i}\boldsymbol{k}\boldsymbol{r}+\mathrm{i}m\varphi_{\boldsymbol{k}}}}{k\sqrt{1-\frac{k_x^2+(k_\parallel+Q)^2}{k^2}}}\left(\mathrm{i}\pi_{lm}(\theta_{\boldsymbol{k}})\hat{\boldsymbol{\theta}}_{\boldsymbol{k}}-\tau_{lm}(\theta_{\boldsymbol{k}})\hat{\boldsymbol{\varphi}}_{\boldsymbol{k}}\right), \qquad (2.81)\end{aligned}$$

where a is the lattice pitch. Then, a comparison with the plane wave representations of the cylindrical waves leads to the connection

$$\sum_{\boldsymbol{R}\in\Lambda_1}\begin{pmatrix}\boldsymbol{M}_{lm}^{(3)}(\boldsymbol{r}-\boldsymbol{R},k)\\ \boldsymbol{N}_{lm}^{(3)}(\boldsymbol{r}-\boldsymbol{R},k)\end{pmatrix}\mathrm{e}^{\mathrm{i}\boldsymbol{k}_\parallel\boldsymbol{R}} = -\frac{\mathrm{i}\pi N_{lm}}{ak\mathrm{i}^{l-m}}\sum_{\boldsymbol{Q}\in\Lambda_1^*}\begin{pmatrix}\tau_{lm}(\theta_{\boldsymbol{k}}) & \pi_{lm}(\theta_{\boldsymbol{k}})\\ \pi_{lm}(\theta_{\boldsymbol{k}}) & \tau_{lm}(\theta_{\boldsymbol{k}})\end{pmatrix}\begin{pmatrix}\boldsymbol{M}_{k_\parallel+Q,m}^{(3)}(\boldsymbol{r},k)\\ \boldsymbol{N}_{k_\parallel+Q,m}^{(3)}(\boldsymbol{r},k)\end{pmatrix}, \qquad (2.82)$$

where we also added the results for the TM modes. In both cases, we find that the TE and TM modes of spherical and cylindrical or spherical and plane waves generally mix in the transformation. That happens because the designations are meant with respect to different surfaces, namely spherical shells and the x-y-plane. However, if we transition to helicity basis, different modes do not mix.

Periodic cylindrical waves to plane waves The last case is a one-dimensional lattice along the x-axis of scattered cylindrical waves. Here, we obtain

$$\sum_{\boldsymbol{R}\in\Lambda_1}\boldsymbol{M}_{k_z,m}(\boldsymbol{r}-\boldsymbol{R},k)\mathrm{e}^{\mathrm{i}\boldsymbol{k}_\parallel\boldsymbol{R}} = \frac{2}{ak\mathrm{i}^{m+1}}\sum_{\boldsymbol{Q}\in\Lambda_1^*}\frac{\mathrm{e}^{\mathrm{i}\boldsymbol{k}\boldsymbol{r}+\mathrm{i}m\varphi_{\boldsymbol{k}}}}{\sqrt{1-\frac{(k_\parallel+Q)^2+k_z^2}{k^2}}}\hat{\boldsymbol{\varphi}}_{\boldsymbol{k}} \qquad (2.83)$$

for the TE cylindrical waves, which is also a pure TE plane wave since they share the pilot vector in their construction. The complete result for both polarizations is

$$\sum_{\boldsymbol{R}\in\Lambda_1}\begin{pmatrix}\boldsymbol{M}_{k_z,m}^{(3)}(\boldsymbol{r}-\boldsymbol{R},k)\\ \boldsymbol{N}_{k_z,m}^{(3)}(\boldsymbol{r}-\boldsymbol{R},k)\end{pmatrix}\mathrm{e}^{\mathrm{i}\boldsymbol{k}_\parallel\boldsymbol{R}} = \frac{2}{ak\mathrm{i}^m}\sum_{\boldsymbol{Q}\in\Lambda_1^*}\frac{1}{\sqrt{1-\frac{(k_\parallel+Q)^2+k_z^2}{k^2}}}\begin{pmatrix}\boldsymbol{M}_{\hat{\boldsymbol{k}}}(\boldsymbol{r},k)\\ \boldsymbol{N}_{\hat{\boldsymbol{k}}}(\boldsymbol{r},k)\end{pmatrix}, \qquad (2.84)$$

which can also be transformed to helicity basis. The change of basis also changes the domain of validity as shown in Fig. 2.5. For example, if we transition from vector spherical waves to plane waves, the circumscribing cylinder can enlarge the domain in the direction of $\hat{\boldsymbol{\rho}}$ as shown by the dashed area. The domain between the spheres, however, is not described faithfully by the vector spherical waves. A similar behavior exists for the other transition. This property can be used later. Note that even for aperiodic cases, a change of basis can be used explicitly to couple particle close to each other [46].

2.3 Lattice sums and the Ewald method

The Ewald method [13] is a useful approach to treat infinite sums. Originally developed for calculations of electrostatic potentials in crystal lattices, the approach itself can be generalized [P4, 47–54].

The fundamental idea is the following. Assume we have a lattice of dimension d with unit vectors $\boldsymbol{u}_i \in \mathbb{R}^d$, $i \in \{1, \dots, d\}$ that consists of all points in the set $\Lambda = \{\sum_{i=1}^d n_i \boldsymbol{u}_i | n_i \in \mathbb{Z}\}$ and a function $f(\boldsymbol{r})$ that we want to sum for all these lattice points

$$D(\Lambda) = \sum_{\boldsymbol{R} \in \Lambda} f(\boldsymbol{R}) \,. \tag{2.85}$$

We, conventionally, call the sum D. In cases where the function $f(\boldsymbol{r})$ is short-ranged, the sum should converge quickly in real space and can be calculated directly. Moreover, if the sum has long-range contributions, it might be beneficial to Fourier transform the sum from the real to the reciprocal space, resulting in the function $\underline{f}(\boldsymbol{q})$ (Appendix A). Then, by making use of Poisson's summation formula given in Eq. (A.5), the sum can be transformed to

$$D(\Lambda) = \frac{(2\pi)^d}{V_d} \sum_{\boldsymbol{Q} \in \Lambda^*} \tilde{f}(\boldsymbol{Q}) \tag{2.86}$$

with $\Lambda^* = \{\sum_{j=1}^d n_j \boldsymbol{v}_j | n_j \in \mathbb{Z}\}$ the reciprocal lattice with unit vectors $\boldsymbol{v}_j$ fulfilling $\boldsymbol{u}_i \boldsymbol{v}_j = 2\pi\delta_{ij}$. A sum that might be tedious to calculate in real space can so become quickly converging in reciprocal space.

In some cases, however, there are short- and long-range interactions that contribute equally to the final value of the sum. Then, the convergence is often poor in both real and reciprocal space. The goal of Ewald's method is to find a way to separate the short- and long-range parts of the function $f(\boldsymbol{r}) = f_{\mathrm{S}}(\boldsymbol{r}) + f_{\mathrm{L}}(\boldsymbol{r})$. This separation then allows us to only transform the long-range contributions to the reciprocal space

$$D(\Lambda) = \underbrace{\frac{(2\pi)^d}{V_d} \sum_{\boldsymbol{Q} \in \Lambda^*} \tilde{f}_{\mathrm{L}}(\boldsymbol{Q})}_{D^{(1)}(\Lambda)} + \underbrace{\sum_{\boldsymbol{R} \in \Lambda} f_{\mathrm{S}}(\boldsymbol{R})}_{D^{(2)}(\Lambda)} \,, \tag{2.87}$$

which then both converge quickly. The major challenge in this method is to find a separation that leads to two equally quickly converging series whereof the long-range part has a simple enough Fourier transform. We use $D^{(1)}(\Lambda)$ and $D^{(2)}(\Lambda)$ later to refer to these parts.

In practice, the sum often excludes the point $\boldsymbol{R} = 0$. Then, to Fourier transform the field it is necessary to add and subtract $f_{\mathrm{L}}(0)$ explicitly such that the decomposition now includes the three parts

$$D(\Lambda \backslash \{0\}) = \underbrace{-f_{\mathrm{L}}(0)}_{D^{(0)}} + D^{(1)}(\Lambda) + D^{(2)}(\Lambda \backslash \{0\}) \,. \tag{2.88}$$

Deriving expressions to calculate these three parts – the origin correction, the reciprocal space sum, and the real space sum – for the translations coefficients of Helmholtz equation solutions are the main objective of Chapter 3.

We derive the lattice sum of translation coefficients for scalar solutions of the Helmholtz equation using a direct approach. We describe the derivation as direct in comparison to the more widely used approach where one uses projections onto the different modes and then has to take a special limit to evaluate the expressions. The direct approach is conceptually simpler and has the additional benefit that it can be applied equally well to complex unit cells and all lattice dimensions, which is not as easily done for the indirect approach, as we show shortly.

For later comparison, we briefly outline the typical approach, which relies on the combination of two expansions. First, we observe the following: Given the Green's function $G_0(\boldsymbol{r}, k)$ of the Helmholtz equation in two or three dimensions – those cases correspond to cylindrical and spherical wave solutions – the quasi-periodic Green's function can be expanded as

$$\sum_{\boldsymbol{R}\in\Lambda} G_0(\boldsymbol{r}' + \boldsymbol{r} - \boldsymbol{R}, k)\mathrm{e}^{\mathrm{i}\boldsymbol{k}_\parallel \boldsymbol{R}} = -\mathrm{i}k \sum_\nu \tau_\nu(k, \boldsymbol{r}, \boldsymbol{k}_\parallel) f_\nu(\boldsymbol{r}', k) \tag{2.89}$$

at $\boldsymbol{r}$ in regular solutions $f_\nu(\boldsymbol{r}', k)$ [54]. Now, we can project onto individual coefficients $\tau_\nu(k, \boldsymbol{r}, \boldsymbol{k}_\parallel)$ by multiplying with the complex conjugate of the angular part of $f_\nu(\boldsymbol{r}', k)$ and integrating over the angles. On the left-hand side, we have to solve the integration and, then, we can take the limit $|\boldsymbol{r}'| \to 0$ and compare the lowest order coefficients on both sides of the equation. However, solving the integral on the left-hand side of the equation can be challenging.

The second observation is that we can alternatively write the Green's function on the left-hand side as singular zeroth order solutions $f_\nu(\boldsymbol{r}', k)$. Then, we can apply the translation coefficients for this function to get a similar expansion to that on the right-hand side and compare coefficients.

For lattices with simple unit cells, expressions are widely available [50, 52–55]. For complex unit cells, however, only certain cases are solved [51, 56] and the results for one-dimensional lattices of spherical waves are generally not known so far [57].

2.4 Plane wave methods for stratified media

In the plane wave basis, we mostly use S-matrices where incoming and outgoing fields are used instead of T-matrices relating incident and scattered fields. Another approach that will be discussed briefly are transfer matrices. They relate the fields on one side of a plane with those on the other side.

For the S-matrix approach using plane waves, we usually assume uniformity in the x-y-direction, such as for a slab of homogeneous material or a periodic system with lattice Λ_2. Then, the at least discrete translational symmetry suggests to expand the field in diffraction orders $\boldsymbol{Q} \in \Lambda_2^*$ instead. Thus, we replace the definition of the plane waves by the three components of the wave vector $\hat{\boldsymbol{k}}$ to the definition in terms of the parallel components $\boldsymbol{k}_\parallel + \boldsymbol{Q}$ as described above. In some cases, we use periodicity in the x-z-plane and the remaining component points in the z-direction. However, the definition of the plane waves is always the ones defined in Eq. (2.15).

The incoming waves are

$$\boldsymbol{\mathcal{E}}_{\mathrm{in}}(\boldsymbol{r};k_0) = \sum_{s=\pm}\sum_{\boldsymbol{Q}} \begin{cases} a_{\boldsymbol{k}_\parallel+\boldsymbol{Q},\uparrow,s}\boldsymbol{A}_{\boldsymbol{k}_\parallel+\boldsymbol{Q},\uparrow,s}(\boldsymbol{r},k_s(k_0)) & z<0 \\ b_{\boldsymbol{k}_\parallel+\boldsymbol{Q},\downarrow,s}\boldsymbol{A}_{\boldsymbol{k}_\parallel+\boldsymbol{Q},\downarrow,s}(\boldsymbol{r},k_s(k_0)) & z>0 \end{cases} \tag{2.90}$$

and the outgoing waves are

$$\boldsymbol{\mathcal{E}}_{\mathrm{out}}(\boldsymbol{r};k_0) = \sum_{s=\pm}\sum_{\boldsymbol{Q}} \begin{cases} b_{\boldsymbol{k}_\parallel+\boldsymbol{Q},\uparrow,s}\boldsymbol{A}_{\boldsymbol{k}_\parallel+\boldsymbol{Q},\uparrow,s}(\boldsymbol{r},k_s(k_0)) & z>0 \\ a_{\boldsymbol{k}_\parallel+\boldsymbol{Q},\downarrow,s}\boldsymbol{A}_{\boldsymbol{k}_\parallel+\boldsymbol{Q},\downarrow,s}(\boldsymbol{r},k_s(k_0)) & z<0 \end{cases}, \tag{2.91}$$

where the coefficient vectors $\boldsymbol{a}_d$ are for waves below the system described by the S-matrix and the vectors $\boldsymbol{b}_d$ are for waves above it. The S-matrix then relates these coefficients by

$$\begin{pmatrix}\boldsymbol{b}_\uparrow \\ \boldsymbol{a}_\downarrow\end{pmatrix} = \underbrace{\begin{pmatrix}\mathbf{S}_{\uparrow\uparrow} & \mathbf{S}_{\uparrow\downarrow} \\ \mathbf{S}_{\downarrow\uparrow} & \mathbf{S}_{\downarrow\downarrow}\end{pmatrix}}_{=\mathbf{S}} \begin{pmatrix}\boldsymbol{a}_\uparrow \\ \boldsymbol{b}_\downarrow\end{pmatrix}. \tag{2.92}$$

Four blocks can be identified: The diagonal ones contain transmission and the off-diagonal blocks reflection coefficients. If we want to couple two S-matrices describing individual layers or layer stacks to get the total transmission and reflection coefficients for the whole system consisting of S-matrices $\mathbf{S}^a$ and $\mathbf{S}^b$ stacked along the z-axis, we can use [39]

$$\mathbf{S}_{\uparrow\uparrow} = \mathbf{S}^b_{\uparrow\uparrow}(\mathbb{1} - \mathbf{S}^a_{\uparrow\downarrow}\mathbf{S}^b_{\downarrow\uparrow})^{-1}\mathbf{S}^a_{\uparrow\uparrow} \tag{2.93a}$$

$$\mathbf{S}_{\downarrow\uparrow} = \mathbf{S}^a_{\downarrow\uparrow} + \mathbf{S}^a_{\downarrow\downarrow}\mathbf{S}^b_{\downarrow\uparrow}(\mathbb{1} - \mathbf{S}^a_{\uparrow\downarrow}\mathbf{S}^b_{\downarrow\uparrow})^{-1}\mathbf{S}^a_{\uparrow\uparrow} \tag{2.93b}$$

$$\mathbf{S}_{\uparrow\downarrow} = \mathbf{S}^b_{\uparrow\downarrow} + \mathbf{S}^b_{\downarrow\downarrow}\mathbf{S}^a_{\uparrow\downarrow}(\mathbb{1} - \mathbf{S}^b_{\downarrow\uparrow}\mathbf{S}^a_{\uparrow\downarrow})^{-1}\mathbf{S}^b_{\downarrow\downarrow} \tag{2.93c}$$

$$\mathbf{S}_{\downarrow\downarrow} = \mathbf{S}^a_{\downarrow\downarrow}(\mathbb{1} - \mathbf{S}^b_{\downarrow\uparrow}\mathbf{S}^a_{\uparrow\downarrow})^{-1}\mathbf{S}^b_{\downarrow\downarrow}\,. \tag{2.93d}$$

By iteratively using the coupling of two neighboring systems, a stack can be described. Furthermore, the layer-doubling technique [39, 52] can be used to efficiently describe periodic systems of finite thickness, exploiting the exponential growth of the number of layers if the result on the left-hand side for coupling two identical S-matrices is reused on the right-hand side.

Additionally, we can also compute the result for an infinite stack of periodically repeating S-matrices. With the third lattice vector being $\boldsymbol{a}_3 = a_z\hat{\boldsymbol{z}}$, the phase difference between two adjacent layers is $\mathrm{e}^{\mathrm{i}k_za_z}$, where k_z needs to be determined. Then, we can express the periodicity conditions as

$$\begin{pmatrix}\mathbf{S}_{\uparrow\uparrow} & \mathbf{S}_{\uparrow\downarrow} \\ 0 & \mathbb{1}\end{pmatrix}\begin{pmatrix}\boldsymbol{a}_\uparrow \\ \boldsymbol{b}_\downarrow\end{pmatrix} = \begin{pmatrix}\mathbb{1} & 0 \\ \mathbf{S}_{\downarrow\uparrow} & \mathbf{S}_{\downarrow\downarrow}\end{pmatrix}\mathrm{e}^{\mathrm{i}k_za_z}\begin{pmatrix}\boldsymbol{a}_\uparrow \\ \boldsymbol{b}_\downarrow\end{pmatrix}, \tag{2.94}$$

where we used $\boldsymbol{b}_\uparrow = \boldsymbol{a}_\uparrow\mathrm{e}^{\mathrm{i}k_za_z}$ and $\boldsymbol{a}_\downarrow = \boldsymbol{b}_\downarrow\mathrm{e}^{-\mathrm{i}k_za_z}$ and rearranged Eq. (2.92) such that the right-hand side has the common exponential dependency. Then, we can invert the matrix on the right-hand side and obtain [39, 52]

$$\begin{pmatrix}\mathbf{S}_{\uparrow\uparrow} & \mathbf{S}_{\uparrow\downarrow} \\ -\mathbf{S}^{-1}_{\downarrow\downarrow}\mathbf{S}_{\downarrow\uparrow}\mathbf{S}_{\uparrow\uparrow} & \mathbf{S}^{-1}_{\downarrow\downarrow}(\mathbb{1} - \mathbf{S}_{\downarrow\uparrow}\mathbf{S}_{\uparrow\downarrow})\end{pmatrix}\begin{pmatrix}\boldsymbol{a}_\uparrow \\ \boldsymbol{a}_\downarrow\end{pmatrix} = \mathrm{e}^{\mathrm{i}k_za_z}\begin{pmatrix}\boldsymbol{a}_\uparrow \\ \boldsymbol{a}_\downarrow\end{pmatrix}, \tag{2.95}$$

which is a useful representation to calculate the band structure of three-dimensional periodic structures. It is essentially an eigenvalue equation. The eigenvectors of the matrix on the left-hand side describe different modes and the eigenvalues v specify the z-component of the modes by $k_z = -\frac{\mathrm{i}}{a_z} \ln v$. Long-lived modes can be selected by setting a threshold on the imaginary part of k_z.

Another representation that is regularly used for stratified media is the transfer matrix. Here, we choose to take the fields on one side of the system in question and relate them to the fields on the other side. Taking the propagation in the positive z-direction, we, therefore, take the vectors $\boldsymbol{a}_d$ as given and want to obtain the vectors $\boldsymbol{b}_d$ as result. Through rearranging Eq. (2.92), we get

$$\begin{pmatrix} \mathbb{1} & -\mathbf{S}_{\uparrow\downarrow} \\ 0 & -\mathbf{S}_{\downarrow\downarrow} \end{pmatrix} \begin{pmatrix} \boldsymbol{b}_\uparrow \\ \boldsymbol{b}_\downarrow \end{pmatrix} = \begin{pmatrix} \mathbf{S}_{\uparrow\uparrow} & 0 \\ \mathbf{S}_{\downarrow\uparrow} & -\mathbb{1} \end{pmatrix} \begin{pmatrix} \boldsymbol{a}_\uparrow \\ \boldsymbol{a}_\downarrow \end{pmatrix} . \tag{2.96}$$

The matrix on the left-hand side can be inverted and we obtain the transfer matrix

$$\begin{pmatrix} \boldsymbol{b}_\uparrow \\ \boldsymbol{b}_\downarrow \end{pmatrix} = \underbrace{\begin{pmatrix} \mathbf{S}_{\uparrow\uparrow} - \mathbf{S}_{\uparrow\downarrow}\mathbf{S}_{\downarrow\downarrow}^{-1}\mathbf{S}_{\downarrow\uparrow} & \mathbf{S}_{\uparrow\downarrow}\mathbf{S}_{\downarrow\downarrow}^{-1} \\ -\mathbf{S}_{\downarrow\downarrow}^{-1}\mathbf{S}_{\downarrow\uparrow} & \mathbf{S}_{\downarrow\downarrow}^{-1} \end{pmatrix}}_{=\boldsymbol{\mathcal{T}}} \begin{pmatrix} \boldsymbol{a}_\uparrow \\ \boldsymbol{a}_\downarrow \end{pmatrix} , \tag{2.97}$$

where we use $\boldsymbol{\mathcal{T}}$ as a symbol to differentiate the transfer matrix from the T-matrix introduced earlier. The opposite transition from transfer matrices to S-matrices can be obtained, analogously.

Transfer matrix method

We now introduce the separate topic of focusing light in layers of anisotropic but homogeneous materials. For the description of light propagation in anisotropic media, we use transfer matrices [58, 59] that can be efficiently combined with the Richards and Wolf method of describing focusing of light with high aperture lenses [14].

As previously, we use the z-axis as the principle direction of propagation. Then, we can use the angular spectrum representation, where the two transverse directions are Fourier transformed (see Appendix A)

$$\boldsymbol{\mathcal{E}}(x, y; z, k_0) = \iint \mathrm{d}k_x \mathrm{d}k_y \underline{\boldsymbol{\mathcal{E}}}(k_x, k_y; z, k_0) \mathrm{e}^{\mathrm{i}(k_x x + k_y y)} , \tag{2.98}$$

with the inverse transformation

$$\underline{\boldsymbol{\mathcal{E}}}(k_x, k_y; z, k_0) = \frac{1}{(2\pi)^2} \iint \mathrm{d}x \mathrm{d}y \boldsymbol{\mathcal{E}}(x, y; z, k_0) \mathrm{e}^{-\mathrm{i}(k_x x + k_y y)} . \tag{2.99}$$

We can propagate the angular spectrum along the z-axis by

$$\underline{\boldsymbol{\mathcal{E}}}(k_x, k_y; z, k_0) = \mathrm{e}^{\mathrm{i}k_z z} \underline{\boldsymbol{\mathcal{E}}}(k_x, k_y; 0, k_0) , \tag{2.100}$$

where k_z is determined by the dispersion relation. There can be multiple values for k_z in anisotropic or chiral media. Instead of Eq. (2.24) used in the majority of this thesis, where we have scalar but chiral constitutive relations, we want to describe anisotropic media here. We start with Maxwell's equations as given in Eq. (2.3). We can now transition to Fourier space, which essentially replaces the nabla operator by $\mathrm{i}\boldsymbol{k}$. In the constitutive relations of Eq. (2.6), we now assume a homogeneous material, i.e., all material parameters are independent of the position $\boldsymbol{r}$. Then, we obtain

$$\left[\begin{pmatrix} \boldsymbol{k}\times & 0 \\ 0 & \boldsymbol{k}\times \end{pmatrix} - k_0 \begin{pmatrix} \boldsymbol{\chi}^{\mathsf{T}}(k_0) - \mathrm{i}\boldsymbol{\kappa}^{\mathsf{T}}(k_0) & \boldsymbol{\mu}(k_0) \\ -\boldsymbol{\epsilon}(k_0) & -\boldsymbol{\chi}(k_0) - \mathrm{i}\boldsymbol{\kappa}(k_0) \end{pmatrix}\right] \begin{pmatrix} \underline{\boldsymbol{\mathcal{E}}}(k_x, k_y; z, k_0) \\ \underline{\boldsymbol{\mathcal{H}}}(k_x, k_y; z, k_0) \end{pmatrix} = 0\,, \tag{2.101}$$

where

$$\boldsymbol{k}\times = \begin{pmatrix} 0 & -k_z & k_y \\ k_z & 0 & -k_x \\ -k_y & k_x & 0 \end{pmatrix} \tag{2.102}$$

is the matrix representation of the cross-product. This equation, in principle, can be solved directly now. All material parameters and the components k_x and k_y are given. The only unknown is k_z. The determinant of the matrix in Eq. (2.101) is a fourth order polynomial in k_z. The four solutions for its root correspond to the two polarizations times the two principle directions of propagation. The kernel of Eq. (2.101) defines the electric and magnetic fields for each of these modes.

However, we restrict ourselves to the achiral, reciprocal case. Then, we can eliminate one of the fields, e.g., the magnetic field, to obtain

$$\boldsymbol{k} \times \boldsymbol{\mu}^{-1}\boldsymbol{k} \times \underline{\boldsymbol{\mathcal{E}}}(k_x, k_y; z, k_0) + k_0^2 \boldsymbol{\epsilon} \underline{\boldsymbol{\mathcal{E}}}(k_x, k_y; z, k_0) = 0\,. \tag{2.103}$$

Again, this is a fourth order equation in k_z when computing the roots of the determinant leading to four solutions $k_{z,i}$. The polarizations and propagation directions corresponding to these four solutions are again given by the kernel of the resulting matrix, which we denote as $\boldsymbol{p}_i$. The polarizations of the magnetic field can then be found by $\boldsymbol{q}_i = \mu^{-1}\boldsymbol{k} \times \boldsymbol{p}_i$. Then, for each pair of k_x and k_y, we can define a four-by-four matrix for the propagation in the medium

$$\mathbf{P} = \begin{pmatrix} \mathrm{e}^{\mathrm{i}k_{z,1}z} & 0 & 0 & 0 \\ 0 & \mathrm{e}^{\mathrm{i}k_{z,2}z} & 0 & 0 \\ 0 & 0 & \mathrm{e}^{\mathrm{i}k_{z,3}z} & 0 \\ 0 & 0 & 0 & \mathrm{e}^{\mathrm{i}k_{z,4}z} \end{pmatrix} \tag{2.104}$$

and another matrix for the tangential components of the polarizations

$$\mathbf{D} = \begin{pmatrix} \boldsymbol{p}_1\hat{\boldsymbol{x}} & \boldsymbol{p}_2\hat{\boldsymbol{x}} & \boldsymbol{p}_3\hat{\boldsymbol{x}} & \boldsymbol{p}_4\hat{\boldsymbol{x}} \\ \boldsymbol{q}_1\hat{\boldsymbol{y}} & \boldsymbol{q}_2\hat{\boldsymbol{y}} & \boldsymbol{q}_3\hat{\boldsymbol{y}} & \boldsymbol{q}_4\hat{\boldsymbol{y}} \\ \boldsymbol{p}_1\hat{\boldsymbol{y}} & \boldsymbol{p}_2\hat{\boldsymbol{y}} & \boldsymbol{p}_3\hat{\boldsymbol{y}} & \boldsymbol{p}_4\hat{\boldsymbol{y}} \\ \boldsymbol{q}_1\hat{\boldsymbol{x}} & \boldsymbol{q}_2\hat{\boldsymbol{x}} & \boldsymbol{q}_3\hat{\boldsymbol{x}} & \boldsymbol{q}_4\hat{\boldsymbol{x}} \end{pmatrix} \tag{2.105}$$

called dynamical matrices [59]. The matching of the tangential components at an interface between two media a and b is then simply expressed as $\mathbf{D}_b^{-1}\mathbf{D}_a$. This matrix and the matrix $\mathbf{P}$ are used as transfer matrices to calculate the electromagnetic fields in stratified media.

In addition to the transfer matrices for anisotropic media, we need to find a mathematical description of the focused beam where we follow [60]. We describe the illumination incoming onto the lens as a spectrum $\boldsymbol{\mathcal{E}}_{\text{illu}}(\rho, \varphi; k_0)$ defined on a two-dimensional plane in polar coordinates. We now assume that this illumination is refracted onto a spherical shell. The azimuthal component $\hat{\boldsymbol{\varphi}}$ of the polarization is unchanged by the refraction and the polar component $\hat{\boldsymbol{\rho}}$ is changed to

$$\hat{\boldsymbol{\vartheta}} = \cos\vartheta \cos\varphi \hat{\boldsymbol{x}} + \cos\vartheta \sin\varphi \hat{\boldsymbol{y}} + \sin\vartheta \hat{\boldsymbol{z}}\,, \tag{2.106}$$

where $\sin\vartheta = \frac{\rho}{f}$ and f the focal length of the lens and, thus, we arrive at

$$\boldsymbol{\mathcal{E}}_{\text{refr}}(\rho, \varphi; -f, k_0) = \sqrt{\frac{Z_b}{Z_a}\cos\vartheta}(\hat{\boldsymbol{\vartheta}} \otimes \hat{\boldsymbol{\rho}} + \hat{\boldsymbol{\varphi}} \otimes \hat{\boldsymbol{\varphi}})\boldsymbol{\mathcal{E}}_{\text{illu}}(\rho, \varphi; k_0)\,, \tag{2.107}$$

where $\otimes$ is the outer product. The square root as prefactor ensures energy conversation upon refraction. The impedance ratio $\frac{Z_b}{Z_a}$ takes a change from material a to material b on each side of the optical system into account, for example when an immersion oil lens is used. In principle this model can be refined further by using transmission functions for the different polarizations, but we omit such factors here. Now, we want to propagate this refracted field to the origin. Therefore, we use the transformation to the angular spectrum and then apply Eq. (2.100)

$$\begin{aligned}\boldsymbol{\mathcal{E}}_{\text{refr}}(x, y; -f, k_0) &= \iint \mathrm{d}k_x \mathrm{d}k_y \underline{\boldsymbol{\mathcal{E}}}(k_x, k_y; -f, k_0)\mathrm{e}^{\mathrm{i}(k_x x + k_y y)} \\ &= \iint \mathrm{d}k_x \mathrm{d}k_y \underline{\boldsymbol{\mathcal{E}}}(k_x, k_y; 0, k_0)\mathrm{e}^{\mathrm{i}(k_x x + k_y y - \sqrt{k^2 - k_x^2 - k_y^2} f)}\end{aligned} \tag{2.108}$$

with $k = k_b = k_0 n_b$ the wave number in the material b. We simplify the expression by using the stationary phase approximation to obtain

$$\boldsymbol{\mathcal{E}}_{\text{refr}}(x, y; -f, k_0) \overset{kf \gg 1}{=} 2\pi\mathrm{i}\frac{\mathrm{e}^{-\mathrm{i}kf}}{f} k_z \underline{\boldsymbol{\mathcal{E}}}\left(\frac{-kx}{f}, \frac{-ky}{f}; 0, k_0\right)\,, \tag{2.109}$$

which can be inverted and becomes in polar coordinates

$$\underline{\boldsymbol{\mathcal{E}}}\left(\frac{k\rho}{f}, \varphi + \pi; 0, k_0\right) = \frac{-\mathrm{i}f\mathrm{e}^{\mathrm{i}kf}}{2\pi k_z}\boldsymbol{\mathcal{E}}_{\text{refr}}(\rho, \varphi; -f, k_0)\,. \tag{2.110}$$

This result combined with Eq. (2.107) now relates the illumination beam to the angular spectrum in the focal plane ($z = 0$). The parameters that define the lens are the focal length f and the numerical aperture $NA = n_b \sin\vartheta$, which defines a maximal value for ρ. We also find that each point in the illumination is mapped to the angular component pointing in the opposite direction as we would already expect from a simple ray optics approach.

Calculating the focusing in anisotropic media is possible with the following procedure: First, the incident beam shape and polarization has to be defined on a grid of values for ρ and φ. A maximal value for ρ is defined by the numerical aperture. The pass of the illumination beam through an additional aperture can be incorporated by adding further restrictions [61]. Second, we transform the beam to an angular spectrum in the focal plane with Eqs. (2.107) and (2.110) for each value on the defined grid. Then, this angular spectrum can be translated by Eq. (2.100) or, equivalently, after mapping them to the eigenmodes in the material by Eq. (2.104). The mapping onto eigenmodes also allows us the use of the transfer matrix approach for interfaces with Eq. (2.105). The whole functionality of calculating focusing into anisotropic media of this is published separately from *treams*, which is discussed in Chapter 4, as a package called *focusaniso*. However, in Section 5.2 an application combining these approaches is discussed.

In summary, this chapter started in Section 2.1 with postulating Maxwell's equations which are the governing equations to describe electromagnetism. For a linear response and assuming locality as well as time-invariance, we describe the interaction of electromagnetic fields with media by a set of parameter given in a six-by-six bi-anisotropic tensor. Further assumptions, i.e., isotropy and reciprocity restrict the coefficients of this tensor to three material parameters: permittivity, permeability, and the chirality parameter, which completely describe the electromagnetic properties of chiral materials. We continue with introducing the Helmholtz wave equation and derive three different solution sets for it: vector spherical, cylindrical, and plane waves. The elements of these solutions can be expressed in the parity or helicity basis. Next, we connect Maxwell's equations and the constitutive relations for chiral media with the Helmholtz equation solutions: chiral media are described straightforwardly by modes of well-defined helicity and achiral media can be described by both, parity and helicity, modes.

With these carefully constructed solution sets, we continue in Section 2.2 by introducing the T-matrix method for vector spherical and cylindrical waves. By separating the field expansion outside of an isolated scatterer into incident and scattered modes, we can concisely encode the response in a single matrix. We provide a short introduction on methods to calculate the T-matrix different particle shapes. Once the T-matrix of a scatterer is known, the analytical properties of the used solution sets allow the efficient calculation of the interaction between scatterers. Furthermore, other operations, such as rotations, can be efficiently expressed. Thus, we can use this framework to solve many different scattering problems.

One major focus of this thesis is solving scattering calculations in the presences of periodic boundary conditions. A first tool to efficiently describe scattering in lattices of different dimensionality are the chosen basis sets and we give expressions to change between these basis sets for scattered waves. However, a particular challenge remains the calculation of the interaction between particles. The arising lattice sums are converging very slowly. In the following chapter, we discuss the treatment of these lattice sums in detail, but the general method, named Ewald summation, is outlined in Section 2.3.

Finally, we conclude with methods for stratified media in Section 2.4, where we usually expand the field in plane waves. We introduce the S-matrix and the transfer matrix method that we use to compute the scattering response in these cases. Moreover, we briefly introduce the Richard and Wolf method to describe focusing processes.

3 | Lattice sums with complex unit cells for solutions of the Helmholtz equation

This chapter provides an in-depth treatment of the quasi-periodic lattice sums for solutions to the Helmholtz equation. The main results of this chapter were published in [P4], the lattice sums described in here are necessary to efficiently use the T-matrix method with periodic boundary conditions, because they appear when summing the translation coefficients of vector spherical and cylindrical waves, for example in Eq. (2.59). These sums converge very slowly with a strong dependence on the lattice dimension. The translation coefficients decay in the limit of long distances $kr \gg 1$ with $(kr)^{-\frac{1}{2}}$ for cylindrical waves and with $(kr)^{-1}$ for spherical waves. However, the number of terms that have to be considered grows with $(kr)^{d'}$ in a lattice with dimension d'. Therefore, the decaying strength of the individual contribution can be outweighed by the increasing number of terms that need to be considered leading to slowly converging sums [52]. Thus, we need to carefully transform these slow direct sums to equivalent sums that converge quickly. Our derivation emphasizes on the following two properties: First, the final expressions should include the case of complex unit cells. Second, the method of derivation should be applicable to all possible lattice dimensions. While the first condition derives from the intention to reduce the restrictions on scattering problems that can be solved with the T-matrix method when periodic boundary conditions are used, the second condition appears to be – superficially – a desire for mathematical beauty. However, having similarities among all expressions is a benefit, because it allows to analyze their structure to gain additional physical insights. Furthermore, it can be used in practice to reduce the programming effort to implement these expressions.

The application of Ewald's method to transform the lattice sums to fast converging series evolved to include an increasing number of cases. The lattice sums for lattices with simple unit cells are most comprehensively treated. Simple unit cells only contain a single scatterer per unit cell, whereas complex unit cells contain multiple scatterers, i.e., the whole lattice can be divided into several sublattices. The case of complex unit cells but with all objects in the unit cell in the same plane as the lattice [54] can be solved analogously to the case of simple unit cells. However, arbitrary complex unit cells are a considerably more complicated case, which we cover here. Lattice sums, where the lattice covers all spatial dimensions, namely spherical waves in three dimensions [49, 55] and cylindrical waves in two dimensions [62], were among the first problems of that kind to be solved with Ewald's method. The treatment in [50] applies and expands the results from [47–49] to spherical waves in two-dimensional lattices. The presence of complex unit cells is subsequently covered in [51]. Several methods for particular other cases followed. These cases are summarized in review articles [53, 54], providing an overview of the main results for lattices with simple unit cells. Complex unit cells are, however, not as widely covered. Besides the results for two-dimensional lattices in [51], cylindrical waves in one-dimensional lattices have been solved previously [56]. Our approach to solve the lattice

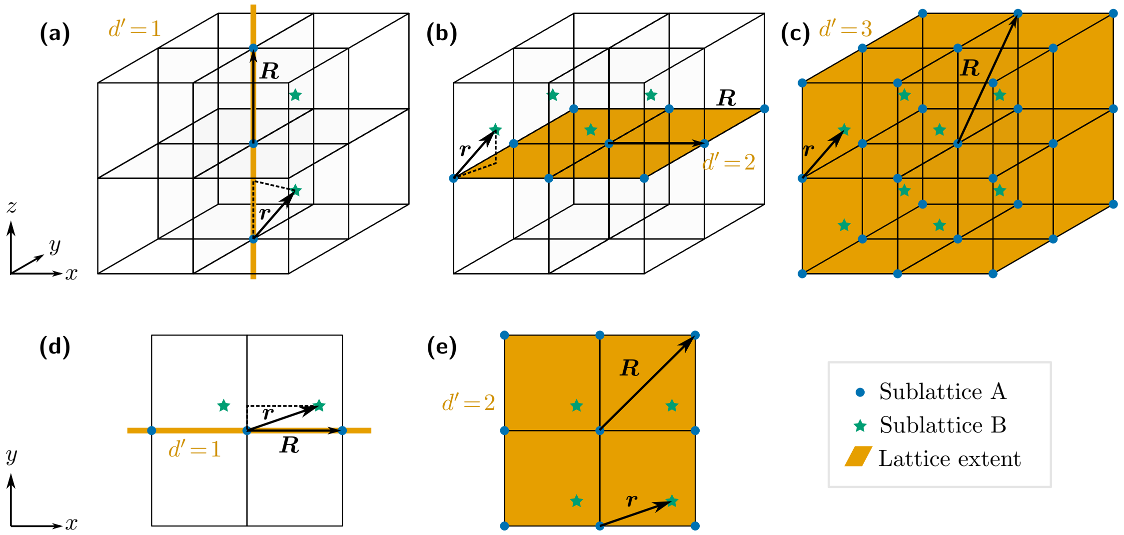

Figure 3.1: The five combinations of spatial dimension $d \in \{2, 3\}$ and lattice dimension $1 \leq d' \leq d$ for which the lattice sum is solved and their orientation. The first row, including panels (a) to (c), are the lattices possible for spherical waves in $d = 3$ spatial dimensions. Panels (d) and (e) in the second row show the lattices with $d = 2$ for the cylindrical waves. Two sublattices are shown in blue circles and green stars. The shift between these sublattices is $\boldsymbol{r}$ and can be decomposed into the component that lies in the space spanned by the lattice, which is shown in orange, and the perpendicular component. This decomposition is indicated by the dashed line. One of the lattice vectors $\boldsymbol{R}$ is shown additionally. Reprinted with permission from [P4]. Copyright 2023 American Physical Society.

sums is similar to the approach in [63] for the case of two-dimensional lattices with simple unit cells. However, we generalize it considerably to cover all cases of lattices for spherical and cylindrical wave solutions.

We treat the lattice sum derivations as follows. First, we define the lattice sum and prepare the common starting point for all cases in Section 3.1. Then, as outlined in Section 2.3, the sum is separated into a real space sum and a reciprocal space sum. The real space sum can be treated quite generally for all cases at once as shown in Section 3.2. The reciprocal space sum requires a more detailed treatment for the various cases in the different parts of Section 3.3. Finally, we examine the derived expressions and discuss the optimal choice of the splitting parameter in Section 3.4.

3.1 Problem definition

We define the lattice sum, which is treated in this chapter, as

$$D_{\nu,d}(\Lambda_{d'}, k, \boldsymbol{k}_\parallel, \boldsymbol{r}) = {\sum_{\boldsymbol{R}\in\Lambda_{d'}}}' f^{(3)}_{\nu,d}(-\boldsymbol{r} - \boldsymbol{R}, k) \mathrm{e}^{\mathrm{i}\boldsymbol{k}_\parallel \boldsymbol{R}}, \tag{3.1}$$

namely a sum over a phased array of singular solutions to the Helmholtz equation. These expressions essentially appear in that form in the lattice sums of translation coefficients of the vector cylindrical and spherical solutions as given in Eqs. (2.50) and (2.51). The sum depends on a range of parameters and variables. First, we have to define the spatial dimension of the solution d, where $d = 2$ corresponds to cylindrical solutions and $d = 3$ to spherical ones. The general index ν either refers to $m \in \mathbb{Z}$ for $d = 2$ or to $l \in \mathbb{N}_0$ and $|m| \leq l$ for $d = 3$. The variables of the lattice sum are the d'-dimensional lattice $\Lambda_{d'}$, where $1 \leq d' \leq d$. The five combinations of lattice sums with these restrictions on d and d' are shown in Fig. 3.1. The remaining three arguments of the lattice sum $D_{\nu,d}(\Lambda_{d'}, k, \boldsymbol{k}_\parallel, \boldsymbol{r})$ are the complex-valued wave number k, the real-valued wave vector components tangential to the lattice $\boldsymbol{k}_\parallel$, and the vector $\boldsymbol{r}$ that corresponds to a translation in the unit cell. Note that, although the wave number k can be complex-valued, the most relevant application of Ewald's method is the case of a real-valued wave number, where the convergence of the lattice sum is generally slowest. The real-valued wave number corresponds to a non-absorbing embedding medium between scatterers and, thus, the longest range of their interaction. We can assume that $\boldsymbol{r} \notin \Lambda_{d'} \backslash \{0\}$ because $\boldsymbol{r}$ coinciding with any lattice vector is – up to a phase factor – equivalent to setting $\boldsymbol{r} = 0$ due to the property

$$D_{\nu,d}(\Lambda_{d'}, k, \boldsymbol{k}_\parallel, \boldsymbol{r} + \boldsymbol{R}) = \mathrm{e}^{-\mathrm{i}\boldsymbol{k}_\parallel \boldsymbol{R}} D_{\nu,d}(\Lambda_{d'}, k, \boldsymbol{k}_\parallel, \boldsymbol{r}) \tag{3.2}$$

for $\boldsymbol{R} \in \Lambda_{d'}$ of the sum. This property is also the reason that the sums are regularly referred to as quasi-periodic lattice sums [54]. Even more strictly, this discrete translational symmetry allows defining $\boldsymbol{r}$ such that it is always in the Wigner-Seitz cell of the lattice, which is beneficial for the convergence of the real space sum. On the right-hand-side of Eq. (3.1), we have the cylindrical solutions defined in Eq. (2.11) for $d = 2$ and the spherical solutions defined in Eq. (2.12) for $d = 3$. The prime next to the sum symbol is the reminder to exclude the point $\boldsymbol{R} = 0$ if $\boldsymbol{r} = 0$. This omission practically removes the undefined value of $f^{(3)}_{\nu,d}(0)$ from the sum, which would correspond to the direct self-interaction of the scattered field from a particle with itself. Effectively, a single contribution is removed from an otherwise periodic function. The vector $\boldsymbol{r} = \boldsymbol{r}_\parallel + \boldsymbol{r}_\perp$ can be decomposed into a component parallel and a component perpendicular to the d'-dimensional lattice Λ as shown in Fig. 3.1. It describes the translation between different sublattices. The one-dimensional lattice is conventionally placed along the z-axis for $d = 3$ and along the x-axis for $d = 2$. The two-dimensional lattice is placed in the x-y-plane.

To separate short- and long-range contributions later, we introduce a particular integral representations of the Hankel function of the first kind, which is [55]

$$H^{(1)}_l(z) = \frac{(-1)^{\frac{l-|l|}{2}} 2}{\mathrm{i}\pi} z^{|l|} \int\limits_{0\mathrm{e}^{-\mathrm{i}\frac{\pi}{2}}}^{\infty} \mathrm{d}t\, t^{2|l|-1} \mathrm{e}^{-\frac{z^2 t^2}{2} + \frac{1}{2t^2}}\,, \ l \in \mathbb{Z}\,. \tag{3.3}$$

We take l as the index instead of m to highlight the similarities with the $d = 3$ case, where we expand the spherical Hankel function of the first kind as

$$h^{(1)}_l(z) = -\mathrm{i}\sqrt{\frac{2}{\pi}} z^l \int\limits_{0\mathrm{e}^{-\mathrm{i}\frac{\pi}{2}}}^{\infty} \mathrm{d}t\, t^{2l} \mathrm{e}^{-\frac{z^2 t^2}{2} + \frac{1}{2t^2}}\,, \ l \in \mathbb{N}_0\,. \tag{3.4}$$

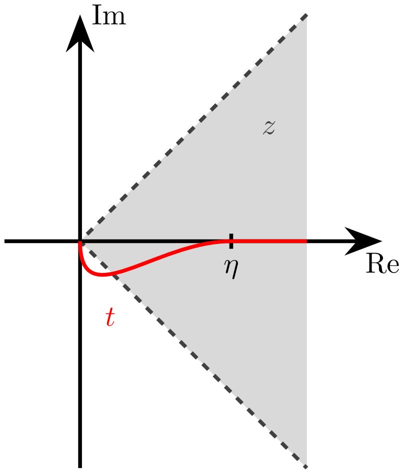

Figure 3.2: Integration contour for the integral representation of the (spherical) Hankel functions. The integrations are defined in Eqs. (3.3) and (3.4). The contour shown in red ensures at $t \to 0$ the convergence of the integral. The domain of values for the argument z where the expressions are valid is shown as gray area. Additionally, we mark the separation value η.

Note that for a convergence of that integral, we require a particular integration contour for $t \to 0$ [49, 55]. Namely, this limit is taken along the negative imaginary axis which is indicated by the phase at the lower integration boundary. We need to keep track of this condition throughout the derivation to choose the correct branch for the complex-valued functions in the result. A visualization of the contour is shown in Fig. 3.2.

Now, we can insert the representations in Eqs. (3.3) and (3.4) into Eq. (3.1) to arrive at the full expression

$$\begin{aligned} D_{\nu,d}(\Lambda_{d'}, k, \boldsymbol{k}_\parallel, \boldsymbol{r}) = {} & \sideset{}{'}\sum_{\boldsymbol{R}\in\Lambda_{d'}} \frac{2\mathrm{e}^{\mathrm{i}\boldsymbol{k}_\parallel \boldsymbol{R}}}{\mathrm{i}\pi} (k|\boldsymbol{r}+\boldsymbol{R}|)^{|l|} \\ & \cdot \int\limits_{0\mathrm{e}^{-\mathrm{i}\frac{\pi}{2}}}^{\infty} \mathrm{d}t\, t^{2|l|-3+d} \mathrm{e}^{-\frac{(k|\boldsymbol{r}+\boldsymbol{R}|t)^2}{2} + \frac{1}{2t^2}} \begin{cases} (-1)^{\frac{l-|l|}{2}} \mathrm{e}^{\mathrm{i}l\varphi_{-\boldsymbol{r}-\boldsymbol{R}}} & d=2 \\ \sqrt{\frac{\pi}{2}} Y_{lm}(-\boldsymbol{r}-\boldsymbol{R}) & d=3 \end{cases}, \end{aligned} \tag{3.5}$$

where we split the integral in two parts by introducing the parameter η. The integration from $0\mathrm{e}^{-\mathrm{i}\frac{\pi}{2}}$ to η is the long-range contribution and is transformed to Fourier space. The short-range contribution corresponds to the remaining integration from η to ∞. Note that we use the notation $Y_{lm}(\boldsymbol{r}) = Y_{lm}(\theta_{\boldsymbol{r}}, \varphi_{\boldsymbol{r}})$ in this chapter.

3.2 Real space sum

First, we examine the short-range contribution, which we can be, for a large part, generally solved for all lattice and space dimensions. Separating the integration over t from the rest, we have to evaluate

$$I_n(z, \eta) = \int\limits_{\eta}^{\infty} \mathrm{d}t\, t^n \mathrm{e}^{-\frac{z^2t^2}{2} + \frac{1}{2t^2}} \tag{3.6}$$

for integers $n \geq -1$. However, the derivations below are valid for $n \in \mathbb{Z}$, which includes also the necessary cases that appear in the reciprocal sum. The integral can be conveniently solved by using the recursion formula

$$I_n(z,\eta) = (n+3)I_{n+2}(z,\eta) - z^2 I_{n+4}(z,\eta) + \eta^{n+3}\mathrm{e}^{-\frac{z^2\eta^2}{2}+\frac{1}{2\eta^2}}\,, \tag{3.7}$$

which is obtained by integrating $\frac{\partial}{\partial t} t^{n+3}\mathrm{e}^{-\frac{z^2t^2}{2}+\frac{1}{2t^2}}$ on the interval $[\eta,\infty)$. This recursion, actually, separates two sets of the integral, namely those for n even and odd. For each of those sets we need two starting values. Hence, we evaluate the integral explicitly for $n \in \{-3,-2,-1,0\}$ (see Appendix H). The recursion formula can be used backward and forward to obtain values for all $n \in \mathbb{Z}$. A similar recursion formula is derived in [50, 63].

Once the integral values are known, we can express the $d = 2$ contribution in real space by

$$D^{(2)}_{l,2}(\Lambda_{d'},k,\boldsymbol{k}_\parallel,\boldsymbol{r}) = \frac{(-1)^{\frac{l-|l|}{2}}2}{\mathrm{i}\pi}\sideset{}{'}\sum_{\boldsymbol{R}\in\Lambda_{d'}} \mathrm{e}^{\mathrm{i}\boldsymbol{k}_\parallel\boldsymbol{R}}(k|\boldsymbol{r}+\boldsymbol{R}|)^{|l|}I_{2|l|-1}(k|\boldsymbol{r}+\boldsymbol{R}|,\eta)\mathrm{e}^{\mathrm{i}l\varphi_{-\boldsymbol{r}-\boldsymbol{R}}} \tag{3.8}$$

and the $d = 3$ contribution by

$$D^{(2)}_{lm,3}(\Lambda_{d'},k,\boldsymbol{k}_\parallel,\boldsymbol{r}) = -\mathrm{i}\sqrt{\frac{2}{\pi}}\sideset{}{'}\sum_{\boldsymbol{R}\in\Lambda_{d'}} \mathrm{e}^{\mathrm{i}\boldsymbol{k}_\parallel\boldsymbol{R}}(k|\boldsymbol{r}+\boldsymbol{R}|)^{|l|}I_{2|l|}(k|\boldsymbol{r}+\boldsymbol{R}|,\eta)Y_{lm}(-\boldsymbol{r}-\boldsymbol{R})\,. \tag{3.9}$$

From the integral in Eq. (3.6), we can roughly estimate that for increasing values of z^2, which corresponds to large values of $|\boldsymbol{R}|$ when $\boldsymbol{r}$ is in the Wigner-Seitz cell, the contributions to the sum are exponentially suppressed. Also, the contribution summed in real space depends on the parameter η in the following way: Larger values of η shift more of the individual term's contribution to the reciprocal space and, conversely, smaller values increase the integration's value. This shift is explored numerically in Subsection 3.4.2.

It was not necessary so far to assume a particular alignment of the lattice with the coordinate axis for our derivation. But, we do so to simplify the reciprocal space sum in the following section. Hence, these alignments can already be used here to simplify the expressions when $\boldsymbol{r}_\perp = 0$. These simplifications are summarized in Table 3.1. The additional symmetry in the expressions leads to selection rules for the $d = 3$ cases. With $d' = 2$, only even values of $l + m$ result in non-vanishing sums and with $d' = 1$ only $m = 0$ terms are non-zero.

3.3 Reciprocal space sum

Finding reciprocal space sum expressions, which converge quickly, requires significantly more work than the real space sums. As a preparation, we need to transform the quasi-periodic sum to a fully periodic sum to apply Poisson's formula. Then, we treat each case separately: Full lattices, i.e., cases where the lattice extends in all spatial directions – mathematically expressed as $d' = d$ – are treated in Subsection 3.3.1, the remaining three cases, where $d' \leq d$, are individually examined in Subsections 3.3.2 to 3.3.4.

Table 3.1: Simplifications of the real space sum for $\boldsymbol{r}_\perp = 0$ in different lattices. Adapted with permission from [P4]. Copyright 2023 American Physical Society.

d	d'	Lattice position	Simplification
3	2	$z = 0$	$Y_{lm}(\theta_{-\boldsymbol{r}_\parallel - \boldsymbol{R}}, \varphi_{-\boldsymbol{r}_\parallel - \boldsymbol{R}}) = Y_{lm}\left(\frac{\pi}{2}, \varphi_{-\boldsymbol{r}_\parallel - \boldsymbol{R}}\right) = \begin{cases} \frac{\sqrt{\frac{2l+1}{4\pi}(l-m)!(l+m)!}(-1)^{\frac{l+m}{2}}}{2^l\left(\frac{l+m}{2}\right)!\left(\frac{l-m}{2}\right)!} \mathrm{e}^{\mathrm{i}m\varphi_{-\boldsymbol{r}_\parallel - \boldsymbol{R}}} & l+m \text{ even} \\ 0 & l+m \text{ odd} \end{cases}$
3	1	$x = 0 = y$	$Y_{lm}(\theta_{-\boldsymbol{r}_\parallel - \boldsymbol{R}}, \varphi_{-\boldsymbol{r}_\parallel - \boldsymbol{R}}) = \sqrt{\frac{2l+1}{4\pi}}(\operatorname{sign}((-\boldsymbol{r}_\parallel - \boldsymbol{R})\hat{\boldsymbol{z}}))^l \delta_{m0}$
2	1	$y = 0$	$\mathrm{e}^{\mathrm{i}l\varphi_{-\boldsymbol{r}_\parallel - \boldsymbol{R}}} = (\operatorname{sign}((-\boldsymbol{r}_\parallel - \boldsymbol{R})\hat{\boldsymbol{x}}))^l$

In each case, we have to correct for the omission of $\boldsymbol{r} = 0$ to always have a fully periodic lattice, which results in

$$\begin{aligned} &D^{(1)}_{\nu,d}(\Lambda_{d'}, k, \boldsymbol{k}_\parallel, \boldsymbol{r}) + D^{(0)}_{\nu,d}(\boldsymbol{r}) \\ &= \sum_{\boldsymbol{R} \in \Lambda_{d'}} \frac{2\mathrm{e}^{\mathrm{i}\boldsymbol{k}_\parallel \boldsymbol{R}}}{\mathrm{i}\pi}(k|\boldsymbol{r}+\boldsymbol{R}|)^{|l|} \int\limits_{0\mathrm{e}^{-\mathrm{i}\frac{\pi}{2}}}^{\eta} \mathrm{d}t\, t^{2|l|-3+d} \mathrm{e}^{-\frac{(k|\boldsymbol{r}+\boldsymbol{R}|t)^2}{2} + \frac{1}{2t^2}} \begin{cases} (-1)^{\frac{l-|l|}{2}} \mathrm{e}^{\mathrm{i}l\varphi_{-\boldsymbol{r}-\boldsymbol{R}}} & d = 2 \\ \sqrt{\frac{\pi}{2}} Y_{lm}(-\boldsymbol{r}-\boldsymbol{R}) & d = 3 \end{cases} \\ &\quad - \delta_{\boldsymbol{r}0} \lim_{\boldsymbol{r} \to 0} \frac{2}{\mathrm{i}\pi}(k|\boldsymbol{r}|)^{|l|} \int\limits_{0\mathrm{e}^{-\mathrm{i}\frac{\pi}{2}}}^{\eta} \mathrm{d}t\, t^{2|l|-3+d} \mathrm{e}^{-\frac{(k|\boldsymbol{r}|t)^2}{2} + \frac{1}{2t^2}} \begin{cases} (-1)^{\frac{l-|l|}{2}} \mathrm{e}^{\mathrm{i}l\varphi_{-\boldsymbol{r}}} & d = 2 \\ \sqrt{\frac{\pi}{2}} Y_{lm}(-\boldsymbol{r}) & d = 3 \end{cases}, \end{aligned} \tag{3.10}$$

where the first term, $D^{(1)}_{\nu,d}(\Lambda_{d'}, k, \boldsymbol{k}_\parallel, \boldsymbol{r})$, is the – fully periodic – sum, which needs to be transformed to reciprocal space, and the second term, $D^{(0)}_{\nu,d}(\boldsymbol{r})$, corresponds to the origin correction. The origin correction is, as indicated by the arguments, independent of the lattice geometry and the wave parameters.

The limit of $\boldsymbol{r} \to 0$ is easily taken due to the factor $|\boldsymbol{r}|^{|l|}$. Thus, only the $l = 0$ term contributes and we arrive at

$$D^{(0)}_{\nu,d}(\boldsymbol{r}) = -\frac{\delta_{l0}\delta_{\boldsymbol{r}0}}{i\pi} \int\limits_{0\mathrm{e}^{-\mathrm{i}\frac{\pi}{2}}}^{\eta} \mathrm{d}t\, \mathrm{e}^{\frac{1}{2t^2}} \begin{cases} \frac{2}{t} & d = 2 \\ \frac{1}{\sqrt{2}} & d = 3 \end{cases}. \tag{3.11}$$

Also, the $l = 0$ part has no angular dependence, so, $D^{(0)}_{\nu,d}(\boldsymbol{r})$ neither has one. By substituting $u = \frac{\mathrm{e}^{-\mathrm{i}\pi}}{2t^2}$, we can transform the previous equation to

$$D^{(0)}_{\nu,d}(\boldsymbol{r}) = \delta_{l0}\delta_{\boldsymbol{r}0} \int\limits_{\frac{\mathrm{e}^{-\mathrm{i}\pi}}{2\eta^2}}^{\infty} \frac{\mathrm{d}u}{u} \mathrm{e}^{-u} \begin{cases} \mathrm{i} & d = 2 \\ \frac{u^{-\frac{1}{2}}}{4} & d = 3 \end{cases}. \tag{3.12}$$

Note that the phase defined in the substitution is necessary to convert the lower boundary to the correct upper limit of $+\infty$. Now, we can identify the integrals as the incomplete gamma function [64–66]

$$D^{(0)}_{\nu,d}(\Lambda_{d'}, k, \boldsymbol{k}_\parallel, \boldsymbol{r}) = \delta_{l0}\delta_{\boldsymbol{r}0}\begin{cases}\frac{\mathrm{i}}{\pi}\Gamma\left(0, \frac{\mathrm{e}^{-\mathrm{i}\pi}}{2\eta^2}\right) & d=2\\ \frac{1}{4\pi}\Gamma\left(-\frac{1}{2}, \frac{\mathrm{e}^{-\mathrm{i}\pi}}{2\eta^2}\right) & d=3\end{cases}. \tag{3.13}$$

The factor $\mathrm{e}^{-\mathrm{i}\pi}$ in the argument indicates the branch choice, namely, for the branch cut along the negative real axis we have to take the value for $-\frac{1}{2\eta^2} - \mathrm{i}\epsilon$ with $\epsilon \to 0^+$ when η is real. Having the origin contribution solved, we can turn to the main difficulty in deriving quickly convergent series, which is transforming the reciprocal lattice sum to simple enough expressions that lend themselves to an implementation in efficient code.

To compute $D^{(1)}_{\nu,d}(\Lambda_{d'}, k, \boldsymbol{k}_\parallel, \boldsymbol{r})$, we first decompose $\boldsymbol{r} = \boldsymbol{r}_\parallel + \boldsymbol{r}_\perp$ into a contribution $\boldsymbol{r}_\parallel$ that lies in the d' dimensional space spanned by the lattice and a perpendicular contribution $\boldsymbol{r}_\perp$ for the remaining $d - d'$ dimensions. Next, we want to transition to the reciprocal space. For this purpose, we separate the real space sum from the rest of the complicated expression by replacing every occurrence of $\boldsymbol{R}$ by $\boldsymbol{r}'$ and add an additional integral $\int_{\mathbb{R}^d} \mathrm{d}^{d'}r'\delta^{(d')}(\boldsymbol{R} - \boldsymbol{r}')$. Then, we can apply Poisson's formula from Eq. (A.5) for

$$\sum_{\boldsymbol{R}\in\Lambda_{d'}} \delta^{(d')}(\boldsymbol{R} - \boldsymbol{r}') = \frac{(2\pi)^{d'}}{V_{d'}} \sum_{\boldsymbol{Q}\in\Lambda^*_{d'}} \mathrm{e}^{\mathrm{i}\boldsymbol{Q}\boldsymbol{r}'}, \tag{3.14}$$

to transform the sum to the reciprocal space. Next, we can also shift the integral variable by $\boldsymbol{r}_\parallel$ in an additional step to simplify the integral over $\boldsymbol{r}'$. This leads to the expression

$$\begin{aligned}D^{(1)}_{\nu,d}(\Lambda_{d'}, k, \boldsymbol{k}_\parallel, \boldsymbol{r}) = {}& \frac{2k^{|l|}}{\mathrm{i}\pi V_{d'}} \sum_{\boldsymbol{Q}\in\Lambda^*_{d'}} \mathrm{e}^{-\mathrm{i}(\boldsymbol{k}_\parallel+\boldsymbol{Q})\boldsymbol{r}_\parallel} \int\limits_{0\mathrm{e}^{-\mathrm{i}\frac{\pi}{2}}}^{\eta} \mathrm{d}t\, t^{2|l|-3+d}\mathrm{e}^{\frac{1}{2t^2}}\\ &\cdot \int_{\mathbb{R}^{d'}} \mathrm{d}^{d'}r'|\boldsymbol{r}' - \boldsymbol{r}_\perp|^{|l|} \exp\left(-\frac{(k|\boldsymbol{r}' - \boldsymbol{r}_\perp|t)^2}{2}\right) \mathrm{e}^{-\mathrm{i}(\boldsymbol{k}_\parallel+\boldsymbol{Q})\boldsymbol{r}'} \begin{cases}(-1)^{\frac{l-|l|}{2}}\mathrm{e}^{\mathrm{i}l\varphi_{\boldsymbol{r}'-\boldsymbol{r}_\perp}} & d=2\\ \sqrt{\frac{\pi}{2}}Y_{lm}(\boldsymbol{r}' - \boldsymbol{r}_\perp) & d=3\end{cases},\end{aligned} \tag{3.15}$$

which serves as a starting point for the following individual derivations. The component $\boldsymbol{r}_\parallel$ only appears as a simple phase factor, making cases where $\boldsymbol{r}_\perp = 0$ almost identical to the simple unit cell case. The expression in Eq. (3.15) is treated now case-by-case. First, we consider full lattices, where $d = d'$. In that case, the vector $\boldsymbol{r}$ lies in the same space as the one spanned by the lattice vectors, so essentially $\boldsymbol{r}_\perp = 0$. This considerably simplifies the lattice sum. The remaining three lattice sums are all treated individually in the following subsections.

3.3.1 Lattices filling all spatial dimensions

In the case of full lattices, we can apply the simplifications $d = d'$ and $\boldsymbol{r}_\perp = 0$ to Eq. (3.15). Then, the spatial integral becomes

$$\int_{\mathbb{R}^d} \mathrm{d}^d r'\, r'^{|l|}\mathrm{e}^{-\frac{(kr't)^2}{2}}\mathrm{e}^{-\mathrm{i}(\boldsymbol{k}_\parallel+\boldsymbol{Q})\boldsymbol{r}'} \begin{cases}\mathrm{e}^{\mathrm{i}l\varphi_{\boldsymbol{r}'}} & d=2\\ Y_{lm}(\boldsymbol{r}') & d=3\end{cases}, \tag{3.16}$$

where, next, we can insert plane wave expansions for the exponential $\mathrm{e}^{-\mathrm{i}(\boldsymbol{k}_\parallel+\boldsymbol{Q})\boldsymbol{r}'}$ that matches the spatial dimension (Appendix G), namely the spherical wave expansion for $d=3$ and the cylindrical wave expansion for $d=2$. By evaluating the angular integral, we get two different expressions for the two cases. In $d=2$ dimensions, the integral becomes

$$(-\mathrm{i})^{|l|}\mathrm{e}^{\mathrm{i}l\varphi_{\boldsymbol{k}_\parallel+\boldsymbol{Q}}}\int\limits_0^\infty \mathrm{d}r'\, r'^{|l|+1}\mathrm{e}^{-\frac{(kr't)^2}{2}} J_{|l|}(\beta k r')\,, \tag{3.17}$$

and in $d=3$ dimensions it is

$$4\pi(-\mathrm{i})^l Y_{lm}(\boldsymbol{k}_\parallel+\boldsymbol{Q})\int\limits_0^\infty \mathrm{d}r'\, r'^{|l|+2}\mathrm{e}^{-\frac{(kr't)^2}{2}} j_l(\beta k r')\,, \tag{3.18}$$

with $\beta=\frac{|\boldsymbol{k}_\parallel+\boldsymbol{Q}|}{k}$. For later use, we also define $\gamma=\sqrt{1-\beta^2}$. Both of these integrals have well-known closed form results [64, Eq. 6.631 4.] and we arrive at

$$D^{(1)}_{\nu,d}(\Lambda_d,k,\boldsymbol{k}_\parallel,\boldsymbol{r})=\frac{4(-\mathrm{i})^l}{\mathrm{i}V_d k^d}\sum_{\boldsymbol{Q}\in\Lambda_d^*}\mathrm{e}^{-\mathrm{i}(\boldsymbol{k}_\parallel+\boldsymbol{Q})\boldsymbol{r}}\beta^{|l|}\int\limits_{0\mathrm{e}^{-\mathrm{i}\frac{\pi}{2}}}^{\eta}\frac{\mathrm{d}t}{t^3}\mathrm{e}^{\frac{\gamma^2}{2t^2}}\begin{cases}\mathrm{e}^{\mathrm{i}l\varphi_{\boldsymbol{k}+\boldsymbol{Q}}} & d=2\\ \pi Y_{lm}(\boldsymbol{k}_\parallel+\boldsymbol{Q}) & d=3\end{cases}, \tag{3.19}$$

where only the integration over t is left. Now, we can substitute $u=\mathrm{e}^{-\mathrm{i}\pi}\frac{\gamma^2}{2t^2}$ to obtain a simple integration over an exponential that can easily be solved. We finally express the result using the upper incomplete gamma function as

$$\begin{aligned}D^{(1)}_{\nu,d}(\Lambda_d,k,\boldsymbol{k}_\parallel,\boldsymbol{r})=&\frac{4(-\mathrm{i})^{l-1}}{V_d k^d}\sum_{\boldsymbol{Q}\in\Lambda_d^*}\mathrm{e}^{-\mathrm{i}(\boldsymbol{k}_\parallel+\boldsymbol{Q})\boldsymbol{r}}\beta^{|l|}\\ &\cdot\gamma^{-2}\Gamma\left(1,\mathrm{e}^{-\mathrm{i}\pi}\frac{\gamma^2}{2\eta^2}\right)\begin{cases}\mathrm{e}^{\mathrm{i}l\varphi_{\boldsymbol{k}+\boldsymbol{Q}}} & d=2\\ \pi Y_{lm}(\boldsymbol{k}_\parallel+\boldsymbol{Q}) & d=3\end{cases}.\end{aligned} \tag{3.20}$$

Here, that seems to be a superfluous step, however, the general structure of the expression shows similarities to the expression derived in the following better.

3.3.2 Two-dimensional lattice for spherical wave solutions

The two-dimensional sum of spherical waves is solved in [50, 51]. Here, we show that our direct approach reproduces these results, without the need to evaluate a limit to obtain the solution. We start by explicitly writing the spherical harmonics as a normalization factor N_{lm}, an exponential for the azimuthal part, and the associated Legendre polynomials

$$\begin{aligned}D^{(1)}_{lm,3}(\Lambda_2,k,\boldsymbol{k}_\parallel,\boldsymbol{r})=&\sqrt{\frac{2}{\pi}}\frac{k^l}{\mathrm{i}V_2}\sum_{\boldsymbol{Q}\in\Lambda_2^*}\mathrm{e}^{-\mathrm{i}(\boldsymbol{k}_\parallel+\boldsymbol{Q})\boldsymbol{r}_\parallel}\int\limits_{0\mathrm{e}^{-\mathrm{i}\frac{\pi}{2}}}^{\eta}\mathrm{d}t\, t^{2l}\mathrm{e}^{\frac{1}{2t^2}}\\ \cdot\int_{\mathbb{R}^2}&\mathrm{d}^2r'(r'^2+z^2)^{\frac{l}{2}}\mathrm{e}^{-\frac{k^2(r'^2+z^2)t^2}{2}}\mathrm{e}^{-\mathrm{i}(\boldsymbol{k}_\parallel+\boldsymbol{Q})\boldsymbol{r}'}N_{l|m|}\mathrm{e}^{\mathrm{i}m\varphi_{\boldsymbol{r}'}}(-1)^{\frac{m-|m|}{2}}P_l^{|m|}\left(\frac{-z}{\sqrt{r'^2+z^2}}\right).\end{aligned} \tag{3.21}$$

The lattice is conventionally placed in the x-y-plane. Thus, the shift perpendicular to the lattice $\boldsymbol{r}_\perp = z\hat{\boldsymbol{z}}$ can be expressed by the z-component. As in the case of $d = d'$, we first focus on the integration over $\boldsymbol{r}'$. However, we now have the difficulty that, in general, $z \neq 0$. The integration over angles can still be performed straightforwardly after using, again, a suitable expansion of the plane wave (Eq. (G.1)). In this case, we use the expansion in cylindrical Bessel functions due to the two-dimensional integration domain for $\boldsymbol{r}'$. The radial integration left after the angular integral is

$$\int\limits_0^\infty \mathrm{d}r'\, r'(r'^2 + z^2)^{\frac{l}{2}} J_{|m|}(\beta k r') \mathrm{e}^{-\frac{(kr't)^2}{2}} P_l^{|m|}\left(\frac{-z}{\sqrt{r'^2 + z^2}}\right) . \tag{3.22}$$

To proceed, we can find an expansion of the associated Legendre polynomials, such that the factor $(r'^2+z^2)^{\frac{l}{2}}$ is eliminated, because it complicates the integral expression especially for odd values of l. We achieve this by using the expansion of the associated Legendre polynomials derived in Appendix C that replaces the complicated integrand involving square roots by a more tractable finite sum over powers of r', that are of the shape

$$\begin{aligned}\int\limits_0^\infty \mathrm{d}r'\, r'^{1+|m|+2s} J_{|m|}(\beta k r') \mathrm{e}^{-\frac{(kr't)^2}{2}} &= \frac{(s+|m|)!}{|m|!\beta k \left(\frac{k^2t^2}{2}\right)^{\frac{1+|m|}{2}+s}} \mathrm{e}^{-\frac{\beta^2}{4t^2}} M_{\frac{1+|m|}{2}+s, \frac{|m|}{2}}\left(\frac{\beta^2}{2t^2}\right) \\ &= \frac{(s+|m|)!}{\beta k}\left(\frac{\beta}{kt^2}\right)^{1+|m|+2s} (-1)^s \mathrm{e}^{-\frac{\beta^2}{2t^2}} \sum_{n=0}^{s} \binom{s}{n} \frac{\left(-\frac{\beta^2}{2t^2}\right)^{-n}}{(s+|m|-n)!} ,\end{aligned} \tag{3.23}$$

which, as can be seen, is an integral that is solved by the Whittaker functions [64, Eq. 6.631 1.]. The combinations of the parameters $\frac{1+|m|}{2} + s$ and $\frac{|m|}{2}$ are special cases of that function that are expressible as finite sums of simpler functions [67], which is summarized in Appendix I.

Combining the result of the angular integral, the expansion of the associated Legendre polynomials, the result of the radial integral, and the expansion of the Whittaker function, we now arrive at the expression

$$\begin{aligned} D^{(1)}_{lm,3}(\Lambda_2, k, \boldsymbol{k}_\parallel, \boldsymbol{r}) = &\sqrt{2(2l+1)(l-m)!(l+m)!}\frac{\mathrm{i}^{m-1}}{V_2 k^2} \sum_{\boldsymbol{Q}\in\Lambda_2^*} \mathrm{e}^{-\mathrm{i}(\boldsymbol{k}_\parallel + \boldsymbol{Q})\boldsymbol{r}_\parallel} \mathrm{e}^{\mathrm{i}m\varphi_{\boldsymbol{k}_\parallel+\boldsymbol{Q}}} \\ &\cdot \int\limits_{0\mathrm{e}^{-\mathrm{i}\frac{\pi}{2}}}^{\eta} \mathrm{d}t\, \mathrm{e}^{\frac{\gamma^2}{2t^2} - \frac{k^2 z^2 t^2}{2}} \sum_{s=0}^{\left\lfloor\frac{l-|m|}{2}\right\rfloor} \sum_{n=0}^{s} t^{2l-2-2|m|-4s+2n} \\ &\cdot \frac{\beta^{|m|+2s-2n}(-kz)^{l-|m|-2s}(-1)^n}{2^{2s+|m|-n}(s+|m|-n)!n!(s-n)!(l-|m|-2s)!} ,\end{aligned} \tag{3.24}$$

which is more complicated than in the full lattice case. Instead of a simple single integral over t, we now have two sums – one from the expansion of the associated Legendre polynomials and one from the expansion of the Whittaker functions – that bring additional factors of t. To proceed, we rearrange the sums such that the inner one is independent of the integral t. This is useful to evaluate certain limits like $\beta \to 0$ or $z \to 0$ later to find simplified expressions. Also, it is beneficial for simple and fast implementations in *treams*, because the evaluation of the integral result can be done independently from the inner sum.

After rearranging the sums according to Eq. (J.1) and substituting $u = \frac{\mathrm{e}^{-\mathrm{i}\pi}\gamma^2}{2t^2}$, we obtain

$$\begin{aligned} &D^{(1)}_{lm,3}(\Lambda_2, k, \boldsymbol{k}_\parallel, \boldsymbol{r}) \\ &\quad = \sum_{\boldsymbol{Q} \in \Lambda_2^*} \mathrm{e}^{-\mathrm{i}(\boldsymbol{k}_\parallel + \boldsymbol{Q})\boldsymbol{r}} \mathrm{e}^{\mathrm{i}m\varphi_{\boldsymbol{k}_\parallel + \boldsymbol{Q}}} \sum_{n=0}^{l-|m|} S_{3,lmn,2}(k, \beta, z) \gamma^{2n-1} \int\limits_{\mathrm{e}^{-\mathrm{i}\pi}\frac{\gamma^2}{2\eta^2}}^{\infty} \frac{\mathrm{d}u}{u} u^{\frac{1}{2}-n} \mathrm{e}^{-u + \frac{(\gamma k z)^2}{4u}}\,, \end{aligned} \tag{3.25}$$

with

$$\begin{aligned} S_{3,lmn,2}(k, \beta, z) = & \frac{\sqrt{(2l+1)(l-m)!(l+m)!}}{(-2)^l \mathrm{i}^m V_2 k^2} \\ & \cdot \sum_{s=n}^{\min(l-|m|, 2n)} \frac{(-kz)^{2n-s} \beta^{l-s}}{(2n-s)!(s-n)!(\frac{l+m-s}{2})!(\frac{l-m-s}{2})!}\,. \end{aligned} \tag{3.26}$$

The phase factor in the substitution is, as for the origin contribution, necessary in the given form to transform the lower boundary to the correct upper limit of $+\infty$ and leads to a particular branch choice for the lower limit to obtain the correct result. The remaining integral needs further treatment in the general case, but for $z = 0$ it simplifies to the gamma function $\Gamma\left(\frac{1}{2} - n, \frac{\mathrm{e}^{-\mathrm{i}\pi}\gamma^2}{2\eta^2}\right)$. In the general case though, it is possible to convert it to the same form as Eq. (3.6). We show this in Appendix H.

The sum over s in $S_{3,lm,2}(k, \beta, z)$ only runs over every other integer: s has to have the same parity as $l + m$ such that the factorials only contain integer arguments. The factor $S_{3,lm,2}(k, \beta, z)$ simplifies greatly for $z = 0$ or $\beta = 0$ with, at maximum, a single summand contributing. If $z = 0$, only the term with $s = 2n$ contributes as

$$S_{3,lmn,2}(k, \beta, 0) = \frac{\sqrt{(2l+1)(l-m)!(l+m)!}}{(-2)^l V_2 k^2} \frac{\beta^{l-2n}}{n! \left(\frac{l-m}{2} - n\right) \left(\frac{l+m}{2} - n\right)}\,, \tag{3.27}$$

which only happens for $l + m$ even and $n \leq \frac{l-|m|}{2}$. For $\beta = 0$, only the $s = l$ term contributes.

The result derived here is equivalent to the result in [51]. This gives us confidence that we can also apply the direct evaluation approach to the one-dimensional lattice case, where expressions for lattices with complex unit cells are not present in literature [57].

3.3.3 One-dimensional lattice for spherical wave solutions

In the case of $d = 3$ and $d' = 1$, we have to evaluate

$$D^{(1)}_{lm,3}(\Lambda_1, k, k_\parallel, \boldsymbol{r}) = \frac{\sqrt{2}k^l}{\mathrm{i}\sqrt{\pi}V_1} \sum_{Q\in\Lambda_1^*} \mathrm{e}^{-\mathrm{i}(k_\parallel+Q)r_\parallel} \int\limits_{0\mathrm{e}^{-\mathrm{i}\frac{\pi}{2}}}^{\eta} \mathrm{d}t\, t^{2l} \mathrm{e}^{\frac{1}{2t^2}}$$
$$\cdot \int\limits_{-\infty}^{\infty} \mathrm{d}r' (r'^2+\rho^2)^{\frac{l}{2}} \mathrm{e}^{-\frac{k^2(r'^2+\rho^2)t^2}{2}} \mathrm{e}^{-\mathrm{i}(k_\parallel+Q)r'} N_{l|m|}(-1)^{\frac{m-|m|}{2}} \mathrm{e}^{\mathrm{i}m\varphi_{-\boldsymbol{r}_\perp}} P_l^{|m|}\left(\frac{r'}{\sqrt{r'^2+\rho^2}}\right), \tag{3.28}$$

where we use an explicit expression for the spherical harmonics again. The lattice is placed along the z-axis. Thus, the absolute value of the shift vector perpendicular to the lattice is $\rho = |\boldsymbol{r}_\perp|$. Furthermore, we can replace the vectors $\boldsymbol{r}_\parallel = r_\parallel \hat{\boldsymbol{z}}$, $\boldsymbol{k}_\parallel = k_\parallel \hat{\boldsymbol{z}}$, and $\boldsymbol{Q} = Q\hat{\boldsymbol{z}}$ through scalar values in a one-dimensional lattice. We use again the closed form expression Eq. (C.12) for the associated Legendre polynomials to eliminate the factor $(r'^2+\rho^2)^{\frac{l}{2}}$. Thereby, the integral over r' becomes

$$\int\limits_{-\infty}^{\infty} \mathrm{d}r' \mathrm{e}^{-\frac{k^2r'^2t^2}{2}} \mathrm{e}^{-\mathrm{i}(k_\parallel+Q)r'} r'^{l-|m|-2s}$$
$$= \frac{(l-m-2s)!\sqrt{2\pi}}{kt} \mathrm{e}^{-\frac{\beta^2}{2t^2}} \left(-\frac{\mathrm{i}\beta}{kt^2}\right)^{l-|m|-2s} \sum_{n=0}^{\left\lfloor\frac{l-|m|}{2}-s\right\rfloor} \frac{\left(-\frac{t^2}{2\beta^2}\right)^n}{(l-|m|-2s-2n)!n!}, \tag{3.29}$$

which is known in literature [64, Eq. 6.462 2.]. We use $\beta = \frac{k_\parallel+Q}{k}$ for the one-dimensional case. We can now collect the results of the integral and the expansion to obtain

$$D^{(1)}_{lm,3}(\Lambda_1, k, k_\parallel, \boldsymbol{r}) = \frac{\sqrt{\frac{2l+1}{\pi}(l-m)!(l+m)!}}{\mathrm{i}kV_1}(-\mathrm{i})^{l+m}$$
$$\cdot \sum_{Q\in\Lambda_1^*} \mathrm{e}^{-\mathrm{i}(k_\parallel+Q)r_\parallel} \int\limits_{0\mathrm{e}^{-\mathrm{i}\frac{\pi}{2}}}^{\eta} \mathrm{d}t\, \mathrm{e}^{\frac{\gamma^2}{2t^2}-\frac{k^2\rho^2t^2}{2}} \mathrm{e}^{\mathrm{i}m\varphi_{-\boldsymbol{r}_\perp}}$$
$$\cdot \sum_{s=0}^{\lfloor\frac{l-|m|}{2}\rfloor} \sum_{n=0}^{\left\lfloor\frac{l-|m|}{2}-s\right\rfloor} \frac{(k\rho)^{2s+|m|}}{2^{2s+|m|+n}(s+|m|)!s!} t^{4s+2|m|+2n-1} \beta^{l-|m|-2s-2n} \frac{(-1)^n}{(l-|m|-2s-2n)!n!} \tag{3.30}$$

with the sum over the reciprocal lattice and two finite sums. We substitute again the integration variable t and rearrange the two finite sums using Eq. (J.2) to arrive at

$$D^{(1)}_{lm,3}(\Lambda_1, k, k_\parallel, \boldsymbol{r})$$
$$= \mathrm{e}^{\mathrm{i}m\varphi_{-\boldsymbol{r}_\perp}} \sum_{Q\in\Lambda_1^*} \mathrm{e}^{-\mathrm{i}(k_\parallel+Q)r_\parallel} \sum_{n=|m|}^{l} S_{3,lmn,1}(k,\beta,\rho) \frac{\gamma^{2n}}{4^n} \int\limits_{\frac{\mathrm{e}^{-\mathrm{i}\pi}\gamma^2}{2\eta^2}}^{\infty} \frac{\mathrm{d}u}{u} u^{-n} \mathrm{e}^{-u+\frac{(\gamma k\rho)^2}{4u}}, \tag{3.31}$$

with the factor

$$\begin{aligned} S_{3,lmn,1}(k,\beta,\rho) =& \frac{(-\mathrm{i})^{l+1}\mathrm{i}^m}{2V_1 k}\sqrt{\frac{2l+1}{\pi}(l-m)!(l+m)!} \\ &\cdot \sum_{s=n}^{\min(2n-|m|,l)} \frac{(k\rho)^{2n-s}\beta^{l-s}}{\left(n-\frac{s+m}{2}\right)!\left(n-\frac{s-m}{2}\right)!(l-s)!(s-n)!}\,, \end{aligned} \tag{3.32}$$

which is independent of the integration. Note that the sum over s contains only values where the factorial has integer argument, namely $s+m$ must be even. The integral simplifies to the incomplete gamma function for $\rho = 0$, similarly to the simplification in the previous section for $z = 0$, and for non-zero values of ρ it can be transformed to the structure of the integral in Eq. (3.6).

The simplification of the factor $S_{3,lmn,1}(k,\beta,\rho)$ for $\rho = 0$ is

$$S_{3,lmn,1}(k,\beta,0) = \begin{cases} \frac{(-\mathrm{i})^{l+1}l!}{2V_1 k}\sqrt{\frac{2l+1}{\pi}}\frac{\beta^{l-2n}}{n!(l-2n)!} & n \le \left\lfloor\frac{l}{2}\right\rfloor \text{ and } m = 0 \\ 0 & \text{otherwise} \end{cases}\,, \tag{3.33}$$

where we find that the sums with $m \neq 0$ are zero for the real space sum due to the restored symmetry.

3.3.4 One-dimensional lattice for cylindrical wave solutions

Eventually, the last case to cover are cylindrical waves on a one-dimensional lattice. A discussion of this case is contained in the supplementary material of [56]. We place the lattice along the x-axis. We write the vectors $\boldsymbol{Q} = Q\hat{\boldsymbol{x}}$, $\boldsymbol{r}_\parallel = r_\parallel\hat{\boldsymbol{x}}$, and $\boldsymbol{k}_\parallel = k_\parallel\hat{\boldsymbol{x}}$ as scalar quantities similar to the one-dimensional lattice case with spherical waves. The shift component perpendicular to the lattice is $\boldsymbol{r}_\perp = y\hat{\boldsymbol{y}}$. We start with

$$\begin{aligned} D_{l,2}^{(1)}(\Lambda_1,k,k_\parallel,\boldsymbol{r}) = \frac{2k^{|l|}(-1)^{\frac{l-|l|}{2}}}{\mathrm{i}\pi V_1} \sum_{Q\in\Lambda_1^*} \mathrm{e}^{-\mathrm{i}(k_\parallel+Q)r_\parallel} \int\limits_{0\mathrm{e}^{-\mathrm{i}\frac{\pi}{2}}}^{\eta} \mathrm{d}t\, t^{2|l|-1}\mathrm{e}^{\frac{1}{2t^2}} \\ \cdot \int\limits_{-\infty}^{\infty} \mathrm{d}r'(r'^2+y^2)^{\frac{|l|}{2}}\mathrm{e}^{-\frac{k^2(r'^2+y^2)t^2}{2}-\mathrm{i}(k_\parallel+Q)r'}\left(\frac{r'-\mathrm{i}\,\mathrm{sign}(l)y}{\sqrt{r'^2+y^2}}\right)^{|l|}\,, \end{aligned} \tag{3.34}$$

where the exponential $\mathrm{e}^{\mathrm{i}l\varphi_{\boldsymbol{r}'-\boldsymbol{r}_\perp}}$ is rewritten such that the factor $(r'^2+y^2)^{\frac{|l|}{2}}$ is eliminated. Thus, similar to the role previously taken by the associated Legendre polynomials the angles $\varphi_{\boldsymbol{r}'-\boldsymbol{r}_\perp}$ and, where applicable, $\theta_{\boldsymbol{r}'-\boldsymbol{r}_\perp}$ are useful to simplify the expressions.

Next, we take the binomial expansion of $(r'-\mathrm{i}\,\mathrm{sign}(l)y)^{|l|}$ to then integrate over the variable r'. This integral evaluates to [64, Eq. 6.462 2.]

$$\int\limits_{-\infty}^{\infty}\mathrm{d}r'\,r'^s\mathrm{e}^{-\frac{kr'^2t^2}{2}}\mathrm{e}^{-\mathrm{i}(k_\parallel+Q)r'} = \frac{s!\sqrt{2\pi}}{kt}\mathrm{e}^{-\frac{\beta^2}{2t^2}}\left(-\frac{\mathrm{i}\beta}{kt^2}\right)^s \sum_{n=0}^{\left\lfloor\frac{s}{2}\right\rfloor}\frac{\left(-\frac{t^2}{2\beta^2}\right)^n}{(s-2n)!n!}\,. \tag{3.35}$$

Inserting this result back into the expression for $D^{(1)}_{l,2}(\Lambda_1, k, k_\parallel, \boldsymbol{r})$, we get

$$
\begin{aligned}
D^{(1)}_{l,2}(\Lambda_1, k, k_\parallel, \boldsymbol{r}) = \frac{2\mathrm{i}^l\sqrt{2}}{\mathrm{i}\sqrt{\pi}kV_1} \sum_{Q\in\Lambda_1^*} \mathrm{e}^{-\mathrm{i}(k_\parallel+Q)r_\parallel} \\
\cdot \int\limits_{0\mathrm{e}^{-\mathrm{i}\frac{\pi}{2}}}^{\eta} \mathrm{d}t\, \mathrm{e}^{\frac{\gamma^2}{2t^2} - \frac{k^2y^2t^2}{2}} \sum_{s=0}^{|l|} \sum_{n=0}^{\lfloor\frac{s}{2}\rfloor} t^{2(|l|-1-s+n)} (-1)^{s+n} \frac{|l|!(-\operatorname{sign}(l)ky)^{|l|-s}\beta^{s-2n}}{(s-2n)!n!2^n(|l|-s)!}
\end{aligned}
\tag{3.36}
$$

including two finite sums that come from the binomial expansion and the integration result. Then, after reordering the sums and substituting the summation variables, we obtain

$$
D^{(1)}_{l,2}(\Lambda_1, k, k_\parallel, \boldsymbol{r}) = \sum_{Q\in\Lambda_1^*} \mathrm{e}^{-\mathrm{i}(k_\parallel+Q)r_\parallel} \sum_{n=0}^{|l|} S_{2,ln,1}(k,\beta,y)\gamma^{2n-1} \int\limits_{\mathrm{e}^{-\mathrm{i}\pi}\frac{\gamma^2}{2\eta^2}}^{\infty} \frac{\mathrm{d}u}{u} u^{\frac{1}{2}-n} \mathrm{e}^{-u+\frac{(\gamma k y)^2}{4u}}\,,
\tag{3.37}
$$

with the factor

$$
S_{2,ln,1}(k,\beta,y) = \frac{(-\mathrm{i})^l 2}{\sqrt{\pi}V_1 k} \sum_{s=n}^{\min(2n,|l|)} \frac{(-\operatorname{sign}(l)ky)^{2n-s}\beta^{|l|-s}}{2^s(2n-s)!(|l|-s)!(s-n)!}
\tag{3.38}
$$

completing the set of lattice summations for all combination of d and d'. Here, the sum over s includes all values in the given range. The integral appearing is similar to the one for the $d = 3$, $d' = 2$ case. Therefore, this part of the result seems to depend on the difference $d - d'$. The factor

$$
S_{2,ln,1}(k,\beta,0) = \begin{cases} \frac{2(-\mathrm{i})^l}{\sqrt{\pi}V_1 k} \frac{\beta^{|l|-2n}}{4^n n!(|l|-2n)!} & n \leq \left\lfloor \frac{|l|}{2} \right\rfloor \\ 0 & \text{otherwise} \end{cases}
\tag{3.39}
$$

can, again, be significantly simplified for the case of $y = 0$.

This result concludes the derivations of suitable expressions for the lattice sum defined in Eq. (3.1). All cases of lattice dimension d' for spherical and cylindrical solutions have been converted to exponentially convergent expressions in the presence of complex unit cells, i.e., for $\boldsymbol{r}_\perp \neq 0$. Furthermore, these expressions reproduce the correct previously known results for $\boldsymbol{r}_\perp = 0$ [54]. The real space sum is given in Eqs. (3.8) and (3.9). The reciprocal space sum requires the specialized expressions for the different lattices in Eqs. (3.20), (3.25), (3.31), and (3.37), and the correction for the omission of the origin is given in Eq. (3.13). The validation of all expressions is mainly covered in the following section.

We want to shortly discuss the general structure of the reciprocal space expressions. Besides the sum over reciprocal lattice vector $\boldsymbol{Q}$, the phase factor $\mathrm{e}^{-\mathrm{i}(\boldsymbol{k}_\parallel+\boldsymbol{Q})\boldsymbol{r}_\parallel}$, and individual prefactors, an integral over u appears, which has a form that mostly depends on $d - d'$. For $\boldsymbol{r}_\perp = 0$, this integral is essentially the incomplete gamma function. The first argument of the incomplete gamma function depends on the value of $d - d'$: For $d - d' = 0$, the argument is 1, for $d - d' = 1$ it is in $\{\frac{1}{2}, -\frac{1}{2}, -\frac{3}{2}, \dots\}$, and for $d - d' = 2$ it is in $\{0, -1, -2, \dots\}$ [53]. This structure is maintained for $\boldsymbol{r}_\perp \neq 0$, but the integral is now given by Eq. (3.6). Moreover, for $d \neq d'$, two finite sums appear. In comparison to the conventional approach presented in Section 2.3, we can avoid the process of taking a limit here and, hence, also the difficulties arising at that step for lattices with complex unit cells.

3.4 Assessment of the derived expressions

We perform several tests to assess our expressions. First, we cover the general accuracy and the achieved speed improvement in Subsection 3.4.1. Second, we discuss the influence of the splitting parameter η between the real and reciprocal space sums on the accuracy and convergence of the individual contributions in Subsection 3.4.2 to arrive at the choice that is finally implemented in *treams*.

3.4.1 Validation of the results by direct sum comparisons

To assess the accuracy of the derived expressions from the previous section, we compare them to the direct sum. Depending on the difference $d - d'$, the direct sum converges with different speed. As a first example, we analyze the expression and, equally important for such complicated mathematical functions, their implementation in *treams* for the following parameters. In the $d = 3$ case, we choose $l = 2$ and $m = 0$, and in the $d = 2$ case we set $m = 0$. Note that for these parameters, there is also a contribution to the lattice sums if we had $\boldsymbol{r}_\perp = 0$: The $d = 3$ and $d' = 2$ case has non-zero values for $l + m$ even and the $d = 3$ and $d' = 1$ case has non-zero values for $m = 0$. Thus, these first examples test if the inclusion of non-zero $\boldsymbol{r}_\perp$ changes the non-zero values correctly by setting the shift vectors to $\boldsymbol{r} = 0.2\hat{\boldsymbol{x}} + 0.1\hat{\boldsymbol{y}} + 0.3\hat{\boldsymbol{z}}$ for $d = 3$ and $\boldsymbol{r} = 0.1\hat{\boldsymbol{x}} + 0.3\hat{\boldsymbol{y}}$ for $d = 2$. The tangential wave vector components are chosen to be $k_\parallel = 0.3$ for the $d' = 1$ lattices, $\boldsymbol{k}_\parallel = -0.1\hat{\boldsymbol{x}} + 0.2\hat{\boldsymbol{y}}$ for the $d' = 2$ lattices, and $\boldsymbol{k}_\parallel = 0.3\hat{\boldsymbol{x}} - 0.1\hat{\boldsymbol{y}} + 0.2\hat{\boldsymbol{z}}$ for the $d' = 3$ lattice. In all cases, we use the common variables $k = 3$ and lattice pitch $a = 1.9$. We use a square or cubic lattice geometry for the two- or three-dimensional lattices, respectively.

In Fig. 3.3, we show the result for the direct sum and the result obtained with the expressions derived above. Each panel shows one combination of d and d'. The first row, panels (a) to (c), shows the $d = 3$ results and the second row the $d = 2$ results. The columns correspond to $d' \in \{1, 2, 3\}$ from left to right. We plot for each lattice sum its real part, its imaginary part, and the relative differences of the value obtained with our approach to the direct sum. For the direct summation, we include an increasing number of lattice points starting with the closest lattice points. For lattices with $d' > 1$ there are different methods to generalize the distance, e.g., one can use the Euler distance $\sqrt{|\boldsymbol{r}_1|^2 + |\boldsymbol{r}_2|^2}$ or the Chebyshev distance $\max(|\boldsymbol{r}_1|, |\boldsymbol{r}_2|)$ between two points $\boldsymbol{r}_1$ and $\boldsymbol{r}_2$. We choose the latter due to a better convergence behavior [54]. Each layer increases the Chebyshev distance by the value of the lattice pitch.

Panel (a) shows the result for $d = 3$ and $d' = 1$, where the direct sum converges to the same value as our expressions. However, during the calculation, the result is highly oscillatory, such that the blue lines appear as solid areas. With 10^5 layers, the relative difference is slightly above 10^{-4}. For $d' = 2$ the convergence is slightly slower as shown in panel (b), even though a maximal number of 1000 layers corresponds to approximately $4 \cdot 10^6$ lattice points considered in the sum, so an order of magnitude more than in the $d' = 1$ case. This highlights how the use of Ewald's method improves the speed of the

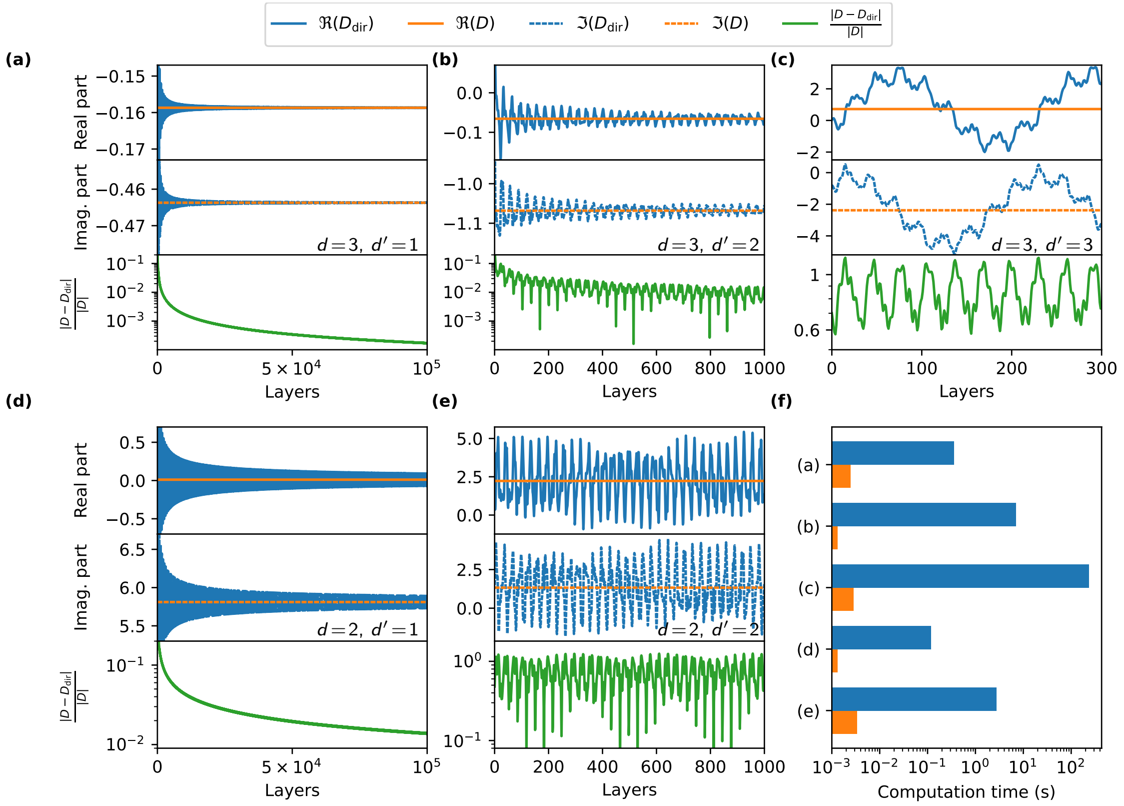

Figure 3.3: Comparison of the direct evaluation and the exponentially fast converging expressions. The panels correspond the five combinations of lattices with dimension d' and spatial dimensions d shown in Fig. 3.1. It can be seen that the exponentially fast convergence shown as orange line matches with the highly oscillatory result of the direct sum in the limiting case of a very larger layer number. Panel (f) shows timings for the exponentially fast sums (orange) and the direct sums (blue). Note that times are presented on logarithmic scale. Adapted with permission from [P4]. Copyright 2023 American Physical Society.

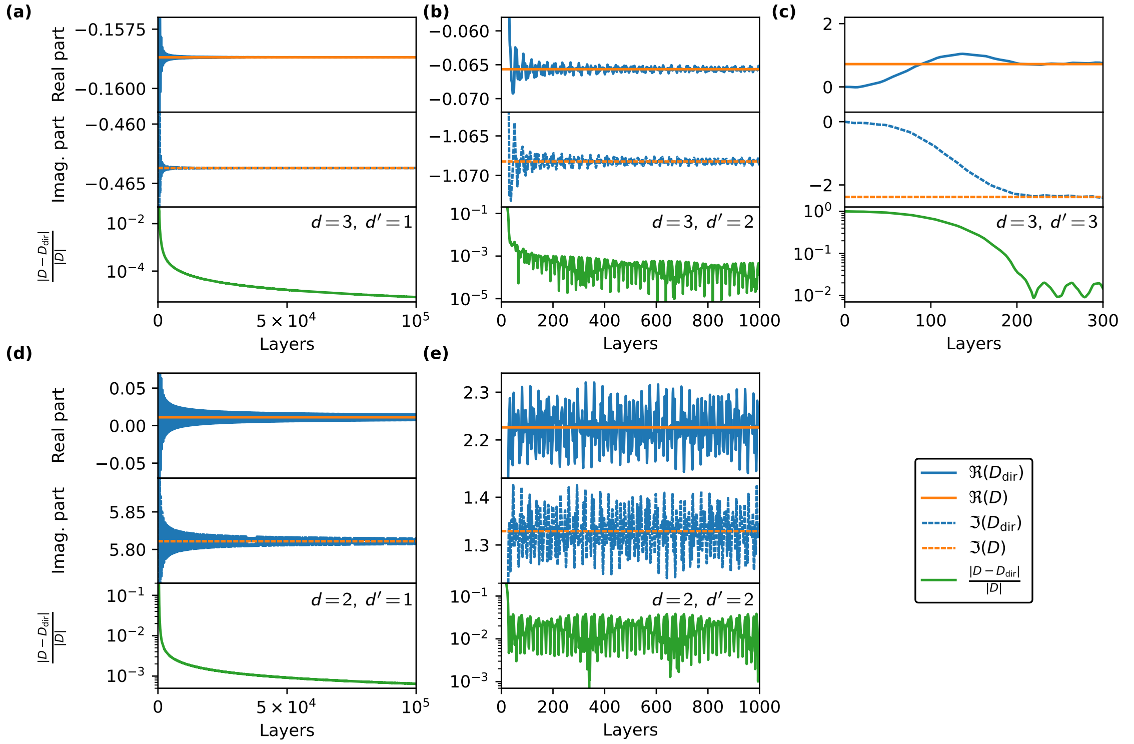

Figure 3.4: Comparison of the direct evaluation with oscillation averaging and the exponentially fast converging expressions. The panels show to the same five combinations of lattices with dimension d' and spatial dimensions d with the same parameters as in Fig. 3.3. However, the direct sum is averaged such that the oscillations around the true value are reduced. Reprinted with permission from [P4]. Copyright 2023 American Physical Society.

calculation especially for higher-dimensional lattices. Even with this high number of particles included, the lattice difference between the two approaches is with 10^{-2} greater than for the $d' = 1$ case. Panel (c) shows the case $d' = 3$, which only exists for the spherical solutions. Here, we include up to 300 layers which means approximately $2 \cdot 10^8$ lattice points considered in the sum. However, the convergence of the direct approach is not even visible, clearly illustrating the usefulness of the Ewald method. We observe, however, that the result obtained with the direct sum oscillates around the value from the expression we derived.

The second row, containing panels (d) and (e), shows the results for the cylindrical solutions, i.e., $d = 2$. The sum for $d' = 1$ in panel (d) converges with a similar speed as the $d = 3$ and $d' = 2$ case in panel (b), achieving also a relative difference of about 10^{-2}. Thus, the convergence of the sums seem to be closely linked to the difference $d - d'$. This can also be seen in panel (e), where – analogous to panel (c) – the direct approach does not lead to a visible convergence, but to an oscillation around the result obtained with Ewald's method.

Panel (f) shows the computation times for the direct sums in comparison to our expressions for the five presented cases. Our expressions compute the final value on a timescale of several milliseconds. Moreover, the time to compute the result shows no strong depen-

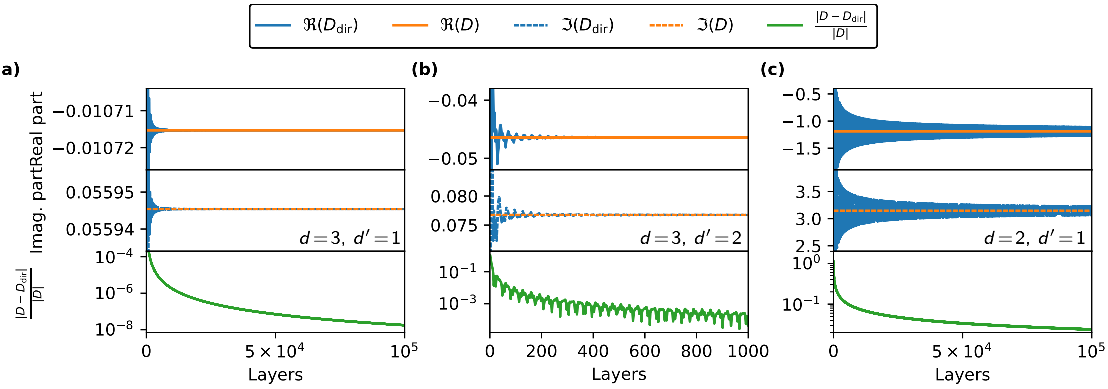

Figure 3.5: Comparison of direct evaluation and the exponentially fast converging expressions for large shifts perpendicular to the lattice. The panels show the three cases, where $d > d'$. Reprinted with permission from [P4]. Copyright 2023 American Physical Society.

dence on the lattice dimensions. This behavior is in strong contrast to the direct sums. Here, the dependence on the lattice dimension is quite strong. It scales, unsurprisingly, similarly as the number of terms that are required for a convergent solution. Even for one-dimensional lattices, where the individual sum takes about 100 ms, our approach is two orders of magnitude faster. This improvement of the computation time gets even stronger for higher-dimensional lattices. In the case of a three-dimensional lattice, the direct sum needs several minutes to be computed.

A common and simple method to improve the direct summation approach is the averaging of the sum for different numbers of layers. The idea behind that approach is to compensate for the oscillation around the true value of the sum. The same sums, but with the use of such an averaging scheme are shown in Fig. 3.4. In panels (a), (b), and (d), where $d > d'$ and we already had convergent sums previously, we find that this approach leads to relative differences approximately an order of magnitude smaller than the ones shown in Fig. 3.3. However, we still need to include a large number of lattice points to achieve this result.

In panels (c) and (e), the improvement due to the averaging is even more substantial in comparison to the simpler approach in Fig. 3.3. Now, these sums converge in the first place and we have a relative difference in the order of 10^{-2}. Overall, our studies show that for all five different combinations of d and d' our approach leads to the same results as could be obtained with the direct approach, but with a dramatically improved speed.

Next, we turn to combinations of l and m in combination with larger values of $|\boldsymbol{r}_\perp|$. Therefore, these studies are only done for the cases with $d > d'$, because $|\boldsymbol{r}_\perp|$ is not present for $d = d'$. In the case $d = 3$, we use $l = 2$ and $m = 1$. The shift vector is $\boldsymbol{r} = 1.5\hat{\boldsymbol{x}} + 1.1\hat{\boldsymbol{y}} + 0.3\hat{\boldsymbol{z}}$ for $d' = 2$ and $\boldsymbol{r} = 0.2\hat{\boldsymbol{x}} + 0.1\hat{\boldsymbol{y}} + 1.3\hat{\boldsymbol{z}}$ for $d' = 1$. For the chosen values of l and m the sum would be zero for $\boldsymbol{r}_\perp = 0$. Thus, this example particularly tests the correct result for lattices with complex unit cells. In the case $d = 2$ and $d' = 1$ we use $m = 2$. The shift perpendicular to the lattice is also increased in this case to $\boldsymbol{r} = 0.1\hat{\boldsymbol{x}} + 1.3\hat{\boldsymbol{y}}$. The remaining parameters of k, $\boldsymbol{k}_\parallel$, and the lattice geometry stay the same as for Fig. 3.3.

Figure 3.5 shows that the direct sum and the exponentially convergent expressions result in the same values. For the chosen parameters, the result for $d = 3$ and $d' = 1$ as shown in panel (a) matches very good. We observe that the direct sum also converges very quickly and the relative difference gets below 10^{-7}. In the other two cases, the convergence is slower and it only reaches accuracies of approximately 10^{-3} and 10^{-1} in panel (b), showing the $d = 3$ and $d' = 2$ case, and panel (c), showing the $d = 2$ and $d' = 1$ case, respectively.

3.4.2 Choice of the splitting parameter

As the only freely settable argument of the expressions we derived, the value of the splitting parameter η assumes an important role in the numerical evaluation of the lattice sums. Its influence mainly appears in two ways: From an analytical perspective, an optimal choice of the splitting parameter means a quick convergence of both sums, but from a numerical perspective, suboptimal convergence has to be balanced with the stability of summing floating point numbers in a computer. We first want to motivate the analytically optimal choice of the splitting parameter. Then, we show that this choice has to be modified to ensure convergence in the actual implementation.

In principle, the addition of the real and reciprocal space sums should always result in the correct total value independently of η. Even more, the limits of $\eta \to 0$ and $\eta \to \infty$ should result in the original sum and its complete Fourier transform, respectively. However, the full sums in real and reciprocal space have poor convergence. So, the correct choice of the splitting parameter ensures a quick convergence of both sums that appear when using Ewald's method. This mathematically optimal choice for square or cubic lattices can be found in [54, 68, 69]. While we do not rigorously cover the derivation here, it can be motivated by a simple argument. The exponential decay of the real space sum in Eqs. (3.8) and (3.9) is primarily a result of the factor

$$\mathrm{e}^{-\frac{k^2(\boldsymbol{r}+\boldsymbol{R})^2\eta^2}{2}} \tag{3.40}$$

in Eq. (3.6). Likewise, for the reciprocal space expression of Eqs. (3.20), (3.25), (3.31), and (3.37), the exponential factor dominating the convergence is

$$\mathrm{e}^{-\frac{(\boldsymbol{k}_\parallel+\boldsymbol{Q})^2}{2k^2\eta^2}} \,. \tag{3.41}$$

A simple balancing of the two exponentials leads to

$$\eta = \frac{1}{k}\sqrt{\frac{|\boldsymbol{k}_\parallel + \boldsymbol{Q}|}{|\boldsymbol{r} + \boldsymbol{R}|}} \,, \tag{3.42}$$

where, subsequently, we neglect $\boldsymbol{r}$ and $\boldsymbol{k}_\parallel$. We can justify this approximation, if these vectors lie in the Wigner-Seitz cell or first Brillouin zone, respectively, because then their length is small in comparison to the real and reciprocal lattice vectors $\boldsymbol{R}$ and $\boldsymbol{Q}$ for an increasing number of layers in the sum. Next, we need the relevant length scales for these vectors. In a one-dimensional, square, or cubic lattice, the obvious choice is the lattice pitch a and the reciprocal lattice pitch $\frac{2\pi}{a}$. Hence, we arrive at an optimal choice of [68–71]

$$\eta = \frac{\sqrt{2\pi}}{ka} \,. \tag{3.43}$$

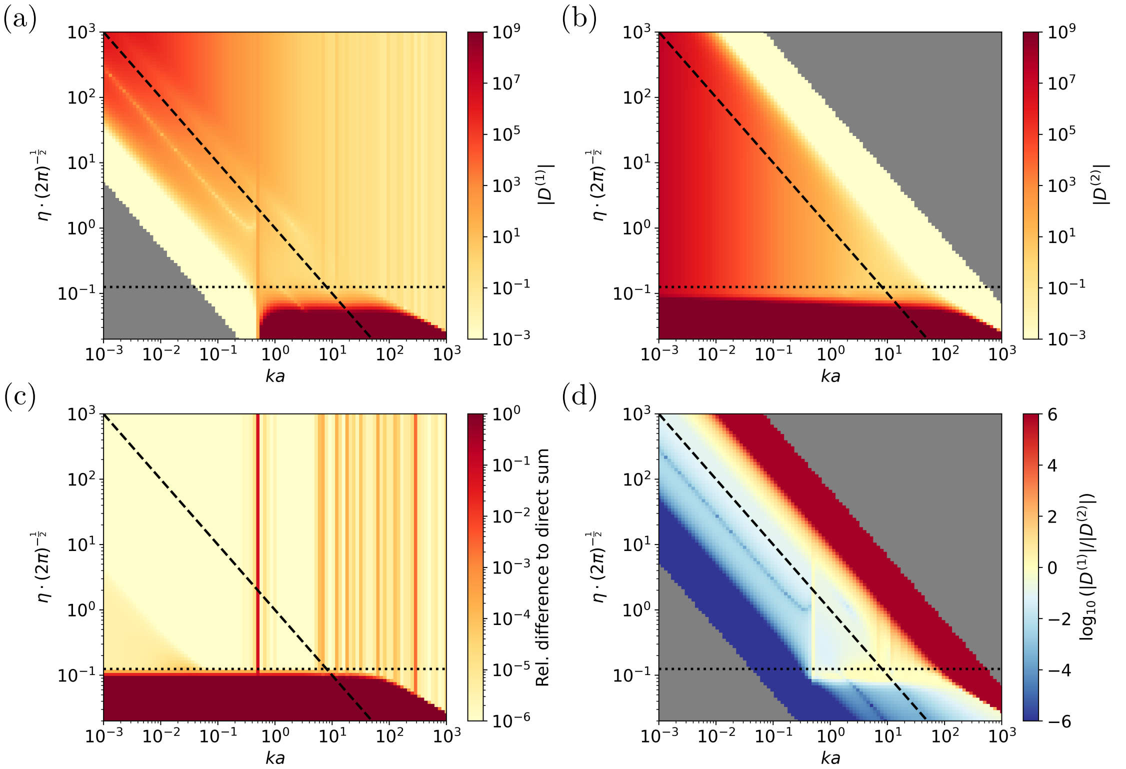

Figure 3.6: Convergence of the real and reciprocal lattice sums depending on wave number k and convergence parameter η. We show the absolute value of the contributions $D^{(1)}$ and $D^{(2)}$ of the lattice sum in panels (a) and (b) on a logarithmic scale. The gray areas correspond to a zero value in the double precision floating point calculation. The chosen example is the lattice sum for cylindrical waves in a one-dimensional lattice with $m = 2$, $k_{\|} = 0.5$, the lattice pitch $a = 1$, and $\boldsymbol{r} = 0.1\hat{\boldsymbol{x}} - 0.2\hat{\boldsymbol{y}}$. The dashed line indicates the values of $\eta = \frac{\sqrt{2\pi}}{ka}$ and the dotted line indicates $\eta = \frac{\sqrt{2\pi}}{8}$. Panel (c) shows the sum of the two sums to the total value and shows the relative difference to the reference value computed with direct summation. Panel (d) shows the logarithmic ratio of reciprocal and real space sum. Areas were either of the values in the ratio are zero appear as gray.

Different methods to generalize this result to non-square or non-cubic lattices have been employed [70–73]. For simplicity, we use the square or cube root of the unit cell area or volume in $d' = 2$ and $d' = 3$, respectively, to obtain the splitting value used in *treams*.

It is known that this analytically optimal choice of η needs to be modified for large wave numbers k in comparison to the lattice pitch [68, 69, 71]. We illustrate the dependence of the real sum, the reciprocal sum, and the total result on k and η in Fig. 3.6. As example, we choose the sum of cylindrical waves on a one-dimensional lattice with pitch $a = 1$. The further parameters are $m = 2$, $k_\parallel = 0.5$, and $\boldsymbol{r} = 0.1\hat{\boldsymbol{x}} - 0.2\hat{\boldsymbol{y}}$. The reciprocal space sum in panel (a) has very small values for small values of k and η. The value zero in the double precision floating point calculation is shown on the logarithmic scale as gray color. However, at larger values of k but values of $\eta < \frac{\sqrt{2\pi}}{8}$, which is indicated by a dotted line, the sum reaches very large absolute values. We further indicate the mathematically optimal value of Eq. (3.43) by a dashed line. Panel (b) shows the behavior of the real space lattice sum. Here, large values of k or η result in vanishing lattice sums. Also, the real space sum results in large values for $\eta < \frac{\sqrt{2\pi}}{8}$. Panel (c) shows a comparison of the value obtained with the exponentially convergent expressions with the direct sum. Over a large region of k and η, our approach results in a good agreement. The main discrepancy is exactly in the area of $\eta < \frac{\sqrt{2\pi}}{8}$, where the large values of the real and reciprocal sum either do not cancel each other to arrive at the correct value or do not converge at all. The only other large differences appear as vertical lines. Here, the lattice sums diverge. This divergence appears directly in the reciprocal space sum as vanishing values of γ. In panel (d), we compare the relative size of reciprocal and real space sum on a logarithmic scale. The reciprocal space contribution dominates in the red region and the real space contribution in the blue region. In the gray areas either the real or reciprocal sum have a vanishing value. The choice of $\eta = \frac{\sqrt{2\pi}}{ka}$ as indicated by the dashed line balances these contributions and, thus, avoids numerical inaccuracies due to the floating point computation. Moreover, it ensures equally quick convergence of both contributions. Thus, this is the default choice for η implemented in *treams*. Deviating from this value either leads to many contributing terms to be considered in the real or reciprocal lattice sum. In the limiting cases, we either arrive at the initial direct sum of Eq. (3.1) or at the pure reciprocal space sum. However, we restrict η in *treams* to values above the dashed line, to avoid the region of very large individual contributions of the real and reciprocal space sum.

We test the choice to follow Eq. (3.43) for the value of η except for large wave numbers k, where we set it to be constant for the other expressions. These studies are shown with one example each in Fig. 3.7. In two and three dimensions, we set the lattice to be hexagonal, with $a = \sqrt{V_2} = 1$ and $a = \sqrt[3]{V_3} = 1$. Moreover, we set $m = 2$ for $d = 2$ and $l = 2$, $m = 0$ for $d = 3$. The shift vectors are $\boldsymbol{r} = 0.1\hat{\boldsymbol{x}} - 0.2\hat{\boldsymbol{y}}$ for $d = 2$ and $\boldsymbol{r} = 0.1\hat{\boldsymbol{x}} - 0.2\hat{\boldsymbol{y}} + 0.2\hat{\boldsymbol{z}}$ for $d = 3$. Lastly, the wave vectors are $k_\parallel = 0.5$, $\boldsymbol{k}_\parallel = 0.5\hat{\boldsymbol{x}} + 0.5\hat{\boldsymbol{y}}$, and $\boldsymbol{k}_\parallel = 0.1\hat{\boldsymbol{x}} + 0.2\hat{\boldsymbol{y}} + 0.3\hat{\boldsymbol{z}}$ for $d' = 1, 2, 3$, respectively. In all four panels of Fig. 3.7, we can observe the very large sum values for small η that, however, is limited to values below the dotted line. Furthermore, we find that in all cases the choice of Eq. (3.43) indeed leads to comparable contributions of the real and reciprocal space sums.

With this study on the splitting parameter, we conclude the chapter. Starting from the definition of the lattice sum in Eq. (3.1) and the integral representations of the Hankel and spherical Hankel functions in Eqs. (3.3) and (3.4), we split the integral into the real

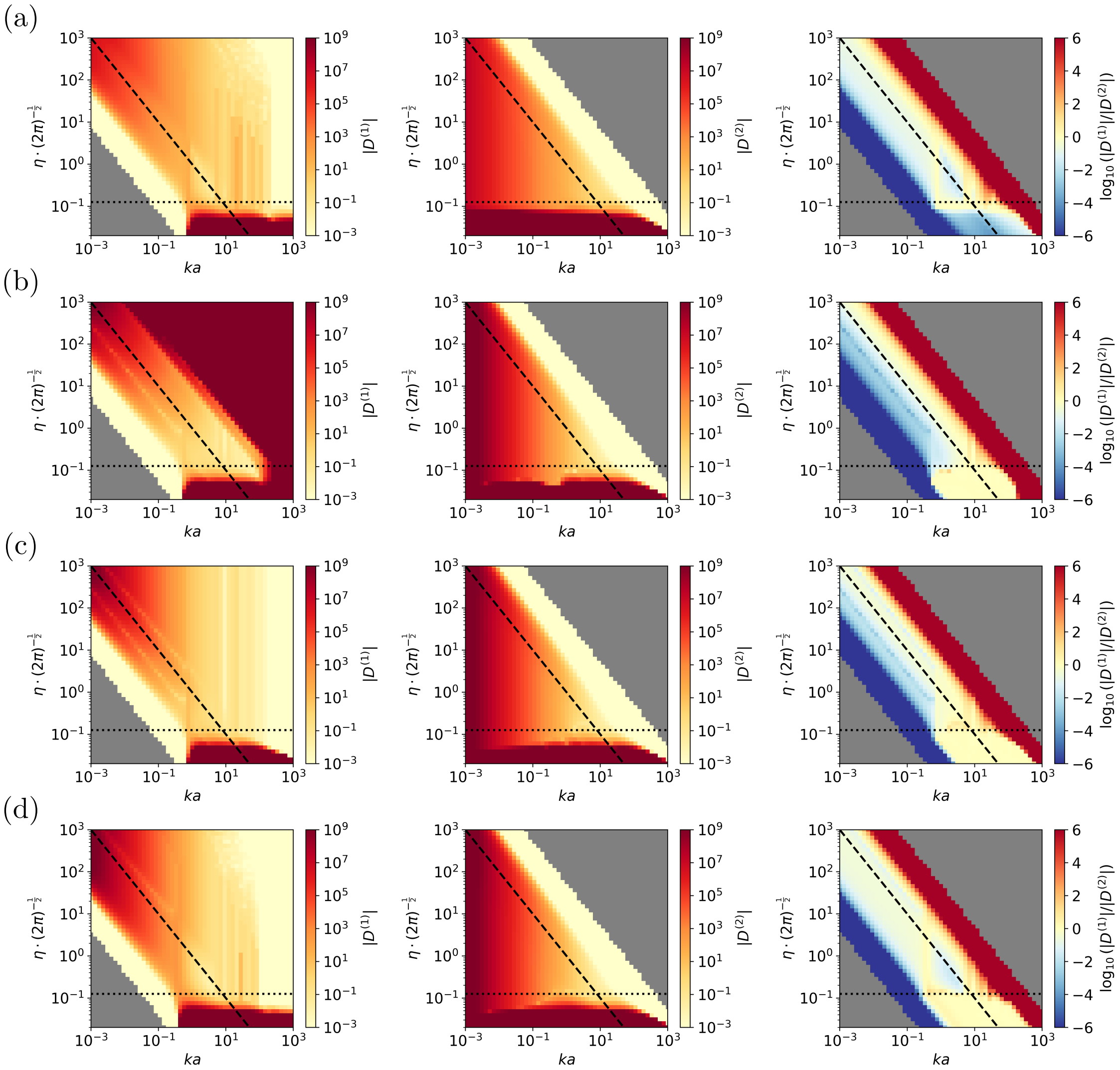

Figure 3.7: Convergence of the real and reciprocal lattice sums depending on wave number k and convergence parameter η for different lattice dimensions. Similar to panels (a), (b), and (d) in Fig. 3.6, we show the individual contributions of the reciprocal sum, the real sums, and their logarithmic ratio for the remaining cases of lattice sums. These are the two-dimensional sum of cylindrical waves in panel (a) and the one-, two- and, three-dimensional sums of spherical waves in panels (b), (c), and (d).

space sum and the contribution to be converted to reciprocal space. For the integral in the real space sum, we find a relatively simple recurrence relation similar to previously known results [50]. For the transformation of the long-range part to a reciprocal space sum, we introduce a second integral over the real space coordinate. We can transform this integral such that it can be solved directly. This is in contrast to the process of taking a limit that is used in the conventional approach. Avoiding the limit also avoids the appearance of other more complicated expressions [57]. Thereby, we can apply our approach to all lattice dimensions, especially in the presence of complex unit cells. We test the derived results by comparison with the direct summation approach, which verifies the accuracy and also shows their usefulness in avoiding the slow convergence and highly oscillatory behavior of the direct sum. We finish with an analysis of the correct choice of the splitting parameters balancing the convergence of the reciprocal space and the real space part of the derived expressions.

4 | The program *treams*

In Chapter 2, we introduced several solution sets to Maxwell's equations and their usage for solving electromagnetic scattering with the T- and S-matrix methods, where we focused in particular on the presence of periodic boundary conditions. In Chapter 3, we derived efficient expressions for the lattice sums, which occur in the solution of such periodic structures. These results are the foundation of the novel Python program *treams*, which is available open-source. We present the program also in a published manuscript describing its core features and functionalities [S1]. The software *treams* is written completely from scratch. However, a preceding program, written in Matlab, was developed by Achim Groner, which implements functions for single layers of two-dimensional lattices of achiral scatterers with simple unit cells [74].

This chapter is structured as follows. Section 4.1 gives an overview of the design goals and core features of *treams*. The structure of *treams* and the implementation of the main functionality are described in Section 4.2. We show examples to validate and examine computations with *treams* in Section 4.3. These examples include self-consistency tests of the results obtained by using different basis sets and direct comparisons of the electric field values with independent results from simulations made with finite-element methods. We use the latter to also benchmark the speed of *treams*. In Section 4.4, we give an overview of the actions taken to assess and maintain the code quality.

4.1 Overview of the program

In essence, *treams* performs scattering calculations based on the T-matrix method for vector spherical and cylindrical waves. The interaction can be calculated with the translation coefficients for finite clusters of particles or for clusters with periodic boundaries. In the case of periodic boundary conditions, we use the highly specialized and efficient methods from Chapter 3. *treams* includes the analytical computation of T-matrices for multi-layered spheres and infinitely long cylinders. For scatterers with other shapes, an interface to load their data into *treams* is implemented. *treams* supports T-matrices without restricting the multipolar order and it can handle them in the local and global basis. All methods are written for the commonly used parity basis and for the helicity basis. The latter greatly simplifies the computations in the presence of chiral matter in the scatterers or the embedding medium.

Before starting to describe *treams* in detail, we shortly outline other important T-matrix codes. While not being an exhaustive treatment, we use this overview to highlight some of the unique features of *treams*. A comprehensive list of scattering software is maintained online [75, 76]. The software NFM-DS is aimed at the calculation of scattering from non-spherical particles, especially with high aspect ratios, by complementing the extended boundary condition method with discrete sources [77, 78]. These particles can also be chiral. Furthermore, the scattering from clusters of these particles can be calculated. *treams*, however, is less aimed at computing the T-matrices but implementing the calculation of their interaction with, in particular, periodic boundary conditions. Another program for non-spherical particles and clusters thereof is FASTMM [79], which combines the T-matrix method with a volume integration method to compute the T-matrix of particles whose shape deviates strongly from spheres. Smuthi is another solver for clusters of particles [80]. While the previous publications focus on the calculation of the T-matrix for non-spherical particles, the focus of Smuthi lies on the correct calculation of their interaction in close proximity. An intermediate plane wave expansion is used to overcome the limitation of the overlapping circumscribing spheres. *treams* does not implement finite clusters of particles on an interface, but it still benefits from using plane wave expansions in two-dimensional periodic system. Thereby, as we demonstrate in Section 4.3, it is possible to place objects, such as disks, on top of a planar film. CELES [81] implements fast methods for clusters of spheres. While being restricted to spheres, the iterative solution approach can handle very large clusters and is further accelerated by using GPU computation with the Cuda-framework. TERMS [82], also provides several algorithms for clusters to solve the interaction problem with high numerical stability and is able to import externally calculated T-matrices. Obviously the biggest difference to all these programs is the inclusion of the periodic boundary conditions in *treams*. Furthermore, *treams* is adapted to treat chiral media in the scatterers as well as chiral embedding media.

The programs MULTEM [39] and MULTEM 2 [83] implement periodic boundary conditions for two-dimensional arrays. Moreover, the plane wave basis and the S-matrix formulation is used to describe arrays efficiently. However, theses programs are limited to spheres as scatterers and simple unit cells. The recently published coed QPMS [57] also implements periodic boundary conditions for T-matrices in one-, two-, and three-dimensional arrays in the parity basis. However, efficient expressions for one-dimensional arrays in complex unit cells are missing. Furthermore, we provide more flexibility for the type of structures by also using T-matrices for vector cylindrical waves.

The program *treams* is intended to provide a framework around various T-matrix methods, with the principal goals to be: easy to use, fast, and comprehensive. Hence, the specialized methods for T-matrix calculations become more accessible for researchers in natural sciences and engineering. Especially with the implementation of the intricate lattice sums, the program or parts of it can be reused for other purposes than those shown here, e.g., the T-matrix method can also be used for acoustic scattering [84].

Although the usability depends also on the cumulated design choices throughout the development, we took several general decisions to improve the success chances. The first step toward an easy to use program is its accessibility. We decided to publish *treams* open-source and free of charge under the permissive MIT license. Thus, *treams* is available to a large audience. Moreover, we use the programming language Python. Programs written in Python are wide-spread in the scientific community, such that many researchers are familiar with Python code and, furthermore, many high-quality introductions and tutorials as well as other infrastructure such as integrated development environments exist. By having *treams* added to the Python Package Index (`https://project.pypi.org/treams`), it is simple to install. To simplify the usage of the program, we provide an extensive documentation that is available online (`https://tfp-photonics.github.io/treams`), which also includes many example scripts with step-by-step explanations. We also use the platform Github (`https://github.com/tfp-photonics/treams`) as a convenient and established way to interact with issues raised by users.

Scientific and numeric computing in Python is often associated with the packages *numpy* [85] and *scipy* [86]. These packages provide many functions for linear algebra, analysis, and statistics. Since potential users might already be familiar with these packages and their interfaces and especially with *numpy*-arrays, which are used to represent vectors, matrices, and other higher-order tensors, we include *treams* into this well-established framework. These packages are also known to be considerably faster than pure Python due to many functionalities being implemented as compiled code or by interfacing to compiled external libraries. Since we want to achieve comparable speeds, we choose to also implement the computationally expensive functions as compiled code. Hence, a fair amount of *treams* is implemented in Cython, which, essentially, is a Python-like language, that gets converted to C code. By using Cython, we can also easily use functions from *scipy*, which offers a Cython-interface to some of its functions besides their Python-interface. The addition of compiled parts to the code base can be a hurdle for users. However, as we explain in Section 4.4, we automatically compile new versions and distribute the pre-compiled Python-packages for all three major operating systems, Microsoft Windows, Apple macOS, and Linux using the Python Package Index. Therefore, we assume that the benefits, in particular the better integration into the *numpy*- and *scipy*-framework and the faster execution times, outweigh the additional complexity of adding non-interpreted code to *treams*.

Besides its core feature of T-matrix calculations with periodic boundary conditions, we aim to provide a comprehensive package for general applications of the T-matrix and S-matrix methods. By using both, parity and helicity modes, as well as the three different basis sets introduced in Subsection 2.1.3, we can cover a wide range of scattering scenarios. Moreover, we implement many transformations within these basis sets, such as rotations or translations. The most important functions are given in Subsection 2.2.3. Furthermore, we include functions to evaluate common quantities such as the extinction, scattering, and absorption cross-sections [23, 31], transmittance and reflectance [39], chirality, or duality breaking [P7]. The structure of all these functions and their modularization, such that parts of *treams* can also be easily reused, is outlined in the following section.

4.2 Main components and their implementation

A coarse overview of the general structure of *treams* is shown in Fig. 4.1. The widest pillar, representing the core of *treams*' functionality, contains classes, methods, and functions, which are directly associated with the scattering processes. Two further pillars provide support to complete the functionality of *treams*: First, classes and methods that define and manipulate ancillary physical quantities with respect to the scattering process and, second, further functions, for example, to import externally computed T-matrices and, also, export them. The main pillar is further subdivided into three levels. The higher levels include a higher complexity of its data structures, which are intended to take work off from the user. However, they come with a slight penalty on execution times. For the lower levels, these data structures are not present, which improves speed and also gives maximal freedom to the user but with less safety nets in the form of additional checks on the given argument. In Subsection 4.2.1, we discuss the underlying low-level functions, and in Subsection 4.2.2, we give an overview how these functions are interfaced by the high-level classes for a more comfortable use.

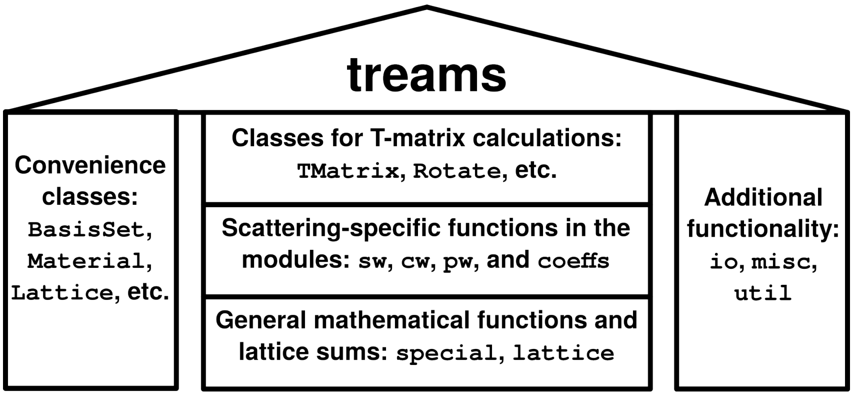

Figure 4.1: General structure of *treams*. The functionality of *treams* can be divided into three pillars. The main part of the code, corresponding to the widest pillar, are functions, classes, and methods that are directly related to the scattering calculations. The second pillar contains classes that are used to describe physical parameters, such as the material parameters or the lattice geometry. The last pillar completes the functionality with, for example, functions to load and store T-matrices. Adapted from [S1].

4.2.1 Low-level functions

At the base of *treams*, we have two subpackages, i.e., parts of the program that are independent from the rest of the code and, therefore, can be reused conveniently. The first subpackage, `lattice`, contains the lattice sums. In there, we mostly implement the mathematical functions as described in Chapter 3. The second package is named `special` in analogy to the module `special` in *scipy*. It contains mathematical functions, e.g., an implementation of the incomplete gamma function for integer and half integer order and complex argument. The next higher level bundles these functions and lattice sums into several modules for applications specific for electromagnetic scattering calculations: they are divided into the categories `sw`, `cw`, and `pw` for functions related to vector spherical, cylindrical, and plane waves, respectively. Finally, we include a fourth package, named `coeffs`, containing functions to calculate the T-matrix coefficients for multi-layered chiral spheres and cylinders given in Subsection 2.2.1 as well as the Fresnel coefficients for the scattering of plane waves at planar interfaces, which are the entries of the S-matrix [P2].

All these functions are implemented in Cython. Most of them are wrapped for the user as so-called *numpy*-universal functions. These functions are tailored for arguments and results in the form of arrays. Hence, they are useful for computational methods using array-like data structures, such as the T- or S-matrices. The individual functions in Cython are implemented for a single argument. Once they are wrapped to be a *numpy*-universal function, the wrapper takes care of iterating over the input and output arguments. The benefits of implementing the functions that way include faster execution speeds, reusing of an established behavior for array-like arguments, and the automatic support of further methods. The faster execution times are achieved by performing all steps in compiled code in comparison to the typically interpreted pure Python. The established behavior for array-like arguments is, for example, the possibility to call a function with arrays as argument to apply the function to all elements. This behavior is further enhanced by the

Table 4.1: Categories of functions included in the subpackage `special`

Category	Example functions	Reference
Common functions	`sphercial_hankel1`, `wignerd`, `incgamma`	
Coordinate conversions	`car2sph`, `car2cyl`	Appendix B
Vector cylindrical waves	`vsw_M`, `vsw_N`	Eq. (2.17)
Vector plane waves	`vpw_M`, `vpw_N`	Eq. (2.15)
Vector spherical harmonics	`vsh_X`, `vsh_Y`, `vsh_Z`	Eq. (2.19)
Vector spherical waves	`vcw_M`, `vcw_N`	Eq. (2.23)

so-called broadcasting, which is a well-defined set of rules on how to combine multiple array-like arguments. We use this property in Listing 4.2. Lastly, the further methods include, e.g., the reduction along an array dimension.

The subpackage `lattice` contains implementations of the expressions derived in the previous chapter. More precisely, the real space sums in Eqs. (3.8) and (3.9) are contained, with specialized functions for the case that the simplifications of Table 3.1 can be applied, and the reciprocal space sums in Eqs. (3.20), (3.25), (3.31), and (3.37) also with their possible simplifications. The functions for the reciprocal space sum also contain the correction for the omission of the origin from Eq. (3.13). The lattice sums can be conveniently obtained with the two functions `lattice.lsumcw` and `lattice.lsumsw`. They automatically dispatch, based on the given arguments, to the correct lattice sum. Moreover, the automatic choice of the parameter η based on the results of Subsection 3.4.2 is implemented in this function. Finally, the subpackage also includes functions for the direct summation `lattice.dsumcw` and `lattice.dsumsw` for reference.

The subpackage `special` contains mathematical functions that are not directly implemented in *scipy* or *numpy*. An overview of the different function categories is given in Table 4.1. A large part of the implemented functions are the basis sets for the vector spherical, cylindrical, and plane waves. To implement these basis sets and to provide implementations of mathematical functions for other parts of *treams*, we added, e.g., the spherical Hankel functions, the Wigner-D symbols, or the incomplete gamma function. Some functions, such as the spherical Hankel functions, can be derived from existing functions, in that case the Hankel functions. Other custom implementations are necessary to include complex arguments, e.g., for the spherical harmonics. The incomplete gamma function and the integral Eq. (3.6) are implemented by their recursion formulas. More complicated recursions are used for the Wigner-D matrix elements [87] and the Wigner-3j symbols [88], which are necessary for the translations and rotations of vector spherical waves. A final set of functions include the coordinate and vector transformation between the three used coordinate systems (Appendix B).

Based on these functions, we add the modules `pw`, `cw`, and `sw`. While the subpackages `special` and `lattice` contain mathematical functions, these modules are intended to combine them for their simplified use in scattering calculations. The module names separate the functions for the different basis sets. An overview of all functions is given in Table 4.2. Many of the transformations defined in Subsection 2.2.3 are included in these modules. Finally, we add the module `coeffs`. It contains functions to compute the analytically known coefficients for multi-layered chiral spheres and cylinders, as well as

Table 4.2: Overview of the functions in the modules `pw`, `sw`, `sw`, and `coeffs`

Module	Function name	Purpose	Equation
`pw`	`to_cw`	Basis change	(2.73)
	`to_sw`	Basis change	(2.72)
	`translate`	Translation	(2.71)
	`permute_xyz`	Permute axis labels	(K.4)
`cw`	`periodic_to_pw`	Basis change	(2.84)
	`rotate`	Rotation	(2.69)
	`to_sw`	Basis change	(2.74)
	`translate`	Translation	(2.51) and (2.54)
	`translate_periodic`	Translation with periodicity	
`sw`	`periodic_to_cw`	Basis change	(2.73)
	`periodic_to_pw`	Basis change	(2.80)
	`rotate`	Rotation	(2.70)
	`translate`	Translation	(2.50) and (2.53)
	`translate_periodic`	Translation with periodicity	
`coeffs`	`mie`	T-matrices of spheres	(2.45)
	`mie_cyl`	T-matrices of cylinders	(2.45)
	`fresnel`	S-matrices for planar interfaces	

the Fresnel coefficients for planar interfaces between chiral media. Due to the inclusion of chiral material parameters, they are implemented using the helicity basis. However, they can easily be transformed to the parity basis, when only achiral media are involved.

As an example for these functions, we can calculate the translation coefficient in helicity basis along the spherical coordinates $kr = 1.2$, $\theta = \frac{\pi}{2}$, and $\varphi = \pi$ by

Listing 4.1: Calculation of a translation coefficient

```
>>> import numpy as np
>>> import treams
>>> treams.sw.translate(2, -2, 1, 1, -1, 1, 1.2, np.pi / 2, np.pi)
(0.40412456738474173-2.826374554471906j)
```

from the mode with $l = 1$, $m = -1$ to the mode $l = 2$, $m = -2$ for positive helicity. However, by using the broadcasting feature, we can easily create, e.g., the full translation matrix for the dipolar modes

Listing 4.2: Calculation of a translation coefficient

```
>>> ms = np.array([-1, 0, 1, -1, 0, 1])
>>> pols = np.array([0, 1, 0, 1, 0, 1)
>>> treams.sw.translate(
...     1,
...     ms[:, None],
...     pols[:, None],
...     1,
...     ms,
...     pols,
...     1.2,
```

```
...     np.pi / 2,
...     np.pi,
...)
array([[ 0.79832728-0.86918395j,  0.        +0.j        ,
        -0.06488414+1.70165747j,  0.        +0.j        ,
         1.09071564+0.36622959j,  0.        +0.j        ],
       [ 0.        +0.j        ,  0.73344315+0.83247352j,
         0.        +0.j        , -1.09071564-0.36622959j,
         0.        +0.j        , -1.09071564-0.36622959j],
       [-0.06488414+1.70165747j,  0.        +0.j        ,
         0.79832728-0.86918395j,  0.        +0.j        ,
         1.09071564+0.36622959j,  0.        +0.j        ],
       [ 0.        +0.j        , -1.09071564-0.36622959j,
         0.        +0.j        ,  0.79832728-0.86918395j,
         0.        +0.j        , -0.06488414+1.70165747j],
       [ 1.09071564+0.36622959j,  0.        +0.j        ,
         1.09071564+0.36622959j,  0.        +0.j        ,
         0.73344315+0.83247352j,  0.        +0.j        ],
       [ 0.        +0.j        , -1.09071564-0.36622959j,
         0.        +0.j        , -0.06488414+1.70165747j,
         0.        +0.j        ,  0.79832728-0.86918395j]])
```

by using lists of all possible combinations of m and the two polarizations, which are indexed with 0 and 1. In the result array, we can observe the non-mixing of modes with opposite helicity, which result in the entries containing the value zero. Most of the additional functions in Table 4.2 behave similarly when called with scalar or array-like arguments.

We conclude the overview of the implemented low-level functions here and refer to the online documentation of all individual functions (`https://tfp-photonics/github.io/treams`). In summary, these functions are implementations of the mathematical expressions derived in the previous chapters. They form the basis of the high-level classes and their methods.

4.2.2 High-level classes and methods

While the low-level functions, in principle, cover all mathematical capabilities of *treams* using only them can be tedious and error prone. Thus, we add another interface to simplify their use. For the final T-matrix and S-matrix classes, we combine two concepts: We introduce the class `PhysicsArray` that is intended to create “physics-informed” *numpy*-arrays and we define a class `Operator` to encode most of the transformations that can be applied to expansions in vector spherical, cylindrical, and plan wave basis sets and, thereby, T- and S-matrices. The class `PhysicsArray` keeps track of physical quantities associated with it, such as the wave number associated with the coefficients it holds. The class `Operator` is intended to replicate the way in which operators are symbolically used in mathematical text. These concepts are accompanied by a range of additional data structures for, e.g., basis sets, material parameters, or lattices. In the following, we first explain the class `PhysicsArray`, and we shortly summarize the ancillary classes for lattices, wave numbers, basis sets, and material parameters. Then, we introduce the class `Operators` and, finally, show how the different parts work together to create the classes for the T- and S-matrices.

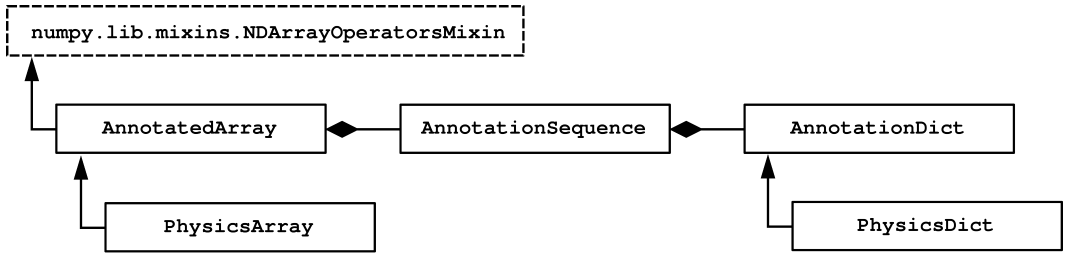

Figure 4.2: Inheritance and composition of `AnnotatedArray` and `PhysicsArray`. The class `AnnotatedArray` is an implementation of custom arrays that are interoperable with *numpy*-arrays, which is achieved through inheriting from `numpy.lib.mixinis.NDArrayOperatorsMixin` and further customizations for using *numpy*-universal functions on them. It keeps track of data annotations in a sequence of dictionaries `AnnotationDict` with one dictionary per array dimension. The child class `PhysicsArray` restricts the annotations to physical parameters as given in Table 4.3.

Two of the relevant concepts used to structure the relation of the different classes is inheritance and composition, which we show with diagrams using simplified elements of the unified modeling language [89], e.g., in Fig. 4.2. The different classes are shown as labeled boxes. Inheritance is used to create a new class based on a more general parent class. This relation is shown as an arrow pointing from the child class to the parent class. We use this, for example, to define the class `PhysicsArray` as a child of the general `AnnotatedArray`. Composition is used, when an instance of one class has an instance of another class as attribute. The owning class is shown with a diamond at the line connecting the composed class.

The class `PhysicsArray`

The class `PhysicsArray` implements functionality to have "physics-informed" *numpy*-arrays. This means that the class keeps track of relevant physical parameters and checks for compliant values, if one, for example, adds or multiplies two arrays. Such a check is useful in cases such as the transformation of the local to the global T-matrix as written in Eq. (2.57): Each row and column of the matrices $\mathbf{C}_{0,j}^{(1)}$ must refer to the correct values of l and m, the polarization, and the position. *treams* does not implement restrictions on the modes and their order, useful to change them, e.g., based on symmetry considerations [57]. Thus, that data needs to be annotated to the matrix. Figure 4.2 shows the inheritance structure of the class `PhysicsArray`. We start with the class `numpy.lib.mixins.NDArrayOperatorsMixin`, which is provided by *numpy*. It implements an interface to obtain comparison operations and arithmetic functions that behave identical to *numpy*-arrays. The class `AnnotatedArray` is used to provide the functionality of keeping track of annotated data. The annotated data is simply collected in a dictionary `AnnotationDict`. Since each dimension of an `AnnotatedArray` can hold its own set of annotations, we collect these dictionaries in a sequence. Now, we can use these annotations, as shown in the following example.

Listing 4.3: Example for using objects of the class `AnnotatedArray`

```
>>> m = AnnotatedArray([[1, 2], [3, 4]], x=("a", "b"))
>>> v = AnnotatedArray([5, 6], x="b")
>>> res = m @ v
>>> print(res)
[17 35]
>>> res.x
'a'
```

We create a two-by-two matrix with an annotations called `x`, holding the values `"a"` and `"b"` for its first and second dimension. We multiply it by a vector with annotation `x = "b"` for its only dimension. For the matrix multiplication, the annotations of the matrix' second dimension and the vector match and the result is a vector, where the annotations `x` is `"a"`. If the annotations do not match, a warning is given:

Listing 4.4: Example of a warning for non-matching annotations

```
>>> v = AnnotatedArray([5, 6], x="b")
>>> w = AnnotatedArray([7, 8], x="c")
>>> res = v + w
AnnotationWarning: at index 0: overwriting key 'x'
>>> print(res)
[12 14]
```

However, by default the computation is still performed. We can also combine a *numpy*-array and an `AnnotatedArray`

Listing 4.5: Example for using `AnnotatedArray` with *numpy*-arrays

```
>>> AnnotatedArray([5, 6], x="b") * np.array([-1, 2])
AnnotatedArray(
    [-5, 12],
    AnnotationSequence(AnnotationDict({'x': 'b'})),
)
```

The *numpy*-array is treated like an `AnnotatedArray` without annotations. The lack of a correspondingly named annotation does not lead to a warning, only contradicting values. In practice, these warnings are intended to notify the user about non-matching parameters, e.g., matrices which are computed for different wave numbers.

The class `AnnotatedArray` is not specifically aimed at arrays containing physics-related quantities. This property is implemented in the child class `PhysicsArray`, where the number of annotations is limited to a fixed set with well-defined properties. Those properties are listed in Table 4.3. The same parameters are also used as arguments to use the class `Operators`. While a detailed discussion of these operators follows below, we want to remark that they are also composed with the class `PhysicsArray` after being wrapped as `OperatorAttribute`, as shown in Fig. 4.3. The type of these parameters is restricted to the seven quantities listed in Table 4.3: The basis set definition in `basis`, especially the information about which modes are included, the definition of the lattice geometry in `lattice`, the wave vector parallel to this lattice in `kpar`, and the definition of the material

Table 4.3: Parameters used in *treams* for annotating objects of the class `PhysicsArray`

Name	Description	Type
`basis`	Definition of the basis set and its modes	`BasisSet`
`k0`	Vacuum wave number	float
`kpar`	Tangential wave vector	`WaveVector`
`lattice`	Lattice definition	`Lattice`
`material`	Material parameters	`Material`
`modetype`	Mode type specification	string
`poltype`	Polarization (parity or helicity modes)	string

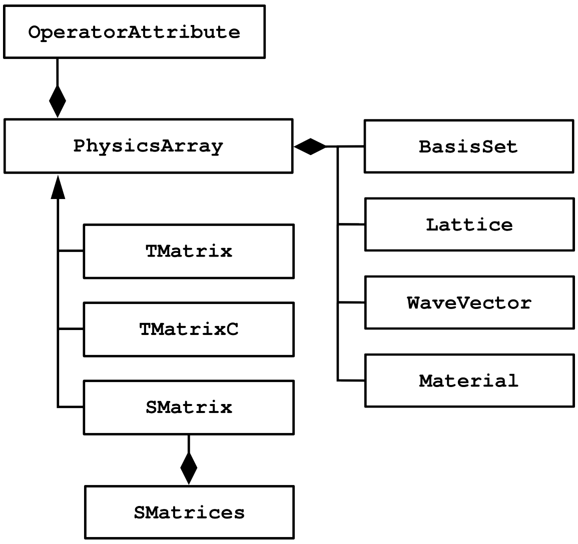

Figure 4.3: Compostion of `PhysicsArray` and its child classes. The class `PhysicsArray` stores a *numpy*-array and combines it with a range of physical parameters as listed in Table 4.3. As shown, four of these parameters, which have custom classes, are part of the class `PhysicsArray` by composition. Furthermore, they are used for a range of `Operators` that are composed with the `PhysicsArray` wrapped as `OperatorAttribute`. The three specialized classes `TMatrix`, `TMatrixC`, and `SMatrix` are derived from `PhysicsArray`. They are the main objects to describe the scattering in the vector spherical, cylindrical, and plane wave basis in *treams*. To completely describe a stratified structure, we combine four S-matrices (see Eq. (2.92)), stored in the class `SMatrices`.

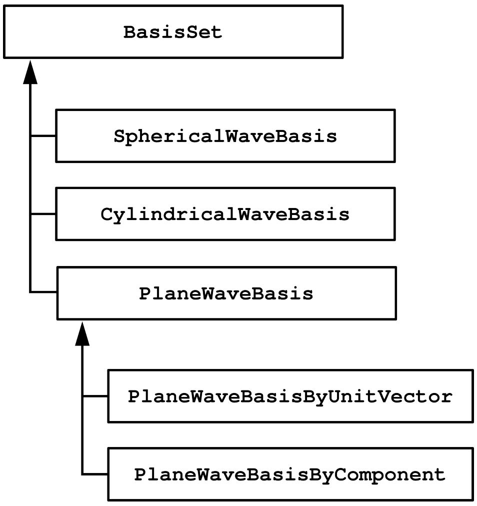

Figure 4.4: Inheritance structure of different types of basis sets. All basis sets in *treams* inherit from the base class `BasisSet`. These are the classes `PlaneWaveBasis`, `CylindricalWaveBasis`, and `SphericalWaveBasis`, corresponding to the solutions defined in Subsection 2.1.3. The plane wave basis is further subdivided to separate the two cases, if the plane wave is defined by the normalized wave vector $\hat{\boldsymbol{k}}$ or by the two components of $\boldsymbol{k}_\parallel$.

parameters in `material` are defined in custom classes to ensure they obey physical restrictions. The vacuum wave number is physically a real-valued number, so represented by a floating point number in `k0`. Lastly, the polarization type `poltype` specifies the use of the helicity or parity modes and the type of mode used, e.g., to differentiate the singular or regular vector spherical waves, is defined in `modetype`.

A short overview of the ancillary classes is given below.

Basis sets The class `BasisSet` contains the indices of the modes and defines their order. Thereby, they can be used to index each individual entry of a vector. For example, for spherical waves those are the values of l, m, and an index for the polarization. Moreover, a local basis can be defined, where additionally an index for the position of the wave's origin is used.

Listing 4.6: Example for spherical wave basis definitions

```
>>> treams.SphericalWaveBasis.default(2)
SphericalWaveBasis(
    pidx=[0 0 0 0 0 0 0 0 0 0 0 0 0 0 0 0],
    l=[1 1 1 1 1 1 2 2 2 2 2 2 2 2 2 2],
    m=[-1 -1  0  0  1  1 -2 -2 -1 -1  0  0  1  1  2  2],
    pol=[1 0 1 0 1 0 1 0 1 0 1 0 1 0 1 0],
    positions=[[0. 0. 0.]],
)
>>> positions = [[0, 0, 1.5], [0, 0, -1.5]]
>>> treams.SphericalWaveBasis.default(1, 2, positions)
SphericalWaveBasis(
    pidx=[0 0 0 0 0 0 1 1 1 1 1 1],
    l=[1 1 1 1 1 1 1 1 1 1 1 1],
```

```
    m=[-1 -1  0  0  1  1 -1 -1  0  0  1  1],
    pol=[1 0 1 0 1 0 1 0 1 0 1 0],
    positions=[[ 0.   0.   1.5], [ 0.   0.  -1.5]],
)
```

The example above shows both cases. First, the spherical wave basis up to the multipole order $l_\text{max} = 2$. Second, the spherical wave basis for only dipoles, but in a local description as indicated by giving two different positions. The base class `BasisSet` is the parent class for different implementations as shown in Fig. 4.4. They are the classes for `SphericalWaveBasis`, which is used in the example above, and the `CylindricalWaveBasis`. The third child class `PlaneWaveBasis` is further subdivided into two separate classes `PlaneWaveBasisByUnitVector` and `PlaneWaveBasisByComponent` to separate the case of using $\hat{\boldsymbol{k}}$ from using $\boldsymbol{k}_\parallel$ to index different modes as described in Subsection 2.1.3.

Material parameters The material parameters are stored as relative permittivity, relative permeability, and the chirality parameter. The class `Material` is used for convenience, to quickly convert between the description of a medium with the aforementioned parameters and other frequently used descriptions, most importantly, the refractive index and the relative impedance.

Lattice The lattice geometry is stored in the class `Lattice`. It can be used for one-, two-, and three-dimensional lattices. Similar to the case of material parameters, it is mainly used to conveniently create frequently used geometries, e.g., hexagonal lattices.

Listing 4.7: Example use of the class `Lattice`

```
>>> treams.Lattice.hexagonal(2)
Lattice([[2.         0.        ]
         [1.         1.73205081]], alignment='xy')
>>> treams.Lattice.hexagonal(2) | treams.Lattice(3, "z")
Lattice([[2.         0.         0.        ]
         [1.         1.73205081 0.        ]
         [0.         0.         3.        ]], alignment='xyz')
```

As shown, it is also possible to combine multiple lattices in a simple manner, which is convenient, if a structure is built in a step-by-step process from multiple lower dimensional lattices, for example as we do later in the example of Fig. 4.8.

Wave vector The wave vector components tangential to the lattice are stored in a separate class to keep track of which Cartesian components of the wave are fixed.

The class `Operators`

The seven parameters from Table 4.4 are also important for using the class `Operator`. The core idea of the class `Operator` is to translate the way how transformations, such as the rotation of a matrix $\mathbf{M}$, are written mathematically, namely

$$\mathbf{R}_z(\varphi)\mathbf{M}\mathbf{R}_z^{-1}(\varphi)\,, \tag{4.1}$$

to a similar representation in a script using *treams*. In Eq. (4.1), $\mathbf{R}_z(\varphi)$ is the abstract representation of the rotation operator for a rotation by the angle φ about the z-axis.

Table 4.4: Operators in *treams*

Name	Description
Rotate	Rotation coefficients for the different basis sets according to Eqs. (2.66), (2.69), and (2.70)
Translate	Translation coefficient along a specified vector, as given in Eqs. (2.53), (2.54), and (2.71)
Permute	Permutation of the labels of the Cartesian axis (see Appendix K)
Expand	Expand the description of the electric field in a different basis or at a different position
ExpandLattice	Similar to `Expand` but assuming periodic boundary conditions
ChangePoltype	Switch between parity and helicity basis
FieldOperator	Parent class to further operators evaluating the fields, e.g., the electric field, at specified coordinates

However, the concrete action of the operator depends on the contents of the matrix $\mathbf{M}$ and related physical parameters. For example, the abstract operator behaves differently, if the matrix contains coefficients for an expansion in the spherical, cylindrical, or plane wave basis, where we need to apply either Eq. (2.66), Eq. (2.69), or Eq. (2.70). Thus, the rotation depends on the definition of the class `BasisSet` for the matrix $\mathbf{M}$. This property can be defined in the annotations of the class `PhysicsArray`. However, to reduce the dependence of the class `Operator` on implementation details, such as the annotations added to the `PhysicsArray`, we simply require a corresponding attribute. For rotations, this is the basis set stored in `basis`. Then, we can use, e.g.,

Listing 4.8: Example use of the class `Operator`

```
1 >>> mat = treams.PhysicsArray(np.eye(6))
2 >>> mat.basis = treams.SphericalWaveBasis.default(1)
3 >>> rot = treams.Rotate(np.pi)
4 >>> rot @ mat @ rot.inv
5 PhysicsArray(
6 ...
```

to write Eq. (4.1) using *treams*. Note the similarity of line 4 with Eq. (4.1). We omit giving the whole output of the function in the listings here. If we directly need the transformation matrix for a particular basis, we can use

Listing 4.9: Direct evaluation of the operator

```
>>> rot(basis=treams.SphericalWaveBasis.default(1))
PhysicsArray(
...
```

For the class `PhysicsArray`, we also provide the operators wrapped as `OperatorAttribute`, which can be used as follows:

Listing 4.10: The class `Operator` as attribute

```
>>> mat.rotate(np.pi/3)
PhysicsArray(
```

```
...
```

This is equivalent to the example in Listing 4.8.

Besides the rotation operator, which we use in the example above, we implement also other common transformations. We list these operators in Table 4.4. The operator `Translate` translates the field, which is described by the coefficients in a particular basis, along a given vector. The classes `Expand` and `ExpandLattice` include the expansion of a given field in a different basis or at a different position, either without or with periodic boundary conditions. The class `ChangePoltype` can be used to change between parity and helicity basis. The operator `Permute` has a special role in *treams*. Due to the use of different alignments of the lattices with respect to the Cartesian axes, it can become necessary to permute the labels of the axes. The most important case, when this becomes necessary, are cylindrical waves in a one-dimensional array. The definition of the cylindrical waves that is used results in a periodicity in the z-direction and the one-dimensional lattice of the cylindrical waves is conventionally placed along the x-axis. However, we usually describe systems with periodicity in two dimensions with the lattice vectors lying in the x-y-plane. Hence, the labels must be permuted according to the procedure detailed in Appendix K. The last class of operators are used to evaluate the field expansion at specified coordinates $\boldsymbol{r}$ to obtain the electric $\boldsymbol{\mathcal{E}}(\boldsymbol{r}; k_0)$, the magnetic field $\boldsymbol{\mathcal{H}}(\boldsymbol{r}; k_0)$, the displacement field $\boldsymbol{\mathcal{D}}(\boldsymbol{r}; k_0)$, the magnetic flux density $\boldsymbol{\mathcal{B}}(\boldsymbol{r}; k_0)$, or the Beltrami fields $\boldsymbol{\mathcal{G}}(\boldsymbol{r}; k_0)$ or $\boldsymbol{\mathcal{F}}(\boldsymbol{r}; k_0)$ (see Appendix D).

The combination of the properties of an `AnnotatedArray` for the predefined set of parameters as listed in Table 4.3 with the operators of Table 4.4 makes the `PhysicsArray` "physics-informed". The `PhysicsArray` is used in *treams* to store the data, e.g., of a plane wave and its expansion into a spherical wave basis.

Listing 4.11: Plane wave expansion in spherical waves

```
1  >>> plw = treams.plane_wave([2, 3, 6], 1, k0=7, material=(1,))
2  >>> treams.Expand(treams.SphericalWaveBasis.default(1)) @ plw
3  PhysicsArray(
4      [ 3.64911124e-01-0.24327408j,  0.00000000e+00+0.j        ,
5       -1.36932032e-16-2.23626979j,  0.00000000e+00+0.j        ,
6       -4.74384461e+00-3.16256307j,  0.00000000e+00+0.j        ],
7      basis=SphericalWaveBasis(
8      pidx=[0 0 0 0 0 0],
9      l=[1 1 1 1 1 1],
10     m=[-1 -1  0  0  1  1],
11     pol=[1 0 1 0 1 0],
12     positions=[[0. 0. 0.]],
13 ),
14     k0=7.0,
15     material=Material(1, 1, 0),
16     modetype='regular',
17     poltype='helicity',
18 )
```

The created plane wave has the defined wave number and material parameters. A suitable basis set for the given wave vector and polarization is created automatically. In line 2, we can then simply use the operator `Expand` to expand the plane wave in the spherical wave basis.

The classes `TMatrix` and `SMatrices`

The classes `TMatrix`, `TMatrixC`, and `SMatrix`, that provide more specialized functionality, are derived form the `PhysicsArray`, as shown in Fig. 4.3. Due to all the preparatory work, where the class `AnnotatedArray` is responsible for warnings, the `PhysicsArray` is responsible for the validation of the parameters in Table 4.3, and since the operators in Table 4.4 are implementing most transformations, we can keep the definition of the class `TMatrix` shorter. It includes mostly specialized functions, e.g., to compute the T-matrix of a sphere. In the example below, we compute T-matrices for a sphere, a dimer of two spheres, and a two-dimensional array. We start by calculating the T-matrix for a chiral sphere with `TMatrix.sphere` in a chiral embedding.

Listing 4.12: T-matrix of a sphere and its average scattering and extinction cross-section

```
 1 >>> lmax = 3
 2 >>> k0 = 2 * np.pi
 3 >>> radius = 0.3
 4 >>> kpar = [0, 0]
 5 >>> mat = treams.Material(
 6 ...     epsilon=4 + 0.1j,
 7 ...     mu=1 + 0.1j,
 8 ...     kappa=0.5 + 0.05j,
 9 ... )
10 >>> embedding = treams.Material(epsilon=1.2, kappa=0.1)
11 >>> sphere = treams.TMatrix.sphere(lmax, k0, radius, [mat, embedding])
12 >>> sphere.xs_sca_avg, sphere.xs_ext_avg
13 (0.5523124393002752, 0.8150074754351935)
```

We compute in line 12, as example, the rotation and polarization average of the scattering and extinction cross-section [23]. We can also define a plane wave and calculate the cross-sections for a particular illumination, for which we use the method `TMatrix.xs`.

Listing 4.13: Polarization-dependent cross-section of a chiral sphere

```
1 >>> minus = treams.plane_wave(kpar, 0, k0=k0, material=embedding)
2 >>> plus = treams.plane_wave(kpar, 1, k0=k0, material=embedding)
3 >>> sphere.xs(plus)
4 (0.7416545069275621, 1.1262954452171179)
5 >>> sphere.xs(minus)
6 (0.36297037167298807, 0.5037195056532691)
```

We first define plane waves with helicity plus and minus. The cross-sections calculated for both helicities in lines 4 and 6 give the average values above. The T-matrix of clusters of scatterers can be computed with `TMatrix.cluster`. We proceed our example by building a dimer structure made from two spheres.

Listing 4.14: Local T-matrix of a dimer

```
>>> positions = [[0, 0, -0.4], [0, 0, 0.4]]
>>> dimer = treams.TMatrix.cluster([sphere, sphere], positions)
>>> dimer_local = dimer.interaction.solve()
>>> dimer_local.xs(plus)
(0.8063538295616933, 1.361945075463769)
```

In line 2, we create the block-diagonal matrix $\mathbf{T}_{\text{diag}}$ introduced in Eq. (2.52). After solving the interaction problem in line 3, we obtain the T-matrix in the local basis. We compute the cross-sections for a positive helicity plane wave illumination directly in the local basis. We can also compute the cross-sections in the global basis, however, we need a higher multipolar order. Here, we expand the field in a global basis with maximal multipolar order 10 by using the correspondingly named operator.

Listing 4.15: Global T-matrix of a dimer

```
>>> dimer_global = dimer_local.expand(
...     treams.SphericalWaveBasis.default(lmax=10)
... )
>>> dimer_global.xs(plus)
(0.806332465067321, 1.3620440875499482)
```

As we see, the results for the local and global basis match to an extraordinary degree. Other transformations, such as rotations are equally possible. As example we use the operator in the form similar to Eq. (4.1).

Listing 4.16: Rotation of a T-matrix

```
>>> rot = treams.Rotate(0, np.pi / 2)
>>> treams.TMatrix(rot @ dimer_global @ rot.inv).xs(plus)
(1.4537126271649905, 2.249697110473253)
```

The dimer is perpendicular to the illumination now and has, therefore, different cross-sections. All these operations are similarly available for cylindrical T-matrices.

We can also compute the S-matrices for an array of those particles. A single object of the class `SMatrix` holds one of the blocks defined in Eq. (2.92) and derives from `PhysicsArray`. To fully describe a layer, we need four S-matrices with matching parameters. These are stored in the class `SMatrices`, which is composed of exactly four S-matrices. We can perform the transition from the T-matrix, where we solve now the interaction in a given lattice, by using Eq. (2.59).

Listing 4.17: Square array of chiral spheres

```
1 >>> square_lat = treams.Lattice.square(0.8)
2 >>> square = treams.SMatrices.from_array(
3 ...     sphere.latticeinteraction.solve(square_lat, kpar),
4 ...     plus.basis
5 ... )
6 >>> square.tr(plus)
7 (0.10257705043268761, 0.049281191151479914)
8 >>> square.tr(minus)
9 (0.6712023070848361, 0.04928119115147981)
```

This step is done in lines 2 to 5. The transmittance and reflectance can now be computed directly from the S-matrices.

Although this example is mostly showing how the different classes can be used and interact, it also shows a counter-intuitive result for chiral structures. Note that the reflectance of the array, consisting of chiral spheres in a chiral embedding medium is exactly the same for plane waves with positive and negative helicity as we see in the second entry in lines 7 and 9. This result can be explained by using the symmetry of the lattice and scatterers on the one hand and reciprocity on the other hand. The reflected wave from a non-diffracting structure with a at least three-fold discrete rotational symmetry, when illuminated with a plane wave of well-defined helicity under normal incidence, flips its helicity [90]. Thus, a plane wave with positive helicity has a reflected wave of pure negative helicity. By using reciprocity we find, that the opposite case of an incoming wave with negative helicity and a purely positive helicity reflected wave must have the same reflection coefficient.

This explanation can be tested numerically by using a rectangular lattice. Then, the rotational symmetry of the lattice is only two-fold instead of the four-fold rotational symmetry of the square lattice. Therefore, we expect different reflectance values.

Listing 4.18: Rectangular array of chiral spheres

```
>>> rectangular_lat = treams.Lattice.rectangular(0.81, 0.79)
>>> rectangular = treams.SMatrices.from_array(
...     sphere.latticeinteraction.solve(rectangular_lat, kpar),
...     plus.basis
... )
>>> rectangular.tr(plus)
(0.11170611461145395, 0.055004933348812145)
>>> rectangular.tr(minus)
(0.6646890023481664, 0.05074200890256325)
```

Indeed, we find, that this is the case. With this short step-by-step example, we conclude this section. The results for more complex examples are provided below and in Chapter 5. As for the low-level functionality, the high-level classes and methods are also documented online in more detail and with many additional examples.

4.3 Validation and benchmark

The program *treams* contains many functions and methods. The verification that each of them returns the correct result for the range of allowed argument values is a large part of the programming work. Furthermore, we need to validate that the different components also correctly interact with each other. On the level of the individual functions, *treams* contains a large testing suite, as we outline in Section 4.4, as part of the quality assessment and maintenance. Here, we want to provide examples, that include full simulations. These validation studies can be separated in two groups. First, we perform self-consistency checks for the various basis sets used in *treams*. Second, we perform direct comparisons with full wave solvers.

As self-consistency tests, we simulate periodic structures of spheres and infinitely long cylinders, because we can compute their scattering response analytically. Each of the examples has a complex unit cell to verify the correctness of the lattice sums and their use in the computation of the translation coefficients. Another important aspect of this simulation are the transitions between the different basis sets implemented in *treams*. The result of the computations are shown in Fig. 4.5. Each of the panels shows a three-dimensional graphics of the scattering structure in gray to indicate the simulated system and three mutually perpendicular cut planes through it. These planes show the real part of one selected component of the calculated electric field. Also, we indicate the transition between basis sets by black dotted lines. By showing the real part of the electric field,

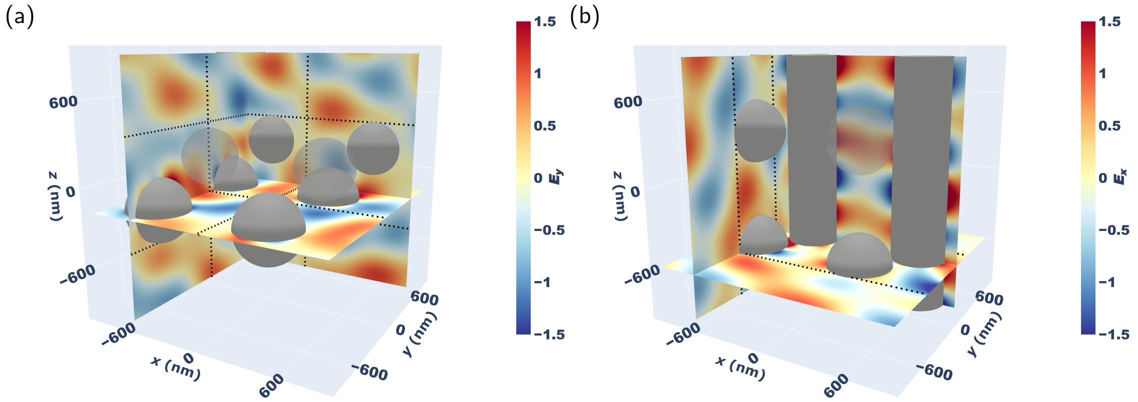

Figure 4.5: Electric field in example lattice structures with complex unit cells combining multiple domains of validity. We show one selected component of the electric field in each of the two examples. Within different regions of the structure different basis sets are used. Therefore, the data is spliced from different parts. The domains, where different expansions are used, are indicated by dashed lines. Panel (a) shows four unit cells of a two-dimensional lattice. Two spheres in each unit cell requires the expression for complex unit cells from Chapter 3. Between the spheres we use the spherical wave basis. Thus, the computation of each field value involves a lattice sum. In the region above and below the lattice, we can use the vector plane wave basis (see Fig. 2.5). Panel (b) shows two unit cells of a two-dimensional lattice in the x-z-plane. Each unit cell contains one cylinder and one chain of spheres. To solve the multi-scattering equations for this structure, we use the one-dimensional lattice sums for vector spherical waves for the chain, then, we use vector cylindrical waves to couple the cylinders and the chain in the second lattice direction, namely along the y-direction. Finally, we can compute the field values in front of and behind this structure using vector plane waves. Adapted from [S1].

an error or deviation in the definition of the complex electric field's phase would become visible.

Panel (a) shows a two-dimensional lattice containing two spheres with relative permittivity $\epsilon = -16 + 0.4\mathrm{i}$. In total four adjacent unit cells of the square lattice with pitch 900 nm are shown and the domain above and below the lattice. The spheres have the radii 225 nm and 195 nm and are separated by the distance vector $\boldsymbol{r} = (240\hat{\boldsymbol{x}} + 300\hat{\boldsymbol{y}} + 360\hat{\boldsymbol{z}})\,\mathrm{nm}$. They are illuminated by a plane wave with the wave vector $\boldsymbol{k} = \frac{2\pi}{600\,\mathrm{nm}}(\sin(\frac{\pi}{6})\cos(\frac{2\pi}{3})\hat{\boldsymbol{x}} + \sin(\frac{\pi}{6})\sin(\frac{2\pi}{3})\hat{\boldsymbol{y}} + \cos(\frac{\pi}{6})\hat{\boldsymbol{z}})$ and TE polarization. We solve the scattering problem using the T-matrices in the spherical wave basis up to order $l_{\max} = 4$. To compute the fields in the region between the spheres, we use the spherical wave basis. Thus, each point at which the field is evaluated requires a separate lattice sum. The electric field component is continuous at the boundary of two neighboring unit cells, confirming the correct implementation of the lattice sums, especially considering the vector $\boldsymbol{k}_\parallel$, which defines the phase relation of the unit cells. The region above and below this lattice can be described in the plane wave basis, which is much more efficient for the evaluation of the fields. At the transition from the domain, where we use the spherical wave basis, to the domain, where we use the plane wave basis, there is also no discontinuity visible.

Panel (b) shows examples using the one-dimensional lattice sums of spherical waves and one-dimensional lattice sums of cylindrical waves to, in total, describe a two-dimensional periodic structure. Instead of the alignment of the lattice with the x-y-plane, we align it here with the x-z-plane. The calculation of the interaction is, essentially, a three step procedure. First, we consider the spheres in the spherical wave basis. In this basis, we calculate their interaction, which involves the one-dimensional lattice sum along the z-axis. The result can be converted to a cylindrical T-matrix. Second, we use the cylindrical T-matrix of the chain and the cylindrical T-matrix for the infinitely long cylinder to calculate their interaction in the cylindrical wave basis. Finally, similar to the procedure for panel (a), we transition to a plane wave description in front of and behind the lattice. Analogously to the computation of the interaction, we also divide the computational domain to calculate the values of the electric field. Between the spheres, only the spherical wave description is valid. Next, between the cylinder and the chain, we use the cylindrical wave basis. These separations are again indicated by dotted lines. Panel (b) also shows no discontinuity between different domains.

While the tests of the calculation in the various different basis sets confirms the consistency of the different approaches within *treams*, we also test it against an independent solution. Moreover, some aspects of the complete functionality of *treams* are not covered so far. This includes, the use of a non-zero chirality parameter, T-matrices for non-spherical particles, and the implementation of planar interfaces, which will all be covered in the next tests.

These comparison tests are also intended to benchmark the speed of calculating solutions with *treams* in comparison to general purpose solvers for Maxwell's equations. Therefore, we also report the computation times. Note, however, that the examples compare mostly the field values close to the scatterers, which is a computationally expensive operation in *treams* for values inside a lattice, because it essentially means, going from the efficient description in an analytical basis set to numerical values. Nevertheless, the computation of the electric field between particles in a lattice benefits greatly from the fast evaluation of the lattice sums as shown in Fig. 3.3 panel (f).

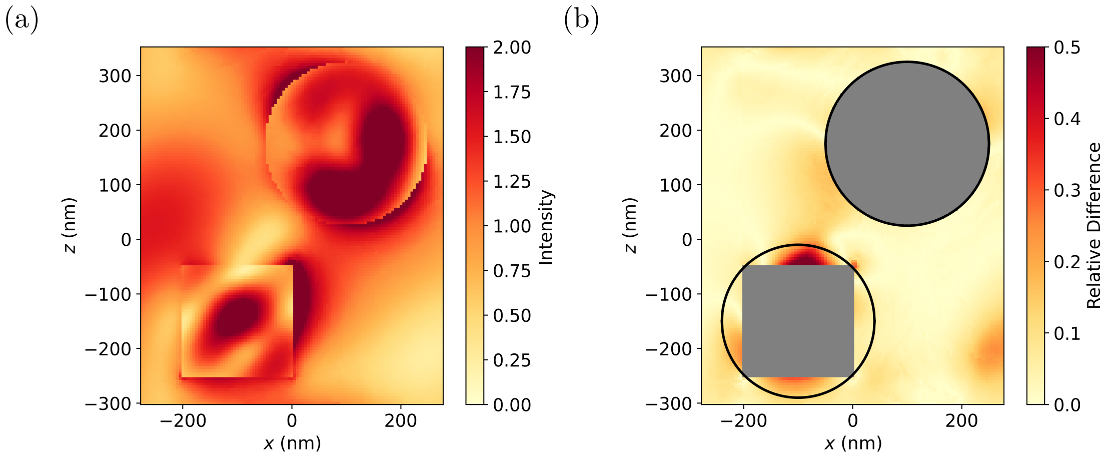

Figure 4.6: Comparison of *treams* with finite-element calculation for a one-dimensional lattice in the spherical wave basis. Panel (a) shows the field intensity obtained with the finite-element method on a cut plane through the unit cell, which is periodically repeated in the z-direction. The unit cell contains a cylinder, which appears as square, and a chiral sphere. Panel (b) shows the relative difference between the finite-element method result and *treams*. The objects are shown as gray areas and the circumscribing spheres are indicated in black.

We compute the T-matrix for the disk, that is used in the examples, with the software JCMsuite, which uses the finite-element method to compute the electromagnetic scattering. The computation of the T-matrix for a single frequency takes 40 s for the solution up to the multipole order $l_{\max} = 3$. The computation in the case of rotationally symmetric particles can be done using a two-dimensional domain. Thus, the solution can be computed with a very fine mesh in comparison to full three-dimensional lattices. The disk has a radius of 100 nm and a height of 200 nm. The relative permittivity is set to $\epsilon = 11$. The T-matrix of the sphere is computed to the order $l_{\max} = 4$ for a chiral sphere with relative permittivity $\epsilon = 3.5 + 0.1\mathrm{i}$, relative permeability $\mu = 2.5 + 0.1\mathrm{i}$, and chirality parameter $\kappa = 0.1 + 0.05\mathrm{i}$. The structure is illuminated by a circularly polarized plane wave with wave vector $\boldsymbol{k} = \frac{2\pi}{600\,\mathrm{nm}}(\sqrt{\frac{3}{8}}\hat{\boldsymbol{x}} + \sqrt{\frac{3}{8}}\hat{\boldsymbol{y}} - \frac{1}{2}\hat{\boldsymbol{z}})$ and positive helicity. The reference simulations are done using the finite-element method with the commercially available program COMSOL Multiphysics. We use a custom alteration of the constitutive relations to include chiral material parameters in COMSOL Multiphysics [91]. We compare the absolute values of the electric fields at each point in the domain, normalized to their sum to get a measure of their relative accuracy.

Figure 4.6 shows the example of a one-dimensional lattice. The cylinder and the sphere form a complex unit cell, which is periodic in the z-direction with the pitch 650 nm. Panel (a) shows the electric field intensity in the unit cell in the x-z-plane computed with COMSOL Multiphysics. The relative difference to *treams* is shown in panel (b). In the region between the particles, we need to compute the fields using the lattice sums. Although the lattice sums are accelerated considerably in comparison to a direct approach, this is computationally expensive in comparison to solving the problem. At the left and right

Table 4.5: Comparison of COMSOL Multiphysics and *treams* computation timings. All times are given in seconds. The computation of the T-matrix with JCMsuite took 40 s.

Figure	COMSOL Multiphysics	*treams*	
		solution	field evaluation
4.6	211	0.5	160
4.7	115	0.2	37
4.8	291	2.0	194

border of panel (b), we can use the cylindrical wave expansion. Besides being considerably faster, this also improves the region of convergence. The black circles show the sizes of the circumscribing spheres of both objects. For the cylinder, the regions below and, especially, above it show deviations between both approaches. This is an expected behavior, because in that region neither the expansion in spherical nor in cylindrical waves is valid. However, on the sides of the cylinder, we benefit from the cylindrical wave expansion not only by the faster computation times but also from the altered computational domains (see Fig. 2.5). We also find a region in the bottom right corner of panel (b) which shows a larger relative difference between both approaches. However, this deviation is likely an artifact of the low field values, which are visible in panel (a).

The solution with COMSOL Multiphysics takes, as given in Table 4.5, 211 s, the solution with *treams* only 0.5 s. Even if the time for computing the T-matrix is included, the total time for the calculation is smaller. Furthermore, each variation of the lattice constant or illumination direction or polarization does not require a recalculation of the T-matrix. However, the evaluation of the electric field takes comparably long with 160 s, because for each value in the near filed the lattice sums have to be computed. For regions, where the one-dimensional chain can be described by cylindrical waves, this limitation does not apply.

In the example of Fig. 4.7, we use the same cylinder and sphere, but in a two-dimensional array that is placed in the x-y-plane. We simulate a honeycomb lattice with the cylinders on one hexagonal sublattice with lattice constant 650 nm and the spheres on the second hexagonal sublattice of the same lattice constant. Both sublattices are shifted with respect to each other by $\frac{650\,\mathrm{nm}}{\sqrt{3}}$. The centers of the scatterers are at different heights, thus, requiring again lattice sums for $\boldsymbol{r}_\perp \neq 0$. The scatterers are placed on a slab with relative permittivity $\epsilon = 6 + 0.1\mathrm{i}$, $\mu = 1.5 + 0.1\mathrm{i}$, and $\kappa = 0.1 + 0.08\mathrm{i}$. Its thickness is 100 nm.

Figure 4.7 shows the intensity in panel (a) and the relative difference of COMSOL Multiphysics and *treams* in panel (b). We find a very good agreement between both methods, besides the region within the circumscribing sphere of the cylinder. We note that the region below the cylinder immediately on top of the slab is represented correctly. This is a result of the transition to a plane wave expansion for computing the coupling of the honeycomb lattice with the slab. Thereby, we can benefit from the different region of convergence. This approach is used for finite clusters also in Smuthi [80]. The spot around $x = -100\,\mathrm{nm}$ and $z = -200\,\mathrm{nm}$ is likely a result of the low overall intensity that causes the large relative difference. The computation times show a similar pattern as for the first example.

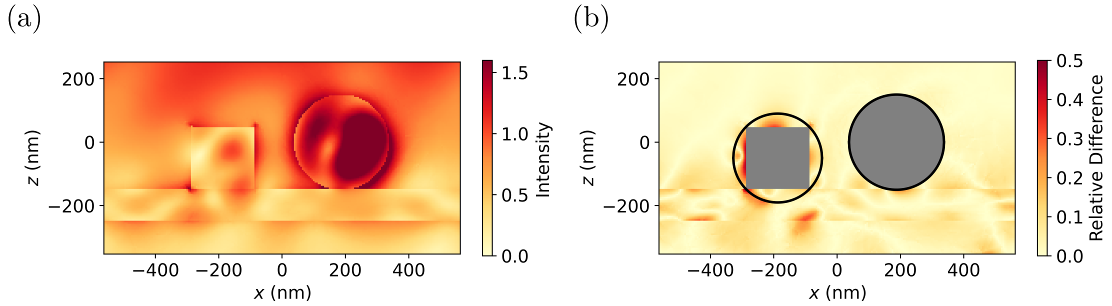

Figure 4.7: Comparison of *treams* with finite-element calculation for a two-dimensional lattice using the spherical wave basis. Panel (a) shows the field intensity obtained with the finite-element method on a cut plane through the unit cell, which is periodically repeated in the x-direction. The unit cell contains a cylinder, which appears as square, and a chiral sphere. Panel (b) shows the relative difference between the finite-element method result and *treams*. The objects are shown as gray areas and the circumscribing spheres are indicated in black.

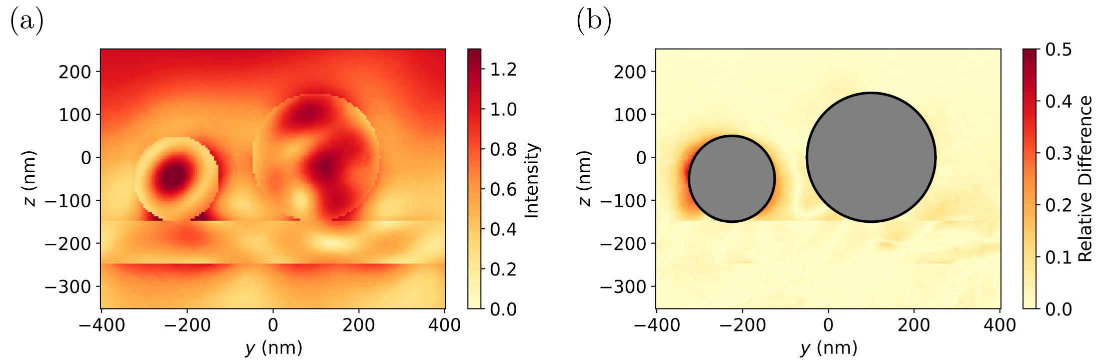

Figure 4.8: Comparison of *treams* with finite-element calculation for a one-dimensional lattice using the cylindrical wave basis. Panel (a) shows the field intensity obtained with the finite-element method on a cut plane through the unit cell, which is periodically repeated in the y-direction. The unit cell contains a chain of cylinders of finite length, which appears as the smaller circle, and a chiral infinitely long cylinder. Panel (b) shows the relative difference between the finite-element method result and *treams*. The objects are shown as gray areas and the circumscribing cylinders are indicated in black.

The last example, shown in Fig. 4.8, is aimed at testing one-dimensional lattices in the cylindrical wave basis. Instead of the sphere used in the previous examples, we have an infinitely long cylinder with 150 nm radius. The other object in the unit cell is a chain of the cylinder with 100 nm radius. The pitch of that chain is 350 nm. We place the infinitely long cylinder and the chain next to each other with a distance of 325 nm on the same slab as in the example for Fig. 4.7. This unit cell is repeated periodically with a lattice constant of 800 nm.

This example tests, in particular, the computation of the coefficients for the scattering from the chiral cylinder, the one-dimensional lattice sums, and the permutation of the axes' labels. The coupling of the cylinders is computed in the x-z-plane. Then, to include the slab, we change the labels such that it lies in the x-y-plane. We find a good agreement of *treams* with the finite-element method result and also similar computation times as in the previous examples.

We conclude that *treams* can solve scattering problems highly efficiently. The combination of the different basis sets is possible seamlessly. Also, we find very good agreement with results computed with the finite-element method, even for complicated systems that also include chiral matter. The solution times using *treams* are drastically reduced by roughly two orders of magnitude in comparison to finite-element methods.

4.4 Quality assessment and maintenance

As a program with a wide range of functions and intended for a wide audience of scientific users, we implemented multiple measures to track, maintain, and, in perspective, further improve the code quality and the infrastructure around the code. These measures make *treams* also compliant with the FAIR data principles: findable, accessible, interoperable, and reusable [92].

The full software development was assisted using the version control software *git*. Thus, all changes and additions to the code during the development are tracked. The repository is published on the widely used platform Github (`https://github.com/tfp-photonics/treams`). Moreover, we use continuous integration to automatically compile new versions and package them to be uploaded to the Python Package Index. An article describing *treams* is submitted to a dedicated journal for scientific code for publication [S1]. Additionally, the program is listed on the platform `https://helmholtz.software/software/treams` for research software. Thereby, we increase the findability of *treams*.

To improve the accessibility of the code, we have an extensive dedicated documentation of the software (`https://tfp-photonics/github.io/treams`). Besides installation instructions and dedicated information for developers, the documentation includes many examples and a detailed reference describing its functions and classes. The documentation uses the software *sphinx* to extract the documentation from the source code. It is automatically updated for newer versions with continuous integration. The publication of the full source code under the permissive MIT license makes *treams* also legally accessible.

The implementation of *treams*, which is described in detail in this chapter, is intended to be interoperable, e.g., by using the interfaces for arrays provided by *numpy* and by also implementing many functions as *numpy*-universal functions. Also, the modularization of *treams* encourages reusing functions, and the MIT license permits such reuse.

In addition to these measures that provide *treams* under the FAIR data principles to the scientific community and the public, we further use several approaches to ensure the quality and correctness of the code. These include foremost the many implemented tests for the functions and classes of *treams* using the package *pytest*. Continuous integration methods are used to automatically run these tests for each change of the code and report the coverage, i.e., the percentage of executed code lines by the test.

In conclusion, this chapter gave an overview of *treams*. We provided an outline of the general considerations in the development of *treams* in Section 4.1. We describe the structure and different components in detail in Section 4.2. While the low-level functions provide full control of the computations to users, another interface to the functionality of *treams* is provided with several different classes. These include the class `Operator` to represent transformations, such as those defined mathematically in Subsection 2.2.3, the class `PhysicsArray` to combine the numerical array with physical properties, and the classes `TMatrix`, `TMatrixC`, and `SMatrices` derived from `PhysicsArray` to provide specialized objects for T-matrices with a spherical or cylindrical wave basis and S-matrices for the plane wave basis. We showed the properties of these classes in several examples. In Section 4.3, we studied the results computed by *treams* and, thus, validated the correct implementation and integration of its various parts. Finally, we outlined the actions taken to maintain and improve the quality of the code and its compliance with the FAIR data principles, such that *treams* is useful for its audience.

5 | Applications of the T-matrix and plane wave methods

This chapter is dedicated to highlight several applications of the T-matrix, S-matrix, and transfer matrix methods described in the previous chapters to highlight the capabilities of *treams*. These applications emerged in close collaboration with different researchers as stated in the beginning of each section. The first example, in Section 5.1, discusses the enhancement of the optical rotation, which is one measurable quantity to characterize the interaction of light with chiral materials. Another related quantity is circular dichroism. We investigate structures to enhance optical rotation based on ideas previously used to investigate circular dichrosim. In Section 5.2, we calculate the focal spot properties in different setups for multi-photon direct laser writing [93, 94]. Section 5.3 describes how *treams* can be used as part of a multi-scale modeling workflow for molecular arrays, and Section 5.4 shows the application of *treams* to homogenize photonic materials by assigning effective material parameters to them.

5.1 Helicity preserving cavities for optical rotation enhancement

The first application revolves around the enhancement of optical rotation in helicity preserving cavities. This work was published in [P2]. The enhancement of the optical rotation is an extension to the work on similar helicity preserving cavities designed to enhance the circular dichroism [P6, P15].

The starting point for that research was the appreciation that many molecules, especially for biochemical or pharmaceutical applications [95], are geometrically chiral. Thus, it is not possible to superimpose such a molecule with its mirror image by any means of rotation or translation. Molecules that have the same chemical structure but differ in their chirality, sometimes also denoted as handedness, are called enantiomers. The distinction of enantiomers is important for many applications because biochemical interactions often show a preference for one particular enantiomer due to the lock-and-key principle [96], for example, in enzymatic reactions. However, chemical reactions are usually not sensitive to chirality, so they cannot be used to distinguish different enantiomers, neither during synthesis nor in sensor applications. A possibility to distinguish different enantiomers are methods based on special physical properties, such as their interaction with chiral light. We can exploit that the geometrical chirality usually also results in an electromagnetic chirality, even though, there is not a one-to-one mapping of geometrical and electromagnetic chirality [P7, 97]. The electromagnetic chirality measures how different the interaction of light with opposite helicity with the molecule is. We can measure the electromagnetic chirality by probing the response of the molecules to light of well-defined helicity. For a dense arrangement of molecules, the electromagnetic chirality manifests in the phenomenological description using material parameters as a non-zero value for the chirality parameter $\kappa(k_0)$. The main challenge in measuring the chirality parameter is its small value [98, 99]. For example, the vibronic resonances of molecules are in the infrared frequency range [99]. The size of the molecule, however, is much smaller than the wavelength leading to small chiral effects.

The chirality parameter can be measured by its influence on circular dichroism and optical rotation. Both quantities, circular dichroism and optical rotation, are phenomena to express the different interaction of matter with light of opposite helicity. The circular dichroism is the differential absorption of positive and negative helicity waves, and the optical rotation is the difference in phase accumulation. The optical rotation is usually observed as the rotation of the polarization plane of a linearly polarized plane wave, which is a superposition of positive and negative helicity plane waves. For the purpose of this investigation, we define the optical rotation as

$$\mathrm{OR} = \frac{1}{2} \arg(E_+ \cdot E_-^*)\,, \tag{5.1}$$

where $E_\pm$ is the complex electric field coefficient after passing through the chiral medium for positive or negative helicity plane waves. In a homogeneous medium, we can associate the optical rotation with the difference in the real part and the circular dichroism with the difference in the imaginary part of the wave numbers $\sqrt{\epsilon(k_0)\mu(k_0)} \pm \kappa(k_0)$ for light of positive and negative helicity. Thus, they probe essentially the real and imaginary part of the chirality parameter $\kappa(k_0)$, analogously to the relation of phase accumulation and absorption with the real and imaginary part of the wave number in an achiral medium. However, the circular dichroism or optical rotation signal and, thereby, the chirality parameter is often not measured in a homogeneous bulk but by using additional structures, that enhance the signal. Hence, the assumption of a homogeneous medium is no longer applicable, and a simple mapping of optical rotation and circular dichroism on the one hand and real and imaginary part of the chirality parameter $\kappa(k_0)$ on the other hand is not possible. As already stated in Subsection 2.1.2, the real and imaginary part of $\kappa(k_0)$ are related by Kramers-Kronig relations, so the full spectrum of the dispersive media parameter contains redundant information. However, the real and reciprocal part of the complex $\kappa(k_0)$ in a finite range of frequencies contain complementary information and can, thus, be combined to provide a more complete picture of the measured sample.

In our model, we assume the molecules are in a solution that surrounds the chirality signal enhancing structures. The purpose of this structure is the creation of a strong chirality density to increase the sensitivity on the chirality parameter. We define the chirality by

$$C(\boldsymbol{r}; k_0) = \frac{|\boldsymbol{G}_+(\boldsymbol{r}; k_0)|^2 - |\boldsymbol{G}_-(\boldsymbol{r}; k_0)|^2}{C_0}\,, \tag{5.2}$$

where we normalize the value to the chirality density of a circularly polarized plane wave C_0 in vacuum. Although many chiral structures that generate a strong chirality density have been proposed [100–108], it is difficult to separate the signals originating from the enhancing structure from the signals that originate from the solution. Therefore, achiral structures are beneficial in many sensing applications [109–123]. Based on designs to enhance the circular dichroism [P6, P15] we use silicon cylinders arranged in a hexagonal array to enhance the optical rotation. Our investigation includes a single array of such

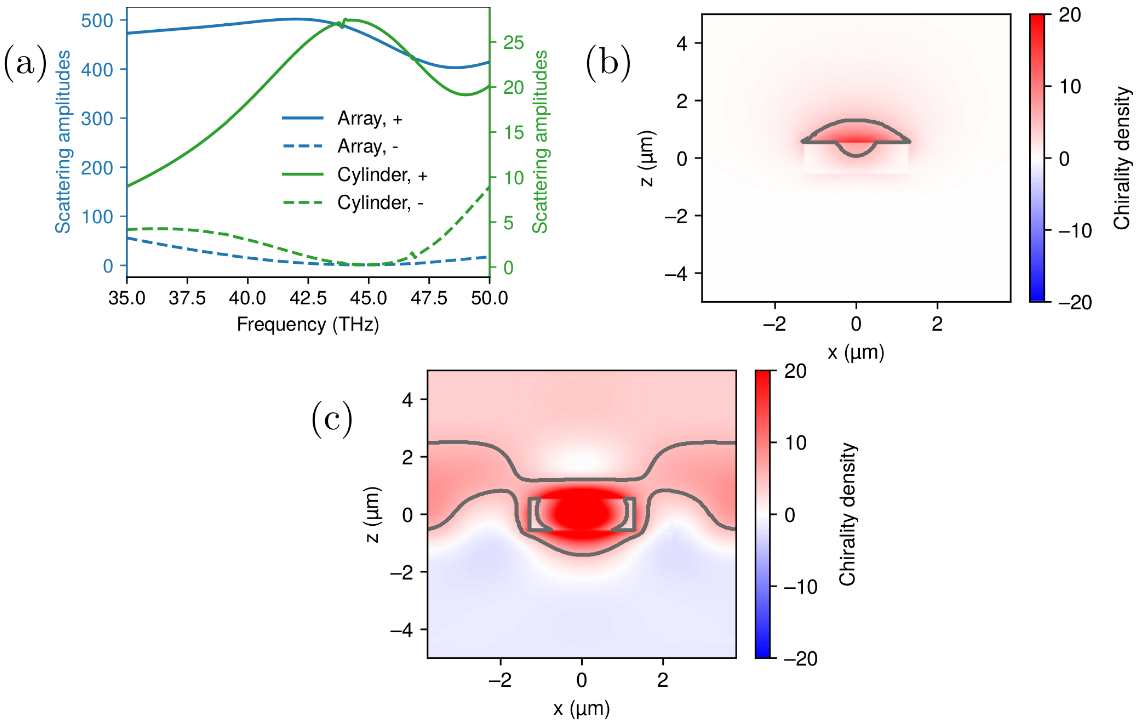

Figure 5.1: Scattering from a single cylinder and a cylinder array under plane wave illumination of positive helicity. Panel (a) shows the sum of the squared absolute values of the scattering coefficients for an illumination with plane waves of positive helicity. The solid lines show the sum for the positive helicity coefficients and the dashed lines the sum for the negative helicity coefficient. In blue, we show the values for the array and in green for the single cylinder. Note the different scales of these amplitudes. Panel (b) shows the local chirality density for the single cylinder, and panel (c) shows it for the cylinder in a hexagonal array. The gray contours indicate the area, where the chirality density exceeds the value of 5. Reprinted with permission from [P2]. Copyright 2021 AIP Publishing.

cylinders and a cavity formed by stacking two of these arrays and, thereby, forming a cavity. The relative permittivity of the cylinders is approximated by the non-dispersive value $\epsilon = 11.9$, and we set the height to 1082 nm. The radius of the cylinder is taken as optimization parameter.

We model the chiral material parameters with a Lorentzian resonance. The resonance is placed in the infrared at the angular frequency $\bar{\omega} = 2\pi \cdot 44.21\,\mathrm{THz}$ and has a width of $\gamma = 0.258\,\mathrm{THz}$ [P15]. The dispersive functions for the relative permittivity, relative permeability, and the chirality parameters are

$$\epsilon(k_0) = \epsilon_{\mathrm{sol}} + \frac{A\epsilon_{\mathrm{sol}}}{1 - \frac{c^2 k_0^2}{\bar{\omega}^2} - \mathrm{i}\frac{c\gamma k_0}{\bar{\omega}^2}} \tag{5.3a}$$

$$\mu(k_0) = 1 + \frac{A\beta}{1 - \frac{c^2 k_0^2}{\bar{\omega}^2} - \mathrm{i}\frac{c\gamma k_0}{\bar{\omega}^2}} \tag{5.3b}$$

$$\kappa(k_0) = \frac{A\sqrt{\beta\epsilon_{\mathrm{sol}}}}{1 - \frac{c^2 k_0^2}{\bar{\omega}^2} - \mathrm{i}\frac{c\gamma k_0}{\bar{\omega}^2}}\,, \tag{5.3c}$$

where the amplitude of the resonance is set to $A = 1.27\cdot 10^{-5}$ and the parameter $\beta = 1.12\cdot 10^{-7}$. The variable β parametrizes the electromagnetic duality of the chiral medium. The solvent permittivity is set to $\epsilon = 1.8912$. These relations fulfill the passivity condition [17]

$$\sqrt{\operatorname{Im}\epsilon(k_0)\operatorname{Im}\mu(k_0)} \geq \operatorname{Im}\kappa(k_0)\,. \tag{5.4}$$

The real part of the Lorentzian decays with k_0^{-2} far away from the resonance, whereas the imaginary part decays with k_0^{-3}. Thus, using the optical rotation for sensing off-resonance could yield higher absolute signals in comparison to circular dichroism.

We first investigate the optical rotation enhancement by a single cylinder. We optimize the cylinder radius for this resonance, to achieve an approximately dual response, by maximizing the scattering response of the same helicity. The dual response is necessary because only a dual scatterer preserves the helicity in the scattering response, which maximizes the measurable chiral signatures. The result of the optimization is shown in panel (a) of Fig. 5.1. The green line shows the sum of the scattering amplitude coefficients squared under the illumination of a circularly polarized plane wave with positive helicity. At the design frequency, the contribution to the helicity-preserving scattering response, which is shown as solid line, is strongest and the helicity-changing scattering, shown as dashed line, is weak.

The interaction within a lattice can change the scattering behavior of the lattice significantly. We use the lattice pitch of $a = 3.807\,\mu\mathrm{m}$ to compare the results of the single cylinder with the response within an array, since it shows a good enhancement of the optical rotation in Fig. 5.2. Note that in this section, the lattice pitch is defined in analogy to [P15] such that the basis vectors of the reciprocal lattice have the length $\frac{2\pi}{a}$. For a hexagonal lattice, it follows that the cylinders in the real lattice have a center to center distance of $\sqrt{\frac{4}{3}}a$. As the blue line in panel (a) of Fig. 5.2 shows, the influence of the lattice mostly broadens the frequency range with a good helicity preserving behavior. Panels (b) and (c) in Fig. 5.2 show the chirality density in the vicinity of the cylinders when illuminated by a plane wave of positive helicity propagating along the z-direction. The single cylinder has no region around it, where the chirality density is negative for positive helicity illumination confirming its high degree of helicity preservation. However, the enhancement of the chirality density is limited to only its immediate vicinity, as indicated by the gray contour line for the threshold value of 5. Panel (c) in Fig. 5.2, showing the chirality density of the cylinder in the array, has a much larger area of positive chirality density and also higher values in the immediate vicinity of the cylinder. Thus, a larger volume of the sample enhances the measurement signal.

We simulate the array for a large parameter sweep from the lattice pitch of $2.3\,\mu\mathrm{m}$ to $4.3\,\mu\mathrm{m}$ in the frequency range between 35 THz to 50 THz. The lower bound of the lattice

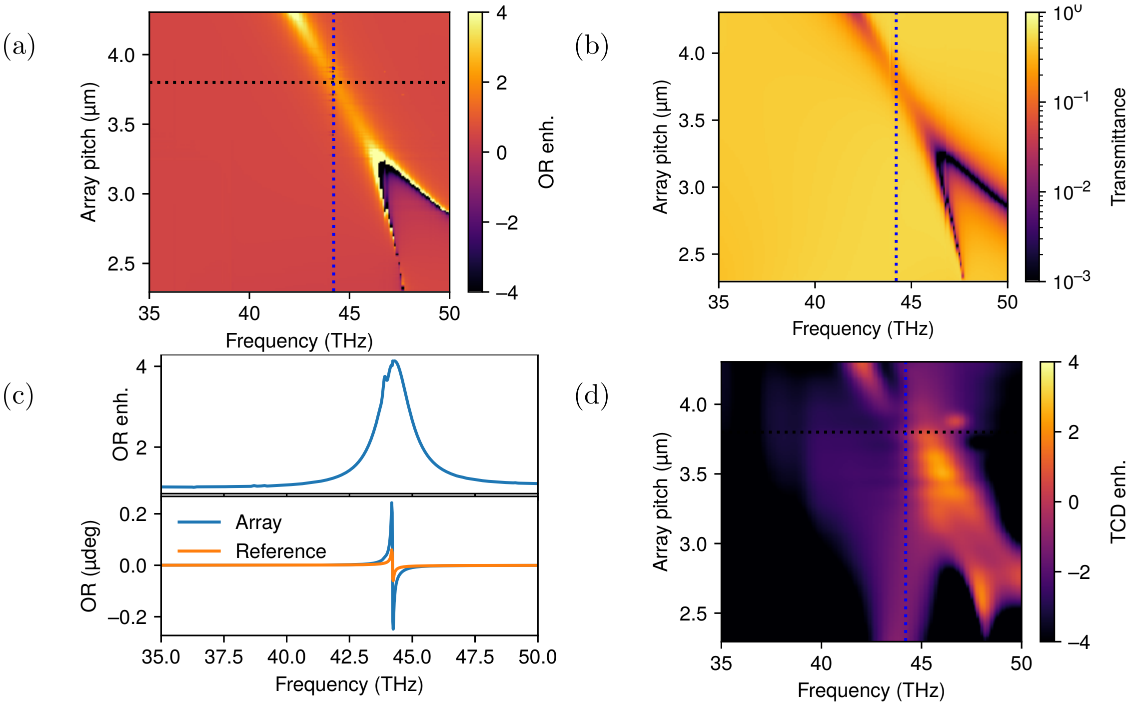

Figure 5.2: Optical rotation and circular dichroism enhancement of a hexagonal array of cylinders. We investigate a single achiral array to enhance the optical rotation around the resonance frequency 44.21 THz, which is shown as blue dotted line for an array pitch between 2.3 µm and 4.3 µm. Panel (a) shows the optical rotation enhancement and panel (b) the transmittance of the lattice. The optical rotation enhancement by the array for a pitch of 3.807 µm is shown in the top of panel (c). At the bottom of panel (c), we show the optical rotation value. Panel (d) shows the circular dichroism in transmittance for the same structure. Reprinted permission from [P2]. Copyright 2021 AIP Publishing.

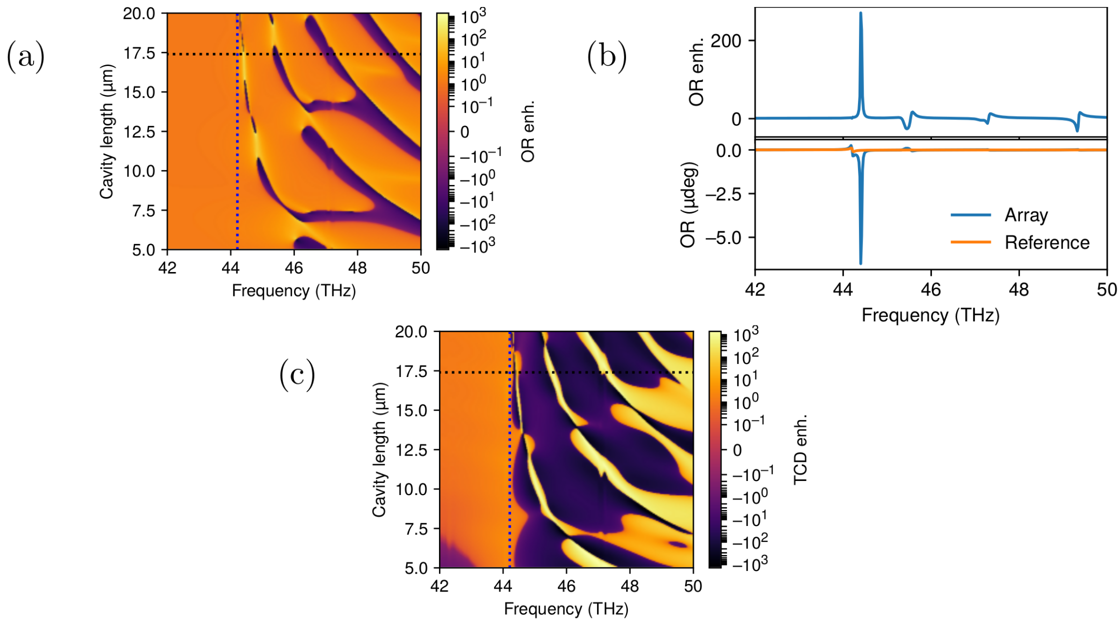

Figure 5.3: Optical rotation and circular dichroism enhancement of an achiral cavity. We use a cavity formed by two hexagonal arrays with the lattice pitch 4.956 µm. In our study, we vary the cavity length between 5 µm and 20 µm. Panel (a) shows the optical rotation enhancement and panel (c) the transmittance circular dichroism enhancement. For the chosen cavity length of 17.4 µm, indicated by the black dotted line, we find an enhancement factor of 270, as shown in panel (b). Reprinted permission from [P2]. Copyright 2021 AIP Publishing.

pitch is defined by the minimal distance to avoid touching cylinders. The upper bound is defined such that higher-order propagating diffraction orders modes are avoided. Otherwise, the definition of the optical rotation signal has to be modified. We use a sample volume with a thickness of 10 µm perpendicular to the lattice to compute the optical rotation. The results for the optical rotation enhancement and the transmittance are shown in panels (a) and (b) of Fig. 5.2. The reference for the enhancement calculation is a homogeneous slab of chiral material of the same thickness. We find sharp lines with strong enhancements for frequencies above approximately 46 THz. However, those enhancement factors are in exactly those regions, where the transmittance is very low, thus, posing a challenge to be used in practice. A broader resonance that can be tuned by the lattice pitch traverses the design frequency of 44.21 THz at the lattice pitch 3.807 µm. Here, we achieve an enhancement factor of roughly 4, as shown in panel (c). For comparison, we also show the transmittance circular dichroism for the single cylinder in panel (d). The transmittance circular dichroism measures the difference in transmittance only instead of using transmittance and reflectance to calculate absorption. Hence, not only the differential absorption contributes to the signal strength. Focusing on the frequency band near the resonance, since the enhancement becomes large due to the low reference value far off-resonance, we also find enhancement values up to 2 for the circular dichroism signal.

The enhancement of chiral signals with a single array is limited to the near-field enhancement of the chirality density. Thus, a limiting factor is the affected sample volume.

In a cavity, strong fields can be obtained covering a large volume. However, a large chirality density is difficult to achieve, because, conventional mirrors flip the helicity for light at normal incidence. By using array structures instead of flat mirrors, light can be diffracted to modes with gracing incidence onto the opposite array. The reflection coefficient gets unity at grazing incidence on the one hand, resulting in a high-quality cavity, and the reflection becomes helicity preserving on the other hand. Thereby, the arrays couple the incident light into guided modes, that experience many consecutive reflections in the structure that acts as a wave guide. A design for such a helicity preserving cavity was investigated previously for the enhancement of circular dichroism, and we use the same radius 1.574 µm and the lattice pitch 4.956 µm for the design of the array [P15].

In Fig. 5.3, we show the enhancement of optical rotation for the frequency range between 42 THz and 50 THz. To identify an optimal cavity, we vary the cavity length between 5 µm and 20 µm. Similar to the previous investigations, we find strong enhancements at sharp lines for frequencies above the resonance 44.21 THz. They are a result of the onset of diffraction, and their position is defined by

$$l\sqrt{k^2 - \left(\frac{2\pi}{a}\right)^2} = 2\pi m \quad , \quad m \in \mathbb{N}\,, \tag{5.5}$$

which is the condition for a 2π phase accumulation within one round-trip of a mode in the cavity. We find the strongest enhancement by a factor of 207 at the cavity length of 17.4 µm. The enhancement is shown as a line plot in panel (b) together with the absolute value of the optical rotation. Panel (c) shows the transmittance circular dichroism for the investigated system, that shows a similar pattern depending on Eq. (5.5) as the optical rotation.

Our simulations assume an infinitely periodic system in the x-y-direction. Since the strong enhancement at the onset of diffraction can be effected detrimentally in systems of finite size, we estimate the required size of the system for the case of a cavity with 17.4 µm length by taking the angle of the first diffraction order and assuming 100 round-trips in the cavity are necessary. This results in a cavity size of approximately 500 µm to achieve the result with finite arrays.

In conclusion, we find that it is possible to not only enhance circular dichroism with array structures or cavities, but also the optical rotation. These studies were performed with a development version of *treams*. Besides their immediate physical findings, they show, how large parameter studies can be performed very efficiently with the methods of *treams*, as long as parameters such as pitch and cavity length are concerned, that do not require the calculation of a new T-matrix. Moreover, by the separation of the optimization of the individual cylinder and the lattice, we benefit from the separation of object and lattice influence in the T-matrix method with periodic boundary conditions.

5.2 Simulation of the electromagnetic fields in 3D direct laser writing

In this section, we discuss the application of the T-matrix and the transfer matrix method to simulate focal spots in multi-photon 3D direct laser writing processes [93, 94, 124]. We examine two examples: First, Subsection 5.2.1 describes the application of the Richards

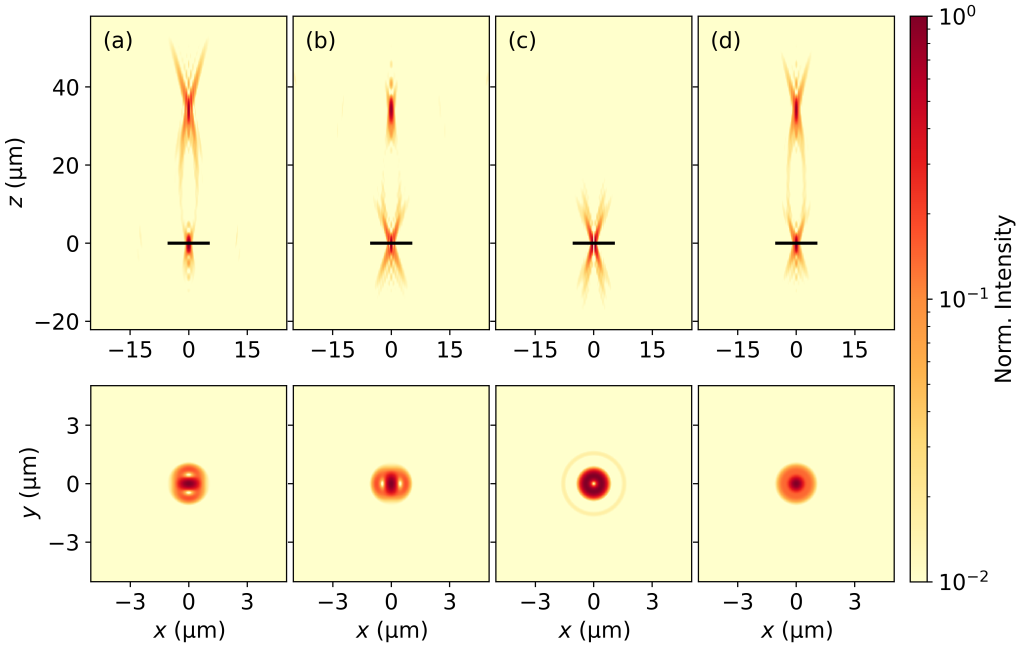

Figure 5.4: Focus calculation in a birefringent medium with director angle $\alpha = 0$. Hence, the extraordinary axis is aligned with the z-direction. From left to right, the panels show the intensity around the focal spot normalized to the peak value of all setups for four different polarizations: (a) x-polarized, (b) y-polarized, (c) azimuthally polarized, and (d) circularly polarized light. The top part of each panel shows the x-z-plane and the bottom part shows a close up of the x-y-plane, as indicated by a black bar in the top part.

and Wolf integrals in combination with the transfer matrix method to calculate the focus in anisotropic media introduced in Section 2.4. Then, we combine the focus calculation with the T-matrix method to study the impact of the presence of additional scatterers with a low refractive index contrast on the focus spot quality in Subsection 5.2.2.

5.2.1 Focusing in anisotropic media

The simulations presented in this section were performed for a collaboration with Alexander Münchinger from the group of Martin Wegener at KIT, who developed and experimentally realized the process of printing in birefringent liquid crystal-based resists to obtain 4D microstructures [P12]. The designation 4D comes from the combination of a structure that can be designed in the three spatial dimensions and, furthermore, having a temporal response to external stimuli, e.g., a temperature change [125–129].

Direct laser writing is an important method for the additive manufacturing of fully three-dimensional microstructures. Essentially, a two-photon absorption process is used to polymerize a resist, which defines the three-dimensional structure that is obtained after development. One important aspect to obtain a fine resolution of the printed structure and a small feature size is having a precisely defined focal spot. However, to obtain a temporal response with the printed structures, liquid crystal-based resists are used

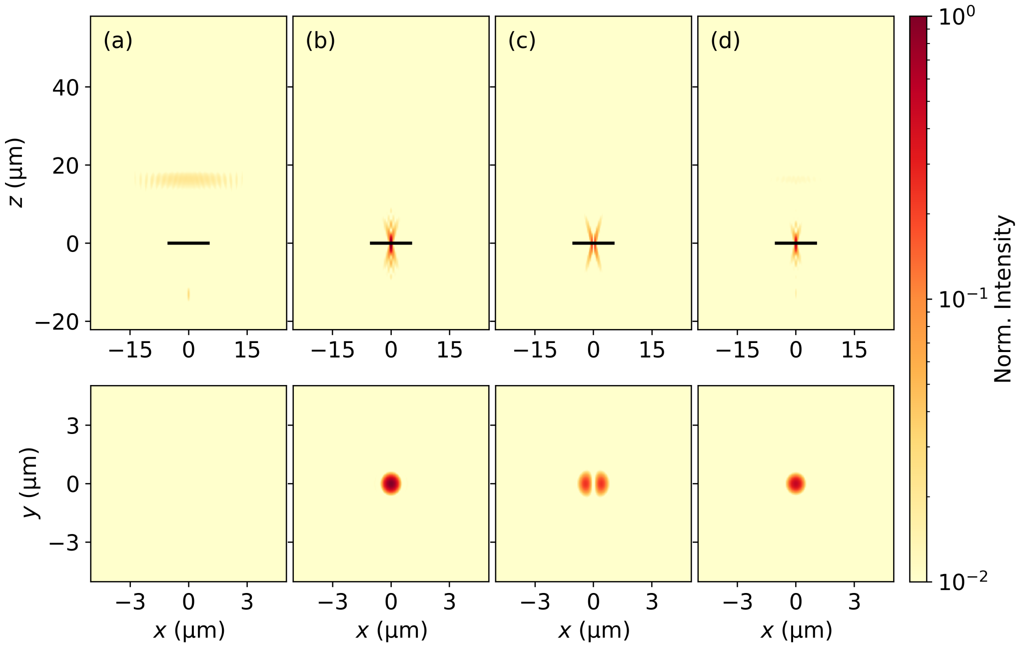

Figure 5.5: Focus calculation in a birefringent medium with director angle $\alpha = \frac{\pi}{2}$. Hence, the extraordinary axis is aligned with the x-direction. From left to right, the panels show the intensity around the focal spot normalized to the peak value of all setups for four different polarizations: (a) x-polarized, (b) y-polarized, (c) azimuthally polarized, and (d) circularly polarized light. The top part of each panel shows the x-z-plane and the bottom part shows a close up of the x-y-plane, as indicated by a black bar in the top part.

that are birefringent [129–131]. Thus, two foci are generally found during the printing process. The presence of two foci can be avoided by a careful choice of the direction of the extraordinary axis of the liquid crystal elastomer and the polarization of the beam focused into the resist. The former can be achieved with a quasi-static electric field applied to the liquid crystal elastomer, thus, defining a director along which it is aligned. This director can also be switched for different parts of the printed structure during the printing, thereby, obtaining a spatial variation of the director in the final structure to more precisely tailor the response to temperature variations.

We examine the focal spot for four different polarization setups: Linear polarization along the x- and y-axis, azimuthal polarization, and circular polarization. Furthermore we analyze three different alignments of the director defined by the angle α with respect to the z-axis in the x-z-plane. We model the resist with an ordinary refractive index of 1.5 and an extraordinary refractive index of 1.7. The objective lens has a numerical aperture of 0.8 and an entrance pupil of 5.3 mm. Between the lens and the birefringent resist we place an isotropic layer of 100 µm thickness with refractive index 1.5, which models the immersion oil of the lens and the cover slip. The monochromatic illumination has a wavelength of 790 nm and a Gaussian profile with a radius of 4.75 mm at which the intensity drops to e^{-2}. Figure 5.4 shows the result for the four polarizations and the angle $\alpha = 0$, i.e., the extraordinary axis is aligned with the z-axis. We use these model parameters

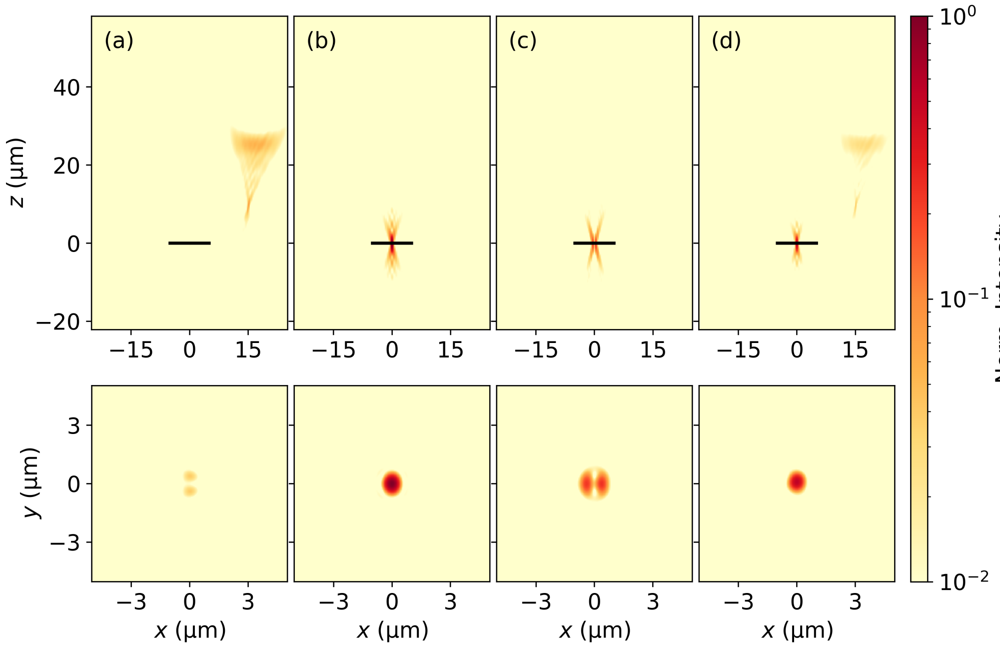

Figure 5.6: Focus calculation in a birefringent medium with director angle $\alpha = \frac{\pi}{4}$. Hence, the extraordinary axis bisects the angle between x- and z-axis. From left to right, the panels show the intensity around the focal spot normalized to the peak value of all setups for four different polarizations: (a) x-polarized, (b) y-polarized, (c) azimuthally polarized, and (d) circularly polarized light. The top part of each panel shows the x-z-plane and the bottom part shows a close up of the x-y-plane, as indicated by a black bar in the top part.

of the illumination and the lens to calculate the angular spectrum of the focused electromagnetic wave according to Eq. (2.110). Then, the angular spectrum is propagated through the anisotropic medium using the transfer matrix algorithm as described in Section 2.4. Linearly polarized light gets focused in two spots corresponding to the ordinary and extraordinary rays. For the azimuthally polarized light, the extraordinary focus can be suppressed. Thereby, it allows the direct laser writing process with a single focal spot, however, with a toroidal shape. Circularly polarized light also creates two foci, like the linear polarizations. In Fig. 5.5, we show the results for the same polarizations but with the director with an angle $\alpha = \frac{\pi}{2}$, i.e., along the x-direction. With x-polarized light, we only observe a weak and distorted focus. In contrast, by using y-polarized light, which is perpendicular to the director, we find a strong well-defined focal spot. In the remaining two cases of azimuthally and circularly polarized light, the focal spot is weaker again, however, it is still comparatively well-defined in a small volume.

The case of an oblique director at an angle of $\alpha = \frac{\pi}{4}$ is shown in Fig. 5.5. The x-polarized illumination shows an off-axis, distorted, and weak focal spot. As can be seen in the x-y plane, a second focal spot, having the shape of a lobe, is present at the position expected for the ordinary rays. The azimuthal polarization has a single larger focal spot. The circularly polarized case shows two foci.

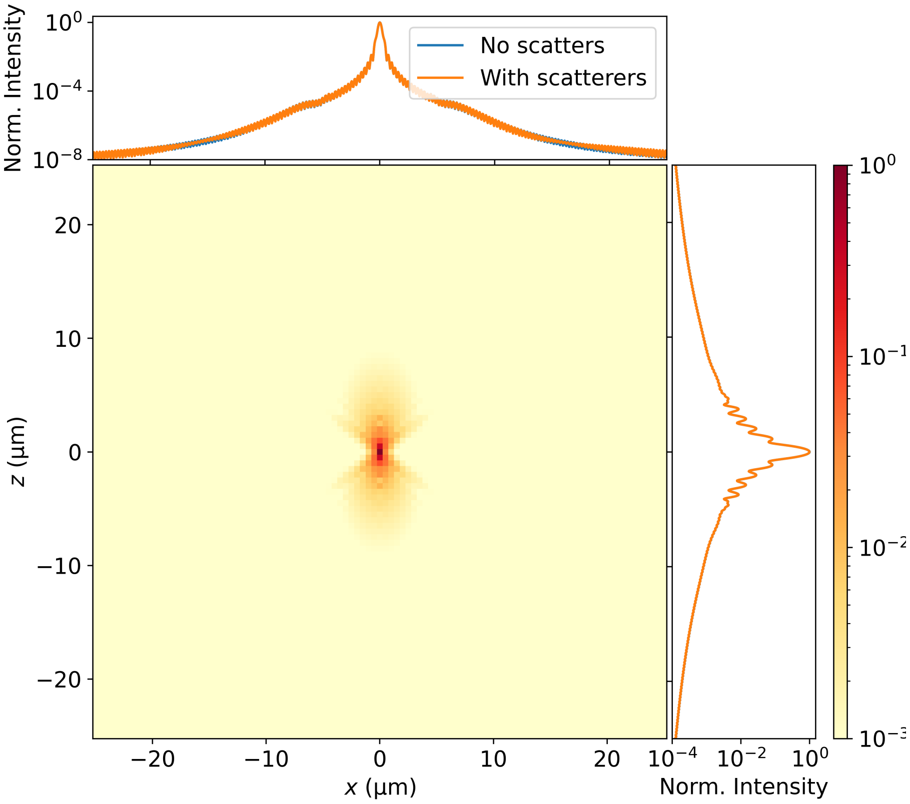

Figure 5.7: Focus calculation in the presence and absence of scatterers.

In summary, depending on the director angle, different polarizations need to be used to obtain a single, well-defined focal spot. We successfully applied the simulation method combining the approach from Richards and Wolf for high numerical aperture lenses with a transfer matrix algorithm to simulate birefringent structures. Besides the results presented here, they were also used in the simulation of the focal spots in an inverted direct laser writing setup, that avoids a large separation of the foci by minimizing the distance the electromagnetic fields travel through the resist [P17].

5.2.2 Focal spot distortions by the presence of large scatterers

We also combined the approach with the ordinary *treams* capabilities to simulate the focus during direct laser writing in the presence of scatterers in the resist. This work is complementary to experimental work using optical coherence tomography for *in-situ* measurements performed and analyzed by Roman Zvagelsky in the group of Martin Wegener at KIT [P21]. These measurements revealed inhomogeneities in five-year old resists in comparison to fresh resists. These differences were interpreted as “blobs” of oligomer groups due to thermal activation. We performed simulations to assess if these inhomogeneities have an influence on the shape of the focal spot.

We model the process with a monochromatic illumination of 790 nm wavelength. We approximate the inhomogeneities as spheres with a radius of 6.5 µm, which is the intermediate value between the observed size between 2.5 µm and 12.5 µm. The density of scatterers is chosen such that their volume matches the experimentally observed volume occupied by the inhomogeneities. The refractive index of the isotropic resist is 1.51 and the refractive index of the inhomogeneities is assumed to be 1.545. We use a maximal multipole order of $l_{\max} = 13$ and simulate these systems in lowest-order Born approximation, i.e., we neglect multi-scattering events. This approximation avoids the computational expensive inversion of the matrix in Eq. (2.52). Figure 5.7 shows the results of the simulations. The central panel shows a cut plane through the focal spot. No distortions are visible. The comparison with the unperturbed focus shape along the x- and z-axis also shows a negligible influence of the inhomogeneities on the shape of the focal spot.

These examples show how *treams* and its methods are flexible enough to interact with other approaches, such as the use of angular spectra for focus calculations and the transfer matrix approach.

5.3 Multi-scale methods for molecular arrays

In this section, we discuss the application of *treams* and its methods as a tool to perform simulations bridging scales from the size of individual molecules to cavities of macroscopic sizes [P18]. The main development of the multi-scale method was done by Benedikt Zerulla, Marjan Krstić, and Ivan Fernandez-Corbaton.

We use the example of surface-anchored metal-organic frameworks (SURMOFs) in a Fabry-Perot cavity formed by silver mirrors [132] to describe how *treams* can be used together with complementary theoretical approaches to allow *ab-initio* multi-scale modeling of complex physical systems. The fabrication of such complicated novel materials and their experimental investigation is a rapidly developing field. However, the theoretical description of these novel materials has to keep up.

Metal-organic frameworks are crystalline structures build from organic molecules to link metal ions [133]. Due to the well-defined chemical bonds, their physical properties are highly configurable. Their applications include luminescence [134], second harmonic generation [135], and Raman scattering [136]. SURMOFs are a class of metal-organic frameworks that are attached to functionalized surfaces [137].

The properties of the SURMOF's building blocks, the linkers and metal ions in their periodic structures can be calculated *ab-initio* using quantum-chemical methods [138, 139]. The polarizability tensors can be calculated with time-dependent density functional theory [140]. These polarizabilites can be related to the dipolar coefficients of the T-matrix [P7]. Thereby, the quantum-chemical simulations and the T-matrix method can be connected. These steps are summarized in the first part of the workflow shown in Fig. 5.8. They are shown in the green boxes of the first row, which include the quantum interaction of the electrons of the molecules. First, the structure of the SURMOF is determined taking into account the full periodic environment of the linkers and metal ions. Second, time-dependent density functional theory is used to calculate the response from an externally applied field, which, then, results in the polarizabilites.

The bottom row of Fig. 5.8 shows the part of the workflow using classical electromagnetic scattering theory. We use the T-matrix of the molecules to simulate the response

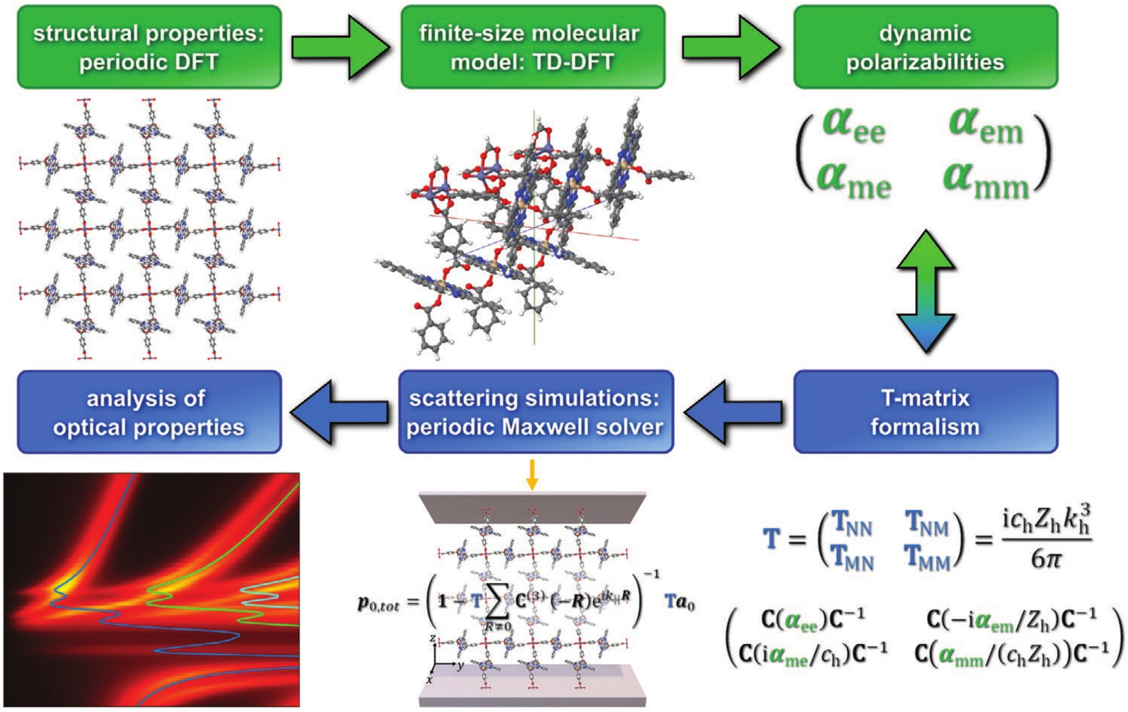

Figure 5.8: Workflow for the *ab-initio* calculation of the optical properties of macroscopic structures containing SURMOFs. The quantum-chemical simulations are shown with green boxes, and the optical simulations are shown in blue. First, the periodic structure of the SURMOFs is calculated. Second, in time-domain density functional theory, the response to an external electromagnetic field is computed. Third, the polarizability tensors are calculated, which, fourth, provide the connection to the dipolar T-matrix and, thus, the electromagnetic scattering simulations. In the fifth step, *treams* is involved to calculate the response, e.g., of the SURMOF in the cavity, bridging from the scale of nanometers for the individual molecules to films of micrometer thickness. Finally, the results allow a theoretical analysis of the structure. Reprinted with permission from [P18]. Copyright 2022 John Wiley and Sons.

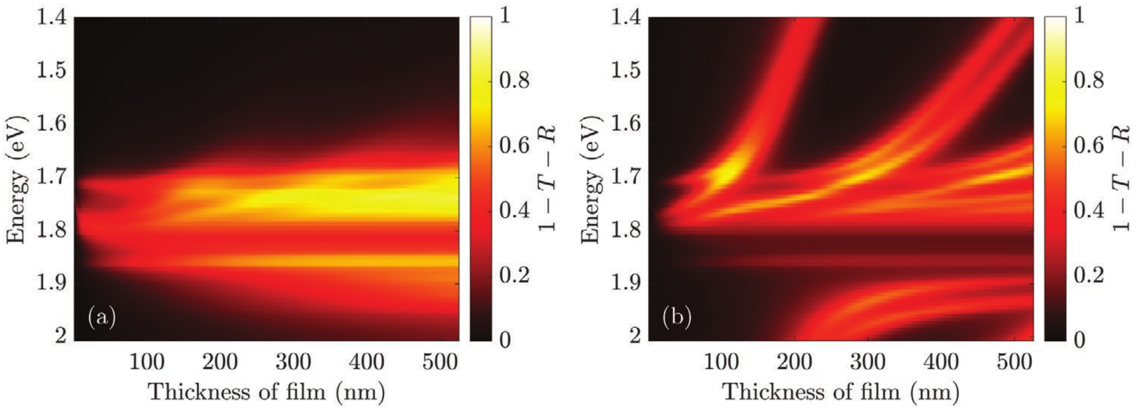

Figure 5.9: Absorption of a circularly polarized plane wave by a Zn-SiPc-SURMOF-2 film. Panel (a) shows the absorption for the film without any additional structure. Panel (b) shows the absorption of the film inside a cavity formed by silver mirrors with 10 nm thickness on the illumination side and 30 nm thickness on the transmission side. Reprinted with permission from [P18]. Copyright 2022 John Wiley and Sons.

of large SURMOFs. By using the T-matrix method with periodic boundary conditions, as implemented in *treams*, we take the full periodic structure of the SURMOFs into account. Furthermore, we can also calculate the interaction with other structures that can be represented by the methods implemented in *treams*. The first step in the second part of the workflow is translating of the dipolar polarizability tensors α_ee, α_em, α_me, and α_mm, which relate the electric and magnetic fields with Cartesian electric and magnetic dipoles, to T-matrices. This step is done by using

$$\begin{pmatrix} \mathbf{T}_\mathrm{NN} & \mathbf{T}_\mathrm{NM} \\ \mathbf{T}_\mathrm{MN} & \mathbf{T}_\mathrm{MM} \end{pmatrix} = \frac{\mathrm{i} c_\mathrm{h} Z_\mathrm{h} k_\mathrm{h}^3}{6\pi} \begin{pmatrix} \mathbf{C}\alpha_\mathrm{ee}\mathbf{C}^{-1} & -\frac{\mathrm{i}}{Z_\mathrm{h}}\mathbf{C}\alpha_\mathrm{em}\mathbf{C}^{-1} \\ \frac{\mathrm{i}}{c_\mathrm{h}}\mathbf{C}\alpha_\mathrm{me}\mathbf{C}^{-1} & \frac{1}{c_\mathrm{h} Z_\mathrm{h}}\mathbf{C}\alpha_\mathrm{mm}\mathbf{C}^{-1} \end{pmatrix} . \tag{5.6}$$

The quantities c_h, Z_h, and k_h are the speed of light, wave impedance, and the wave number in the host medium, respectively. The matrix

$$\mathbf{C} = \begin{pmatrix} \frac{1}{\sqrt{2}} & \frac{\mathrm{i}}{\sqrt{2}} & 0 \\ 0 & 0 & 1 \\ \frac{1}{\sqrt{2}} & -\frac{\mathrm{i}}{\sqrt{2}} & 0 \end{pmatrix} \tag{5.7}$$

gives the transition from Cartesian to spherical dipoles [P7, P14]. The three-by-three blocks $\mathbf{T}_{ij}$, where the indices refer to the functions defined in Eq. (2.23), define the T-matrix in dipolar approximation. In principle, the inclusion of higher order multipoles is possible. However, for the small size of the molecules, they have a negligible contribution. By calculating the interaction of the scattered fields from each molecule in the periodic arrangement using *treams*, we can calculate and analyze the optical properties of SURMOFs in cavities, for example. The layer-doubling technique is extremely useful to implement the calculation of thick layers of SURMOFs, because it allows an exponential scaling of the thickness [39, 52, 141].

In a concrete example, a molecular array consisting of stacked sheets of Zn-paddle-wheels and Si-Phthalocyanine linker molecules form a type-2 SURMOF [132], which we abbreviate with Zn-SiPc-SURMOF-2. The unit cell size is 21 Å by 21 Å by 11 Å for a single sheet. To obtain the T-matrix for an approximately round object, three stacked unit cells are used in the calculation of the polarizabilities. Figure 5.9 shows the simulation of absorption from a film consisting of Zn-SiPc-SURMOF-2 with up to 500 nm thickness in the range between 1.4 eV to 2 eV, which corresponds to the wavelengths 885 nm and 620 nm. In panel (a), showing the result for the SURMOF illuminated by a circularly polarized plane wave without a cavity surrounding the structure, we find multiple resonances in the range between 1.7 eV and 1.9 eV. This mode structure changes drastically in cavity consisting of a 10 nm thickness silver mirror on the illumination side and a 30 nm thickness mirror on the transmission side. The permittivity of the silver mirrors is taken from [142]. The resonances are strongly bent due to the cavity. Furthermore, we find that every mode appears in pairs, which is a result of the SURMOFs anisotropy. We can use these results, together with a further analysis of the mode structures, to refine the interpretation of experimental findings [132].

We conclude that the methods of *treams* are extremely useful in describing large molecular arrays, and we can bridge from the nanometer size of a unit cell to several hundreds of nanometer thickness materials in optical structures. Novel applications of this method combine it with the homogenization method presented in the following section to model even more complicated systems [P19].

5.4 T-matrix based homogenization methods

This section covers the use of the T-matrix method and lattice sums as one step in the workflow to homogenize artificial photonic materials, where the individual components can be described by T-matrices [P20]. This project was mainly developed by Benedikt Zerulla, Ramakrishna Venkitakrishnan, and Ivan Fernandez-Corbaton.

In effective medium theories, the electromagnetic response from a discrete structure of scatterers is described by effective material parameters. The process of calculating these material parameters starting from the discrete structure is called homogenization, and a field of active research [143–159]. Having an effective medium description is useful to avoid computationally expensive simulations of the detailed response of every constituent of the homogenized material. Furthermore, different shapes of the macroscopic object are correctly described by the material parameters.

A widely used and simple approach for the homogenization are the Clausius-Mossotti relations [16]. However, these relations only take dipole contributions into account. Furthermore, many approaches suffer from conditions that are not generally fulfilled. Often, a sparse lattice that, at the same time, has a lattice constant much smaller than the wavelength is required. Other methods are based on the retrieval of the effective parameters, by simulating a reference object, often a slab of the material to be homogenized, and performing an optimization of the material parameters to replicate the transmission and reflection for multiple angles of incidence. Such methods have the downside to already explicitly using a concrete shape, i.e. a slab, for the homogenization itself. Furthermore, the retrieved parameters can be non-unique [158, 160] The homogenization based on T-matrix calculations with periodic boundary conditions is a novel approach to address these issues. It is emphasized, that no fit or something similar is necessary. Instead, effective material

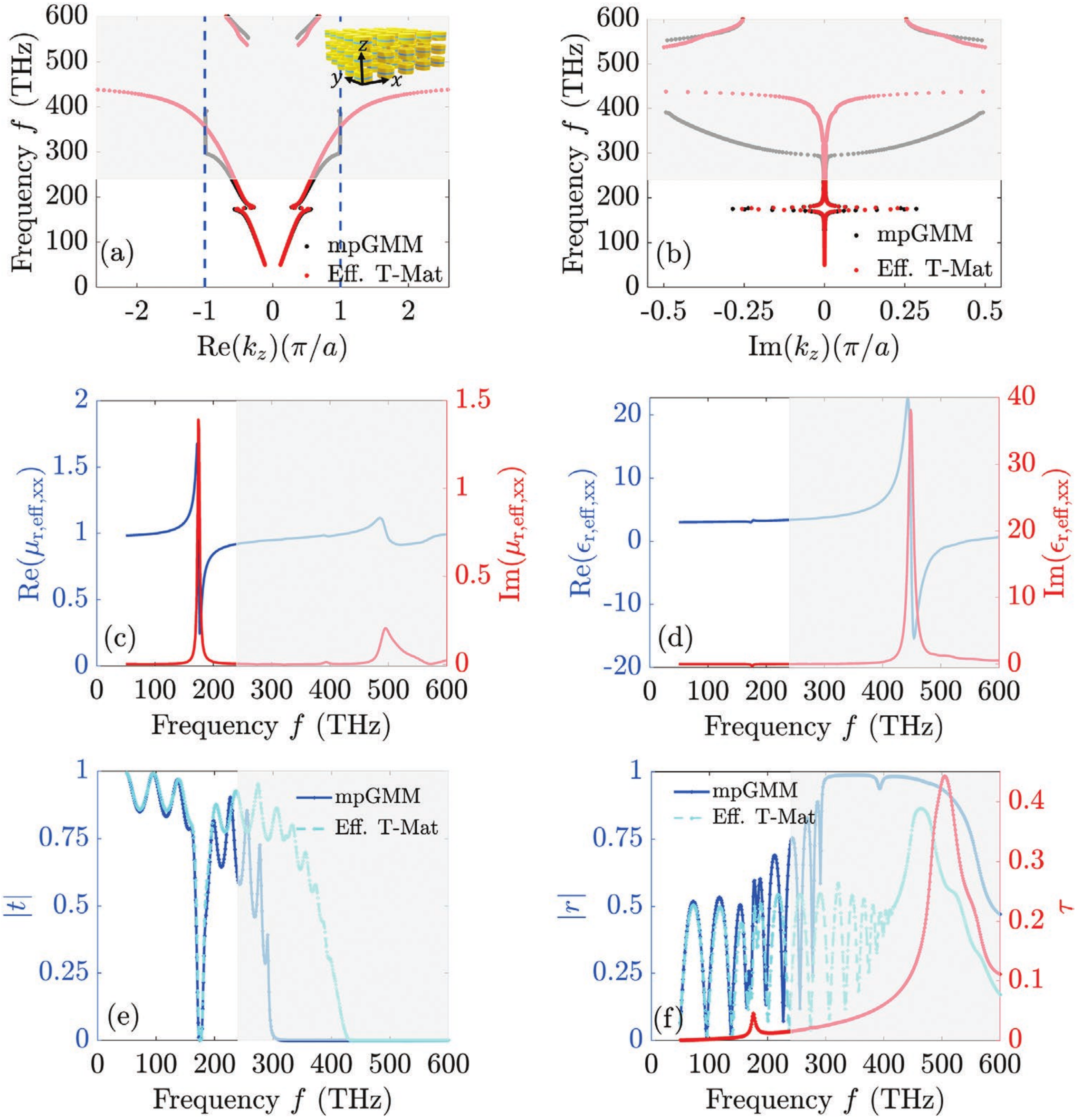

Figure 5.10: Homogenization of a cut-plate pair metamaterial. The abbreviation mpGMM is used for a predecessor software of *treams*, which we also developed. It has a subset of *treams* functionality. Panels (a) and (b) shows the band structure of the metamaterial computed with the approach of Eq. (2.95), which for a given frequency and fixed wave vector components k_x and k_y calculates the value of k_z for permissible modes. Large imaginary components of k_z, as shown in panel (b) in the range above 300 THz indicate band gaps. Panels (c) and (d) show the permeability and permittivity obtained with the homogenization. These parameters are used to compute the transmission and reflection parameters of the homogenized material, shown in panels (e) and (f). Reprinted with permission from [P18]. Copyright 2022 John Wiley and Sons.

properties of the entire material are explicitly expressed based on the scattering properties of the constituents, as expressed by the T-matrix.

The starting point of the calculation is the T-matrix of the individual scatterer and the lattice geometry. Using Eq. (2.60), we can calculate the T-matrix in the full three-dimensional lattice. This step is independent of the shape of the homogenized object. The result of including the lattice interaction is the T-matrix $\tilde{\mathbf{T}}(\boldsymbol{k}_\parallel)$. However, it depends on the direction of the wave vector of the illumination, as emphasized by the argument. This dependence is know as spatial dispersion. To avoid this explicit dependence on the direction of the wave vector for the illumination, we use a method that has similarities with the approach to calculate a T-matrix with plane wave illuminations [33], but its validity to find a wave vector independent T-matrix can be shown rigorously [P20]. We assume many different illumination directions $\boldsymbol{k}_i$ and decompose the incident field in vector spherical waves $\boldsymbol{a}_{\boldsymbol{k}_i}$. Then, using $\tilde{\mathbf{T}}(\boldsymbol{k}_i)$, we can calculate the scattered wave coefficients $\boldsymbol{p}_{\boldsymbol{k}_i}$ for each such illumination. This approach needs many evaluations of the lattice sums for three-dimensional lattices and, therefore, greatly benefits from the expressions implemented in *treams*. With the incident and scattered field coefficients, we can define the linear system of equations

$$\begin{pmatrix} \boldsymbol{p}_{\boldsymbol{k}_1} & \cdots & \boldsymbol{p}_{\boldsymbol{k}_N} \end{pmatrix} = \mathbf{T}_{\text{eff}} \begin{pmatrix} \boldsymbol{a}_{\boldsymbol{k}_1} & \cdots & \boldsymbol{p}_{\boldsymbol{k}_N} \end{pmatrix} \tag{5.8}$$

for N different illuminations and the unknown effective T-matrix $\mathbf{T}_{\text{eff}}$, which is independent of the illumination direction. We solve the equation for $\mathbf{T}_{\text{eff}}$. Next, we want to relate the effective T-matrix to the six-by-six anisotropic tensor defined in Eq. (2.6). Hence, we use the inverse of Eq. (5.6) to obtain the polarizability matrices relating the external electromagnetic field to the polarization. This step requires an approximation, since it only takes into account dipolar contributions. Note, however, that higher-order multipoles are still considered in the interaction, i.e., they tend to renormalize the dipole coefficients. Furthermore, it is possible to compare the dipolar coefficients of $\mathbf{T}_{\text{eff}}$ with the higher order multipoles to estimate the validity of this approximation. Having obtained the polarizabilities, we take into account the depolarization matrix $\mathbf{L}$ to relate the external fields with the internal fields in a unit volume [144]. This matrix is a purely lattice dependent quantity. In a cubic lattice it is $\mathbf{L} = \frac{1}{3}\mathbb{1}$, but results for more complicated lattices are known [161]. Combining the transition from the T-matrix to polarizabilities and the depolarization matrix, we obtain

$$\begin{pmatrix} \boldsymbol{\epsilon} & \mathrm{i}\boldsymbol{\kappa} \\ -\mathrm{i}\tilde{\boldsymbol{\kappa}}^\mathsf{T} & \boldsymbol{\mu} \end{pmatrix} = \mathbb{1} - \frac{\mathrm{i}6\pi n}{k_0^3} \left[\mathbb{1} + \frac{\mathrm{i}6\pi n}{k_0^3} \begin{pmatrix} \mathbf{T}_{\text{ee}}^{\text{car}}\mathbf{L} & \mathbf{T}_{\text{em}}^{\text{car}}\mathbf{L} \\ \mathbf{T}_{\text{me}}^{\text{car}}\mathbf{L} & \mathbf{T}_{\text{mm}}^{\text{car}}\mathbf{L} \end{pmatrix} \right]^{-1} \begin{pmatrix} \mathbf{T}_{\text{ee}}^{\text{car}} & \mathbf{T}_{\text{em}}^{\text{car}} \\ \mathbf{T}_{\text{me}}^{\text{car}} & \mathbf{T}_{\text{mm}}^{\text{car}} \end{pmatrix} \tag{5.9}$$

for the homogenized parameters, where $\mathbf{T}_{ij}^{\text{car}} = \mathbf{C}^{-1}\mathbf{T}_{ij}\mathbf{C}$ are the dipolar coefficients of the T-matrix in parity basis converted to the Cartesian basis and n is the concentration of scatterers. In a reciprocal material, we have $\boldsymbol{\kappa} = \tilde{\boldsymbol{\kappa}}$. This equation can also be adapted to include the permittivity of the host medium.

An example for the homogenization of a complex photonic material is shown in Fig. 5.10. The unit cell of the cubic lattice with 200 nm pitch consists of a cut-plate pair, which is expected to exhibit a magnetic resonance at low frequencies [162]. Two gold layers with 30 nm thickness, where we use the permittivity from [163], are separated by an insulator with 5 nm thickness with $\epsilon = 2.25$. The rather thin layer pushes the antisymmetric mode of the coupled plates towards extremely long wavelengths, which is the key to achieve a magnetic response deep subwavelength. The radius of the cut-plate pair is 90 nm. It is shown in the inset of panel (a). Before homogenizing this photonic material, we analyze its band structure, which is obtained on the base of Eq. (2.95). Panels (a) and (b) show the real and imaginary parts of k_z of the lowest order mode computed with this method as black dots. These dots are labeled mpGMM in the legend, which is the abbreviation of the predecessor software of *treams* using the same methods. We find a band gap above 300 THz, indicated by the large imaginary components of k_z. The dispersion relation of the homogenized material parameters is shown in red. It has a good agreement with the dispersion relation except in the region where the bands are strongly modified at the Bragg resonance near the Brillouin zone edges. Note that these regions, where the homogenization is not possible can be identified *a-priori* by the mode bending at the edge of the Brillouin zone. In all panels, this region is indicated by the grayed-out areas. Panels (c) and (d) show real and imaginary part of one component of the relative permittivity and the relative permeability tensor as retrieved with the procedure described above. We find a strong magnetic resonance, which was also visible in the band structure diagrams. Panels (e) and (f) show the reflection and transmission coefficients obtained from the simulation of nine stacked layers of the cut-plate pairs and from a homogeneous slab of 1800 nm thickness with the derived material parameters. We find a very good agreement in the *a-priori* identified areas where the homogenization is possible. Panel (f) shows, furthermore, the quantity

$$\tau = \sqrt{\frac{\mathrm{Tr}\left[(\mathbf{T}_{\mathrm{eff}}^{\mathrm{dip}} - \mathbf{T}_{\mathrm{eff}})^\dagger (\mathbf{T}_{\mathrm{eff}}^{\mathrm{dip}} - \mathbf{T}_{\mathrm{eff}})\right]}{2\left[\mathrm{Tr}(\mathbf{T}_{\mathrm{eff}}^{\mathrm{dip}\dagger}\mathbf{T}_{\mathrm{eff}}^{\mathrm{dip}}) + \mathrm{Tr}(\mathbf{T}_{\mathrm{eff}}^\dagger \mathbf{T}_{\mathrm{eff}})\right]}}\,, \tag{5.10}$$

which can be used to determine the validity of the homogenization. In essence, this quantity measures the dipolar content of the T-matrix as a normalized quantity. For a value close to zero, the T-matrix is purely dipolar. A reasonably small value in this parameter is acceptable to consider the material as homogenizable in the dipolar limit.

This example highlights how the three-dimensional lattice sums implemented in *treams* can be used for the homogenization of photonic media by assigning effective material parameters to it and how its methods can also be used to calculate the band structure. Thus, in summary, we demonstrated the versatility of *treams*: It is useful for large parameter studies and computations using chiral matter. It can be interfaced with other methods as shown in the focus calculations. It can be used as part of sophisticated multi-scale modeling workflows, as shown for molecular arrays. Finally, we showed its application to homogenize photonic materials by assigning effective parameters.

6 | Conclusions

This thesis shows how the T-matrix method and related approaches can be used to study electromagnetic scattering with chiral matter in periodic structures. Based on the solution of the multi-scattering equations combined with a unified approach to evaluate the arising lattice sums, we implemented and published a novel program *treams*. The derived methods have several unique capabilities compared to other approaches to solve Maxwell's equations, which we highlight in various applications analyzing physical problems of contemporary interest. We give a summary of our main results in Section 6.1. The derived methods and applications also have great potential for further research. We outline several research directions based on the results of this thesis in Section 6.2.

6.1 Summary

The electromagnetic scattering calculations of this thesis are based on the theory derived in Chapter 2. We carefully construct different basis sets solving Maxwell's equations, namely the vector spherical, cylindrical, and plane waves. By considering, in particular, constitutive relations for chiral materials, we define these basis sets not only using parity modes but also with modes of well-defined helicity, which greatly simplifies the description of electromagnetic fields in chiral media. Furthermore, the preservation of helicity under transformations, such as translations, renders these modes an efficient tool for scattering calculations. We formulate the T-matrix method for vector spherical and cylindrical waves for two cases: Finite clusters and periodic arrays. To make this approach as versatile as possible, the equations to describe scattering in periodic arrays incorporate the case of complex unit cells, i.e., unit cells containing multiple objects. Furthermore, we show connections between the different basis sets, which are incredibly useful for efficient descriptions of the total response of periodic structures: One-dimensional arrays of vector spherical waves solutions can be effectively described by vector cylindrical waves, and two-dimensional arrays of vector spherical waves and one-dimensional arrays of vector cylindrical waves can be described by plane waves. To describe scattering in a plane wave basis, we usually use the related S-matrix or transfer matrix descriptions instead of the T-matrix.

While the multi-scattering equations can be expressed concisely using the T-matrix method with the above-mentioned basis sets, a major challenge in solving them for periodic structures are slowly converging lattice sums. We treat these lattice sums in detail in Chapter 3 using a unified approach based on Ewald's method. The results are also published in [P4]. We find exponentially fast converging expressions, for one-, two-, and three-dimensional lattices of spherical and cylindrical waves. Again, we emphasize on expressions for complex lattices, such that they can be combined with the results of Chapter 2 for possible cases. We extensively test the accuracy and convergence of these expressions and demonstrate a speed-up of the lattice sums by several orders of magnitude.

We publish an implementation of the T-matrix method based on the multiple different basis sets and their combination with the derived lattice sum expressions in the open-source software package *treams*. This software is described in Chapter 4 and in [S1]. For T-matrix calculations, *treams* has the following features:

- T-matrices for chiral multi-layered spheres and cylinders can be calculated analytically,
- an interface to externally calculated T-matrices is implemented,
- the interaction of T-matrices can be solved in clusters and complex periodic arrangements, where exponentially convergent lattice sums are used,
- transformations of T-matrices, such as translations or rotations, are included,
- the transitions between expansions in different basis sets are available, and
- many quantities to analyze the results, such as cross-sections, transmittance, reflectance, or circular dichroism, are provided from the calculation results.

To simplify the access to all these and further features for the user, we provide an interface combining a class for "physics-aware" arrays and a mathematics-inspired implementation of operators. These data structures track and use physical parameters throughout the computation and, hence, ensure unintentional changes or incompatible operations. Moreover, an emphasis is placed on integrating *treams* into the framework of scientific software published for Python. Continuous integration methods are used to test, document, and package each novel version of *treams*, such that the correctness of the calculations is monitored, and all available resources are kept up-to-date.

We demonstrate the unique capabilities to solve physical problems at several examples in Chapter 5. In the first example, we analyze the use of helicity preserving structures to enhance the chirality density for sensing applications, especially for optical rotation. The optical rotation is, besides the circular dichroism, a promising possibility to distinguish enantiomers of a molecules. Especially with helicity preserving cavities, we find strong enhancement factors [P2] comparable to previous results for similar cavities used for the enhancement of circular dichroism [P6, P15]. The necessary large parameter sweeps for the analysis are considerably simplified with fast solution approaches implemented in *treams*. Unique to these cavities is the enhancement of the chirality density not just at some isolated points but rather over an extended spatial domain. This is decisive for future applications.

The second example revolves around the prediction of the focal spot in different setups for multi-photon direct laser writing. In particular, we analyze different setups for avoiding multiple focal spots in birefringent liquid-crystal based resists [P12]. Furthermore, we combine the focal spot calculation using angular spectrum calculations with the T-matrix approach to predict the influence of inhomogeneities in the resist on the focus [P21]. Thereby, we show the flexibility of *treams* to be interfaced with other methods. Another application of this method, that is not presented in this thesis, is our analysis of an inverted printing setup that minimizes the propagation distance through the resist [P17].

Our third example uses the capabilities of *treams* as part of a workflow for the *ab-initio* multi-scale modeling of molecular arrays. Such arrays have applications in optics for, e.g., luminescence or Raman scattering. Starting from the quantum level with time-dependent density functional theory computations, we can obtain polarizabilities of the constituent molecules. The connection of the quantum-chemical calculations to the T-matrix [P7] can then be used to bridge from the nanometer scale of the individual molecular unit cells to orders of magnitude larger array structures [P18]. Finally, the fourth example demonstrates how *treams* can be used to homogenize periodic photonic materials based on the T-matrix of the individual unit cell [P20]. Outside of the scope of this thesis but using *treams* is further work, that combines the connection to quantum-chemical simulations and homogenization approaches [P19] or that analyses second-harmonic generation by molecular arrays [S2].

Besides the applications mentioned earlier, we contributed with the presented methods to further scientific publications, which we want to briefly summarize as well. The derived lattice sums and their implementation in *treams* was used to investigate atomic chains forming one-dimensional moiré lattices [P5]. To investigate amorphous nanostructures for light-harvesting on top of solar cells, the lattice sums are used to calculate the interaction of larger super-cells, where a carefully chosen size of the super-cell avoids the appearance of artifacts arising due to the periodicity [P16]. Such studies are only possible by having the lattice sum expression derived for complex unit cells. Furthermore, one benefits greatly from a fast implementation of the lattice sums. By having an analytical approach to describe the scatterers and their lattice interaction, a general framework to treat metasurfaces has been derived [P14] and inverse design approaches for bound states in the continuum were used [P9]. By using the combination of T-matrices and a description of time-varying scatterers [164–166], it is also possible to analyze four-dimensional metamaterials [P8]. We furthermore used the methods to simulate clusters of particles fabricated with self-assembly methods [P10, P11, P13].

Thus, we have demonstrated the usefulness of the combination of the T-matrix method, especially, its versatility by using different basis sets and modes of well-defined helicity and fast lattice sums for the implementation of periodic boundary conditions.

6.2 Outlook

In the following, we want to outline multiple possible developments based on the results of this thesis. Starting with the currently implemented methods, automatically differentiable programs can be explored. These approaches allow the use of gradient based optimizations that can be leveraged for the inverse design of structures. By having many analytic formulas for operations, the T-matrix method is an excellent candidate for this method. Furthermore, by being a method that relies on many linear algebra operations, *treams* can benefit from acceleration by using computations on graphical processing units GPUs. Furthermore, instead of using the T-matrix method for electromagnetic scattering, it can also be applied to acoustic scattering [84]. Thus, many of the results of this thesis could be reused or adapted to analyze acoustics.

A future enhancement of to *treams* could be including of T-matrices with distributed sources. By describing an object by multipole expansions at multiple origins, similar to the use of a local T-matrix for a cluster, the domain in the vicinity of the scatterer that is excluded by the Rayleigh hypothesis can be reduced [167]. This approach could enlarge the scope of *treams* considerably, e.g., by making close packings of objects with high aspect ratio possible. Another interesting possibility is the inclusion of not only finite and infinite systems, but also semi-infinite lattices, which can be used to analyze surface effects, such as surface second harmonic generation. Therefore, approaches to efficiently calculate semi-infinite lattice sums can be investigated [168–171] or S-matrix based methods can be used [172]. Moreover, the exploration of the influence of defects in the lattice structure is a potential future research endeavor.

Bibliography

[1] D. Schurig *et al.*, “Metamaterial Electromagnetic Cloak at Microwave Frequencies,” Science **314**, 977–980 (2006).

[2] S. Liu *et al.*, “Huygens’ Metasurfaces Enabled by Magnetic Dipole Resonance Tuning in Split Dielectric Nanoresonators,” Nano Letters **17**, 4297–4303 (2017).

[3] K. Koshelev *et al.*, “Asymmetric Metasurfaces with High- Q Resonances Governed by Bound States in the Continuum,” Physical Review Letters **121**, 193903 (2018).

[4] A. Overvig and A. Alù, “Diffractive Nonlocal Metasurfaces,” Laser & Photonics Reviews **16**, 2100633 (2022).

[5] N. Engheta, “Four-dimensional optics using time-varying metamaterials,” Science **379**, 1190–1191 (2023).

[6] P. L. McMahon, “The physics of optical computing,” Nature Reviews Physics, 1–18 (2023).

[7] I. Rodríguez-Ruiz *et al.*, “Photonic Lab-on-a-Chip: Integration of Optical Spectroscopy in Microfluidic Systems,” Analytical Chemistry **88**, 6630–6637 (2016).

[8] M. Deubel *et al.*, “Direct laser writing of three-dimensional photonic-crystal templates for telecommunications,” Nature Materials **3**, 444–447 (2004).

[9] O. Shekhah *et al.*, “Step-by-Step Route for the Synthesis of Metal—Organic Frameworks,” Journal of the American Chemical Society **129**, 15118–15119 (2007).

[10] S. Dey *et al.*, “DNA origami,” Nature Reviews Methods Primers **1**, 1–24 (2021).

[11] E. Popov, ed., *Gratings: Theory and Numeric Applications, Second Revisited Edition*, 2nd ed. (Institut Fresnel, AMU, 2014).

[12] P. C. Waterman, “Matrix formulation of electromagnetic scattering,” Proceedings of the IEEE **53**, 805–812 (1965).

[13] P. P. Ewald, “Die Berechnung optischer und elektrostatischer Gitterpotentiale,” Annalen der Physik **369**, 253–287 (1921).

[14] B. Richards and E. Wolf, “Electromagnetic diffraction in optical systems, II. Structure of the image field in an aplanatic system,” Proceedings of the Royal Society of London. Series A. Mathematical and Physical Sciences **253**, 358–379 (1959).

[15] P. M. Morse and H. Feshbach, *Methods of theoretical physics* (McGraw-Hill, New York, 1953).

[16] J. D. Jackson, *Classical Electrodynamics* (John Wiley & Sons Inc, July 27, 1998), 832 pp.

[17] G. Kristensson, *Scattering of Electromagnetic Waves by Obstacles* (SciTech Publishing Inc, Dec. 1, 2016), 760 pp.

[18] R. W. Boyd, *Nonlinear optics*, 3rd ed (Academic Press, Amsterdam ; Boston, 2008), 613 pp.

[19] F. W. J. Olver *et al.*, eds., *NIST digital library of mathematical functions*, Release 1.1.11, (Sept. 15, 2023) `http://dlmf.nist.gov/`.

[20] I. Fernandez-Corbaton, X. Zambrana-Puyalto, and G. Molina-Terriza, "Helicity and angular momentum: A symmetry-based framework for the study of light-matter interactions," Physical Review A **86**, 042103 (2012).

[21] L. Silberstein, "Elektromagnetische Grundgleichungen in bivektorieller Behandlung," Annalen der Physik **327**, 579–586 (1907).

[22] A. Lakhtakia, *Beltrami fields in chiral media* (World Scientific, Singapore; River Edge, NJ, 1994).

[23] M. I. Mishchenko, L. D. Travis, and D. W. Mackowski, "T-matrix computations of light scattering by nonspherical particles: A review," Journal of Quantitative Spectroscopy and Radiative Transfer **55**, 535–575 (1996).

[24] H. Huang *et al.*, "Propagation of Waves in Randomly Distributed Cylinders Using Three-Dimensional Vector Cylindrical Wave Expansions in Foldy–Lax Equations," IEEE Journal on Multiscale and Multiphysics Computational Techniques **4**, 214–226 (2019).

[25] G. Mie, "Beiträge zur Optik trüber Medien, speziell kolloidaler Metallösungen," Annalen der Physik **330**, 377–445 (1908).

[26] L. Tsang, J. A. Kong, and R. T. Shin, *Theory of Microwave Remote Sensing (Wiley Series in Remote Sensing and Image Processing)* (Wiley-Interscience, 1985).

[27] D. W. Mackowski, "Discrete dipole moment method for calculation of the T matrix for nonspherical particles," Journal of the Optical Society of America A **19**, 881–893 (2002).

[28] A. Rahimzadegan *et al.*, "Minimalist Mie coefficient model," Optics Express **28**, 16511–16525 (2020).

[29] C. F. Bohren, "Light scattering by an optically active sphere," Chemical Physics Letters **29**, 458–462 (1974).

[30] Q.-C. Shang *et al.*, "Scattering from a multilayered chiral sphere using an iterative method," Journal of Quantitative Spectroscopy and Radiative Transfer **173**, 72–82 (2016).

[31] F. Frezza, F. Mangini, and N. Tedeschi, "Introduction to electromagnetic scattering: tutorial," Journal of the Optical Society of America A **35**, 163–173 (2018).

[32] G. Demésy, J.-C. Auger, and B. Stout, "Scattering matrix of arbitrarily shaped objects: combining finite elements and vector partial waves," Journal of the Optical Society of America A **35**, 1401–1409 (2018).

[33] M. Fruhnert *et al.*, "Computing the T-matrix of a scattering object with multiple plane wave illuminations," Beilstein Journal of Nanotechnology **8**, 614–626 (2017).

[34] X. Garcia-Santiago *et al.*, "Decomposition of scattered electromagnetic fields into vector spherical wave functions on surfaces with general shapes," Physical Review B **99**, 045406 (2019).

[35] N. Asadova, “Inverse design of three-dimensional arrangements of scatterers,” Master’s thesis (Karlsruhe Institute of Technology (KIT), Oct. 2022).

[36] S. Stein, “Addition theorems for spherical wave functions,” Quarterly of Applied Mathematics **19**, 15–24 (1961).

[37] O. R. Cruzan, “Translational addition theorems for spherical vector wave functions,” Quarterly of Applied Mathematics **20**, 33–40 (1962).

[38] R. N. S. Suryadharma *et al.*, “Studying plasmonic resonance modes of hierarchical self-assembled meta-atoms based on their transfer matrix,” Physical Review B **96**, 045406 (2017).

[39] N. Stefanou, V. Yannopapas, and A. Modinos, “Heterostructures of photonic crystals: frequency bands and transmission coefficients,” Computer Physics Communications **113**, 49–77 (1998).

[40] E. C. Le Ru, W. R. C. Somerville, and B. Auguié, “Radiative correction in approximate treatments of electromagnetic scattering by point and body scatterers,” Physical Review A **87**, 012504 (2013).

[41] D. A. Varshalovich, A. N. Moskalev, and V. K. Khersonskii, *Quantum Theory of Angular Momemtum* (World Scientific Pub Co Inc, Oct. 11, 1988), 528 pp.

[42] G. Molina-Terriza, “Determination of the total angular momentum of a paraxial beam,” Physical Review A **78**, 053819 (2008).

[43] G. Han, Y. Han, and H. Zhang, “Relations between cylindrical and spherical vector wavefunctions,” Journal of Optics A: Pure and Applied Optics **10**, 015006 (2007).

[44] R. C. Wittmann, “Spherical wave operators and the translation formulas,” IEEE Transactions on Antennas and Propagation **36**, 1078–1087 (1988).

[45] G. Cincotti *et al.*, “Plane wave expansion of cylidrical functions,” Optics Communications **95**, 192–198 (1993).

[46] D. Theobald *et al.*, “Plane wave coupling formalism for T-matrix simulations of light scattering by non-spherical particles,” Physical Review A **96**, 033822 (2017).

[47] J. Korringa, “On the calculation of the energy of a Bloch wave in a metal,” Physica **13**, 392–400 (1947).

[48] W. Kohn and N. Rostoker, “Solution of the Schrödinger Equation in Periodic Lattices with an Application to Metallic Lithium,” Physical Review **94**, 1111–1120 (1954).

[49] F. S. Ham and B. Segall, “Energy Bands in Periodic Lattices—Green’s Function Method,” Physical Review **124**, 1786–1796 (1961).

[50] K. Kambe, “Theory of Low-Energy Electron Diffraction (I. Application of the Cellular Method to Monatomic Layers),” Zeitschrift für Naturforschung A **22**, 322–330 (1967).

[51] K. Kambe, “Theory of Low-Energy Electron Diffraction (II. Cellular Method for Complex Monolayers and Multilayers),” Zeitschrift für Naturforschung A **23**, 1280–1294 (1968).

[52] J. B. Pendry, *Low Energy Electron Diffraction: The Theory and Its Application to Determination of Surface Structure (Techniques of physics)* (Academic Press, 1974).

[53] A. Moroz, “Quasi-periodic Green’s functions of the Helmholtz and Laplace equations,” Journal of Physics A: Mathematical and General **39**, 11247–11282 (2006).

[54] C. M. Linton, “Lattice Sums for the Helmholtz Equation,” SIAM Review **52**, 630–674 (2010).

[55] V. Eyert, *The augmented spherical wave method: a comprehensive treatment*, Second edition, Lecture Notes in Physics 849 (Springer, Heidelberg, 2012), 379 pp.

[56] K. Amemiya and K. Ohtaka, “Calculation of Transmittance of Light for an Array of Dielectric Rods Using Vector Cylindrical Waves: Complex Unit Cells,” Journal of the Physical Society of Japan **72**, 1244–1253 (2003).

[57] M. Nečada and P. Törmä, “Multiple-Scattering T-Matrix Simulations for Nanophotonics: Symmetries and Periodic Lattices,” Communications in Computational Physics **30**, 357–395 (2021).

[58] P. Yeh, “Electromagnetic propagation in birefringent layered media,” Journal of the Optical Society of America **69**, 742 (1979).

[59] P. Yeh, *Optical waves in layered media*, Wiley Series in Pure and Applied Optics (Wiley, New York, 1988), 406 pp.

[60] L. Novotny and B. Hecht, *Principles of nano-optics*, 2nd ed (Cambridge University Press, Cambridge, 2012), 564 pp.

[61] S. Wang *et al.*, “Optical sharper focusing in an anisotropic crystal,” Journal of the Optical Society of America A **32**, 1026 (2015).

[62] K. Ohtaka, T. Ueta, and K. Amemiya, “Calculation of photonic bands using vector cylindrical waves and reflectivity of light for an array of dielectric rods,” Physical Review B **57**, 2550–2568 (1998).

[63] H. Solbrig, “On the Ewald Summation Technique for 2D Lattices,” physica status solidi (a) **72**, 199–205 (1982).

[64] I. S. Gradštejn and I. M. Ryžik, *Table of Integrals, Series, and Products*, edited by D. Zwillinger (Elsevier Science, Sept. 18, 2014), 1184 pp.

[65] R. B. Paris, *Chapter 8 Incomplete Gamma and Related Functions*, 2022.

[66] M. Abramowitz and I. A. Stegun, eds., *Handbook of Mathematical Functions* (Dover Publications Inc., June 1, 1965), 1046 pp.

[67] W. Magnus, F. Oberhettinger, and R. P. Soni, *Formulas and theorems for the special functions of mathematical physics*, Third, Vol. 52, Die Grundlehren Der Mathematischen Wissenschaften in Einzeldarstellungen (Springer, Berlin, 1966).

[68] F. Capolino, D. Wilton, and W. Johnson, “Efficient computation of the 2-D Green’s function for 1-D periodic structures using the Ewald method,” IEEE Transactions on Antennas and Propagation **53**, 2977–2984 (2005).

[69] F. Capolino, D. R. Wilton, and W. A. Johnson, “Efficient computation of the 3D Green’s function for the Helmholtz operator for a linear array of point sources using the Ewald method,” Journal of Computational Physics **223**, 250–261 (2007).

[70] K. E. Jordan, G. R. Richter, and P. Sheng, “An efficient numerical evaluation of the Green’s function for the Helmholtz operator on periodic structures,” Journal of Computational Physics **63**, 222–235 (1986).

[71] G. Lovat, P. Burghignoli, and R. Araneo, “Efficient Evaluation of the 3-D Periodic Green’s Function Through the Ewald Method,” IEEE Transactions on Microwave Theory and Techniques **56**, 2069–2075 (2008).

[72] A. Kustepeli and A. Martin, “On the splitting parameter in the Ewald method,” IEEE Microwave and Guided Wave Letters **10**, 168–170 (2000).

[73] I. Stevanoviæ and J. R. Mosig, “Periodic Green’s function for skewed 3-D lattices using the Ewald transformation,” Microwave and Optical Technology Letters **49**, 1353–1357 (2007).

[74] A. Groner, “Analysing diffraction from periodically arranged scatterers while considering their T-Matrix,” Master’s thesis (Karlsruhe Institute of Technology (KIT), June 2018).

[75] T. Wriedt and J. Hellmers, “New Scattering Information Portal for the light-scattering community,” Journal of Quantitative Spectroscopy and Radiative Transfer, X Conference on Electromagnetic and Light Scattering by Non-Spherical Particles **109**, 1536–1542 (2008).

[76] J. Hellmers and T. Wriedt, “New approaches for a light scattering Internet information portal and categorization schemes for light scattering software,” Journal of Quantitative Spectroscopy and Radiative Transfer, XI Conference on Electromagnetic and Light Scattering by Non-Spherical Particles: 2008 **110**, 1511–1517 (2009).

[77] A. Doicu, Yu. A. Eremin, and T. Wriedt, “Convergence of the T-matrix method for light scattering from a particle on or near a surface,” Optics Communications **159**, 266–277 (1999).

[78] T. Wriedt, “Review of the null-field method with discrete sources,” Journal of Quantitative Spectroscopy and Radiative Transfer, IX Conference on Electromagnetic and Light Scattering by Non-Spherical Particles **106**, 535–545 (2007).

[79] J. Markkanen and A. J. Yuffa, “Fast superposition T-matrix solution for clusters with arbitrarily-shaped constituent particles,” Journal of Quantitative Spectroscopy and Radiative Transfer **189**, 181–188 (2017).

[80] A. Egel *et al.*, “Extending the applicability of the T-matrix method to light scattering by flat particles on a substrate via truncation of sommerfeld integrals,” Journal of Quantitative Spectroscopy and Radiative Transfer **202**, 279–285 (2017).

[81] A. Egel *et al.*, “CELES: CUDA-accelerated simulation of electromagnetic scattering by large ensembles of spheres,” Journal of Quantitative Spectroscopy and Radiative Transfer **199**, 103–110 (2017).

[82] D. Schebarchov *et al.*, “Multiple scattering of light in nanoparticle assemblies: User guide for the terms program,” Journal of Quantitative Spectroscopy and Radiative Transfer **284**, 108131 (2022).

[83] N. Stefanou, V. Yannopapas, and A. Modinos, “MULTEM 2: A new version of the program for transmission and band-structure calculations of photonic crystals,” Computer Physics Communications **132**, 189–196 (2000).

[84] P. C. Waterman, “T-matrix methods in acoustic scattering,” The Journal of the Acoustical Society of America **125**, 42–51 (2009).

[85] C. R. Harris *et al.*, “Array programming with NumPy,” Nature **585**, 357–362 (2020).

[86] P. Virtanen *et al.*, “SciPy 1.0: fundamental algorithms for scientific computing in Python,” Nature Methods **17**, 261–272 (2020).

[87] H. Dachsel, “Fast and accurate determination of the Wigner rotation matrices in the fast multipole method,” The Journal of Chemical Physics **124**, 144115 (2006).

[88] Y.-l. Xu, “Efficient Evaluation of Vector Translation Coefficients in Multiparticle Light-Scattering Theories,” Journal of Computational Physics **139**, 137–165 (1998).

[89] J. Rumbaugh, I. Jacobson, and G. Booch, *The unified modeling language reference manual*, 2nd ed, The Addison-Wesley Object Technology Series (Addison-Wesley, Boston, 2005), 721 pp.

[90] I. Fernandez-Corbaton, “Forward and backward helicity scattering coefficients for systems with discrete rotational symmetry,” Optics Express **21**, 29885–29893 (2013).

[91] F. Graf, “Electromagnetically Dual Nanostructures for Enhanced Circular Dichroism Spectroscopy,” Master’s thesis (Karlsruhe Institute of Technology (KIT), Feb. 2018).

[92] M. Scheffler *et al.*, “FAIR data enabling new horizons for materials research,” Nature **604**, 635–642 (2022).

[93] S. Maruo, O. Nakamura, and S. Kawata, “Three-dimensional microfabrication with two-photon-absorbed photopolymerization,” Optics Letters **22**, 132–134 (1997).

[94] L. Yang *et al.*, “Multi-material multi-photon 3D laser micro- and nanoprinting,” Light: Advanced Manufacturing **2**, 296–312 (2021).

[95] L. A. Nguyen, H. He, and C. Pham-Huy, “Chiral Drugs: An Overview,” International Journal of Biomedical Science : IJBS **2**, 85–100 (2006).

[96] J.-P. Behr, ed., *The lock-and-key principle: the state of the art–100 years on*, Perspectives in Supramolecular Chemistry v. 1 (Wiley, Chichester [England] ; New York, 1994), 325 pp.

[97] M. Vavilin and I. Fernandez-Corbaton, “Multidimensional measures of electromagnetic chirality and their conformal invariance,” New Journal of Physics **24**, 033022 (2022).

[98] L. D. Barron, *Molecular light scattering and optical activity* (Cambridge University Press, Cambridge, 2004).

[99] L. A. Nafie, *Vibrational optical activity: principles and applications* (Wiley, Chichester, West Sussex, 2011), 378 pp.

[100] E. Hendry *et al.*, “Ultrasensitive detection and characterization of biomolecules using superchiral fields,” Nature Nanotechnology **5**, 783–787 (2010).

[101] B. Auguié *et al.*, “Fingers Crossed: Optical Activity of a Chiral Dimer of Plasmonic Nanorods,” The Journal of Physical Chemistry Letters **2**, 846–851 (2011).

[102] E. Hendry *et al.*, “Chiral Electromagnetic Fields Generated by Arrays of Nanoslits,” Nano Letters **12**, 3640–3644 (2012).

[103] M. Hentschel *et al.*, “Three-Dimensional Chiral Plasmonic Oligomers,” Nano Letters **12**, 2542–2547 (2012).

[104] M. Schäferling *et al.*, “Tailoring Enhanced Optical Chirality: Design Principles for Chiral Plasmonic Nanostructures,” Physical Review X **2**, 031010 (2012).

[105] Y. Zhao *et al.*, “Chirality detection of enantiomers using twisted optical metamaterials,” Nature Communications **8**, 14180 (2017).

[106] L. V. Poulikakos *et al.*, “Chiral Light Design and Detection Inspired by Optical Antenna Theory,” Nano Letters **18**, 4633–4640 (2018).

[107] M. Rajaei *et al.*, “Giant Circular Dichroism at Visible Frequencies Enabled by Plasmonic Ramp-Shaped Nanostructures,” ACS Photonics **6**, 924–931 (2019).

[108] T. Iida *et al.*, “Super-chiral vibrational spectroscopy with metasurfaces for high-sensitive identification of alanine enantiomers,” Applied Physics Letters **117**, 101103 (2020).

[109] A. O. Govorov *et al.*, “Theory of Circular Dichroism of Nanomaterials Comprising Chiral Molecules and Nanocrystals: Plasmon Enhancement, Dipole Interactions, and Dielectric Effects,” Nano Letters **10**, 1374–1382 (2010).

[110] M. Schäferling, X. Yin, and H. Giessen, “Formation of chiral fields in a symmetric environment,” Optics Express **20**, 26326–26336 (2012).

[111] A. García-Etxarri and J. A. Dionne, “Surface-enhanced circular dichroism spectroscopy mediated by nonchiral nanoantennas,” Physical Review B **87**, 235409 (2013).

[112] M. L. Nesterov *et al.*, “The Role of Plasmon-Generated Near Fields for Enhanced Circular Dichroism Spectroscopy,” ACS Photonics **3**, 578–583 (2016).

[113] C.-S. Ho *et al.*, “Enhancing Enantioselective Absorption Using Dielectric Nanospheres,” ACS Photonics **4**, 197–203 (2017).

[114] E. Mohammadi *et al.*, “Nanophotonic Platforms for Enhanced Chiral Sensing,” ACS Photonics **5**, 2669–2675 (2018).

[115] A. Vázquez-Guardado and D. Chanda, “Superchiral Light Generation on Degenerate Achiral Surfaces,” Physical Review Letters **120**, 137601 (2018).

[116] J. Garcia-Guirado *et al.*, “Enhanced chiral sensing with dielectric nano-resonators,” Nano Letters, `10.1021/acs.nanolett.9b04334` (2019).

[117] F. Graf *et al.*, “Achiral, Helicity Preserving, and Resonant Structures for Enhanced Sensing of Chiral Molecules,” ACS Photonics **6**, 482–491 (2019).

[118] B. Semnani *et al.*, “Spin-Preserving Chiral Photonic Crystal Mirror,” Nov. 20, 2019.

[119] M. L. Solomon *et al.*, "Enantiospecific Optical Enhancement of Chiral Sensing and Separation with Dielectric Metasurfaces," ACS Photonics **6**, 43–49 (2019).

[120] S. Droulias and L. Bougas, "Absolute Chiral Sensing in Dielectric Metasurfaces Using Signal Reversals," Nano Letters **20**, 5960–5966 (2020).

[121] M. Hanifeh and F. Capolino, "Helicity maximization in a planar array of achiral high-density dielectric nanoparticles," Journal of Applied Physics **127**, 093104 (2020).

[122] M. Hanifeh, M. Albooyeh, and F. Capolino, "Optimally Chiral Light: Upper Bound of Helicity Density of Structured Light for Chirality Detection of Matter at Nanoscale," ACS Photonics **7**, 2682–2691 (2020).

[123] M. L. Solomon *et al.*, "Fluorescence-Detected Circular Dichroism of a Chiral Molecular Monolayer with Dielectric Metasurfaces," Journal of the American Chemical Society **142**, 18304–18309 (2020).

[124] V. Hahn *et al.*, "3-D Laser Nanoprinting," Optics and Photonics News **30**, 28–35 (2019).

[125] J. del Barrio and C. Sánchez-Somolinos, "Light to Shape the Future: From Photolithography to 4D Printing," Advanced Optical Materials **7**, 1900598 (2019).

[126] C. M. González-Henríquez, M. A. Sarabia-Vallejos, and J. Rodriguez-Hernandez, "Polymers for additive manufacturing and 4D-printing: Materials, methodologies, and biomedical applications," Progress in Polymer Science **94**, 57–116 (2019).

[127] X. Kuang *et al.*, "Advances in 4D Printing: Materials and Applications," Advanced Functional Materials **29**, 1805290 (2019).

[128] S. Joshi *et al.*, "4D printing of materials for the future: Opportunities and challenges," Applied Materials Today **18**, 100490 (2020).

[129] C. A. Spiegel *et al.*, "4D Printing at the Microscale," Advanced Functional Materials **30**, 1907615 (2020).

[130] T. J. White and D. J. Broer, "Programmable and adaptive mechanics with liquid crystal polymer networks and elastomers," Nature Materials **14**, 1087–1098 (2015).

[131] L. Tan, A. C. Davis, and D. J. Cappelleri, "Smart Polymers for Microscale Machines," Advanced Functional Materials **31**, 2007125 (2021).

[132] R. Haldar *et al.*, "Guest-responsive polaritons in a porous framework: chromophoric sponges in optical QED cavities," Chemical Science **11**, 7972–7978 (2020).

[133] S. L. James, "Metal-organic frameworks," Chemical Society Reviews **32**, 276–288 (2003).

[134] R. Gao, M. S. Kodaimati, and D. Yan, "Recent advances in persistent luminescence based on molecular hybrid materials," Chemical Society Reviews **50**, 5564–5589 (2021).

[135] T. Viswanathan *et al.*, "Enhancement of Second-Order Nonlinear Optical Properties of Centrosymmetric Ferrocenyl Borasiloxane by a Broken-Symmetry Approach," The Journal of Physical Chemistry C **125**, 8732–8740 (2021).

[136] Y. Wang *et al.*, "Stimulated Raman scattering signal amplification in ethanol molecules via resonant cascading," Applied Physics Letters **118**, 121102 (2021).

[137] J.-L. Zhuang, A. Terfort, and C. Wöll, “Formation of oriented and patterned films of metal–organic frameworks by liquid phase epitaxy: A review,” Coordination Chemistry Reviews, Chemistry and Applications of Metal Organic Frameworks **307**, 391–424 (2016).

[138] R. Bast *et al.*, “The ab initio calculation of molecular electric, magnetic and geometric properties,” Physical Chemistry Chemical Physics **13**, 2627–2651 (2011).

[139] T. Helgaker *et al.*, “Recent Advances in Wave Function-Based Methods of Molecular-Property Calculations,” Chemical Reviews **112**, 543–631 (2012).

[140] C. Holzer, “An improved seminumerical Coulomb and exchange algorithm for properties and excited states in modern density functional theory,” The Journal of Chemical Physics **153**, 184115 (2020).

[141] G. Gantzounis and N. Stefanou, “Layer-multiple-scattering method for photonic crystals of nonspherical particles,” Physical Review B **73**, 035115 (2006).

[142] Y. Jiang, S. Pillai, and M. A. Green, “Realistic Silver Optical Constants for Plasmonics,” Scientific Reports **6**, 30605 (2016).

[143] J. B. Pendry, “Negative Refraction Makes a Perfect Lens,” Physical Review Letters **85**, 3966–3969 (2000).

[144] A. Ishimaru *et al.*, “Generalized constitutive relations for metamaterials based on the quasi-static Lorentz theory,” IEEE Transactions on Antennas and Propagation **51**, 2550–2557 (2003).

[145] P. A. Belov and C. R. Simovski, “Homogenization of electromagnetic crystals formed by uniaxial resonant scatterers,” Physical Review E **72**, 026615 (2005).

[146] M. G. Silveirinha, “Nonlocal homogenization model for a periodic array of $ϵ$-negative rods,” Physical Review E **73**, 046612 (2006).

[147] D. R. Smith and J. B. Pendry, “Homogenization of metamaterials by field averaging (invited paper),” Journal of the Optical Society of America B **23**, 391–403 (2006).

[148] M. G. Silveirinha, “Metamaterial homogenization approach with application to the characterization of microstructured composites with negative parameters,” Physical Review B **75**, 115104 (2007).

[149] M. G. Silveirinha, “Generalized Lorentz-Lorenz formulas for microstructured materials,” Physical Review B **76**, 245117 (2007).

[150] M. G. Silveirinha and P. A. Belov, “Spatial dispersion in lattices of split ring resonators with permeability near zero,” Physical Review B **77**, 233104 (2008).

[151] A. Alù, “First-principles homogenization theory for periodic metamaterials,” Physical Review B **84**, 075153 (2011).

[152] A. V. Chebykin, M. A. Gorlach, and P. A. Belov, “Spatial-dispersion-induced birefringence in metamaterials with cubic symmetry,” Physical Review B **92**, 045127 (2015).

[153] A. Ciattoni and C. Rizza, “Nonlocal homogenization theory in metamaterials: Effective electromagnetic spatial dispersion and artificial chirality,” Physical Review B **91**, 184207 (2015).

[154] G. T. Papadakis, P. Yeh, and H. A. Atwater, “Retrieval of material parameters for uniaxial metamaterials,” Physical Review B **91**, 155406 (2015).

[155] K. Mnasri *et al.*, “Beyond local effective material properties for metamaterials,” Physical Review B **97**, 075439 (2018).

[156] K. Mnasri *et al.*, “Homogenization of wire media with a general purpose nonlocal constitutive relation,” Journal of the Optical Society of America **36**, F99–F108 (2019).

[157] K. Mnasri *et al.*, “Retrieving effective material parameters of metamaterials characterized by nonlocal constitutive relations,” Physical Review B **99**, 035442 (2019).

[158] T. Repän, R. Venkitakrishnan, and C. Rockstuhl, “Artificial neural networks used to retrieve effective properties of metamaterials,” Optics Express **29**, 36072–36085 (2021).

[159] A. N. M. S. Hossain, I. Tsukerman, and V. A. Markel, “Homogenization of periodic structures: One layer is “bulk”,” Europhysics Letters **138**, 35001 (2022).

[160] C. R. Simovski, “On electromagnetic characterization and homogenization of nanostructured metamaterials,” Journal of Optics **13**, 013001 (2010).

[161] A. Aharoni, “Demagnetizing factors for rectangular ferromagnetic prisms,” Journal of Applied Physics **83**, 3432–3434 (1998).

[162] C. Menzel *et al.*, “Extreme coupling: A route towards local magnetic metamaterials,” Physical Review B **89**, 155125 (2014).

[163] S. Babar and J. H. Weaver, “Optical constants of Cu, Ag, and Au revisited,” Applied Optics **54**, 477–481 (2015).

[164] I. Sekulic, J. W. You, and N. C. Panoiu, “T-matrix method for calculation of second-harmonic generation in clusters of spherical particles,” Journal of Quantitative Spectroscopy and Radiative Transfer **268**, 107643 (2021).

[165] G. Ptitcyn *et al.*, “Scattering of light by spheres made from a time-modulated and dispersive material,” in 2021 Fifteenth International Congress on Artificial Materials for Novel Wave Phenomena (Metamaterials) (Sept. 2021), pp. 347–349.

[166] G. Ptitcyn *et al.*, “Floquet–Mie Theory for Time-Varying Dispersive Spheres,” Laser & Photonics Reviews **17**, 2100683 (2023).

[167] A. G. Lamprianidis, C. Rockstuhl, and I. Fernandez-Corbaton, “Transcending the Rayleigh Hypothesis with multipolar sources distributed across the topological skeleton of a scatterer,” Journal of Quantitative Spectroscopy and Radiative Transfer **296**, 108455 (2023).

[168] C. Craeye, A. Tijhuis, and D. Schaubert, “An efficient MoM formulation for finite-by-infinite arrays of two-dimensional antennas arranged in a three-dimensional structure,” IEEE Transactions on Antennas and Propagation **52**, 271–282 (2004).

[169] C. Craeye and F. Capolino, “Accelerated computation of the free space Green’s function of semi-infinite phased arrays of dipoles,” IEEE Transactions on Antennas and Propagation **54**, 1037–1040 (2006).

[170] C. M. Linton and P. A. Martin, “Semi-Infinite Arrays of Isotropic Point Scatterers. A Unified Approach,” SIAM Journal on Applied Mathematics **64**, 1035–1056 (2004).

[171] C. M. Linton, “Schlömilch series that arise in diffraction theory and their efficient computation,” Journal of Physics A: Mathematical and General **39**, 3325–3339 (2006).

[172] L. C. Botten *et al.*, “Photonic band structure calculations using scattering matrices,” Physical Review E **64**, 046603 (2001).

[173] G. Czycholl, *Theoretische Festkörperphysik. Grundlagen: Phononen und Elektronen in Kristallen*, 4. Auflage (Springer Spektrum, Berlin Heidelberg, 2016), 410 pp.

Appendix

A Fourier transform and Poisson's formula

We use the following definition of the function $f(t)$ depending on the time t in terms of its Fourier transform $\tilde{f}(k_0)$

$$f(t) = c \int_{-\infty}^{\infty} \mathrm{d}k_0 \, \tilde{f}(k_0) \, \mathrm{e}^{-\mathrm{i}ck_0 t} \,, \tag{A.1}$$

where we express the dependence in frequency space by the wave number $k_0 = \frac{\omega}{c}$ instead of the angular frequency ω using the speed of light in vacuum c. The inverse transformation is then defined by

$$\tilde{f}(k_0) = \frac{1}{2\pi} \int_{-\infty}^{\infty} \mathrm{d}t \, f(t) \, \mathrm{e}^{\mathrm{i}ck_0 t} \,. \tag{A.2}$$

Similarly, for a function $f(\boldsymbol{r})$ in real space depending on the spatial coordinates $\boldsymbol{r} \in \mathbb{R}^d$, we define

$$f(\boldsymbol{r}) = \int_{\mathbb{R}^d} \mathrm{d}^d \boldsymbol{q} \underline{f}(\boldsymbol{q}) \mathrm{e}^{\mathrm{i}\boldsymbol{q}\boldsymbol{r}} \tag{A.3}$$

and its inverse

$$\underline{f}(\boldsymbol{q}) = \frac{1}{(2\pi)^d} \int_{\mathbb{R}^d} \mathrm{d}^d \boldsymbol{r} f(\boldsymbol{r}) \mathrm{e}^{-\mathrm{i}\boldsymbol{q}\boldsymbol{r}} \,, \tag{A.4}$$

where $\boldsymbol{q} \in \mathbb{R}^d$ is the reciprocal space coordinate vector.

Furthermore, these definitions lead to the Poisson sum formula for a lattice $\Lambda_d = \{\sum_{i=1}^d n_i \boldsymbol{u}_i | n_i \in \mathbb{Z}\}$ of dimension d, where $\boldsymbol{u}_i \in \mathbb{R}^d, \ i \in \{1, \dots, d\}$ are its basis vectors, given by [173]

$$\sum_{\boldsymbol{R} \in \Lambda_d} f(\boldsymbol{R}) = \frac{(2\pi)^d}{V_d} \sum_{\boldsymbol{Q} \in \Lambda_d^*} \underline{f}(\boldsymbol{Q}) \,. \tag{A.5}$$

The vectors $\boldsymbol{Q}$ are elements of the reciprocal lattice $\Lambda_d^* = \{\sum_{i=1}^d n_i \boldsymbol{v}_i | n_i \in \mathbb{Z}\}$, with basis vectors $\boldsymbol{v}_j \in \mathbb{R}^d, \ j \in \{1, \dots, d\}$ fulfilling $\boldsymbol{v}_j \boldsymbol{u}_i = 2\pi \delta_{ij}$.

B Cylindrical and spherical coordinate systems

The cylindrical coordinates ρ, φ, and z are implicitly defined by

$$x = \rho \cos\varphi \tag{B.1a}$$

$$y = \rho \sin\varphi \tag{B.1b}$$

$$z = z \tag{B.1c}$$

in terms of the Cartesian coordinates x, y, and z. Likewise, the spherical coordinates r, θ, and φ are

$$x = r\sin\theta\cos\varphi \tag{B.2a}$$
$$y = r\sin\theta\sin\varphi \tag{B.2b}$$
$$z = r\cos\theta\,. \tag{B.2c}$$

With these definitions, a distinction between φ in cylindrical and spherical coordinates is not necessary because it coincides. The unit vectors in these coordinate systems that form a right-handed set are $\hat{\boldsymbol{\rho}}$, $\hat{\boldsymbol{\varphi}}$, and $\hat{\boldsymbol{z}}$ in cylindrical coordinates and $\hat{\boldsymbol{r}}$, $\hat{\boldsymbol{\theta}}$, and $\hat{\boldsymbol{\varphi}}$ in spherical coordinates, where the unit vectors are defined by

$$\hat{\boldsymbol{\rho}} = \hat{\boldsymbol{x}}\cos\varphi + \hat{\boldsymbol{y}}\sin\varphi \tag{B.3a}$$
$$\hat{\boldsymbol{\varphi}} = -\hat{\boldsymbol{x}}\sin\varphi + \hat{\boldsymbol{y}}\cos\varphi \tag{B.3b}$$
$$\hat{\boldsymbol{r}} = \hat{\boldsymbol{x}}\sin\theta\cos\varphi + \hat{\boldsymbol{y}}\sin\theta\sin\varphi + \hat{\boldsymbol{z}}\cos\theta \tag{B.3c}$$
$$\hat{\boldsymbol{\theta}} = \hat{\boldsymbol{x}}\cos\theta\cos\varphi + \hat{\boldsymbol{y}}\cos\theta\sin\varphi - \hat{\boldsymbol{z}}\sin\theta\,. \tag{B.3d}$$

The ambiguity of φ for $x = 0 = y$ is lifted by setting $\varphi = 0$ in that case. If additionally $z = 0$, we also set $\theta = 0$.

We also use these coordinates in reciprocal space for the wave vectors $\boldsymbol{k}$ with Cartesian components k_x, k_y, and k_z instead of $\boldsymbol{r}$ with Cartesian components x, y, and z. We then use the following notation: k instead of r, k_ρ instead of ρ, $\hat{\boldsymbol{k}}$ instead of $\hat{\boldsymbol{r}}$. For all other quantities $\boldsymbol{k}$ is added as subscript, e.g., $\varphi_{\boldsymbol{k}}$.

C Associated Legendre polynomials and spherical harmonics

The spherical harmonics used in this thesis are defined as

$$Y_{lm}(\theta,\varphi) = \sqrt{\frac{2l+1}{4\pi}\frac{(l-m)!}{(l+m)!}}P_l^m(\cos\theta)\mathrm{e}^{\mathrm{i}m\varphi}\,, \tag{C.1}$$

where the polar dependency is given by the associated Legendre polynomials, which can be derived from the Legendre polynomials $P_l(x)$ by

$$P_l^m(x) = (-1)^m\left(1-x^2\right)^{\frac{m}{2}}\frac{\mathrm{d}^m}{\mathrm{d}x^m}P_l(x) \tag{C.2}$$
$$= \frac{(-1)^m}{2^l l!}\left(1-x^2\right)^{\frac{m}{2}}\frac{\mathrm{d}^{l+m}}{\mathrm{d}x^{l+m}}\left(x^2-1\right)^l\,. \tag{C.3}$$

In the second equation, we used Rodrigues' formula. While the first equation, strictly speaking, is only valid for $m \geq 0$ the second equation of this definition can be extended to $|m| \leq l$. However, associated Legendre polynomials of opposite m are related by

$$P_l^{-m}(x) = (-1)^m\frac{(l-m)!}{(l+m)!}P_l^m(x)\,. \tag{C.4}$$

A very useful representation of the associated Legendre polynomials for this thesis in case of the often encountered argument of $\cos\theta = \frac{z}{\sqrt{\rho^2+z^2}}$ is

$$P_l^{|m|}\left(\frac{z}{\sqrt{\rho^2+z^2}}\right) = \sum_{j=0}^{\lfloor\frac{l-|m|}{2}\rfloor} \frac{(-1)^{j+|m|}(l-2j)!}{2^l(l-|m|-2j)!}\binom{l}{j}\binom{2l-2j}{l}\frac{z^{l-|m|-2j}\rho^{|m|}}{\sqrt{\rho^2+z^2}^{l-2j}} \tag{C.5}$$

that is obtained by applying Eq. (C.2) to

$$P_l(x) = \frac{1}{2^l}\sum_{j=0}^{\lfloor\frac{l}{2}\rfloor}(-1)^j\binom{l}{j}\binom{2l-2j}{l}x^{l-2j}\,. \tag{C.6}$$

First, we pull out the factors independent of the sum

$$\begin{aligned}P_l^{|m|}\left(\frac{z}{\sqrt{\rho^2+z^2}}\right) =& \frac{(-1)^{|m|}\rho^{|m|}}{2^l\sqrt{\rho^2+z^2}^l}\sum_{j=0}^{\lfloor\frac{l-|m|}{2}\rfloor}\frac{(-1)^j(l-2j)!}{(l-|m|-2j)!}\binom{l}{j}\binom{2l-2j}{l}\\ &\cdot\sum_{s=0}^{j}\binom{j}{s}\rho^{2s}z^{l-|m|-2s}\,.\end{aligned} \tag{C.7}$$

After rearranging the two sums to get a factor independent of z and ρ, we have

$$\begin{aligned}P_l^{|m|}\left(\frac{z}{\sqrt{\rho^2+z^2}}\right) =& \frac{(-1)^{|m|}\rho^{|m|}}{2^l\sqrt{\rho^2+z^2}^l}\sum_{s=0}^{\lfloor\frac{l-|m|}{2}\rfloor}\frac{\rho^{2s}z^{l-|m|-2s}}{s!}\\ &\cdot\sum_{j=s}^{\lfloor\frac{l-|m|}{2}\rfloor}\frac{(-1)^j(2l-2j)!}{(l-|m|-2j)!(l-j)!(j-s)!}\,.\end{aligned} \tag{C.8}$$

The second sum now fulfills the formula

$$f(l,m,s) = \sum_{j=s}^{\lfloor\frac{l-m}{2}\rfloor}\frac{(-1)^j(2l-2j)!}{(l-m-2j)!(l-j)!(j-s)!} = \frac{(-1)^s(l+m)!2^{l-m-2s}}{(l-m-2s)!(s+m)!}\,, \tag{C.9}$$

for integer values l, m, and s with $l \geq m$. This can be proven by recursion via

$$f(l+1,m,s) = 2(f(l,m,s)+(l+m)f(l,m-1,s)) \tag{C.10}$$

and the starting value

$$f(l,-l,s) = \delta_{ls}(-1)^l\,. \tag{C.11}$$

Hence, we get

$$P_l^m\left(\frac{z}{\sqrt{\rho^2+z^2}}\right) = \frac{(-1)^{\frac{|m|+m}{2}}}{\sqrt{\rho^2+z^2}^l}\sum_{s=0}^{\lfloor\frac{l-|m|}{2}\rfloor}\frac{(-1)^s(l+m)!\rho^{2s+|m|}z^{l-|m|-2s}}{2^{2s+|m|}(l-|m|-2s)!(s+|m|)!s!}\,, \tag{C.12}$$

where we used Eq. (C.4) to also include negative values of m.

D Displacement field and magnetic flux density expansion

Based on the expansions in Eqs. (2.31) and (2.32) and the constitutive relations Eq. (2.7), we can expand the displacement field by

$$\boldsymbol{\mathcal{D}}(\boldsymbol{r}; k_0) = \frac{1}{Z(k_0)} \sum_{s=\pm 1} \sum_{\nu} s n_s(k_0) a_{\nu s} \boldsymbol{A}_{\nu s}(\boldsymbol{r}, k_s(k_0)) \,, \tag{D.1}$$

the magnetic flux density as

$$\boldsymbol{\mathcal{B}}(\boldsymbol{r}; k_0) = -\mathrm{i} \sum_{s=\pm 1} \sum_{\nu} s n_s(k_0) a_{\nu s} \boldsymbol{A}_{\nu s}(\boldsymbol{r}, k_s(k_0)) \,, \tag{D.2}$$

and the alternative definition of the Riemann-Silberstein vectors

$$\begin{aligned} \boldsymbol{\mathcal{F}}_\pm(\boldsymbol{r}; k_0) &= \frac{\frac{\boldsymbol{\mathcal{D}}(\boldsymbol{r}; k_0)}{\epsilon(k_0)} \pm \mathrm{i} \frac{\boldsymbol{\mathcal{B}}(\boldsymbol{r}; k_0)}{n(k_0)}}{\sqrt{2}} \\ &= \sqrt{2} \frac{n_\pm(k_0)}{n(k_0)} \sum_{\nu} a_{\nu\pm} \boldsymbol{A}_{\nu\pm}(\boldsymbol{r}, k_\pm(k_0)) = \frac{n_s(k_0)}{n(k_0)} \boldsymbol{\mathcal{G}}_\pm(\boldsymbol{r}; k_0) \end{aligned} \tag{D.3}$$

that diagonalize the equations in chiral media like the fields $\boldsymbol{\mathcal{G}}_\pm(\boldsymbol{r}; k_0)$.

E Interface matrices for spheres and cylinders

We define the following quantities

$$a^{n\nu}_{s\sigma} = \left(\frac{(\tilde{x}_s z_l^{(n)}(\tilde{x}_s))'}{\tilde{x}_s} z_l^{(\nu)}(x_\sigma) - s\sigma z_l^{(n)}(\tilde{x}_s) \frac{(x_\sigma z_l^{(\nu)}(x_\sigma))'}{x_\sigma} \right) \frac{\tilde{Z} - s\sigma Z}{Z} \tilde{x}_s^2 \tag{E.1}$$

$$A^{n\nu}_{s\sigma} = \left(Z_l^{(n)\prime}(\tilde{x}_s) Z_l^{(\nu)}(x_\sigma) - s\sigma Z_l^{(n)}(\tilde{x}_s) Z_l^{(\nu)\prime}(x_\sigma) \right) \frac{\tilde{Z} - s\sigma Z}{Z} \tilde{x}_s \,, \tag{E.2}$$

where $n, \nu \in \{1, 3\}$ indicate the (spherical) Bessel and Hankel functions, and $s, \sigma \in \{-1, 1\}$ indicate the polarization. The quantities with a tilde use the material parameters outside the interface and those without one use the material parameters inside the interface. These quantities can then be used to give the compact closed-form matrix expressions

$$\mathbf{M} = -\frac{\mathrm{i}}{2} \begin{pmatrix} a^{31}_{--} & a^{31}_{-+} & a^{33}_{--} & a^{33}_{-+} \\ a^{31}_{+-} & a^{31}_{++} & a^{33}_{+-} & a^{33}_{++} \\ -a^{11}_{--} & -a^{11}_{-+} & -a^{13}_{--} & -a^{33}_{-+} \\ -a^{11}_{+-} & -a^{11}_{++} & -a^{13}_{+-} & -a^{33}_{++} \end{pmatrix} \tag{E.3}$$

for spheres and

$$\mathbf{M} = -\frac{\mathrm{i}\pi}{4} \begin{pmatrix} A^{31}_{--} & A^{31}_{-+} & A^{33}_{--} & A^{33}_{-+} \\ A^{31}_{+-} & A^{31}_{++} & A^{33}_{+-} & A^{33}_{++} \\ -A^{11}_{--} & -A^{11}_{-+} & -A^{13}_{--} & -A^{33}_{-+} \\ -A^{11}_{+-} & -A^{11}_{++} & -A^{13}_{+-} & -A^{33}_{++} \end{pmatrix} \tag{E.4}$$

for cylinders under illumination perpendicular to their surface.

F Translation coefficients for vector spherical waves

The translation coefficients for the vector spherical waves used in Eqs. (2.50) and (2.53) are given by [26, 36, 37]

$$\begin{aligned} A_{\lambda\mu lm}(\boldsymbol{r},k) = {} & \frac{\mathrm{i}^{\lambda-l}(-1)^m}{2}\sqrt{\frac{(2l+1)(2\lambda+1)}{l(l+1)\lambda(\lambda+1)}}\mathrm{e}^{\mathrm{i}(m-\mu)\varphi} \\ & \cdot \sum_{p=\max(|l-\lambda|,|m-\mu|)}^{l+\lambda} (2p+1)\mathrm{i}^p[l(l+1)+\lambda(\lambda+1)-p(p+1)] \\ & \cdot \sqrt{\frac{(p-m-\mu)!}{(p+m+\mu)!}} \begin{pmatrix} l & \lambda & p \\ m & \mu & \mu-m \end{pmatrix} \begin{pmatrix} l & \lambda & p \\ 0 & 0 & 0 \end{pmatrix} z_p^{(n)}(kr)P_p^{m-\mu}(\cos\theta) \end{aligned} \tag{F.1}$$

and

$$\begin{aligned} B_{\lambda\mu lm}(\boldsymbol{r},k) = {} & \frac{\mathrm{i}^{\lambda-l}(-1)^m}{2}\sqrt{\frac{(2l+1)(2\lambda+1)}{l(l+1)\lambda(\lambda+1)}}\mathrm{e}^{\mathrm{i}(m-\mu)\varphi} \\ & \cdot \sum_{p=\max(|l-\lambda|,|m-\mu|)}^{l+\lambda-1} (2p+1)\mathrm{i}^p\sqrt{((l+\lambda+1)^2-p^2)((p^2-(l-\lambda)^2)} \\ & \cdot \sqrt{\frac{(p-m-\mu)!}{(p+m+\mu)!}} \begin{pmatrix} l & \lambda & p \\ m & -\mu & \mu-m \end{pmatrix} \begin{pmatrix} l & \lambda & p-1 \\ 0 & 0 & 0 \end{pmatrix} z_p^{(n)}(kr)P_p^{m-\mu}(\cos\theta)\,, \end{aligned} \tag{F.2}$$

where the terms in brackets are the Wigner 3j-symbols [88]. The sum over p only needs to include values where $l+\lambda+p$ is even or odd, respectively.

G Plane wave expansion

In Chapter 3, we use the plane wave expansions [15] in cylindrical waves

$$\mathrm{e}^{-\mathrm{i}\boldsymbol{kr}} = \sum_{l=-\infty}^{\infty} (-\mathrm{i})^{|l|} J_{|l|}(kr)\mathrm{e}^{\mathrm{i}l(\varphi_{\boldsymbol{k}}-\varphi_{\boldsymbol{r}})} \tag{G.1}$$

and in spherical waves

$$\mathrm{e}^{-\mathrm{i}\boldsymbol{kr}} = 4\pi\sum_{l=0}^{\infty}\sum_{m=-l}^{l} (-\mathrm{i})^l j_l(kr) Y_{lm}(\theta_{\boldsymbol{k}},\varphi_{\boldsymbol{k}}) Y^*_{lm}(\theta_{\boldsymbol{r}},\varphi_{\boldsymbol{r}})\,. \tag{G.2}$$

H Real and reciprocal space integral

The integral

$$I_n(z,\alpha) = \int_\alpha^\infty \mathrm{d}t\, t^n \mathrm{e}^{-\frac{z^2t^2}{2}+\frac{1}{2t^2}} \tag{H.1}$$

appears in the derivation of quickly converging series of Chapter 3. It is evaluated for complex-valued variables $z, \alpha \in \mathbb{C}$ and for the integer index $n \in \mathbb{Z}$. The values with $n \geq -1$ appear in the real space sum and the values $n \leq 0$ in the reciprocal space sum, as shown below. With the recursion Eq. (3.7), we need for starting values for which we choose $n \in \{-3, -2, -1, 0\}$. The starting value for $n = 0$ and $n = -2$ can be derived by examining the combination [50, 55]

$$zI_0(z,\alpha) \pm \mathrm{i}I_{-2}(z,\alpha) = \int_\alpha^\infty \mathrm{d}t \left(z \pm \frac{\mathrm{i}}{t^2}\right) \mathrm{e}^{-\frac{(zt \mp \frac{\mathrm{i}}{t})^2}{2} \mp \mathrm{i}z} \tag{H.2a}$$

$$= \mathrm{e}^{\mp \mathrm{i}z} \sqrt{2} \int_{\frac{1}{\sqrt{2}}(\alpha z \mp \frac{\mathrm{i}}{\alpha})}^\infty \mathrm{d}u \, \mathrm{e}^{-u^2} \tag{H.2b}$$

$$= \sqrt{\frac{\pi}{2}} \mathrm{e}^{\mp \mathrm{i}z} \operatorname{erfc}\left(\frac{\alpha z \mp \frac{\mathrm{i}}{\alpha}}{\sqrt{2}}\right) \tag{H.2c}$$

first. As shown, it can be transformed to a complementary error function integral. Implementations for the evaluation of this function are widely available. By undoing the sum or difference above, we find

$$I_0(z,\alpha) = \frac{\sqrt{\pi}}{2\sqrt{2}z} \left(\mathrm{e}^{-\mathrm{i}z} \operatorname{erfc}\left(\frac{\alpha z - \frac{\mathrm{i}}{\alpha}}{\sqrt{2}}\right) + \mathrm{e}^{\mathrm{i}z} \operatorname{erfc}\left(\frac{\alpha z + \frac{\mathrm{i}}{\alpha}}{\sqrt{2}}\right)\right) \tag{H.3}$$

$$I_{-2}(z,\alpha) = \frac{-\mathrm{i}\sqrt{\pi}}{2\sqrt{2}z} \left(\mathrm{e}^{-\mathrm{i}z} \operatorname{erfc}\left(\frac{\alpha z - \frac{\mathrm{i}}{\alpha}}{\sqrt{2}}\right) - \mathrm{e}^{\mathrm{i}z} \operatorname{erfc}\left(\frac{\alpha z + \frac{\mathrm{i}}{\alpha}}{\sqrt{2}}\right)\right). \tag{H.4}$$

The other two cases can be evaluated by expanding the exponential in the integral as a power series. Then, we can immediately identify the incomplete gamma function to arrive at the series

$$I_{-1}(z,\alpha) = \frac{1}{2} \int_{\frac{z^2t^2}{2}}^\infty \frac{\mathrm{d}u}{u} \mathrm{e}^{-u} \mathrm{e}^{\frac{z^2}{4u}} \tag{H.5a}$$

$$= \frac{1}{2} \sum_{n=0}^\infty \frac{1}{n!} \left(\frac{z^2}{4}\right)^n \int_{\frac{z^2t^2}{2}}^\infty \mathrm{d}u \, u^{-n-1} \mathrm{e}^{-u} \tag{H.5b}$$

$$= \frac{1}{2} \sum_{n=0}^\infty \frac{1}{n!} \left(\frac{z^2}{4}\right)^n \Gamma\left(-n, \frac{z^2t^2}{2}\right). \tag{H.5c}$$

The equivalent procedure leads to

$$I_{-3}(z,\alpha) = \sum_{n=0}^\infty \frac{1}{n!} \left(\frac{z^2}{4}\right)^{n+1} \Gamma\left(-n-1, \frac{z^2t^2}{2}\right) \tag{H.6}$$

for $n = -3$.

In the reciprocal sum integral we find

$$\int\limits_{\mathrm{e}^{-\mathrm{i}\pi}\frac{\gamma^2}{2\eta^2}}^{\infty} \frac{\mathrm{d}u}{u}\, u^n \mathrm{e}^{-u+\frac{(\gamma k z)^2}{4u}} \tag{H.7}$$

with integer or half integer value n. By substituting $2u = (k\gamma z t)^2$, we arrive at

$$2\left(\frac{k^2\gamma^2 z^2}{2}\right)^n \int\limits_{\frac{\mathrm{e}^{-\mathrm{i}\frac{\pi}{2}}}{kz\eta}}^{\infty} \mathrm{d}t\, t^{2n-1} \mathrm{e}^{-\frac{(k\gamma z t)^2}{2}+\frac{1}{2t^2}} = 2\left(\frac{k^2\gamma^2 z^2}{2}\right)^n I_{2n-1}\left(k\gamma z, -\frac{\mathrm{i}}{kz\eta}\right) , \tag{H.8}$$

where we can easily identify the integral, for which we derived all necessary starting values to apply the recursion formula in Eq. (3.7).

I Whittaker function

The Whittaker function with parameters $\frac{1+|m|}{2} + s$ and $\frac{|m|}{2}$ can be written as [67]

$$M_{\frac{1+|m|}{2}+s,\frac{|m|}{2}}(z) = \frac{\mathrm{e}^{\frac{z}{2}} z^{\frac{1-|m|}{2}} |m|!}{(|m|+s)!} \frac{\mathrm{d}^s}{\mathrm{d}z^s}(\mathrm{e}^{-z} z^{|m|+s}) \tag{I.1}$$

for $m \in \mathbb{Z}$ and $s \in \mathbb{N}_0$. We use the generalized product rule for higher order derivatives

$$\frac{\mathrm{d}^s}{\mathrm{d}z^s}(f(z)g(z)) = \sum_{n=0}^{s} \binom{s}{n} \left(\frac{\mathrm{d}^{s-n}}{\mathrm{d}z^{s-n}} f(z)\right) \left(\frac{\mathrm{d}^n}{\mathrm{d}z^n} g(z)\right) , \tag{I.2}$$

to rewrite Eq. (I.1) as

$$M_{\frac{1+|m|}{2}+s,\frac{|m|}{2}}(z) = \mathrm{e}^{-\frac{z}{2}} |m|! \sum_{n=0}^{s} \binom{s}{n} \frac{z^{\frac{1+|m|}{2}} (-z)^{s-n}}{(|m|+s-n)!} \tag{I.3}$$

and, thereby, in a closed-form expression.

J Sum manipulations

The following finite double sums appear in five cases of the derivation of the lattice sums in Chapter 3. They are manipulated such that their argument takes a simple form. In the case of spherical waves in three dimensions (Subsection 3.3.2), we have

$$\begin{aligned}\sum_{s=0}^{\left\lfloor\frac{l-|m|}{2}\right\rfloor} \sum_{n=0}^{s} a_{s,n} &= \sum_{s=0}^{\left\lfloor\frac{l-|m|}{2}\right\rfloor} \sum_{w=l-|m|-2s}^{l-|m|-s} a_{s,w-l+|m|+2s} \\ &= \sum_{w=0}^{l-|m|} \sum_{s=\left\lceil\frac{l-|m|-n}{2}\right\rceil}^{\min\left(l-|m|,\left\lfloor\frac{l-|m|}{2}\right\rfloor\right)} a_{s,w-l+|m|+2s} \\ &= \sum_{w=0}^{l-|m|} \sum_{v=w}^{\min(l-|m|,2w)} a_{\frac{l-|m|-2w+v}{2},v-w} ,\end{aligned} \tag{J.1}$$

where the sum over v only takes every other value. Next, for spherical waves in a one-dimensional lattice (Subsection 3.3.3), it is

$$\begin{aligned}\sum_{s=0}^{\lfloor\frac{l-|m|}{2}\rfloor}\sum_{n=0}^{\left\lfloor\frac{l-|m|}{2}\right\rfloor-s} a_{s,n} &= \sum_{s=0}^{\lfloor\frac{l-|m|}{2}\rfloor}\sum_{w=|m|+2s}^{\left\lfloor\frac{l+|m|}{2}\right\rfloor+s} a_{s,w-|m|-2s}\\ &= \sum_{w=|m|}^{l}\sum_{s=\max\left(0,n-\lfloor\frac{l+|m|}{2}\rfloor\right)}^{\left\lfloor\frac{w-|m|}{2}\right\rfloor} a_{s,w-|m|-2s}\\ &= \sum_{w=|m|}^{l}\sum_{v=w}^{\min(2n-|m|,l)} a_{w-\frac{v+|m|}{2},v-w}\,,\end{aligned} \tag{J.2}$$

with again v only taking every other value in the sum. The last case are cylindrical waves in a one-dimensional lattice (Subsection 3.3.4), where we have

$$\begin{aligned}\sum_{s=0}^{|l|}\sum_{n=0}^{\lfloor\frac{s}{2}\rfloor} a_{s,n} &= \sum_{s=0}^{|l|}\sum_{w=|l|-s}^{|l|-\lceil\frac{s}{2}\rceil} a_{s,w+s-|l|}\\ &= \sum_{w=0}^{|l|}\sum_{s=|l|-w}^{\min(|l|,2|l|-2w)} a_{s,w+s-|l|}\\ &= \sum_{w=0}^{|l|}\sum_{v=w}^{\min(2w,|l|)} a_{v+|l|-2w,v-w}\,.\end{aligned} \tag{J.3}$$

K Permutation of Cartesian axes

We want to derive the coefficients that are encoding the change in the definition of the plane waves in parity and helicity basis, when we permute the axes labels from x, y, and z to a system with $x = y'$, $y = z'$, and $z = x'$. By relabeling the axes, the wave vector is now written as $\boldsymbol{k} = k_x\hat{\boldsymbol{x}} + k_y\hat{\boldsymbol{y}} + k_z\hat{\boldsymbol{z}} = k_z\hat{\boldsymbol{x}}' + k_x\hat{\boldsymbol{y}}' + k_y\hat{\boldsymbol{z}}'$.

We introduce the vectors $\boldsymbol{m}_{\boldsymbol{k}}$ and $\boldsymbol{n}_{\boldsymbol{k}}$ that are the vector part of $\boldsymbol{M}_{\hat{\boldsymbol{k}}}(\boldsymbol{r})$ and $\boldsymbol{N}_{\hat{\boldsymbol{k}}}(\boldsymbol{r})$ defined in Eq. (2.15), namely

$$\boldsymbol{m}_{\boldsymbol{k}} = \mathrm{i}\frac{k_y\hat{\boldsymbol{x}} - k_x\hat{\boldsymbol{y}}}{k_{xy}} \tag{K.1a}$$

$$\boldsymbol{n}_{\boldsymbol{k}} = \frac{-k_xk_z\hat{\boldsymbol{x}} - k_yk_z\hat{\boldsymbol{y}} + k_{xy}^2\hat{\boldsymbol{z}}}{kk_{xy}}\,, \tag{K.1b}$$

with $k_{xy} = \sqrt{k_x^2 + k_y^2}$. In the coordinate system with permuted axes labels, these vectors are

$$\boldsymbol{m}'_{\boldsymbol{k}} = \mathrm{i}\frac{k_x\hat{\boldsymbol{x}}' - k_z\hat{\boldsymbol{y}}'}{k_{xz}} = \mathrm{i}\frac{k_x\hat{\boldsymbol{z}} - k_z\hat{\boldsymbol{x}}}{k_{xz}} \tag{K.2a}$$

$$\boldsymbol{n}'_{\boldsymbol{k}} = \frac{-k_zk_y\hat{\boldsymbol{x}}' - k_xk_y\hat{\boldsymbol{y}}' + k_{xz}^2\hat{\boldsymbol{z}}'}{kk_{xz}} = \frac{-k_zk_y\hat{\boldsymbol{z}} - k_xk_y\hat{\boldsymbol{x}} + k_{xz}^2\hat{\boldsymbol{y}}}{kk_{xz}}\,, \tag{K.2b}$$

where k_{xz} is defined analogously to k_{xy}. The projections of the vectors in Eq. (K.1) onto those in Eq. (K.2) are

$$-\boldsymbol{m}'_{\boldsymbol{k}}\boldsymbol{m}_{\boldsymbol{k}} = -\frac{k_y k_z}{k_{xy}k_{xz}} \tag{K.3a}$$

$$-\boldsymbol{m}'_{\boldsymbol{k}}\boldsymbol{n}_{\boldsymbol{k}} = -\mathrm{i}\frac{k_x k_{xy}^2 + k_x k_z^2}{k k_{xy} k_{xz}} = -\mathrm{i}\frac{k_x k}{k_{xy}k_{xz}} \tag{K.3b}$$

$$\boldsymbol{n}'_{\boldsymbol{k}}\boldsymbol{m}_{\boldsymbol{k}} = -\mathrm{i}\frac{k_x k_y^2 + k_x k_{xz}^2}{k k_{xy} k_{xz}} = -\mathrm{i}\frac{k_x k}{k_{xy}k_{xz}} \tag{K.3c}$$

$$\boldsymbol{n}'_{\boldsymbol{k}}\boldsymbol{n}_{\boldsymbol{k}} = \frac{-k_z k_y k_{xy}^2 + k_z k_y k_x^2 - k_z k_y k_{xz}^2}{k^2 k_{xy} k_{xz}} = -\frac{k_y k_z}{k_{xy}k_{xz}}\,, \tag{K.3d}$$

where the minus sign comes from $\boldsymbol{m}_{\boldsymbol{k}}^2 = -1$ in the convention we use. In summary, these coefficients can be written compactly as

$$\frac{1}{k_{xy}k_{xz}}\begin{pmatrix} -k_y k_z & -\mathrm{i}k k_x \\ -\mathrm{i}k k_x & -k_y k_z \end{pmatrix}, \tag{K.4}$$

which becomes

$$\begin{pmatrix} 0 & -\mathrm{i} \\ -\mathrm{i} & 0 \end{pmatrix} \tag{K.5}$$

for $k_x = k_y = 0$ and

$$\begin{pmatrix} -\frac{k_y}{k} & 0 \\ 0 & -\frac{k_y}{k} \end{pmatrix} \tag{K.6}$$

for $k_x = k_z = 0$. The transformations in the helicity basis are

$$\frac{-k_y k_z \mp \mathrm{i}k k_x}{k_{xy}k_{xz}} \tag{K.7}$$

for helicity ±1.

Acknowledgements

Writing a doctoral thesis is always an important milestone in one's scientific and, moreover, personal development. Thus, it is an excellent opportunity to acknowledge the received support, because the own individual small steps and – although considerably rarer – larger leaps are only made possible by the help of many other people. Summarizing all these contributions and mentioning everyone in few sentences here is a substantial task. So, if I forgot someone, I want to ask for leniency upfront.

I want to thank Carsten Rockstuhl for his outstanding supervision: for the very balanced mix of receiving scientific guidance and advice on the one hand and the opportunity to explore and develop ideas with great freedom on the other hand. I substantially benefited from his broad knowledge and attention to details. Additionally, I highly appreciate his ability to create and maintain the inspiring environment. I also want to thank Vassilios Yannopapas for volunteering to review and assess my work. Furthermore, I want to thank Ivan Fernandez-Corbaton for all the advice received in countless discussions. I am thankful for the frequent encouragement and motivation.

As this thesis shows, a large part of my work grew on and benefited from the collaboration with other scientists within the working group and also with other institutes. I want to thank all co-authors for the great and inspiring cooperation. It greatly broadened my scientific knowledge and allowed me to learn about many exciting and interesting topics and viewpoints.

I also want to thank the people with whom I shared the office for all the moments I needed a quick answer – which could result in hour long discussions from time to time – or for having a welcome distraction from the daily work. Over the years, these were Radius Suryadharma, Aso Rahimzadegan, Theodosios Karamanos, Yannick Augenstein, Mitchell Whittam, David Dams, and Xuchen Wang. Of course, I also want to thank all the other current and former members of the group for providing a superb environment for scientific work, but, moreover, for the great atmosphere that really made it a pleasure to come to the office. A special thanks goes to Benedikt Zerulla for the proof-reading of this thesis.

I want to dedicate the last paragraph expressing my gratitude to my friends and family, because the work on and the writing of a doctoral thesis is not something one can leave on the campus when going home in the evening. The successes and challenges become also part of the life outside of the office. I am immensely grateful to Barbara Dietel, for all her love and support. Furthermore, I want to thank my parents Charlotte Beutel and Günther Beutel for all their help and advice bringing me to where I am today.

Selbstständigkeitserklärung

Eidesstattliche Versicherung gemäß § 13 Absatz 2 Ziffer 3 der Promotionsordnung des Karlsruher Instituts für Technologie (KIT) für die KIT-Fakultät für Physik:

1. Bei der eingereichten Dissertation zu dem Thema „A holistic framework for electromagnetic scattering simulations based on the T-matrix method “ handelt es sich um meine eigenständig erbrachte Leistung.

2. Ich habe nur die angegebenen Quellen und Hilfsmittel benutzt und mich keiner unzulässigen Hilfe Dritter bedient. Insbesondere habe ich wörtlich oder sinngemäß aus anderen Werken übernommene Inhalte als solche kenntlich gemacht.

3. Die Arbeit oder Teile davon habe ich wie folgt / bislang nicht[1] an einer Hochschule des In- oder Auslands als Bestandteil einer Prüfungs- oder Qualifikationsleistung vorgelegt.

   Titel der Arbeit: A holistic framework for electromagnetic scattering simulations based on the T-matrix method

   Hochschule und Jahr: KIT-Fakultät für Physik, 2023

   Art der Prüfungs- oder Qualifikationsleistung: Dissertation

4. Die Richtigkeit der vorstehenden Erklärungen bestätige ich.

5. Die Bedeutung der eidesstattlichen Versicherung und die strafrechtlichen Folgen einer unrichtigen oder unvollständigen eidesstattlichen Versicherung sind mir bekannt.

Ich versichere an Eides statt, dass ich nach bestem Wissen die reine Wahrheit erklärt und nichts verschwiegen habe.

Ort und Datum

Unterschrift

---

[1] Nicht Zutreffendes streichen. Bei Bejahung sind anzugeben: der Titel der andernorts vorgelegten Arbeit, die Hochschule, das Jahr der Vorlage und die Art der Prüfungs- oder Qualifikationsleistung.